REACTION FRONTS IN POROUS MEDIA: CONTINUUM MODELLING IN FUNDAMENTAL CONFIGURATIONS AND APPLICATIONS TO GEOSCIENCE

Danielle Victoria Bullamore

A thesis submitted in accordance with the requirements for the degree of Doctor of Philosophy

THE UNIVERSITY OF LEEDS

Centre for Doctoral Training in Fluid Dynamics

School of Computer Science

April 2025

Intellectual Property and Publication Statements

The candidate confirms that the work submitted is her own, except where work which has formed part of jointly authored publications has been included.

The contribution of the candidate and the other authors to this work has been explicitly indicated below. The candidate confirms that appropriate credit has been given within the thesis where reference has been made to the work of others.

The work in chapter 3 of the thesis is being prepared for submission to the Journal of Fluid Mechanics under the title: *Two-phase reaction fronts in porous media: control of emergent structure, sharpness and regime analysis.*, D.V. Bullamore and S. Pegler.

The work in chapter 4 of this thesis is being prepared for submission to the Journal of Fluid Mechanics under the title: *'Reactive injection into a porous medium'*, D.V. Bullamore and S. Pegler.

The work in chapter 5 of this thesis is being prepared for submission to the Geologist Magazine with authors D.V. Bullamore, S. Piazolo and S. Pegler.

Work included in this thesis has been presented at the following conferences

- UK Fluids Conference: 2021, 2022, 2023
- APS-DFD Annual Meeting: 2022, 2023

Acknowledgements

Thanks to my lead supervisor Sam Pegler for his continued support and enthusiasm throughout my PhD. Thanks to my second supervisor Sandra Piazolo for trusting us to jump into the deep end mathematically and bring it back to geology in the end. I'd like to thank the CDT in Fluid Dynamics for giving me the chance to even do this research. Across the CDT, there's too many people to name and working alongside you all for some of the last 5 years has been a pleasure.

A huge thank you goes to my friends, firstly to Rachael & Amy who've put up with me for an awfully long time now. I couldn't have done this without you both. Thanks to Giulia & Julie for the many hours spent drinking tea in the office. I owe my ongoing sanity in the production of this thesis to my ballet and aerial class instructors & friends, the evenings I've spent doing no maths at all were exactly what I needed.

Finally, and perhaps most importantly, I'd like to thank my family for their support through this PhD. I'm still not entirely sure they get what I've done, but they've supported me throughout.

This work was supported by the EPSRC Centre for Doctoral Training in Fluid Dynamics (EP/S022732/1).

Abstract

Reactive flows in porous media are characterised by the development of a moving reaction front separating reacted and unreacted regions. These fronts are observed in many geoscience settings, such as mantle dynamics and hydrous flow in crustal rock. The connection between reacted and unreacted regions can involve either a smooth or sudden near-interfacial transition, in each of porosity and reactant concentration. This thesis studies the contributions of transport and reaction to the control of the transition in fundamental geometries, and seeks to demonstrate the quantitative use of the resulting relationships in geoscience examples. This thesis presents generalised novel regime diagrams for the dynamics of reaction fronts in fundamental configurations.

The first of these configurations is the generation of a planar reaction front, supplied by a constant flux of fluid. A detailed mathematical study of its predictions to classify emergent regimes and their parametric controls is conducted. The limiting late-time regimes are the sharp and the diffusionless regime, characterised by the separation of scales between the porosity and concentration transitions and by the controlling balance of transport respectively. The second configuration is a reaction front supplied by a local point source, with a constant radial flux. A detailed asymptotic analysis of the emergent regimes and their parametric controls is performed. In this configuration the reaction front tends towards sharpness irrespective of the Péclet number, with the Péclet number instead controlling whether the front tends towards the 1D reaction front in a quasi constant-flux regime.

The third problem addressed in this thesis is to begin to understand the instability of planar reaction fronts. The conditions for the linear stability of planar reaction fronts in the sharp porosity transition limit are derived. The resultant dispersion relation is applied to geoscience applications, demonstrating scenarios for which the linear model can and cannot predict emergent instability.

Contents

List of Figures

List of Tables

Nomenclature

D	Diffusivity of chemical species [$m^2\ s^{-1}$]
$R(c, \phi)$	Reaction rate function
W, V	Reaction front propagation speed [$m\ s^{-1}$]
Ψ_s	Sphericity of a particle [-]
$\boldsymbol{f}$	Body force [Pa]
κ	Permeability of porous host [m^2]
μ	Fluid viscosity [$N\ s\ m^{-2}$]
ν	Volumetric ratio of fluid produced to solid consumed [-]
ϕ	Porosity of a solid [-]
ϕ_0	Initial porosity of a solid [-]
ϕ_*	Maximum porosity of a solid [-]
$\boldsymbol{q}$	Fluid flux [$m^2\ s^{-1}$]
ρ_i	Density [$kg\ m^{-3}$, subscripts S (solid), F (bulk fluid)]
$\boldsymbol{u}$	Fluid velocity [$m\ s^{-1}$]
c	Concentration of reactant [$mol\ m^{-3}$]
c_0	Inlet concentration of reactant [$mol\ m^{-3}$]
c_P	Reaction rate coefficient for produced species [$mol\ m^{-3}$]
c_R	Reaction rate coefficient for consumed species [$mol\ m^{-3}$]
d_p	Volume equivalent spherical diameter [m]

$f(\phi)$ Reaction rate dependence on ϕ

k Reaction rate parameter [s^{-1}]

p Fluid pressure [Pa]

w Concentration of product [mol m^{-3}]

1

Introduction

The flow of reactive fluids in porous media arises throughout the natural and industrial world, across a wide range of scales. Examples include the flow of fresh or saline water through porous ice and snow [e.g. Poulikakos and Kazmierczak, 1988, Meyer and Hewitt, 2017], the forced or natural weathering of porous rocks [e.g. Hinch and Bhatt, 1990, Merino and Banerjee, 2008, Szymczak and Ladd, 2009], and reactive two-phase flows in the Earth's mantle and magma reservoirs [e.g. Katz and Weatherley, 2012, Pec et al., 2017, Edmonds et al., 2019]. The physical and chemical interactions between interstitial fluids and porous solids lead to complex coupled interactions between fluid dynamics, transport processes, reaction kinetics and solid structure.

Industrially, 'acid treatment' of oil fields is a frequently used technique in order to enhance oil recovery [e.g. Williams et al., 1979]. In this scenario, an acid is injected under high pressure into porous bed rock in order to dissolve away blockages (and in the case of carbonates, the bed rock itself) to increase the permeability of the rock. Out of this context arose some of the first observations of the 'reaction-infiltration' instability wherein the injected acid appears to generate preferential pathways through the approximately homogenous bedrock.

A key phenomenon in such flows is the development of a *reaction front*, a zone of transition in both the porosity and the chemical (or thermal) concentration of a reactive agent

between reacted and unreacted regions (figure 1.1). Reaction fronts form from the interaction between molecular (or thermal) diffusion of the reactive agent, its advection within the fluid, and the kinetic transfer of material between solid and fluid components. The resolution of these effects can produce either relatively sharp, near-interfacial transitions in porosity, or smooth large-scale transitions relative to the length scales of the flow. Figure 1.1 shows a schematic representation of a reaction front, in two simple geometries, in which the porosity (shown as grey circles) and concentration, varying from dark purple (high concentration) to white (low concentration) vary across the front region. A planar reaction front (figure 1.1(a)) can be thought of as arising in the case where flow is generated at a planar boundary, such as flow originating from the edge of a melt vein. The radial reaction front shown in figure 1.1(b) originates from a point source of injection. Control of reaction front dynamics in each geometry remains an open question, and in particular understanding how the two geometries generally relate to one another remains unstudied.

Prior work in the geophysical and industrial fields [e.g. Hinch and Bhatt, 1990, Chadam et al., 1986] has sought to understand the resolution of those effects. In order to study models of reaction fronts with reduced complexity, each studies the contributing effects that are important in their applications. Unifying these limiting scenarios that prior work has studied into a general model allows us to understand where in the intermediate parameter spaces each model applies and to understand what effects are most critical.

Another equally important phenomenon in these reactive flows is the development of 'reactive infiltration instabilities', referred to as *porosity channels, fingers* and *melt channels* [Chadam et al., 1986, Aharonov et al., 1995, Grodzki and Szymczak, 2019], which broadly speaking are localised regions of higher flux through pathways of increased permeability (generated by reaction), which causes a finger like advancement of the reaction front ahead of the stable reaction front. As the permeability of the region becomes higher, it is easier for fluid to advance through the medium by following these pathways which in turn, increases the permeability further creating an unstable feedback loop where focusing into the fingers continues to increase. Figure 1.2 shows samples of rocks obtained from the South Island of New Zealand which show evidence of reactive infiltration instability.

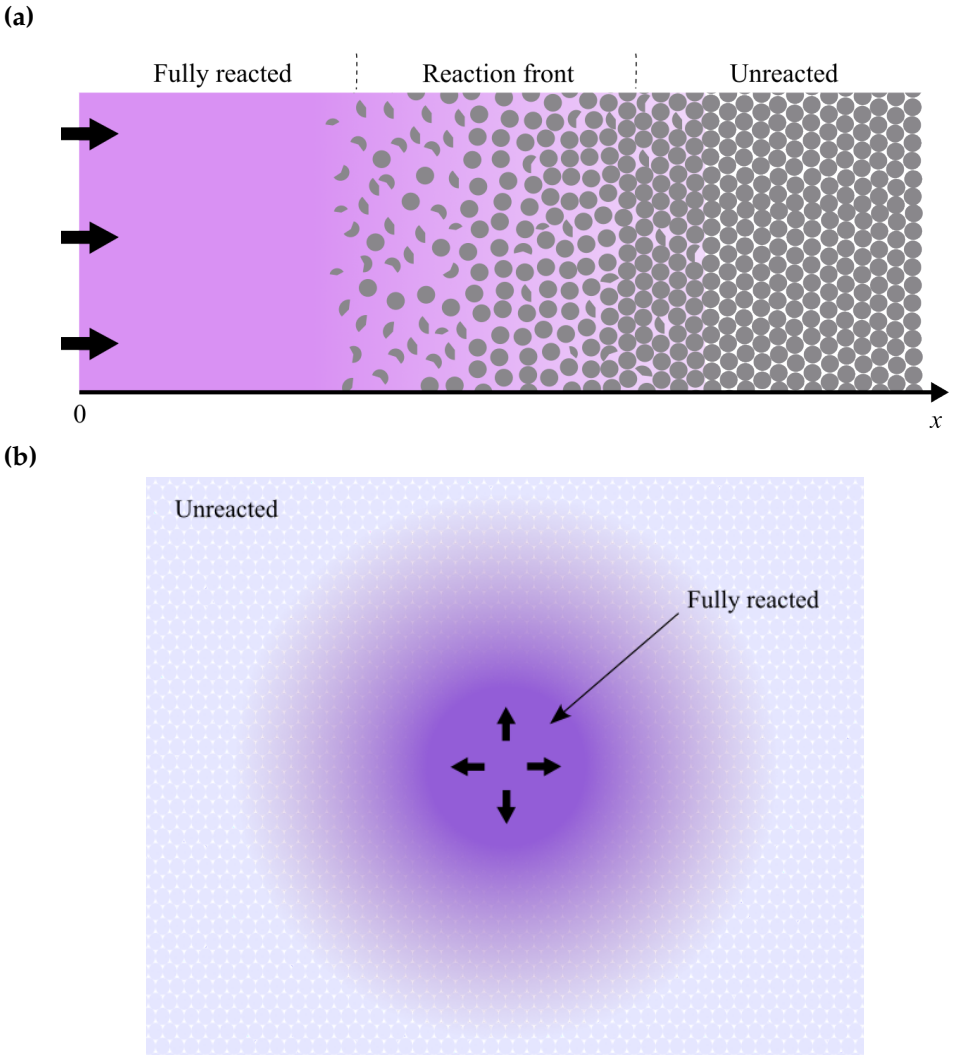

Figure 1.1: Schematic diagrams depicting (a) a planar reaction front fed by a uniform 1D source and (b) an axisymmetric reaction front fed by a constant flux point source. The concentration of reactant decreases smoothly from high concentration (dark purple) to low concentration (white) and porosity from high (no particles) to low porosity (densely packed particles).

A vein through the centre of each sample is filled with white granodioritic rock, where melt would have flowed and reacted with the host rock on the side walls, generating the pink *garnet reaction zone* which is seen having started to develop fingers of preferential flow and reaction.

Prior work motivated by industrial applications [e.g. Hinch and Bhatt, 1990] have studied the growth of fingers from reaction fronts with no diffusion, to try to understand how the growth is controlled. Prior work motivated by geophysical applications have sought to understand the growth of fingers from the reaction front [Chadam et al., 1986, Szymczak and Ladd, 2012], as well as fingers that grow from a uniform background flow in the scenario of mantle upwelling [Rees Jones and Katz, 2018, Rees Jones et al., 2021]. Experimentally, Spruzeniece [2016], Pec et al. [2017, 2020], Beaudoin et al. [2018] have studied the generation of this instability across a range of geological materials. In each case, samples of known composition were placed in a bath of reactive fluid under pressure to induce flow and scanned using techniques such as electron microscopy periodically to observe the developed reaction front over time. A limitation of experimental research in this area is that the results of experiments are fairly specific to their set up, include all physics, and extrapolation to e.g. smaller flowrates, or higher pressure scenarios is not necessarily possible. Field observation is also limited as one cannot observe reactive fingers as they grow, but instead a snapshot in time of where they existed at some earlier time. Thus temporal analysis of field examples requires the comparison of different samples.

Numerical simulations, such as the discrete network model used in Koehn et al. [2021], have advantages in this regard as one can include all the physics necessary to ones problem, and subject to proper numerical treatment are able to simulate a wide parameter space. Numerical treatments always have some associated numerical error which must be quantified. Numerical modelling from a continuum approach [e.g. Szymczak and Ladd, 2013] has largely focused on the linear stability of reaction fronts, rather than on the non-linear dynamics.

Theoretical treatments, as I carry out in this thesis, and as carried out by e.g. Chadam et al. [1986] and Hinch and Bhatt [1990] require a simplified physical model of the natural phenomenon in order to produce analytical results which may be used to analyse phe-

Figure 1.2: Images of rock samples from the South Island of New Zealand, showing evidence of melt fingers in a reaction front driven from a vein. Pen for scale.

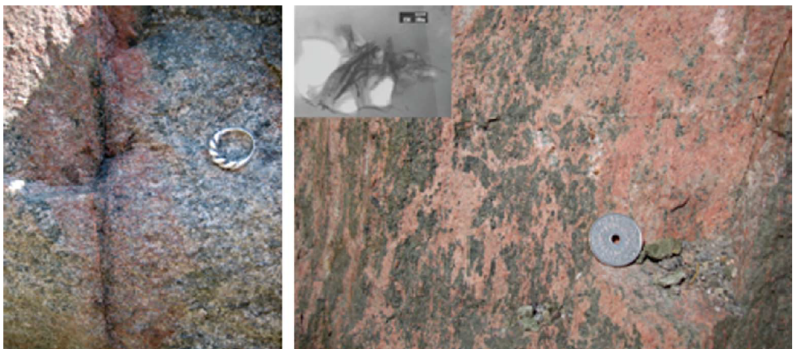

Figure 1.3: Images of rock samples from the Bamble sector, S.E Norway, showing evidence of hydrous infiltration of granite rock [Putnis, 2021]. The regions of red rock indicate the flow routes of water through the rock, with which the host rock has reacted to become red. Ring for scale.

nomena within the theoretical framework. In the case of theoretical models, one must be selective in the physics included and therefore rely on this being the most important physics. For example, we will neglect certain physical effects such as deformation of the porous medium throughout our work. However, this thesis covers the development of a broad parameter space by relaxing some of the assumptions that are made in existing literature. The application of theoretical results to compare and subsequently interpret field observations heuristically remains to be done, thus quantitative application of the theoretical results in this thesis to observation in geoscience is performed in a preliminary way here.

1.1 Research aims and questions

In this thesis I present new theoretical modelling of a fluid with a reactive component that flows through a porous medium and reacts to consume some of the porous solid, altering the porosity in turn. The aim of this modelling is to develop understanding of the parametric and temporal controls on the reactive flow behaviour, and to apply these new results to examples in geoscience. These aims are summarised:

Research aims

- To develop understanding of the temporal evolution of reactive flow upon initiation into an unaltered domain.
- To develop understanding of the regimes that reaction fronts may occur within if they reach steady flow
- To apply results of first principles modelling of reactive flow in porous media to scenarios in geoscience and understand where this type of modelling works.

The specific research questions that I seek to address are:

Research questions

RQ1. How do reaction fronts evolve in fundamental geometries?

RQ2. What controls the extent of chemical and porosity transitions in steadily propagating 1D fronts?

RQ3. How does a radially decaying flux influence reaction fronts versus a constant uniform flux?

RQ4. How does the stability of 1D reaction fronts inform understanding of reactive fronts in geological porous media?

The specifics of these questions are detailed in Chapter 2, putting them into the context of the detailed background.

1.2 Thesis outline

This thesis contains 7 chapters. Chapter 2 introduces key background, including geological motivation for this study, reviews existing mathematical work around reacting porous medium and develops the general continuum model studied in this thesis. This is followed by Chapters 3–6 of novel scientific research.

Chapter 3 develops a 1D model for reactive flow, outlines the implementation of the method of lines to solve the model formulation in 1D, describes the temporal evolution of 1D reaction fronts as a function of parameters, fundamentally ending in a travelling wave system. This is studied and the parameter space is partitioned based upon asymptotic behaviour. This Chapter represents the work of a paper, which is being prepared for submission to the *Journal of Fluid Mechanics* under the title *'Two-phase reaction fronts in porous media: control of emergent structure, sharpness and regime analysis.'*

Chapter 4 develops an axisymmetric model for reactive injection into porous media and a temporal regime diagram explaining the development of reaction fronts in axisymmetry is developed. This is motivated by the fact that infiltration by a reactive flow can occur locally as well as in one-dimensional along a boundary and therefore allows for differing dynamics. This Chapter describes the fundamental regimes arising and partitions the parameter space to describe the late-time evolution of concentration and porosity in this domain. This Chapter forms the basis of a publication under the title *'Reactive injection into a porous medium'* which is being prepared for submission to the *Journal of Fluid Mechanics*.

Chapter 5 develops an analysis of the linear stability of the diffusive limit of the one dimensional reaction front. It then develops applies the result of the stability analysis to geological settings in which reactive infiltration instability may or may not arise and seeks to use the linear stability results to form a toolkit for understanding geological scenarios. This forms the basis of a paper drafted for submission to the *Geologist Magazine*, for an audience of geologists.

Chapter 6 outlines the extension of the method of lines solver to the two-dimensional domain and validates the use of the method of false transients to do so. Initial results

validate the predicted wavelength of instability and demonstrate how initial conditions can alter reaction fronts.

Finally, Chapter 7 provides a general discussion of the findings of this work, in the specific light of the research questions above, and finishes with conclusions on the limitations of this work and potential areas for future work.

2

Background

This Chapter reviews the motivation for this study, theory and model development of previous works which investigate reaction fronts in porous media. It begins with an overview of the geological motivation for understanding the parametric control of reaction fronts and reactive infiltration instabilities, and an overview of geological knowledge of the transport of fluids (melt and aqueous fluids) through a porous host rock. It then reviews mathematical works motivated by a wide range of instances of reaction fronts and the theories developed in those works, before also reviewing mathematical treatments of reactive infiltration instabilities. Finally I put the research questions of section 1.1 into the context of the existing work in this area of study.

2.1 Geological context

Two-phase flows arise in many geological settings, owing to complex temperature and pressure profiles as we move through the Earth's lithosphere. Such flows may control the melting or partial melting of crustal rock and magma. It is thought that this melting can induce flow of molten rock through host rock of a different composition, resulting in two-phase compositions which are preserved and can be observed in the field. While the amount of free fluid in the Earth's crust is small relative to solid, it is thought to play a major role in many processes, including the flow of lithospheric and asthenospheric

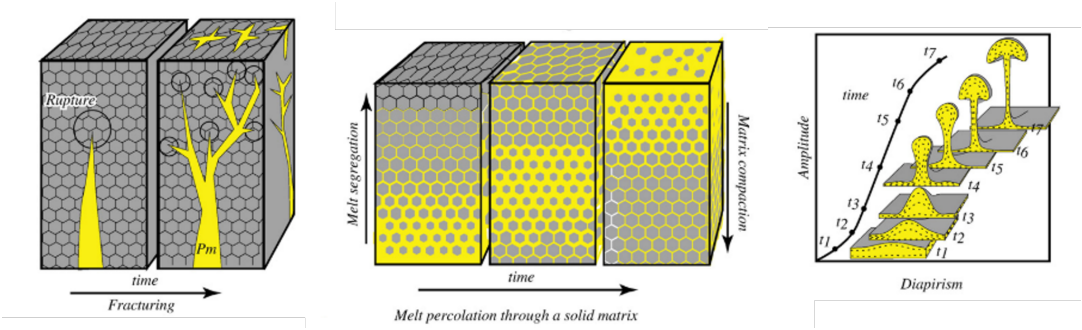

Figure 2.1: Schematic representation of mechanisms of melt segregation through a solid host material. Left to right: fracturing, melt percolation and diapirism. Images from Vanderhaeghe [2009].

melt and magma [e.g. Katz and Weatherley, 2012, Pec et al., 2017, Edmonds et al., 2019], weathering [Merino and Banerjee, 2008, Szymczak and Ladd, 2011b], and earthquake generation [Sibson, 1996]. Dunite channels are formed in the asthenosphere, [Braun and Kelemen, 2002].

The transport of melt, 'melt escape', and of other fluid through the host rock can be theorised as either a locally or non-locally driven event; some mechanisms of transport are shown schematically in figure 2.1. In this context when we discuss 'local' transport, it is the transport of a large volume of fluid through a localised region such as a fracture or a weakened area leading to a diapir. 'Non-locally' driven melt transport is by percolation throughout the whole solid medium, and this can be localised due to instability, but the background mechanism of flow occurs throughout the medium. Fracturing and diapirism are localised effects caused by excess fluid pressure. Broadly speaking, fracturing tends to occur in a brittle host whilst diapirism arises by ductile deformation [Vanderhaeghe, 2009]. In this work, we focus on the scenario in the middle panel of figure 2.1, the 'non-local' migration of melt through a porous host material and explore whether this can explain melt flow patterns which are preserved in geology.

Non-local flow through the porous host was proposed in Weinberg [1999] as an alternative to fracturing, given that there is difficulty in initiating fractures due to the high pressure required. Whilst the porosity of crustal rock is generally low, it is broadly accepted that porous flow through the host rock occurs. Mesoscale intrusions could form widely connected sheets of melt within the crustal rock, creating high throughput pore networks.

The resultant magma sheets may be located preferentially to take advantage of high permeability foliations and bedding planes. This apparent self-organisation of the magma to preferential, high permeability channels and sheets has lead to investigation of feedback mechanisms to support this [Weinberg and Regenauer-Lieb, 2010].

The drivers of pervasive flow could include tectonic pumping, magma wedging into low-viscosity host rock and volatile driven intrusion, [Kelemen et al., 1995b, Holtzman et al., 2003, Hewitt, 2010]. Holtzman et al. [2003] performed experiments which developed segregated melt-rich layers under shear stress, which suggests that stress on the host can organise flow such that high permeability sheets are formed facilitating rapid extraction of magma. Pervasive flow of magmas has also been proposed in the context of transport to mid-ocean ridges. Hewitt [2010] investigated melting in convecting magma mush, with the opportunity for in situ melt to connect and form a porous network. Prior work proposed that transport through the network happens at a rate which maintains chemical equilibrium with the surrounding rock; however inferences from the geochemistry of erupted melts show chemical disequilibrium, suggesting a much faster organised network of melt transport ought to arise (Kelemen et al. [1995b]).

This motivates this study of reactive flow in porous media because in geological contexts, fluid infiltration and reactions with the host rock can result in changes to the composition of the host rock which affect its mechanical and hydrodynamic properties. These chemical changes are preserved and ideally a geologist would like to be able decipher the conditions under which these changes occurred. For example, is it possible identify if transport of a chemical in the fluid is advection or diffusion limited?

2.1.1 Characteristic fluids in geological porous media

In the geological context, fluids flowing through a porous medium are generally classified as *melt* or *hydrous* fluids. Fluid mechanically, the difference between the two arises in their differing viscosities. Melt (molten rock) is thought to have viscosity $\mu \approx 10$–10^2 Pa s [e.g. Spiegelman, 1993, Pec et al., 2017], whilst hydrous fluids are significantly less viscous, $\mu \approx 10^{-4}$–10^{-3} Pa s [Hack and Thompson, 2011]. The consequence of this for fluid flow

through a porous medium can be seen in the form of Darcy's law

$$\boldsymbol{q} = \frac{-\kappa}{\mu}\nabla p,$$

which tells us that for a given pressure gradient, ∇p, a fluid with higher viscosity μ will flow with a slower flux $\boldsymbol{q}$ than that with a lower viscosity. Typically, hydrous fluids percolate through porous rocks in the lithosphere faster than melt does. Hydrous melts, a mixture of the two, fall in between the two and can vary greatly based on their composition. Models such as Giordano et al. [2008] are well calibrated for calculation of the fluid viscosity at high temperatures where experimental measurement is not practical.

2.1.2 Fluid induced reactions in geological porous media: Nature and effects

Where fluid flow through geological porous media is thought to occur, the signature of that flow is often seen in the chemical composition of the rocks. Where a melt has solidified within a porous host, it is marked by a different composition to the residual host. One such signature in regions with rising magma is that the melt becomes undersaturated in a component during its ascent, and thus that component is transferred from the solid to the fluid as it rises [Kelemen et al., 1995a]. A key dissolution reaction that occurs in this instance can be written schematically as

$$\text{magma}_1\ (\text{l}) + \text{pyroxene}\ (\text{s}) \longrightarrow \text{magma}_2\ (\text{l}) + \text{olivine}\ (\text{s}),$$

[Rees Jones and Katz, 2018] where (l) denotes a component in the liquid and (s) a component in the solid phase. The subscripts 1 and 2 indicate magmas of different compositions. This is known as a replacement reaction, replacing the pyroxene in the host rock with olivine, and it is thought to explain geological observations of tabular dunites (almost purely olivine by composition) as evidence of such reactions occurring in the Earth's crust [Kelemen et al., 1992, Spiegelman and Kelemen, 2003]. Tabular dunites are lenses of olivine found within a larger body of pyroxene, which are likely the regions of host rock through which the highest fluxes of melt occurred. Figure 2.2 shows an example of large scale dunite (lighter regions in the image) preserved in a region of harzburgite.

An example of a hydrous reaction (the associated patterning of which is shown in fig-

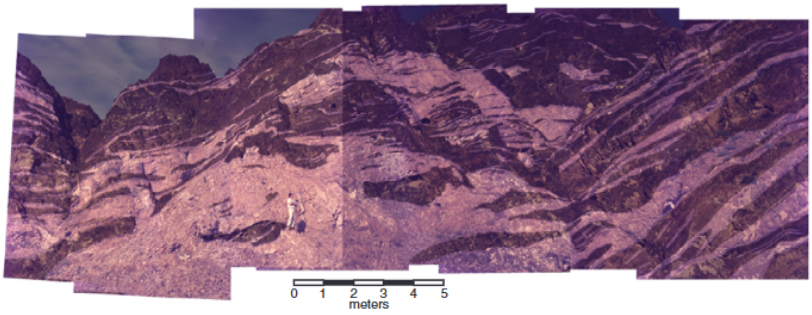

Figure 2.2: Photomosaic from Braun and Kelemen [2002] of dunites in the Muscat massif. Lighter regions are dunite rocks, darker regions are residual harzburgite. The maximum measured channel in this region is O(100 m).

ure 1.3) is a combination dissolution-precipitation reaction that results in pink hematite occlusions in granitic rock. The first step is the dissolution of feldspar by water

$$\text{hydrous fluid (l)} + \text{feldspar (s)} \longrightarrow \text{acidic hydrous fluid (l)} + Fe^{2+}\,\text{(aq)},$$

this reaction that produces Fe^{2+} ions and increases the acidity of the fluid at the same time. As a consequence of the increase acidity, the produced Fe^{2+} ions are converted to Fe^{3+}. At a later point, the Fe^{3+} precipitates as hematite (pink) where it is recrystallised in host granite,

$$Fe^{3+}\,\text{(aq)} + \text{hydrous fluid}_1\,\text{(l)} \longrightarrow \text{hydrous fluid}_2\,\text{(l)} + Fe_2O_3\,\text{(s)}$$

forming the pink or red coloured occlusions of hematite seen in figure 1.3.

There are many rich and complex reactions that occur when a fluid flows through a host rock, a broad selection of which can be found in e.g. Putnis [2021] with accompanying images of the patterning that develops as a result.

2.1.3 Paradigms for modelling reactive flow

The two main bodies of work studying reactive flow in porous media stem from two fundamental paradigms, which can be thought of as the 'reaction front flow' and the 'pervasive flow'. Pervasive flow, studied by [e.g. Aharonov et al., 1995, Spiegelman and Kelemen, 2001, Rees Jones and Katz, 2018] amongst others, typifies a scenario in which fluid is continuously rising through a porous medium, as depicted in in the central panel of figure 2.1. In this configuration, there is a uniform background flow with transfer of

material between the solid and porous medium. Works such as Aharonov et al. [1995] and Rees Jones and Katz [2018] study the stability of such flows and how mechanical and chemical interactions change their stability. The instability, and thus the spatial variation in porosity and concentration, that emerges in pervasive flow extends throughout the domain.

The other paradigm of the reaction front flow is the one we focus on in this thesis and is shown schematically in figure 1.1. In this scenario, a reaction front is formed when a reactive fluid is introduced into a porous medium and results in a localised reactive region that propagates through the porous medium. Unlike the pervasive flow paradigm, the chemical interaction of the fluid and host solid does not span the whole domain. This set up has been the basis of prior works, e.g. [e.g. Chadam et al., 1986, Chadam, 1993, Szymczak and Ladd, 2013].

2.1.4 Geoscientific modelling of reactive flow in porous media

Modelling of reactive flow in porous media for geoscience applications is generally either numerical or experimental in nature. These are complementary to one another, with experimental studies carried out using geological materials or analogous materials and numerical modelling having the capacity for including relevant physics. Here I briefly discuss the existing literature in this area.

Experimentally, Kelemen et al. [1995b] present analogue experiments on the dissolution of salt by water flowing, under gravity, through a porous bed composed of salt grains and glass ballotini. These experiments demonstrated the emergence of channels of high fluid flux, with channel growth over time. This work hypothesised pervasive reactive porous flow as an alternative to the extraction of mid-oceanic ridge basalts by fracture.

The later experimental studies of Pec et al. [2017, 2020] performed laboratory experiments on samples with compositions found in mid-oceanic ridges in order to understand how the lithology of the host affected channelisation. This work produced a range of chemical and mechanical results for different lithologies, providing a dataset of responses for future numerical modelling.

A simpler reaction studied experimentally is the replacement reaction of a single crystal of KBr in aqueous KCl by Beaudoin et al. [2018], in which the chlorine in solution replaces the bromine and as a result the porosity of the crystal is increased. Imaging techniques and processing are used to identify regions of high porosity, and it is seen here that fingers of high porosity KCl are generated over time.

2.1.5 Numerical modelling of reactive flow

Parallel to the experimental developments, there are three main bodies of work over the last roughly thirty years, which study high order numerical models of reactive flow in porous media, with a view to understanding melt pathways and patterns arising from flow in the upper mantle. An early work, Spiegelman and Kelemen [2003] developed a numerical model which demonstrates the growth of channels in an upwelling scenario. The typical domain comprises a vertical channel of height L through which fluid is driven upward by a pressure gradient and can dissolve solid as it does so. The solubility of the chemical species in the fluid phase is linearly dependent on height, such that fluid has the capacity to dissolve more of the host rock as it rises. This work demonstrated that chemical variation observed in geological samples, such as variation of trace element concentrations, can be explained by melt channelisation. Advances in numerical schemes, such as the work done in Spiegelman et al. [2016] to develop effective solvers for high non-linear viscoplastic flow allow for more complex modelling of the fluid and the porous medium. Further work building upon this, e.g. Sim et al. [2020] studied a suite of two-phase models applied to mid-ocean ridges, in order to understand melt focusing below mid-ocean ridges and its relevance to the lithosphere-asthenosphere boundary. Their work shows how melt transport is sensitive to the host medium permeability, and they provide new constraints on the mantle rheology and permeability required to reproduce the steep inclines in chemical composition seen in geology.

In the context of upwelling in the mantle, with a view to understanding dunite channels, Liang et al. [2010] developed high resolution numerical modelling of reactive dissolution in a porous medium. This study showed that high-porosity dunite channels are transient, near-crustal parts of melt migration pathways which begin deeper in the mantle with

harzburgite and lherzolite. The size of the dunite channel is dependent on the geometry of the lower portions of the melt pathway. Further work in this group has continued to study the transient nature of dunite channels, for example Hesse et al. [2011] studied the conditions required for compaction-dissolution waves, in which the location of dunite regions changes in time, to form as opposed to channels which are approximately static. This work found that waves are favoured when there is increased upwelling of solid and when the solubility gradient of chemical species is low. Their later work, Schiemenz et al. [2011] continued to study these dynamics in a deforming porous medium numerically, with findings including how the depth of dunite material is controlled by complex interplay of the flow physics and chemical composition.

A complementary body of work around the same time, including Katz and Weatherley [2012], Turner et al. [2017], Bo et al. [2018] also studied pervasive flow in an upwelling column. Katz and Weatherley [2012] numerically studied how the heterogeneity of the mantle affects the pathways of melt transports. Modelling a mantle with heterogeneities that melt at a lower temperature than the bulk mantle, they found that the preferential melting of the heterogeneities influences where melt channels grow and also that the segregation of melt from these heterogeneities can create pools of trapped melt which cannot ascend. This body of work was extended by Turner et al. [2017] to explore the role of mantle grain size and non-Newtonian viscosity of the melt in focusing melt flow. An overarching theme in these works is that there is complex interplay between how features of the mantle and of the melt affect the melt focusing, therefore Bo et al. [2018] focused on melt heterogeneities and studied how chemical species in the melt are distributed through the melting column when the melt source has temporal and spatial variations.

Numerical modelling of reactive flow in porous media has been carried out by e.g Koehn et al. [2021] who study the infiltration of a grain aggregate with high permeability grain boundaries by a reacting fluid under pressure which is increased with time, using the hydrodynamical code 'Latte'. This treatment solves a discrete model for solid displacement using 'particles on a spring' with particles located on a triangular mesh connected by springs and for fluid flow on a regular square mesh, passing information between the two. Their study seeks to understand the parameter space of Damköhler and Péclet

number for which reaction is isolated along grain boundaries and that for which reaction spreads through the grain-scale porosity structure too. This work showed that the patterns observed in rocks are a complex function of the interplay between reaction and transport mechanisms.

2.2 Modelling reactive flow in porous media

Reactive flows in porous media form two-phase flows in which the evolution of both fluid and solid must be accounted for. General continuum models have been developed that couple the viscous dynamics of the interstitial fluid to reactive transfer between the fluid and solid, motivated by the flow of partially molten rock through porous rock [McKenzie, 1984]. Such two-phase models build on Darcy's Law for fluid flow in a porous medium, extending it to allow for the transfer of material between the host solid and the interstitial fluid, the transport of reactive components, and the evolution of the porosity of the deforming solid matrix. Examples of scenarios modelled previously in this way include flow in the Earth's lithosphere [e.g. Coogan et al., 2000, Lissenberg et al., 2013, Turner et al., 2017], where molten magma flows within a reactive, porous crystal mush. Another is the growth of mushy layers in various geological, cryospheric and metallurgical contexts, where a dendritic porous medium grows as a result of solidification under constitutional supercooling [e.g. Worster, 1986, Feltham et al., 2006]. Studies motivated by flow in the Earth's upper mantle have, in particular, considered the specific configuration of a horizontal porous layer containing a reactive flow driven by buoyancy under vertical differential chemical solubilities [Aharonov et al., 1995, Kelemen et al., 1995b, Rees Jones and Katz, 2018]. The focus of these studies is the reaction-infiltration instability resulting from flow focusing into higher permeability pathways across the layer.

There are a few ways that one can begin to model the deformation of the porous medium. For example, Rees Jones and Katz [2018] incorporate the compaction of the medium by the conservation equation

$$\frac{\partial(\rho_S(\phi_* - \phi))}{\partial t} + \boldsymbol{\nabla} \cdot ((\phi_* - \phi)\boldsymbol{v}_s) = -\rho_s k R(c, \phi), \tag{2.1}$$

where $\boldsymbol{v}_s$ is the solid velocity, generated by compaction of the porous medium modelled by

$$\boldsymbol{\nabla} \cdot \boldsymbol{v}_s = P/\zeta, \tag{2.2}$$

where P is the compaction pressure and ζ is the bulk viscosity of the medium. Rees Jones and Katz [2018] assume that ζ is a constant. More works e.g. Rees Jones et al. [2021] consider shear deformation of the porous host too.

As we begin to put together a conservation model to study such a problem, we begin with a rigid porous medium, with porosity $\phi(\boldsymbol{x}, t)$ where $\boldsymbol{x} = (x, y, z)$ is position and t time, containing an incompressible interstitial fluid (schematically, figure 1.1). The rate of decrease of the solid fraction as a result of the reaction (or, equivalently, the rate of increase of its porosity) satisfies

$$\frac{\partial(\rho_S(\phi_* - \phi))}{\partial t} = -\rho_s k R(c, \phi), \tag{2.3}$$

where ρ_S is the solid density, ϕ_* is the porosity of the solid after all reactable material is consumed, $R(c, \phi)$ is the reaction rate, k is the kinetic rate constant of the reaction, and $R(c, \phi)$ is a function of order unity encapsulating the dependence of reaction rate on the local concentration and porosity. The flow is not divergence free as the volume occupied by the incompressible fluid changes over time. The volume of fluid is changed by evolving porosity ϕ as opposed to by fluid compression.

In works with a more complex solid model, [e.g. McKenzie, 1984, Rees Jones and Katz, 2018] the conservation of solid mass also has terms which allow for deformation of the porous solid. In thermal contexts, k is correspondent with the heat transfer coefficient across the microscale solid-fluid interface. For $\phi_* = 1$, all the material in the solid is reactable (e.g. pure dissolving salt grains). Cases of $\phi_* < 1$ represent a solid comprised of a combination of reactable and non-reactable material as assumed in studies of chemical weathering [e.g. Hinch and Bhatt, 1990].

Concurrently to the reduction in solid mass described by (2.3), the reaction generates fluid at a mass rate of $\rho_s k R(c, \phi)$. The equation of mass conservation for the fluid can then be

written

$$\frac{\partial(\rho_F \phi)}{\partial t} + \boldsymbol{\nabla} \cdot (\rho_F \phi \boldsymbol{u}) = \rho_s k R(c, \phi), \tag{2.4}$$

where ρ_F is the bulk fluid density, $\boldsymbol{u}(\boldsymbol{x}, t)$ is the interstitial fluid velocity, and $\phi \boldsymbol{u}$ is the Darcy flux.

Assuming constant solid density ρ_s in (2.3), expanding (2.4) and substituting (2.3) into (2.4) yields the conservation equation

$$\phi \frac{\partial \rho_f}{\partial t} + \phi \boldsymbol{u} \cdot \boldsymbol{\nabla} \rho_f + \rho_f \boldsymbol{\nabla} \cdot (\phi \boldsymbol{u}) = (\rho_s - \rho_f) k R(c, \phi). \tag{2.5}$$

The fluid density at a given time can be described by a weighted average of the density of the incoming solvent and the density of dissolved solid,

$$\rho_f = \frac{V_f^* \rho_f^* + V_s \rho_s}{V_f^* + \delta V_{sol}}$$

where ρ_f^* and V_f^* are the density and volume of incoming fluid respectively, ρ_s and V_s are the density and volume of the solid which has been dissolved, and δV_{sol} is the change in fluid volume due to the transfer of material. We assume that ρ_f is approximately constant in space and time on the left hand side of equation (2.5), [cf. Chadam et al., 1986, Aharonov et al., 1995, Rees Jones and Katz, 2018]. We can thus rearrange for

$$\boldsymbol{\nabla} \cdot (\phi \boldsymbol{u}) = (\nu - 1) k R(c, \phi), \tag{2.6}$$

representing the conservation of the total mass of both the fluid and solid, where

$$\nu = \frac{\rho_s (V_f^* + \delta V_{sol})}{\rho_f^* V_f^* + \rho_s V_s},$$

is a dimensionless constant referred to as the *production ratio* representing the ratio of change in volume of fluid to the change in volume of solid during reaction. Darcy flux $\phi \boldsymbol{u}$ is thus instantaneously related non-locally to the reaction rates throughout the flow. For modelling the reactions in mantle dynamics [e.g. Aharonov et al., 1995, Rees Jones

and Katz, 2018], a value of $\nu = 1$ is generally used, assuming $\rho_s \approx \rho_f^*$ and $\delta V_{sol} \approx V_s$. For melting materials, the volume of fluid generated is typically comparable to that of the volume of solid lost, and therefore $\nu \approx 1$ is characteristic ($\nu \approx 0.92$ for the melting of ice to water, for example). Previous work focused on dissolution of minerals, [e.g. Chadam et al., 1986, Szymczak and Ladd, 2009, 2013] in aqueous fluid typically assumes $\nu = 0$, assuming that $\delta V_{sol} \ll V_f^*$ and that $\rho_s V_f^* \ll \rho_f^* V_f^* + \rho_s V_s$. This may not hold strictly for all cases of dissolution. We combine the density and volumetric changes into the parameter ν to allow us to span the assumptions used in these prior works. We can be more precise as to the value of ν when we were interested in modelling a specific host and fluid interaction.

The evolution of a reactive component $c(\boldsymbol{x}, t)$ in the fluid phase is governed by the advection-diffusion-reaction equation [e.g. Aharonov et al., 1995], given by

$$\frac{\partial(\phi c)}{\partial t} + \boldsymbol{\nabla} \cdot (\phi \boldsymbol{u} c) = \boldsymbol{\nabla} \cdot (D\phi \boldsymbol{\nabla} c) - c_R k R(c, \phi), \tag{2.7}$$

where D is the molecular diffusivity of the reactant in the fluid, and c_R is a consumption coefficient, representing the molar mass of reactant required to consume a unit volume of solid (in thermal contexts, c_R is correspondent with the specific latent heat capacity). The work of Hinch and Bhatt [1990] takes the limit $D \to 0$. The evolution of a product component $w(\boldsymbol{x}, t)$ in the fluid phase, is governed by the advection-diffusion-reaction equation [e.g. Aharonov et al., 1995], given by

$$\frac{\partial(\phi w)}{\partial t} + \boldsymbol{\nabla} \cdot (\phi \boldsymbol{u} w) = \boldsymbol{\nabla} \cdot (D\phi \boldsymbol{\nabla} w) + c_P k R(c, \phi). \tag{2.8}$$

In the case of an equilibrium governed reaction [e.g. Chadam et al., 1986], the reaction rate R may be given as $R(c, w, \phi)$ where the reaction rate reduces as w approaches some equilibrium value w_{eq}. In the work carried out in this thesis, we do not consider the evolution of a product component.

2.2.1 Darcy's law: momentum conservation

For general contexts, closure of the conservation model requires an equation for momentum conservation. Typically, for laminar flows in porous media this would take the form of Darcy's law

$$\phi \boldsymbol{u} = -\frac{\kappa(\phi)}{\mu}\nabla p + \boldsymbol{f}, \tag{2.9}$$

where $\kappa(\phi)$ is a specified empirical relationship between permeability and porosity, μ is the fluid viscosity, $p(\boldsymbol{x}, t)$ is the pore pressure, and $\boldsymbol{f}$ is the body force.

Permeability-porosity model

It is necessary in these models to employ a permeability-porosity relationship; one option is a simple power-law permeability model,

$$\kappa = \kappa_0 \left(\frac{\phi}{\phi_0}\right)^n, \tag{2.10}$$

in which the permeability is a power-law function of porosity, typically $n = 2 - 3$ [cf. Aharonov et al., 1995, Rees Jones and Katz, 2018]. There are more complex functions available such as the Carman-Kozeny relationship,

$$\kappa = \Psi_S^2 \frac{\phi^3 d_p^2}{180(1-\phi)^2},$$

where Ψ_S is the sphericity of the grains, d_p is the diameter of a volume equivalent spherical particle, and ϕ is the porosity of the bed. The Carman-Kozeny parameterisation allows for the inclusion of pore scale dynamics on the Darcy scale which can influence the permeability of the porous medium. The connectivity of the pore space also influences the microscale flow and may be included in more complex models. There are bodies of work, such as Hinch and Bhatt [1990] which model permeability as a function of reactant concentration, $\kappa = \kappa(w)$, in either the solid or fluid phase.

2.2.2 Modelling reaction kinetics

Models of reaction kinetics [e.g. Atkins et al., 2022] typically specify that the reaction rate, $R(c, \phi)$, is an increasing function of both the surface area of the fluid-solid interface, and of the local concentration of reactant c that feeds the reaction:

$$R(c, \phi) = g(c)f(\phi), \tag{2.11}$$

where $g(c)$ is specified empirical function of the chemical species concentrations in the fluid. The simplest function $g(c)$ tends to be

$$g(c) = \Pi_i^I(c_i^j), \tag{2.12}$$

for I reactant species where $j > 0$, this satisfies $g(0) = 0$ for reactant i.e. reaction ceases when all reactant is consumed. In this simplest instance, we assume that the concentration of a product species has no influence on the reaction rate. The function $f(\phi)$ is a specified empirical function of the porosity satisfying $f(\phi_*) = 0$ and $f(0) = 1$, i.e. reaction ceases when all reactable material is exhausted. One simple and smooth option is to set $f(\phi) = (1-\phi/\phi_*)^m$, where $m > 0$ is an exponent of order unity. Crucially, the joint proportionality of R on both $g(c)$ and $f(\phi)$ ensures that the reaction rate vanishes if either the local concentration of reactant or the local surface area available for reaction is zero, thus allowing for uniform states of fully reacted solid ($\phi \approx \phi_*$) and unreactive ($c \approx 0$) fluid (figure 1.1).

More complex functions $g(c)$ can allow for reversible reactions with the form

$$g(c) = \Pi_i^I(c_i^j) - \alpha\Pi_k^K(w_k^j),$$

with I reactant species and K product species,where again $j > 0$. The constant α is the ratio of the kinetic rate constant of the backward (precipitation) reaction to the kinetic rate constant k of the forward (dissolution) reaction. Other options used to model the porosity dependence of reaction in prior work include $m = 1$ [Aharonov et al., 1995] and using the

Heaviside function [e.g. Szymczak and Ladd, 2013, Grodzki and Szymczak, 2019], with

$$f(\phi) = \begin{cases} 1, & \phi > \phi_* \\ 0, & \phi = \phi_*. \end{cases}$$

2.3 Travelling wave reaction fronts & their stability

In reactive flows in porous media, a key feature that emerges is the development of a *reaction front*. The reaction front is a region of flow through which the fluid and solid phases transition from their unreacted state to their fully reacted state. Figure 2.3 shows schematically two scenarios: (a) a reaction front where the porosity and concentration vary on roughly the same order of magnitude, and (b) a reaction front where the porosity varies on a much smaller scale than the concentration (n.b. the extremity of the scale separation is reduced here for readability).

Prior fluid-mechanical studies that incorporate the dynamics of reaction fronts in porous media can be classified into two general approaches. One prior framework considers the reaction front as an idealised sharp interface separating unreacted and reacted regions [e.g. Chadam et al., 1986]. The separation of the domain into these two regions allows the solution of the advection-diffusion equation for concentration subject to uniform porosity. The interface between the two evolves subject to a kinematic condition which is effectively a Stefan condition describing the boundary between the two.

A second framework [Hinch and Bhatt, 1990] models a reaction front using a two-phase continuum theory formed of an advection-reaction equation governing reactant concentration coupled to a porosity evolution equation, motivated by the forced chemical weathering of porous rocks by acid-laden fluid. Compared to the Stefan-type models noted in the preceding paragraph, the model is more complex in terms of allowing for a non-interfacial porosity transition but is simplified in terms of neglecting diffusion of the reactive component. Hinch and Bhatt [1990] calculate steady travelling-wave solutions to their diffusionless model and use these as a basic state for the analysis of transverse reaction-infiltration instabilities, yielding a fundamentally different theory compared to

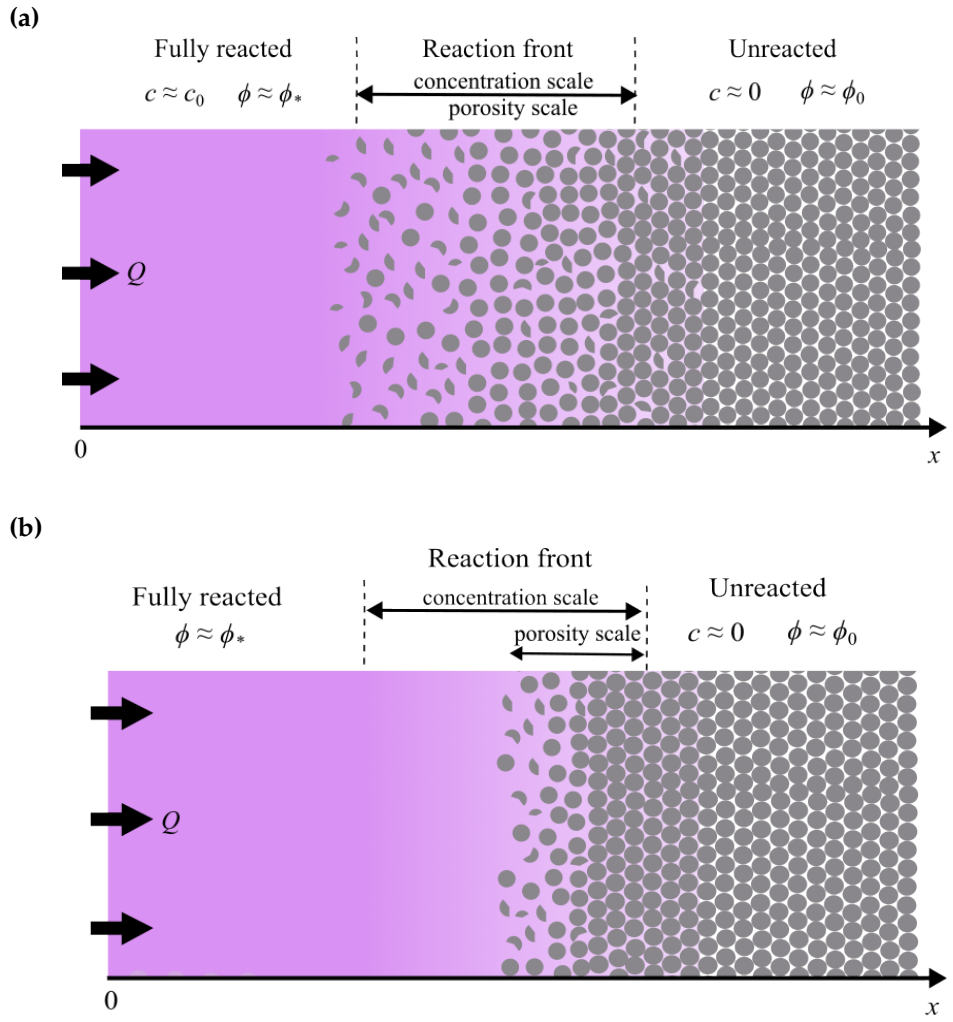

Figure 2.3: Schematic diagrams depicting (a) a reaction front in which porosity and concentration transition over regions of roughly the same size, and (b) a reaction front in which the porosity transition occurs in a smaller region than the concentration transition.

the Stefan-type model reviewed above. The next two sections review in detail the specific models of Chadam et al. [1986] and Hinch and Bhatt [1990]. In the latter half of this section, work building upon each of those models is then reviewed.

2.3.1 The sharp porosity transition diffusion limited model

Chadam et al. [1986] present one of the first mathematical studies of the reactive infiltration instability. Their analysis begins with the assumption that the stable reaction front depends only on the x direction, independent of the transverse co-ordinate y, with equations (2.3), (2.4), and (2.8) in the specific case of $\nu = 0$ which represents a reaction that does

not increase fluid volume, typically a dissolution reaction. Thus their governing system reads

$$\frac{\partial(\phi)}{\partial t} + \boldsymbol{\nabla} \cdot (\phi \boldsymbol{u}) = 0, \tag{2.13}$$

$$\frac{\partial(1-\phi)}{\partial t} = -R(c, \phi), \tag{2.14}$$

$$\frac{\partial(\phi c)}{\partial t} + \boldsymbol{\nabla} \cdot (\phi \boldsymbol{u} c) = \boldsymbol{\nabla} \cdot (D\phi \boldsymbol{\nabla} c) + c_{R,p} k R(c, \phi). \tag{2.15}$$

where c is the concentration of a product solute which the incoming fluid is undersaturated with. Note that in this work, the chemical is a product rather than a reactant but the mathematics is equivalent. Darcy's law

$$\phi \boldsymbol{u} = -\frac{\kappa}{\mu} \boldsymbol{\nabla} p \tag{2.16}$$

governs the fluid velocity $\boldsymbol{u}$. The reaction rate is modelled by

$$R = (c_{eq} - c)(\phi_* - \phi)^{2/3}, \tag{2.17}$$

where c is the product concentration with $j = 1, \quad \alpha = 1$ as described by (2.12). The parameter c_{eq}, the maximum concentration of c, plays the role of a reactant which facilitates the reaction but is not consumed. Summarily, the reaction rate falls as the concentration of c approaches c_{eq}. The boundary conditions at the inlet are

$$c \to 0, \qquad \phi \to \phi_*, \qquad \frac{\partial p}{\partial x} \to -\frac{q}{\kappa_u}, \qquad (x \to -\infty) \tag{2.18}$$

the third of which is equivalent to stating a fixed fluid flux, $\phi u = \frac{q}{\mu}$ at the source, sustained by a constant pressure gradient as $x \to -\infty$. The boundary conditions downstream are

$$c \to c_{eq}, \qquad \phi \to \phi_0, \qquad (x \to \infty). \tag{2.19}$$

In this framework, it is instructional to taking the limit of *large solid density*, $c_{eq} \ll c_R$, which states that the solid molar density of a species is much greater than the solute

concentration. The large solid density limit allows us to define a small parameter

$$\varepsilon = \frac{c_{eq}}{c_R} \ll 1 \tag{2.20}$$

, and we then scale the system of equations (2.13)–(2.15) by

$$c = c_{eq}\hat{c}, \qquad x = (D/kc^{eq})^{1/2}\hat{x}, \qquad p = \frac{D}{\kappa(\phi_*)}\hat{p}, \qquad t = (kc_{eq})^{-1}/\varepsilon\hat{t}, \tag{2.21}$$

as done by Chadam et al. [1986]. Scaling the equations and neglecting hats reveals that the time derivatives in (2.14) and (2.15) are O(ε), and so can be neglected for the system:

$$\frac{\partial\phi}{\partial t} + \boldsymbol{\nabla}\cdot(\phi\boldsymbol{u}) = 0, \tag{2.22}$$

$$R(c,\phi) = 0, \tag{2.23}$$

$$\boldsymbol{\nabla}\cdot(\phi\boldsymbol{u}c) = \boldsymbol{\nabla}\cdot(\phi\boldsymbol{\nabla}c) + R(c,\phi). \tag{2.24}$$

The domain is partitioned into two regions based on (2.23), i.e. there is a region where $\phi = \phi_*$ 'the altered region' and one where $c = 1$, the unaltered region, with a jump at the interface between the two. This allows us to write the model for each of the two regions as

$$\phi = \phi_*, \qquad \nabla^2 p = 0, \qquad c = 1 \tag{2.25}$$

in the downstream unaltered region, and in the upstream altered region

$$\phi = \phi_0, \qquad \nabla^2 p = 0, \qquad \boldsymbol{\nabla}\cdot(\phi_0\boldsymbol{\nabla}c + \phi c\boldsymbol{\nabla}p) = 0, \tag{2.26}$$

with the evolution of the interface between the two located at $F = 0$, modelled by

$$\frac{\partial F}{\partial t} + \boldsymbol{W}\cdot\boldsymbol{\nabla}F = 0, \tag{2.27}$$

where

$$\boldsymbol{W} = \frac{c_0/c_R}{(\phi_* - \phi_0)}\boldsymbol{q},$$

with $\boldsymbol{q}$ the incoming fluid flux, is the advancement velocity of the interface. As functions

of (x, t), these equations can be directly solved for

$$c = \begin{cases} e^{(\alpha z)}, & (z < 0) \\ 1, & (z > 0) \end{cases}, \qquad p = \begin{cases} qz, & (z < 0) \\ \beta q z, & (z > 0) \end{cases} \tag{2.28}$$

where $\alpha = -q\beta$ and $\beta = \kappa_d/\kappa_u$ the ratio of permeability in the unreacted to reacted regions. The advancement velocity $\boldsymbol{W} = W\hat{\boldsymbol{x}}$ where $W = c_0 q/(c_R(\phi_* - \phi_0))$, with $\boldsymbol{q} = q\hat{\boldsymbol{x}}$. Working on the basis that permeability is increased by reaction, $\beta < 1$.

A linear stability analysis, with perturbations of the form

$$F(y, t) = x + \delta\psi(y, t), \tag{2.29}$$

$$p(y, t) = p(x) + \delta\psi(y, t)\hat{p}(x), \tag{2.30}$$

$$c(y, t) = c(x) + \delta\psi(y, t)\hat{c}(x), \tag{2.31}$$

where δ is a small parameter such that terms in the governing equations $O(\delta^2)$ or smaller are negligible. The structure function ψ is defined by

$$\psi(y, t) = e^{\sigma t}\cos(my). \tag{2.32}$$

Transforming the x co-ordinate to a new co-ordinate ζ such that $\zeta = 0$ at the interface, Chadam et al. [1986] yield two ODEs for $\hat{p}$ and $\hat{c}$ respectively, which are solved to derive the dispersion relation

$$\sigma = \frac{2W}{(1+\beta)(1-\Phi)}(\alpha + (1-\beta)m - \sqrt{\alpha^2 + 4m^2}). \tag{2.33}$$

The dispersion relation (2.33) takes the form of a parabola with a global maximum $\sigma_*(m_*)$ with $\sigma_* > 0$. There is a cut off wavenumber m_0 which means that small wavelength perturbations $m > m_*$ decay. I neglect the detailed derivation of this result from the ODEs here, as I will derive it later in Chapter 5 from my own generalised model and confirm that this is recovered in the correct limit.

2.3.2 Diffusionless reaction fronts

Motivated by industrial flushing of porous rock, Hinch and Bhatt [1990] considered reaction fronts in a formulation without diffusion. This work studies reaction front profiles for a pair of reactants, one in the solid and one in the fluid component and assumes that the porosity $\phi \approx \phi_0$ in their conservation equations,

$$\phi \frac{\partial c}{\partial t} + \boldsymbol{\nabla} \cdot (\phi \boldsymbol{u} c) = -kwc, \tag{2.34}$$

$$w_R(1-\phi)\frac{\partial w}{\partial t} = -kwc. \tag{2.35}$$

where c is the reactant concentration in the fluid and w is the concentration of the second reactant in the solid. The parameter w_R is a stoichiometric constant. The form of the rate of reaction is thus

$$R(c, w) = kwc \tag{2.36}$$

Having assumed that $\phi \approx \phi_0$ everywhere, Hinch and Bhatt [1990] formulate that the permeability, κ is a function

$$\kappa = \kappa(w) \tag{2.37}$$

of w the solid reactant concentration rather than of porosity. The typical behaviour of permeability is that κ increases as w decreases (solid reactant is consumed), although this can have various functional forms and is left unspecified for now. The dimensional boundary conditions on the reaction concentrations for their 1D travelling wave solution are

$$c \to c_0, \quad w \to 0, \quad \text{as } x \to -\infty, \tag{2.38}$$

and

$$c \to 0, \quad w \to w_0, \quad \text{as } x \to \infty. \tag{2.39}$$

Finally, the incompressibility condition

$$\boldsymbol{\nabla} \cdot (\phi \boldsymbol{u}) = 0, \tag{2.40}$$

is applied. The basic travelling wave state derived by Hinch and Bhatt [1990] assumed solutions which are functions of (x, t) only and $\kappa(w)$ is not needed to solve the 1D flow. The steadily moving reaction front is recovered by moving into the frame of the reaction front $z = x - Vt$ with velocity $\boldsymbol{u} = u\mathbf{e}_x$ and uniform fluid flux $\phi u = U$ by incompressibility (2.40),

$$-\phi V c' + U c' = -kcw = -w_R(1-\phi)Vw'. \tag{2.41}$$

Integrating once, and applying the boundary conditions we obtain the front velocity

$$V = \frac{U}{\phi + \alpha^{-1}} \tag{2.42}$$

where

$$\alpha = \frac{c_0}{w_R w_0 (1-\phi)} \tag{2.43}$$

is the acid capacity number. The reaction front profiles are thus obtainable by direct integration of the separable differential equations (2.41), giving

$$c = c_0 \frac{1}{1 + e^{\beta(x-Vt)}}, \quad \text{and} \quad w = w_0 \frac{e^{\beta(x-Vt)}}{1 + e^{\beta(x-Vt)}}, \tag{2.44}$$

which can be written in terms of the logistic function $f(\beta(Vt - x))$, for $c = c_0 f(\beta(Vt - x))$ and $w = w_0 f(\beta x - Vt)$ respectively, where β^{-1} is the Damköhler thickness of the front defined by

$$\beta^{-1} = \frac{V}{k w_0 \alpha}. \tag{2.45}$$

Note that Hinch and Bhatt [1990] incorrectly give the form of (2.44) with exponents $e^{(\beta x - Vt)}$ rather than $e^{\beta(x-Vt)}$ and this has been corrected here. The linear stability of this basic state for various $\kappa(w)$ permeability models, relating permeability to solid concentration rather

than porosity, is then carried out with perturbations of the form

$$w(y,t) = w(x) + \delta\psi(y,t)\hat{w}(x), \tag{2.46}$$

$$c(y,t) = c(x) + \delta\psi(y,t)\hat{c}(x), \tag{2.47}$$

$$u = \phi + \psi(y,t)\hat{u}(x) \tag{2.48}$$

$$v = \psi(y,t)\hat{v}(x), \tag{2.49}$$

$$p = \int^{x} \frac{\mu(\phi + \alpha^{-1})}{\kappa(e^x/(1+e^x))} dx + \psi(y,t)\hat{p}(x), \tag{2.50}$$

where

$$\psi(y,t) = e^{\sigma t}\cos(my). \tag{2.51}$$

For a simple permeability-concentration relationship $\kappa = \kappa_0(1 - \delta w/w_0)$, where $\delta \ll 1$, representing a small linear dependence of permeability on w. This is a first order Taylor approximation of a decreasing function of w, δ can be tuned to represent a more or less rapidly decreasing function for a small deviation of w away from w_0.

The governing model for these perturbations is solved asymptotically in the limits of small and large wavenumber giving

$$\sigma = \begin{cases} \frac{1}{2}m & (m \ll 1) \\ \frac{1}{6} & (m \gg 1). \end{cases} \tag{2.52}$$

The result above suggests that the 1D reaction fronts in this regime are always unstable to reactive infiltration, with no particular preferred wavelength. They are equally unstable to all large m wave modes in the asymptotic limit. Interestingly this is a key difference from the diffusion-limited context of Chadam et al. [1986] which has stable wave modes.

2.3.3 Bridging the diffusion-dominated and sharp interface regimes for small acid capacity.

Szymczak and Ladd [2013] and Szymczak and Ladd [2014] unify the modelling of Chadam et al. [1986] and Hinch and Bhatt [1990] for small acid capacity, incorporating diffusion-limited and diffusion-less reaction fronts in one model. Their system of governing equa-

tions (2.3), (2.4), (2.7) and (2.9) are written as

$$\frac{\partial(\phi)}{\partial t} + \boldsymbol{\nabla} \cdot (\phi \boldsymbol{u}) = 0, \tag{2.53}$$

$$\frac{\partial(1-\phi)}{\partial t} = -R(c, \phi), \tag{2.54}$$

$$\frac{\partial(\phi c)}{\partial t} + \boldsymbol{\nabla} \cdot (\phi \boldsymbol{u} c) = \boldsymbol{\nabla} \cdot (D\phi \boldsymbol{\nabla} c) - c_R k R(c, \phi), \tag{2.55}$$

where $\nu = 0$. The reaction rate is defined by $R(c, \phi) = c\theta(\phi_* - \phi)$ where $\theta(\phi_* - \phi)$ the Heaviside step function. The limit of small acid capacity $\gamma_a = c_0/(c_R(\phi_* - \phi_0))$ is taken, resulting in the time derivative of concentration in (2.55) being negligible. In effect, small acid capacity results in a separation of time scales in which the concentration equation adjusts on a fast time scale to a steady state for the given position z_* of the start of the reactive region, such that the time derivative in (2.55) and (2.53) can be neglected, but the reacted region advances on a slow time scale, such that the time derivative in (2.54) remains important. The resulting ODE system in the translating co-ordinate z is

$$v_0 \frac{\partial c}{\partial z} - D\frac{\partial^2 c}{\partial z^2} = -c_R k R(c, \phi), \tag{2.56}$$

$$U\frac{\partial \phi}{\partial z} = kR(c, \phi), \tag{2.57}$$

where v_0 is the fluid velocity, which is constant throughout the domain in one dimension.

To span the sharp interface and diffusion-dominated regimes, it is necessary to define the step position $z_F = 0$ of Chadam et al. [1986] in a way that it can be relaxed to allow porosity ϕ to vary more smoothly. The critical front position is the furthest downstream position for which $\phi = \phi_*$, indicating the furthest extent of completely reacted. This position z_* is the critical position at which porosity departs from the upstream fully reacted value. This definition, based upon the departure from ϕ_* rather than the position of a step between ϕ_* and ϕ_0 allows them to relax the assumption that $\phi = \phi_0$ everywhere downstream, and similarly allows for concentration c to vary in the downstream region as well.

Having defined the reaction front position within the context of their smooth model, Szymczak and Ladd [2013] are able to define length scales based upon the extent of the concentration transition upstream and downstream of the front position, these are

referred to as l_u and l_d. Equation (2.56) can be solved analytically upstream of z_F, where $\phi = \phi_0$ identically for the upstream concentration length scale l_u giving

$$c = c_0 \left(1 - \frac{e^{z/l_u}}{1 + Pe}\right), \quad \phi = \phi_*, \qquad l_u = \frac{D}{v_0}, \tag{2.58}$$

where Pe is a Péclet number defined on the downstream length scale. Downstream, where $z > z_F$, the concentration and porosity field can both be solved for analytically thanks to the choice of reaction rate $R(c, \phi)$ to find that the downstream concentration length scale, giving

$$c = c_0 \frac{e^{-z/l_d}}{1 + Pe^{-1}}, \qquad l_d = \frac{2D}{\sqrt{v_0^2 + 4Dk} - v_0}, \tag{2.59}$$

and

$$\phi = \phi_* - (\phi_* - \phi_0)e^{-z/l_d}, \tag{2.60}$$

where porosity decays on the same scale as concentration. The Péclet number is defined on the scale of the downstream length scale $Pe = v_0 l_d / D$, and is equal to the ratio of the upstream and downstream length scales.

The length scales on which the overall reaction front transitions occur are thus dependent on which of l_u and l_d is greater. In the case that l_d is greater, the porosity and concentration transition on approximately the same scale. However in the case that l_u is greater, concentration transition occurs over a larger distance than porosity as porosity is uniform upstream. The controlling parameter on the ratio l_u/l_d is $B = Dkc_R/v_0^2$. Qualitatively, we see that thin front problem of Chadam et al. [1986] is recovered where $B \gg 1$, with the diffusionless limit being recovered when $B \ll 1$.

Szymczak and Ladd [2014] go on to perform a linear stability analysis of their 1D solutions, using the position z_F as their reaction front location. The result is a fifth-order differential equation for the dispersion relation. In the limit of small porosity contrast $(\phi_* - \phi_0) \ll \phi_0$, the growth rate has a closed analytical form.

A detailed quantitative demonstration and regime analysis of the conditions under which either the diffusionless or thin front limit of the 1D basic states arises has yet to be con-

ducted. Further, the analyses of Szymczak and Ladd [2013, 2014] assume the specific limits of small acid capacity number and that the dissolution reaction produces no additional volume of fluid. It remains an open question how the conditions for the regime transitions are altered in these more general cases.

2.3.4 Other theoretical work on reaction fronts

Other work building on Chadam et al. [1986], Hinch and Bhatt [1990] has sought to further understand the controls of transition zones in porosity and concentration in reaction fronts and their instabilities. These initial works focused on steadily propagating reaction fronts. Szymczak and Ladd [2011a] studied the instability of the initial 'inlet' flow in which the reaction front is not yet fully formed. This instability is of importance where the initial porosity of the host medium is small with the possibility of a large porosity increase e.g in limestone formations (karst topography) rather than in sandstones where there is minimal dissolvable material. This work is carried out in the convection dominated (Hinch and Bhatt [1990]) limit, with the addition of diffusion perpendicular to the initial flow.

The inlet instability is also the focus of Szymczak and Ladd [2012] which develops a linear stability analysis of the inlet instability with diffusion in all directions. This work finds that the non-steady dissolution front is unstable to a wide range of wavelengths, suggesting inherently two-dimensional dynamics for this specific scenario.

2.4 Reactive infiltration instabilities in an axisymmetric geometry

Moving beyond the stability of 1D fronts, Grodzki and Szymczak [2019] studied the stability of reaction fronts for reactive infiltration from a point source. Their governing model is broadly equivalent to (2.13)–(2.15), with $\rho_R = 0$ but with a radial co-ordinate system and a chemical which is depleted in reaction. Thus taking the same limit of large solid density to give rise to the 'sharp-diffusion limited' model of Chadam et al. [1986]

gives

$$\nabla \cdot (\phi \boldsymbol{u} c) - D\phi \nabla^2 c = 0, \quad r < r_F \tag{2.61}$$

$$\nabla^2 p_u = 0, \quad r < r_F \tag{2.62}$$

$$\nabla^2 p_d = 0, \quad r > r_F \tag{2.63}$$

$$\dot{\boldsymbol{R}}_F \cdot \boldsymbol{n}_{R_F} = -S_* D\phi_1 (\nabla c) \cdot \boldsymbol{n}_{R_F} \tag{2.64}$$

where $\boldsymbol{R}_F$ is the front location, $\boldsymbol{n}_{R_F}$ is the normal vector to the front, p_u and p_d are the pressure upstream and downstream of the reaction front. The assumption is made that r_F grows slowly such that the flow field around it is approximately static. We define $\boldsymbol{R}_F = r_F \hat{\boldsymbol{r}}$, and solve for r_F to yield the basic state solution to this model, given by

$$p_u = -\frac{\mu Q}{2\pi\kappa_u} \log \frac{r}{r_F(t)}, \quad p_d = -\frac{\mu Q}{2\pi\kappa_d} \log \frac{r}{r_F(t)}, \tag{2.65}$$

$$c = c_0 \left(1 - \left(\frac{r}{r_F(t)}\right)^{\lambda}\right), \quad r < r_F(t) \tag{2.66}$$

$$r_F(t) = \sqrt{R_0^2 + \frac{SQ}{\pi} t} \tag{2.67}$$

where

$$\lambda = \frac{Q}{2\pi D \phi_*}$$

is the Péclet number measuring the ratio of convection to diffusion in the system. Underpinning this model is a quasi-steady assumption, as in section 2.3.1, that the porosity jump position $r_F(t)$ advances slowly such that a steady profile for c relative to this position forms. Looking at the form of equation (2.67), we see that the quasi-steady assumption holds given $S \ll 1$, the small acid capacity limit. The solution above describes a sharp porosity transition located at $r_F(t)$ with pressure defined piecewise upstream and downstream of this position. The concentration profile exists upstream $r < r_F$ of the porosity transition.

A linear stability analysis is performed with perturbations of the form

$$\boldsymbol{R} = \boldsymbol{R}_F(t) + \delta\psi(t,\theta)\hat{\boldsymbol{r}}, \tag{2.68}$$

$$p_u = p_u^0 + \delta\psi(t,\theta)\hat{p}_u(r), \tag{2.69}$$

$$u_u = u_u^0 + \delta\psi(t,\theta)\hat{u}_u(r) \tag{2.70}$$

$$c_u = c_u^0 + \delta\psi(t,\theta)\hat{c}_u(r), \tag{2.71}$$

where $\psi(t,\theta) = F(t)\cos(m\theta)$, with the polar angle θ and $m \in \mathbf{N}$ is the wave number. As the basic state is time dependent, $F(t)$ is not in general exponential, nonetheless this system does take the form $F(t) = e^{\sigma t}$ with

$$\sigma = \frac{U_0}{l_u(1+\beta)}\left(1 - \sqrt{1 + 4\left(\frac{m}{Pe}\right)^2} + \frac{m}{Pe}(1-\beta) - \frac{1}{Pe}(1+\beta)\right). \tag{2.72}$$

The above dispersion relation $\sigma(m)$ plots a curve which has a global maximum σ_*, and there are Péclet numbers for which this is negative, meaning that the system is globally stable. Similar to the results of Chadam et al. [1986] and Szymczak and Ladd [2014] the maximum σ_* can take positive values, and there is a cut off wavenumber $m = m_0$ above which perturbations are stable and will decay in time. It is possible to have stable parameters for which $\sigma < 0$ for all m in this geometry, unlike Chadam et al. [1986].

2.5 Contributions of this thesis

Generally, the development and systematic investigation of the evolution of a continuum two-phase model of reaction fronts that classifies and analyses simplifying regime types across a wide parameter space is yet to be conducted. Having revised the prior work on reaction fronts and reactive infiltration instability, I now expand upon the specifics of the research questions outlined in section 1.1.

Research Question 1

How do reaction fronts evolve in fundamental geometries?

Prior work on reaction fronts in simple domains (1D, axisymmetry, 2D) has predomi-

nantly focused on steady travelling wave reaction fronts, and their instability, with the exception of Szymczak and Ladd [2011a] which studied the instability of early time reaction fronts. Early work studied the particular limiting case of the small acid capacity limit, and the further limits of the diffusionless case [Hinch and Bhatt, 1990] and the thin front limit [Chadam et al., 1986]. More recently, Szymczak and Ladd [2013, 2014] unified the diffusionless and thin front limit for the case of small acid capacity with a transition position defined to bridge into the smooth diffusionless case. Prior work has also been concerned with the specific case of $\nu = 0$, typical of dissolution reactions in which no fluid volume is gained in reaction. In this thesis I examine quantitatively the question of the conditions for the emerge of the different regimes in parameter space. Specifically, I will examine the question of the relative satisfaction of the properties of porosity sharpness in the travelling wave states and the relative importance of diffusion, along with new asymptotic theories of these limiting regimes. I solve the governing system numerically, study the emergent temporal dynamics and employ asymptotic analysis for a novel understanding of the controlling parameters on reaction front behaviour.

Research Question 2

What controls the extent of chemical and porosity transitions in steadily propagating 1D fronts?

The extent of steadily propagating 1D fronts has been primarily investigated by Szymczak and Ladd [2013, 2014] in the distribution of the chemical front ahead and behind the porosity transition location, now defined to bridge the sharp and smooth cases studied in earlier work. Their study uses upstream and downstream decay length scales of concentration in order to quantify how the two transitions are connected. In this work, I take a new approach to understanding the limiting length scales without defining a front position. I study the inner boundary layer of the thin-front limit to understand the limiting behaviour of the porosity transition.

A detailed quantitative demonstration and regime analysis of the conditions under which either the sharp or diffusionless regime arises has yet to be conducted. In this thesis, I explore the extent of the reaction front more generally by developing new understanding of

what controls the overall front thickness in both concentration and porosity to understand how they relate to each other. As further generalisations, I will allow for general acid capacity number (Stefan number) and consider the effects of general production ratio. It remains unknown quantitatively how the relative sharpness of a porosity transition is controlled outside of the small acid capacity limit.

Research Question 3
How does a radially decaying flux influence reaction fronts versus a constant uniform flux?

As outlined previously, Grodzki and Szymczak [2019] is one of the first works to consider reaction fronts which grow from a local or point source, working in a quasi-steady sharp framework to study the instability of these fronts. The intriguing element of these fronts is that the flux of fluid to the front decays as it moves away from the point source.

In this thesis, I study systematically the regimes which emerge over time in axisymmetric reaction fronts and develop a novel regime diagram which helps to understand the spatial scales of porosity and concentration transition in this geometry, and how this geometry relates to the 1D planar front dynamics. In particular, it remains unknown how the quasi-steady and sharp regime from which the work of Grodzki and Szymczak [2019] develops emerges in time and how parameters control whether or not this assumed basic state is valid. In this work, I will understand how sharp, non-sharp and quasi 1D transition zones emerge temporally in the radial geometry.

Research Question 4
How does the stability of 1D reaction fronts inform understanding of reactive fronts in geological porous media?

In this thesis, I begin to assess the agreement between the linear stability analysis of reactive infiltration instability and new geological samples. Field observations from e.g. Daczko and Halpin [2009] are used to guide an assessment of the instability of an interfacial planar flow as a potential mechanism for those observations. I also present a comparison of these predictions with samples and scenarios that have previously been

studied in the context of geological reactive infiltration instabilities, showing where the theory is still not able to predict the wavelengths observed. This new exposition explores the instabilities of reaction fronts in observed geological samples that do and do not match this theory, then goes on to consider how one can develop the dispersion relation as a toolkit for understanding of geological observation, providing the opportunity to understand better the timescales and parametric control on the wavelengths of reactive fingers that are preserved in geoscience.

3

Regime analysis of one-dimensional reaction fronts

This Chapter presents an analysis of reaction fronts formed by uniform flow of reactive fluid from a planar boundary. This configuration is fundamental to understanding the development of reaction fronts over time, and the control of their transitional length scales. This Chapter is the basis of a paper drafted for submission to the Journal of Fluid Mechanics, under the title *Two-phase reaction fronts in porous media: control of emergent structure, sharpness and regime analysis*. The authors are D. Bullamore and S. Pegler.

3.1 Introduction

The reaction of fluid with a porous medium, either through a chemical or physical process, is a fundamental phenomenon arising in natural and industrial applications across a wide range of scales. As discussed earlier in Chapter 2, examples include the forced or natural weathering of porous rocks [e.g. Hinch and Bhatt, 1990, Merino and Banerjee, 2008, Szymczak and Ladd, 2009], reactive two-phase flows in the Earth's mantle and magma reservoirs [e.g. Katz and Weatherley, 2012, Pec et al., 2017, Edmonds et al., 2019], and cryospheric applications to ice and snow [e.g. Poulikakos and Kazmierczak, 1988, Meyer and Hewitt, 2017]. The physical or chemical reactions between interstitial fluids and

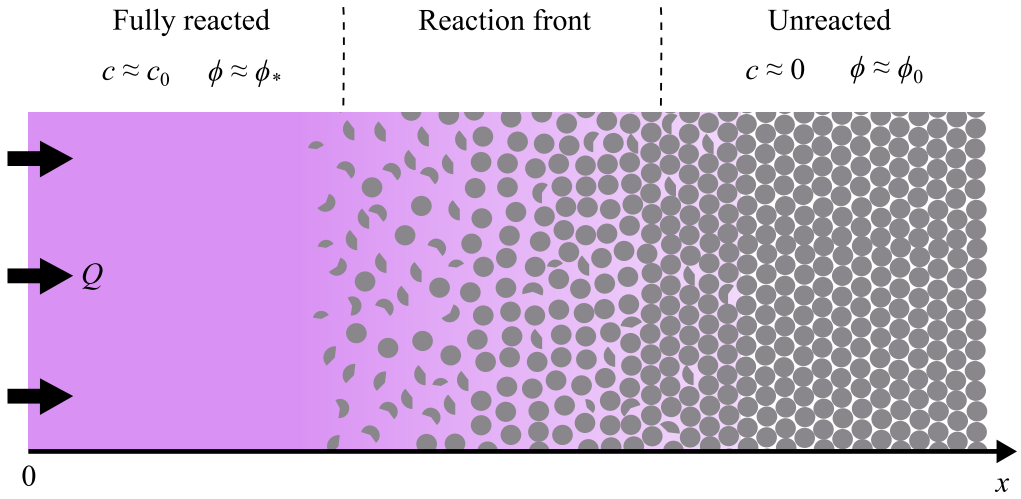

Figure 3.1: Schematic of the configuration, showing the reaction front generated by injection of a reactant-laden fluid into a reactive porous medium. The system partitions into three broadly defined regions: the reacted region, where the concentration is given by the inlet value c_0 and the porosity is at its maximum value ϕ_*; the reaction front, where both the concentration and porosity fields undergo a spatial transition; and the unreacted region, where the reactant is depleted $c = 0$, and the porosity is at its initial (unreacted) value $\phi = \phi_0$. The case $\phi_* \approx 1$ is depicted. The concentration of the reactant is shown as a smooth gradient from high concentration (dark purple) to low concentration (white), which can transition over a distinct spatial scale to that of the porosity.

porous solids lead to complex coupled interactions between fluid dynamics, transport processes, reaction kinetics, and solid structure.

Figure 3.1 depicts a key phenomenon in such flows, the development of a *reaction front*. The reaction front is a zone of transition in both the porosity and the chemical (or thermal) concentration of a reactive agent between reacted and unreacted regions. Reaction fronts form from an interaction between chemical (or thermal) diffusion of the reactive agent, its advection within the fluid, and the kinetic transfer of material between solid and fluid phases. The combination of these effects can produce either relatively sharp, near-interfacial transitions in porosity, or smooth large-scale transitions relative to the length scales of the flow. It remains a fundamental question how the structure and characteristic length scales of reaction fronts are related to the underlying physical parameters. A key theoretical question is whether there is a dimensionless number that characterises the relative sharpness of porosity transitions in two-phase reactive flows, and what controls the relative importance of advection versus diffusion in the emergent dynamics. Generally, the development and systematic investigation of the predictions of a two-phase model

of reaction fronts that classifies and analyses simplifying regime types across parameter space is yet to be conducted.

Of the two main paradigms for studying reactive flow in porous media (section 2.1.3), our focus is the fundamental one-dimensional configuration of an advancing *reaction front*, where the intrusion of a reactive fluid into a porous medium generates an emergent structure in which reactive consumption and transport balance in a moving frame (figure 3.1). The configuration characterises a transitional zone through which porosity and concentration fields vary over some undetermined length scale to connect two fair field regions of reacted and unreacted regions.

Prior fluid-mechanical studies that incorporate the dynamics of reaction fronts in porous media were previously classified into two general approaches. These approaches are the 'sharp diffusion-limited' front [e.g. Chadam et al., 1986, Szymczak and Ladd, 2014], and the diffusionless front [e.g. Hinch and Bhatt, 1990], reviewed in Chapter 2. The one-dimensional basic states in the two theoretical approaches of Chadam et al. [1986] and Hinch and Bhatt [1990] apply distinct assumptions that form mutually exclusive theoretical limits: the first allows for diffusion but assumes an interfacial porosity transition; the second allows for a non-interfacial porosity transition but neglects diffusion. An understanding of the conditions under which either of these simplifying properties applies, as well as the development of a unified theory that is able to consistently relax both of these assumptions, remains an open question.

Szymczak and Ladd [2013] unified both diffusionless and interfacial porosity transition, in the limit of small acid capacity. Defining the transition position such that it exists in the smooth interface transition as well. Further specialising to $R(c, \phi) = c\theta(\phi_* - \phi)$ where the porosity dependence of the chemical reaction rate is a Heaviside function θ allows this work to gain analytical profiles of the concentration transition on either side of their transition position, and the profile of porosity downstream decays with the downstream concentration transition. As a consequence, it can be inferred from this work that there are two limiting behaviours of the transitional length scales, controlled by the parameter $B = KD/Q^2$ which measured the relative influence of reaction, diffusion and advection on the flow. The first is that the upstream concentration length dominates, and the

porosity transition is much smaller than it resulting in a 'sharp' porosity transition. The second is that the downstream concentration length dominates, and so both porosity and concentration transition on approximately the same scale.

It remains unknown how the emergence of these simplified regimes is controlled when the reactive capacity of the fluid is non-negligible, how the relative sharpness of a porosity transition and internal balance of transport and reaction are connected through an intermediate parameter space. A generalised theoretical analysis of the regimes and asymptotic properties of one-dimensional reaction fronts, relaxing the small acid capacity limit and allowing for a generalised reaction rate depending on porosity and concentration, remains to be conducted. The aim of the present contribution is to fill this gap. We propose a new continuum two-phase analysis of reaction fronts, present an integrated form of the model, solve the model to establish the parametric controls on relative sharpness, develop analytical theories of their structure, and formulate the demarcating criteria for simplified regimes.

The generalised model we propose comprises a one-dimensional two-phase continuum theory governing the transport of a reactive component under advection, diffusion and reactive transfer, coupled to an evolution equation for the solid porosity, governed by the system (2.3)–(2.7). Mathematically, the model comprises a non-linear advection-diffusion-reaction system wherein the reaction rate is modelled as an increasing function of both the local concentration of reactant and local solid fraction. The continuum theory thereby creates a general mathematical framework able to internally ascertain conditions for smooth versus sharp fronts, and the key role of diffusion. The regimes we establish allow for a general reaction model but in order to simplify the parameter space we focus on the simple co-linear reaction rate in surface area of the solid and reactant concentration. We also assume that these states are stable, with the expectation that in 2D these would become unstable under some parametric control.

Our results will extend the prior work of Szymczak and Ladd [2013] with a complementary analysis of bridging the interfacial and diffusionless regimes with generalisation to include reactions which produce fluid and to relax the 'small acid capacity limit'. Our analysis will yield a host of new theoretical developments, including a generalised integrated

second-order system for travelling wave states, explicit theoretical predictions for the transition length scales, regime diagrams elucidating the fundamental regime reductions, and detailed asymptotic analyses of limiting regimes.

Section 3.2 develops the 1D formulation of the conservation model for reaction fronts and validates the numerical approach to solving this. Section 3.3 presents a showcase of numerical solutions to the time-dependent equations, and identifies the progression of transient flow regimes preceding a final travelling wave state. Section 3.3.2 conducts a detailed analysis of the travelling wave states, yielding predictions for the emergent relative sharpness and relative importance of diffusion in regime diagrams, and develops analytical theories of both the limiting regimes. Section 3.5 summarises the key results for demarcating criteria of the two limiting regimes and their structural characteristics in dimensional form.

3.2 Model Development

Consider a rigid porous medium with porosity field $\phi(\boldsymbol{x}, t)$, where $\boldsymbol{x} = (x, y, z)$ is position and t time, containing an incompressible interstitial fluid (figure 3.1). The fluid is assumed to react with a component of the solid with the effect of changing the local volumes of both the fluid and solid, and hence the porosity of the medium. This situation typifies, for example, the dissolution of rock by acid-laden interstitial fluid, water flowing through a medium composed of (or containing) dissolvable material (e.g. salt grains), or the flow of warm fluid through a melting porous solid. The common feature in these situations is that the fluid contains a component (either solutal, thermal or chemical) that controls the rate of consumption and is transported within the flow through advective and diffusive processes. Our exposition will use the terminology and notation corresponding to a chemical or solutal reactive component, with an interstitial fluid that contains a dissolved reactive component of mass concentration $c(\boldsymbol{x}, t)$. Corresponding equations with a temperature field instead of a concentration field could in principle be used to describe the introduction of a fluid into a melting porous matrix (appendix A). The governing

system of equations for such a flow, as laid out in section 2.2 is

$$\frac{\partial \phi}{\partial t} = kR(c, \phi), \tag{3.1}$$

$$\boldsymbol{\nabla} \cdot (\phi \boldsymbol{u}) = (\nu - 1) kR(c, \phi), \tag{3.2}$$

$$\frac{\partial (\phi c)}{\partial t} + \boldsymbol{\nabla} \cdot (\phi \boldsymbol{u} c) = \boldsymbol{\nabla} \cdot \left(D \phi \boldsymbol{\nabla} c \right) - c_R kR(c, \phi), \tag{3.3}$$

$$\phi \boldsymbol{u} = -\frac{\kappa}{\mu} \boldsymbol{\nabla} p, \tag{3.4}$$

assuming that the body force $\boldsymbol{f} = \boldsymbol{0}$ in Darcy's law. For the general closure of the model we employ the permeability-porosity relation

$$\kappa = \kappa_0 \left(\frac{\phi}{\phi_0} \right)^n, \tag{3.5}$$

and a simple reaction model

$$R(c, \phi) = c f(\phi) \tag{3.6}$$

where $f(\phi)$ is a specified empirical function of the porosity satisfying $f(\phi_*) = 0$ and $f(0) = 1$, i.e. reaction ceases when all reactable material is exhausted. We retain general $f(\phi)$ where possible in our theoretical results, and set $f(\phi) = (1 - \phi/\phi_*)^m$ for our illustrative numerical results, where $m > 0$ is an exponent of order unity. Crucially, the joint proportionality of R on both c and $f(\phi)$ ensures that the reaction rate vanishes if either the local concentration of reactant or the local surface area available for reaction is zero, thus allowing for stable uniform states of fully reacted ($\phi \approx \phi_*$) porous medium and of unreactive ($c \approx 0$) fluid (figure 3.1). On the basis that porosity is a volumetric ratio that scales as L^3 for a given length scale L, and surface area scales as L^2, we adopt $m = 2/3$ for our illustrative solutions [cf. Chadam et al., 1986].

3.2.1 One dimensional model

In one dimension, the velocity has one component defined by $\boldsymbol{u} = u(x,t)\hat{\boldsymbol{x}}$ and all variables depend on (x,t) only. The system (3.1)–(3.3) then reads

$$\frac{\partial \phi}{\partial t} = kR(c,\phi), \tag{3.7}$$

$$\frac{\partial (\phi u)}{\partial x} = (\nu - 1)kR(c,\phi), \tag{3.8}$$

$$\frac{\partial (\phi c)}{\partial t} + \frac{\partial (\phi u c)}{\partial x} = \frac{\partial}{\partial x}\left(D\phi \frac{\partial c}{\partial x}\right) - c_R kR(c,\phi), \tag{3.9}$$

and Darcy's law is not required for closure of the model in one dimension. There are three spatial derivatives in the system: one in (3.8) and two in (3.9). Hence, the system requires a total of three boundary conditions on the dependent variables u and c. We can impose either a constant inlet Darcy flux Q at $x = 0$ according to

$$\phi(0,t)u(0,t) = Q, \tag{3.10}$$

or a constant inlet pressure P_0. In this Chapter we impose constant flux Q. We specify two conditions on the concentration field given by

$$c(0,t) = c_0, \qquad \lim_{x\to\infty} c = 0, \tag{3.11}$$

where c_0 is a constant representing the mass concentration of reactant supplied at $x = 0$, and the latter specifies that the reactant is fully depleted downstream. We impose the initial conditions

$$c(x,0) = 0, \qquad \phi(x,0) = \phi_0, \tag{3.12}$$

such that the system is initially free of reactant with unreacted porosity ϕ_0.

Equations (3.7)–(3.9) form a coupled parabolic–elliptic differential system describing the evolution of the porosity and concentration fields. Compared to prior models of reaction-front dynamics, our model differs from Stefan-type theories [e.g. Chadam et al., 1986, Szymczak and Ladd, 2011a] by allowing for smooth transitions within a general continuum two-phase theory. The model differs most fundamentally from the two-phase model

Terms scaled	Time scale	Length scale
Advective ~ Diffusive	D/U^2	D/U
Reactive ~ Diffusive	K^{-1}	$(D/K)^{1/2}$
Advective ~ Reactive	K^{-1}	U/K

Table 3.1: Intrinsic scales arising from the three possible dominant balances in the governing system (3.9) where $K = c_R k/\phi_*$ is the reaction rate factor and $U = Q/\phi_*$ is the advection rate.

of Hinch and Bhatt [1990] by incorporating diffusion in (3.9). Specifically, their model is recovered upon neglecting diffusion, taking $\nu \to 0$, $\phi_0 \to \phi_*$, and setting $m = 1$. In addition to including diffusion, our model also generalises Hinch and Bhatt [1990] secondarily by allowing for significant deviations in porosity from the background value ($0 < \phi_0 < 1$) and general production ratios ν.

We remark that for $\nu = 1$, corresponding to situations where the total volume of material is conserved, (3.8) can be integrated subject to (3.10) to yield the simpler local relationship between velocity and porosity given by $u = Q/\phi$. In this case, we can eliminate u from (3.9) using $u = Q/\phi$, reducing it to

$$\phi\frac{\partial c}{\partial t} + Q\frac{\partial c}{\partial x} = \frac{\partial}{\partial x}\left(D\phi\frac{\partial c}{\partial x}\right) - (c_R + c)kR(c,\phi). \tag{3.13}$$

The governing equation for the reactive component $c(x,t)$ is then given by a single purely parabolic equation, coupled to the porosity evolution equation (3.7).

3.2.2 Intrinsic scales and dimensionless model

Reading left to right, we refer to the respective terms of (3.9) after $\phi\partial c/\partial t$ as the advective term, the diffusive term and the reactive term. Scaling any two of these terms reveals a set of three possible combinations of intrinsic length and time scales in the problem (table 3.1). There are three distinct length scales: an advective–diffusive length scale D/U, a reactive–diffusive length scale $(D/K)^{1/2}$ and an advective–reactive length scale U/K, where $K = c_R k/\phi_*$ is a rate factor, or inverse time scale, associated with the reaction. There are two distinct timescales: an advective–diffusive timescale D/U^2, and a kinetic timescale K^{-1}. It should be noted that, since there are multiple intrinsic length and time

scales on which the dynamics may act, there is not a single natural length nor timescale that applies generally. The relevant scales that emerge in any given context are instead controlled internally by the dynamics, with the relative importance of advection, diffusion and reaction unknown *a priori*. Accordingly, there is no natural Péclet number (the ratio of diffusion to advection) nor Damköhler number (the ratio of reaction to advection) in the problem, which likewise form emergent quantities.

Without loss of generality, we use the advective-diffusive scalings represented by the first row of table 3.1 to conduct a non-dimensionalisation. Thus, we let

$$x = \left(\frac{D}{U}\right)\hat{x}, \quad t = \left(\frac{D}{U^2}\right)\hat{t}, \quad u = U\hat{u}, \quad c = c_0\hat{c}, \quad \phi = \phi_*\hat{\phi}.$$

On dropping hats, (3.7)–(3.9) become

$$\frac{\partial \phi}{\partial t} = BSR(c, \phi), \tag{3.14}$$

$$\frac{\partial}{\partial x}(\phi u) = (\nu - 1)BSR(c, \phi), \tag{3.15}$$

$$\phi\left(\frac{\partial c}{\partial t} + u\frac{\partial c}{\partial x}\right) = \frac{\partial}{\partial x}\left(\phi\frac{\partial c}{\partial x}\right) - (1 + \nu Sc)BR(c, \phi), \tag{3.16}$$

where $B = KD/U^2$ is a dimensionless number, $S = c_0/c_R$ is a Stefan number, and $R(c, \phi) = cf(\phi)$, with $f(\phi) = (1 - \phi)^m$. The boundary conditions on the concentration and fluid flux in (3.10) and (3.11) become

$$c(0, t) = 1, \qquad \lim_{x\to\infty} c = 0. \tag{3.17}$$

With $\Phi = \phi_0/\phi_*$, the initial conditions (3.12) become

$$c(x, 0) = 0, \qquad \phi(x, 0) = \Phi. \tag{3.18}$$

In addition to the reactive exponent m used to specify the function $f(\phi)$, the dimensionless system above depends on the four key numbers:

$$B = \frac{KD}{U^2}, \qquad S = \frac{c_0}{c_R}, \qquad \Phi = \frac{\phi_0}{\phi_*}, \qquad \nu. \tag{3.19}$$

The parameter B is the ratio of the advective-diffusive transport time scale D/U^2 to the kinetic time scale K^{-1}. It is a key emergent controlling parameter as previously found by Szymczak and Ladd [2013], equivalent to H in their published work. The parameter forms a key dimensionless number in reaction-front dynamics that represents a unification of the controls due to the advective flux, diffusivity and reactivity. Larger B represents faster reaction rates, larger diffusivities, and slower input rates. Estimates in illustrative applications (Appendix A) give $B \gtrsim 10^{-10}$, with the possibility for $B \gg 1$ for small flow rates $U \to 0$. Thus, both large and small limits of B are relevant to applications.

The second parameter S is a Stefan number, it is related to the acid capacity number used in prior works by $S = (\phi_* - \phi_0)\gamma_a$. In chemical contexts, S represents the ratio of the inflow concentration c_0 to the reactive consumption coefficient c_R. Small S corresponds to situations where a large volume of input fluid can dissolve a relatively smaller volume of the solid. In thermal contexts, S would represent the ratio of specific heat capacity of the fluid to the specific latent heat capacity required to melt the solid. Illustrative parameter values in applications (Appendix A) indicates that $S \lesssim 10$ is typical, and hence both large and small limits of S are physically relevant.

The parameter Φ is the ratio of the unreacted porosity ϕ_0 to the fully reacted porosity ϕ_*. The case $\Phi \approx 1$ corresponds to a system where there is relatively little reactive solid material in the medium, as can apply to complex minerals. Conversely, $\Phi \approx 0$ corresponds to situations where the porous medium consists primarily of reactable solid, as would apply to a bed of grains comprised of a single reactable material, for example.

Finally, as noted above, the production ratio ν is the ratio of the rate of increase in fluid volume to the rate of decrease of solid volume during reaction. The value generally ranges between $0 \leq |\nu| \leq O(1)$ across applications encompassing dissolution, chemical weathering, melting, and lithospheric melt extraction (Appendix A). Negative ν may be possible in the case of dissolving a salt which mixes well enough to reduce the solute density, the effect of negative ν is beyond the scope of this work.

3.2.3 Numerical modelling approach

We develop a numerical scheme that solves the equations using the method of lines, where the spatial derivatives are discretised using centred or upwind finite differences, and time-stepping is conducted using a stiff integrator.

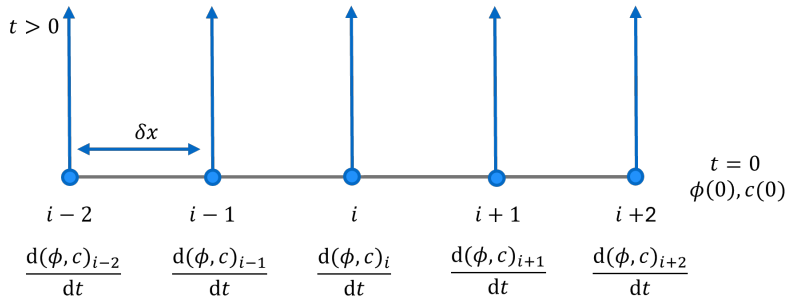

Figure 3.2: Schematic diagram of the method of lines. The domain is discretised in the spatial direction, resulting in a system of ODEs at each spatial node which can then be solved using a time stepping algorithm.

For our numerical solutions to the time-dependent system (figure 3.5), we focus on the simplifying case $v = 1$ for which the parabolic equation (3.13) can be used in place of (3.15) and (3.16). We solve (3.14) and the dimensionless form of (3.13) numerically using the method of lines, shown schematically in figure 3.2. Let $c_i(t)$ and $\phi_i(t)$ represent the concentration and porosity over a regular grid, where $1 \leq i \leq n$ is the spatial index and n is the total number of nodes. We discretise the spatial derivatives in (3.14) and the dimensionless form of (3.13) using centred differences for the second-order derivative and an upwind derivative for the advective term. The resulting coupled dynamical system for $2 \leq i \leq n-1$ is

$$\frac{\mathrm{d}\phi_i}{\mathrm{d}t} = SBR(c_i, \phi_i) \tag{3.20}$$

$$\frac{\mathrm{d}c_i}{\mathrm{d}t} = \frac{c_{i+1} - 2c_i + c_{i-1}}{(\delta x)^2} + \frac{1}{\phi_i}\left(\frac{\phi_i - \phi_{i-1}}{\delta x} - 1\right)\frac{c_i - c_{i-1}}{\delta x} - \frac{(1 + Svc_i)BR(c_i, \phi_i)}{\phi_i}, \tag{3.21}$$

where $R(c_i, \phi_i) = c_i f(\phi_i)$. At the boundaries, $i = 1$ and n, we maintain the Dirichlet conditions (3.17) by applying $\mathrm{d}c_1/\mathrm{d}t = \mathrm{d}c_n/\mathrm{d}t = 0$. The initial conditions of (3.18) are imposed by setting $c_1(0) = 1$ and $c_i(0) = 0$ for $2 \leq i \leq n$, and $\phi_i(0) = \Phi$ for $1 \leq i \leq n$.

The initial-value problem for $c_i(t)$ and $\phi_i(t)$ is solved using the LSODA solver from the

python package `scipy.integrate.solve_ivp`, which switches adaptively between non-stiff and stiff methods for computational efficiency.

Mesh sensitivity testing

The sensitivity of the solution to grid size was studied in 1D by running a selection of cases on meshes of varying δx. Table 3.2 summarises the characteristics of the set of meshes which we use to verify that the numerical results are domain and grid size independent. The profiles of concentration and porosity at $t = 1$ for each of these cases are plotted in figure 3.3 (a) concentration, and (b) porosity, showing close agreement between the meshes converging towards the most refined mesh; in (a) the purple curve, and in (b) the blue curve.

ID	initial domain length, L	δx	B	S	ϕ_0
A0	10	0.1	10	1	0.5
A1	10	0.05	10	1	0.5
A2	10	0.025	10	1	0.5
A3	10	0.0125	10	1	0.5

Table 3.2: Table of simulation runs used in the grid sensitivity analysis of the 1D method of lines.

To further assess the influence of the grid spacing over time, we calculate the mean absolute value of the deviation of porosity and concentration from the uniform initial condition across the domain,

$$\bar{x} = \frac{\sum_i^N |x_i - x_{t=0}|}{N}, \tag{3.22}$$

where subscription i is the node index, summed over all nodes up to the last node N. Figure 3.4 plots the temporal evolution of $\bar{c}$ and $\bar{\phi}$ for the cases A0-A3 as summarised in table 3.2, showing agreement between the meshes and convergence as δx is reduced. All of these meshes resolve the solution well, as shown in figure 3.3 where there is very little change in the solution at time $t = 1$ between meshes but we see that the mean $\bar{c}$ and $\bar{\phi}$ which change over time are effected by the mesh resolution. We opt to use mesh A2 with $\delta x = 0.025$ for our numerical modelling as it produces high resolution results without the additional expense of using mesh A3.

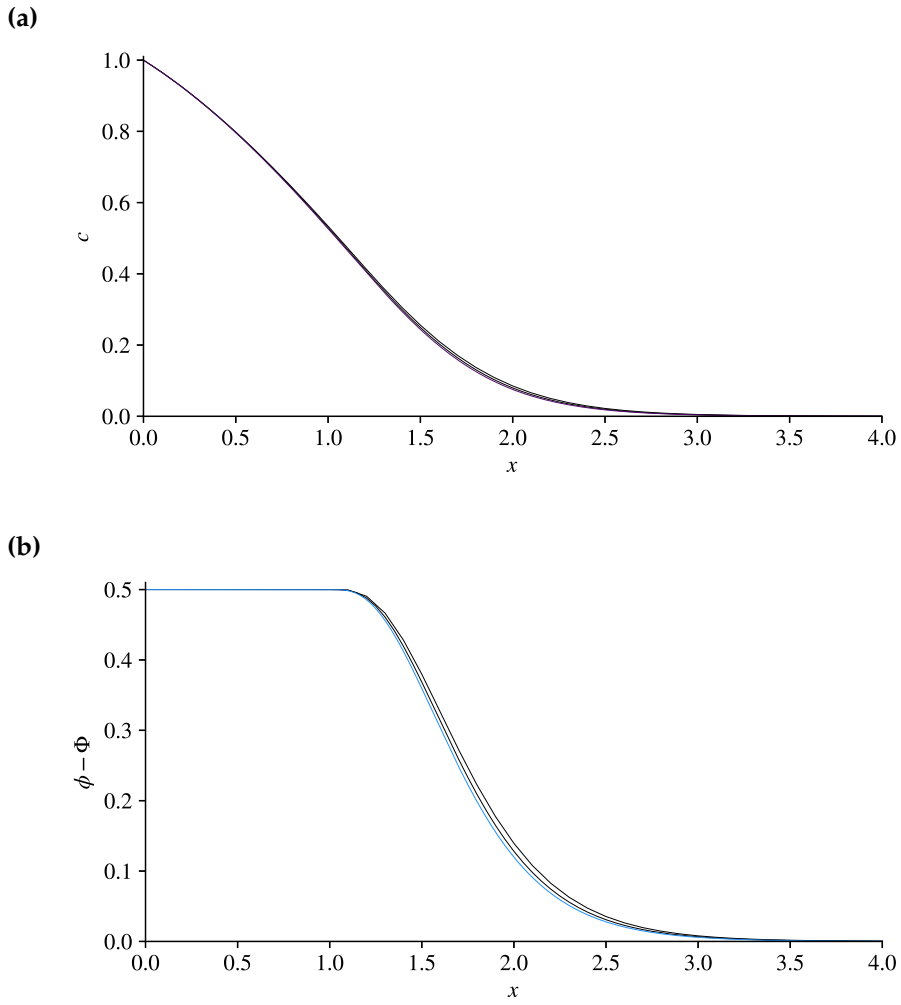

Figure 3.3: (a) Concentration c and (b) porosity ϕ for time $t = 1$ plotted for the cases A0, A1, A2 (black lines), A3 (purple for concentration, blue for porosity) showing convergence towards the most refined (purple/blue) as the mesh is refined. The details of the meshes are given in table 3.2.

Domain length

The theoretical domain has a far field boundary conditions $\partial c/\partial x_{x\to\infty} \to 0$ and in turn $\partial\phi/\partial x_{x\to\infty} \to 0$ also in that region. As such the domain length is chosen to ensure that the downstream far field, where there is no reaction, is sufficiently far from the reaction front to have a negligible effect on the dynamics. We perform domain rescaling when necessary, using the condition

$$\partial c/\partial x(x = 0.8L) = -\varepsilon$$

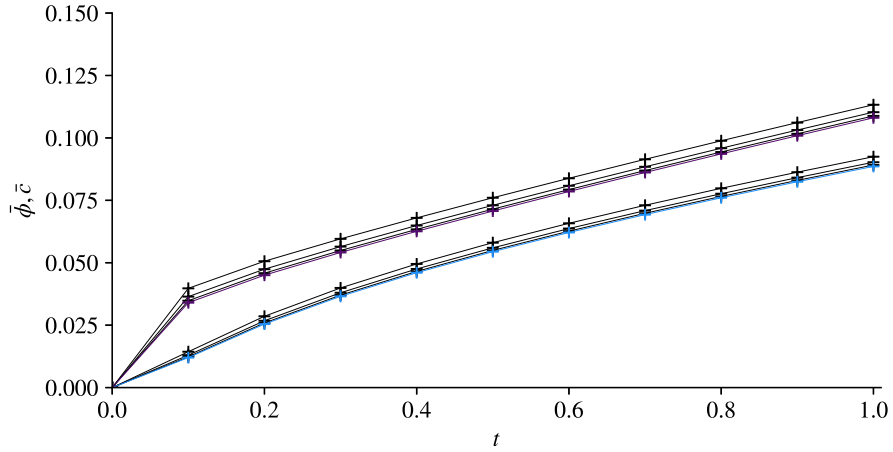

Figure 3.4: Profiles of mean $\bar{c}$ (purple) and $\bar{\phi}$ (blue) against time for the case A3. Overlaid for each is those variables cases A0, A1, A2 in black, demonstrating convergence of the results as the mesh is refined. Details of the meshes are given in table 3.2.

such that when $\partial c/\partial x$ reaches the threshold non-zero value $-\varepsilon$ at a position 80% of the way through the domain, the solution is saved as a cubic spline. This spline is then transferred to a larger domain, with sufficiently small δx for mesh independence, and the time-dependent solver is resumed. Further independent validation of the 1D numerical solutions is provided later in section 3.3 against the analytical asymptotic regimes.

3.3 Evolution towards a travelling-wave state

To demonstrate the key transient dynamics of the system, we present a suite of time-dependent solutions to (3.14)–(3.16) in figure 3.5.Each panel shows the evolution of the spatial profile of the concentration, $c(x,t)$, and of the porosity, $\phi(x,t)$, at a progression of times for (a)–(c) $B = 0.01$, and (d)–(f) $B = 100$, both for fixed Stefan number $S = 1$, initial relative porosity $\Phi = 0.5$, production ratio $\nu = 1$, and reactive exponent $m = 2/3$.

3.3.1 Transient regimes

The solutions at the early time of $t = 5 \times 10^{-4}$ in both examples ($B = 0.01$ and 100) of figure 3.5 exhibit a convex concentration profile, and a porosity still close to its starting value, $\phi \approx \Phi$. This early regime is dominated by diffusion, with negligible contributions

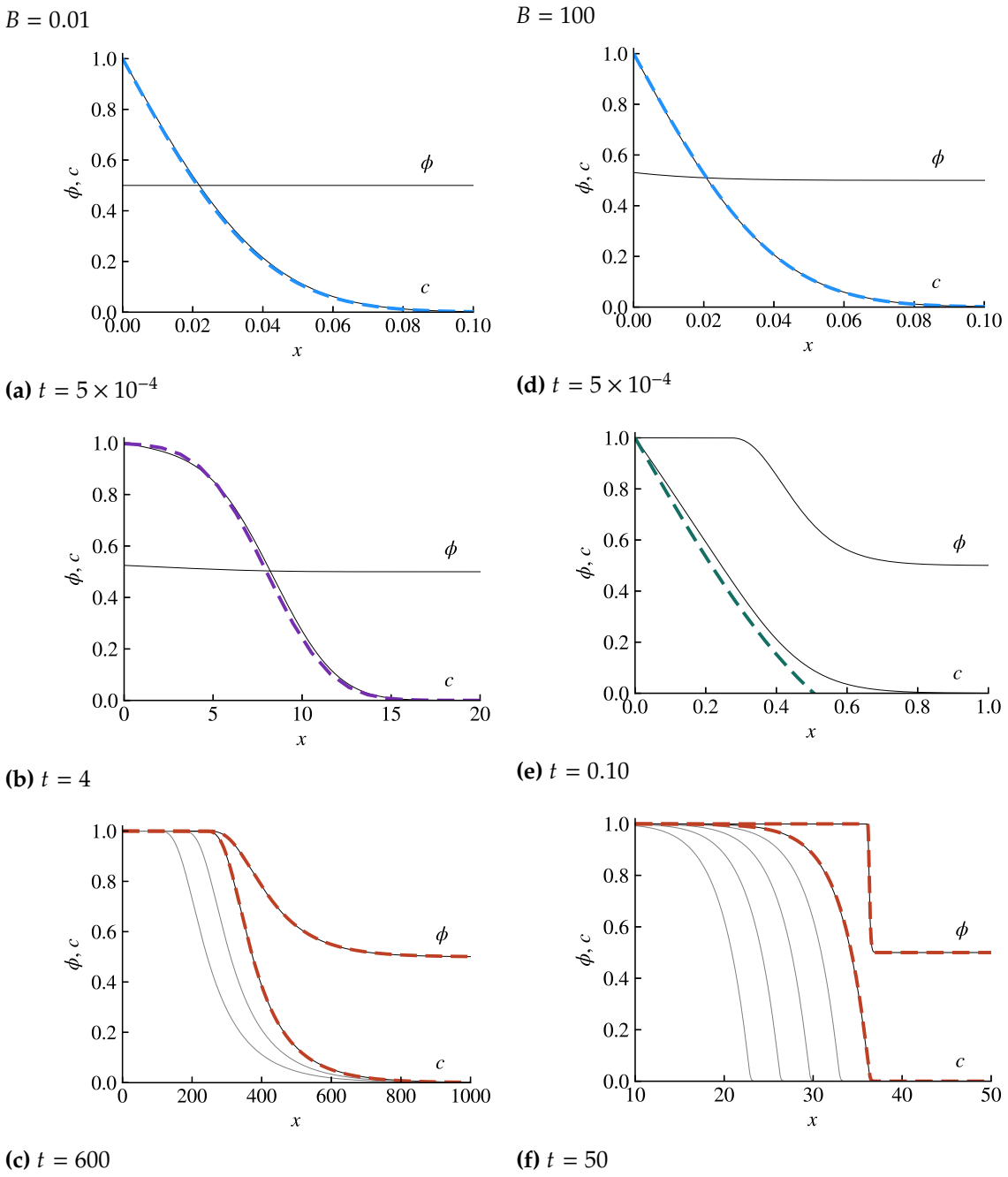

Figure 3.5: Time-dependent numerical solutions (3.14)-(3.16) describing the evolutions of the concentration $c(x,t)$ and porosity $\phi(x,t)$ profiles, for (a)–(c) $B = 0.01$ and (d)–(f) $B = 100$, each shown at progressive times. For both examples, we set the Stefan number $S = 1$, dimensionless initial porosity $\Phi = 0.5$, and production ratio $\nu = 1$. In (a) and (d), the early-time diffusive regime (3.24) is shown as a blue dashed curve. In (b), the advective-diffusive intermediate regime (3.27) is shown as a dashed purple curve. In (e), the reactive-diffusive intermediate regime (3.33) is shown as a dashed green curve. Panels (c) and (f) show the concentration at progressive times $t = 400$, 500 and 600, and $t = 30$, 35, 40, 45 and 50 respectively, highlighting the final travelling-wave state. The solution to the travelling-wave system (3.35)–(3.36) is shown at the final times as a red dashed curve in each case.

due to both advection and reaction, with (3.16) reducing to

$$\frac{\partial c}{\partial t} = \frac{\partial^2 c}{\partial x^2}, \qquad c(0,t) = 1, \qquad \lim_{x\to\infty} c = 0, \tag{3.23}$$

representing simple diffusion from a maintained solute source. The above supports the exact similarity solution [e.g. Carslaw and Jaeger, 1959] given by

$$c(x,t) = \operatorname{erfc}\left(\frac{x}{2\sqrt{t}}\right), \tag{3.24}$$

which we have overlaid as a dashed blue curve in figures 3.5(a) and 3.5(d). The agreement confirms that pure diffusion provides the very first transient regime.

As a result of the intervention of either advection or reaction in (3.16), new intermediate transient regimes will emerge. In order to assess which of advection or reaction intervenes first, we note that, in accordance with the scalings underlying the diffusive regime (3.24), namely $c \sim 1$ and $x \sim \sqrt{t}$, the terms scale according to

$$\frac{\partial c}{\partial t} \sim \frac{\partial^2 c}{\partial x^2} \sim t^{-1}, \qquad u\frac{\partial c}{\partial x} \sim t^{-1/2}, \qquad (1 + S\nu c)BR(c,\phi) \sim \beta \equiv N_* B, \tag{3.25}$$

where $\beta \equiv N_* B$ is a constant proportional to B and $N_* = \max(1, S\nu)$. The rate of change of concentration will therefore become comparable to the advective term, $\partial c/\partial t \sim u\partial c/\partial x$, once $t^{-1} \sim t^{-1/2}$ or, in other words, once $t \sim 1$. Further, the reactive term is important once $\partial c/\partial t \sim \beta$ or $t^{-1} \sim \beta$, implying that $t \sim \beta^{-1} = \tau_R$ is a dimensionless timescale on which reaction has an appreciable effect. The two key time scales, $t \sim 1$ and $t \sim \tau_R$, correspond dimensionally to the advective-diffusive and diffusive-reactive time scales (table 3.1). The value of β controls which of the two time scales occurs first.

From the combination of the two conditions for breakdown, namely, $t \gg 1$ if $\beta \ll 1$ and $t \gg \beta^{-1}$ if $\beta \gg 1$, it follows that, in general, the flow transitions away from the diffusive regime (3.24) once $t \sim \min(1, \beta^{-1})$. For the parameter values $B = 0.01$ and $B = 100$ used for figure 3.5, this criterion is $t \sim 1$ and $t \sim 10^{-2}$, respectively, which is in keeping with the observation of the regime at $t = 5 \times 10^{-4}$ in both examples. Once $t \sim \min(1, \beta^{-1})$, one of two new intermediate regimes will arise depending on whether advection or reaction

intervenes dominantly before the other. These regimes provide temporary transient states that are conceptually important in their own right as the final states that would apply in the complete absence of either reaction or advection independently.

Intermediate transient advective–diffusive regime if $\beta \ll 1$

If $\tau_R = \beta^{-1} \gg 1$, then the timescale on which advection intervenes is faster than the timescale on which reaction intervenes, implying the emergence of a temporary regime dominated by advection and diffusion alone. With reaction neglected, the porosity is still close to its starting value, $\phi \approx \Phi$, and (3.16) reduces to

$$\frac{\partial c}{\partial t} + v_0 \frac{\partial c}{\partial x} = \frac{\partial^2 c}{\partial x^2}, \tag{3.26}$$

where $v_0 = 1/\Phi$. The solution to the above subject to conditions (3.17) is

$$c = \frac{1}{2}\text{erfc}\left(\frac{x - v_0 t}{2\sqrt{t}}\right), \tag{3.27}$$

representing a classical diffusive $t^{1/2}$ self-similar expansion moving in the frame of the constant flow. Figure 3.5(b) shows the prediction of (3.27) as a purple dashed curve at $t = 4$, giving good agreement with the numerical solution and thus verifying its emergence.

This advective-diffusive regime will necessarily break down by the reactive time scale $t \sim \tau_R = \beta^{-1}$, and hence applies only as a transient regime in an intermediate time range of $1 \ll t \ll \beta^{-1}$. For the example of figure 3.5(b), for which $\beta^{-1} = 100$, this range is $1 \ll t \ll 100$, which is in keeping with its realisation at $t = 4$.

Intermediate transient reactive–diffusive regime if $\beta \gg 1$

If instead $\tau_R = \beta^{-1} \ll 1$, then the effects of reaction will intervene sooner than advection, leading to a temporary regime dominated by diffusion and reaction only. Upon neglecting

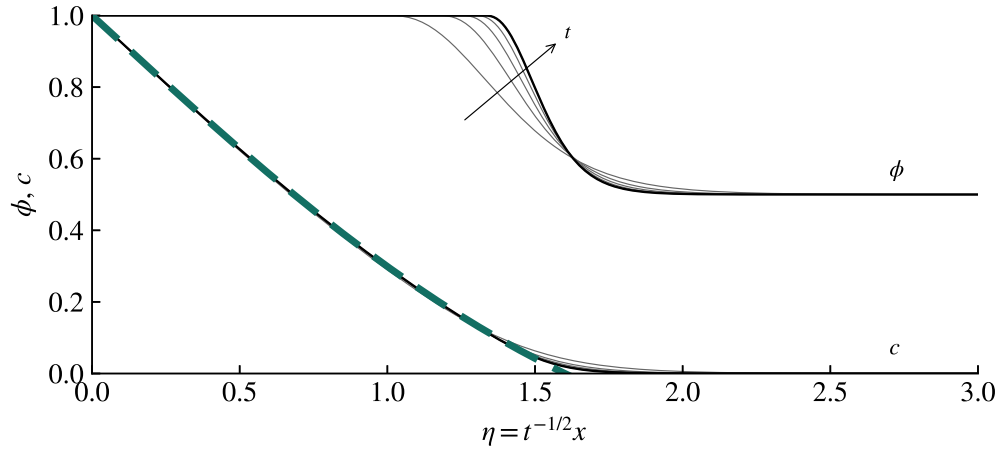

Figure 3.6: A numerical solution to the simplified reactive-diffusive model (3.28)–(3.29) for parameters $B = 100$, $S = 1$, $\phi_0 = 0.5$, and $\nu = 1$, showing its convergence towards the intermediate Stefan theory (3.33) overlaid as a dashed green curve. The profiles of the concentration $c(x,t)$ and porosity $\phi(x,t)$ are plotted against the similarity coordinate $\eta = t^{-1/2}x$ in increments of 0.2 from $t = 0.2$ to 1.

advection, the reduced form of the system (3.14)–(3.16) is

$$\frac{\partial \phi}{\partial t} = BSR(c,\phi), \tag{3.28}$$

$$\phi \frac{\partial c}{\partial t} = \frac{\partial}{\partial x}\left(\phi \frac{\partial c}{\partial x}\right) - (1 + S\nu c)BR(c,\phi). \tag{3.29}$$

A numerical solution to this reduced model (figure 3.6) shows that its predictions evolve to form a sharp porosity jump after a sufficient time, with

$$\phi(x,t) \sim \begin{cases} 1 & \text{if } x < x_N(t), \\ \Phi & \text{if } x > x_N(t), \end{cases} \tag{3.30}$$

where $x = x_N(t)$ represents a moving effectively interfacial porosity transition. In view of this property, it is clear that the solutions to the diffusive-reactive system (3.28)–(3.29) evolve asymptotically towards those of a classical Stefan problem.

In this regime, the piecewise uniformity of the porosity field and the conservation of reactant across the interface (appendix C) yield the simplified leading-order governing

equation and corresponding Stefan condition given by

$$\frac{\partial c}{\partial t} = \frac{\partial^2 c}{\partial x^2}, \qquad \dot{x}_N = -S_* \frac{\partial c}{\partial x}(x_N, t), \tag{3.31}$$

with the input and continuity conditions $c(0,t) = 1$ and $c(x_N(t), t) = 0$, where

$$S_* = (1 - \Phi)^{-1} S \tag{3.32}$$

is an effective Stefan number which accounts for the solid fraction as well as the fluid properties, equivalent to the acid capacity number γ_a in earlier works such as Szymczak and Ladd [2013]. The solution to the system above is given by the classical similarity solution [e.g. Carslaw and Jaeger, 1959],

$$c = 1 - \frac{\operatorname{erf}(\eta/2)}{\operatorname{erf}(\eta_N/2)}, \tag{3.33}$$

where $\eta = t^{-1/2} x$ and η_N satisfies the implicit algebraic equation

$$\sqrt{\pi} \eta_N e^{(\eta_N/2)^2} \operatorname{erf}(\eta_N/2) = 2 S_*. \tag{3.34}$$

For our illustrative value of $S = 1$ and $\Phi = 0.5$, we have $S_* = 2$ and (3.34) yields $\eta_N \approx 1.60$. The concentration field predicted by (3.33) is plotted as a dashed green curve in figures 3.5(e) and 3.6, showing good agreement with the numerical solution to (3.28)–(3.29).

Notably, the results above have demonstrated how a reactive-diffusive continuum two-phase theory can reduce asymptotically to an idealised Stefan problem to leading order. Within the context of the full model, the solution (3.33) represents only a transient intermediate regime that arises for cases of $\beta \gg 1$ that occurs only after enough time that the porosity step has developed, but not so long that the effects of advection have yet to intervene significantly, i.e. $\beta^{-1} \ll t \ll 1$. For the example of figure 3.5(e), this range is $0.01 \ll t \ll 1$, which is in keeping with the observation of the regime at $t = 0.1$.

3.3.2 Final travelling-wave state

Once $t \gtrsim \max(\beta^{-1}, 1)$, both advection and reaction will have necessarily affected the dynamics significantly, and a transition to a final state involving all three terms of (3.16) will establish. From the late-time progressions of the final solutions in our illustrative examples (figures 3.5(c) and 3.5(f)), we observe that the final regimes form steady travelling-wave states translating forwards with a constant speed V. To develop a system for this final state, we recast (3.14)–(3.16) in terms of a moving coordinate $z = x - Vt$, and write them in their original conservative forms (3.7)–(3.9), giving

$$-V\phi' = BSR(c, \phi), \tag{3.35}$$

$$\big(\phi u\big)' = (1 - \nu)V\phi', \tag{3.36}$$

$$\big(\phi c(u - V) - \phi c'\big)' = S^{-1}V\phi', \tag{3.37}$$

where primes denote $\mathrm{d}/\mathrm{d}z$, and $R(c, \phi) = c\, f(\phi)$, with conditions

$$\lim_{z\to-\infty} c = 1, \qquad \lim_{z\to-\infty} (\phi u) = 1, \qquad \lim_{z\to\infty} c = 0, \qquad \lim_{z\to\infty} \phi = \Phi. \tag{3.38}$$

Equations (3.35)–(3.38) form a fourth-order differential system for $\phi(z)$ and $c(z)$ describing a transition between a uniformly reacted state upstream and a uniformly unreacted state downstream. The system is translationally invariant in z, and hence we must set a reference for the z coordinate. Without loss of generality, we choose this as the centre of the porosity transition, with $\phi(0) = (1 + \Phi)/2$.

Favourably, both (3.36) and (3.37) accommodate first integrals. The integral of (3.36) subject to the two upstream ($z \to -\infty$) conditions of (3.38) yields the equation

$$\phi u = 1 - V(1 - \nu)(1 - \phi). \tag{3.39}$$

The above provides a general relationship between the Darcy flux ϕu and porosity field ϕ. In particular, it implies that the Darcy flux transitions to $1 - V(1 - \nu)(1 - \Phi)$ as $z \to \infty$, giving its total reduction as a result of reactive consumption.

The first integral of (3.37) subject to the two downstream ($z \to \infty$) conditions in (3.38) yields

$$\phi c(u - V) - \phi c' = S^{-1}V(\phi - \Phi). \tag{3.40}$$

Upon now further applying the two upstream ($z \to -\infty$) conditions of (3.38), the above yields the explicit expression for the dimensionless travelling-wave speed,

$$V = \frac{S_*}{1 + S_*}. \tag{3.41}$$

Thus, the speed of the reaction front is known *a priori* and independently controlled by the effective Stefan number S_*. The result of (3.41) can alternatively be derived using global reactant conservation (appendix C).

The system can now be considered in terms of (3.35), (3.39) and (3.40) alone. Using (3.39) to substitute for u in (3.40), we arrive at a final integrated two-variable system:

$$V\phi' = -BSR(c, \phi), \tag{3.42}$$

$$\phi c' + S^{-1}V(\phi - \Phi) = c(1 - V + \nu V(1 - \phi)), \tag{3.43}$$

with conditions

$$\lim_{z \to -\infty} c = 1, \qquad \lim_{z \to -\infty} (\phi u) = 1. \tag{3.44}$$

Equations (3.42)–(3.44) form a novel two-variable system describing the porosity and concentration profiles in travelling-wave states. These can be mapped to (2.56) (integrating this once more) and (2.57), derived in Szymczak and Ladd [2013] upon taking the appropriate limit of small acid capacity and $\nu \to 0$ as done in their work.

Equations (3.42)–(3.43) can be interpreted as a dynamical system in z in the two variables $\phi(z)$ and $c(z)$. Phase-plane analysis reveals two fixed points: an unstable node $(\phi, c) = (1, 1)$ representing the upstream fully reacted state; and a saddle point $(\phi, c) = (\Phi, 0)$ representing the downstream unreacted state. Our solution of interest forms the unique trajectory connecting these two states. We solve (3.42)–(3.43) numerically using the LSODA integrator from the `scipy` Python package, which switches adaptively between variable orders of non-stiff Adams time-stepping and stiff backwards differentiation formulae.

Since phase-plane trajectories diverge towards saddles, for stability we opt to integrate backwards in z, starting from the downstream conditions (3.38) and marching towards the node. Thus, we initiate the integrator by setting $c(z_0) + \delta$ and $\phi(z_0) = \Phi + \delta$, where z_0 is an arbitrary reference position and δ is a small number, and integrate backwards to a large negative value of z. We then translate the z-coordinate to satisfy our normalisation $\phi(0) = (1 + \Phi)/2$. Two illustrative numerical solutions are overlaid as red dashed curves in figures 3.5(c) and 3.5(f), showing direct agreement with the independently determined predictions of our time-dependent solver.

Critical spatial onset of the porosity transition

We note that the travelling-wave form of the mass conservation equation of the solid (3.42) can be integrated exactly by separation to yield an analytical expression relating the porosity $\phi(z)$ and the concentration field $c(z)$. For $0 \leq m < 1$, this integral yields

$$\phi = \begin{cases} 1 & (z < z_*), \\ 1 - \left(A \displaystyle\int_{z_*}^{z} c(z)\, \mathrm{d}z \right)^{\frac{1}{1-m}} & (z > z_*), \end{cases} \tag{3.45}$$

where $A = (1 - m)(1 - \Phi)(1 + S_*)B$, and z_* is constrained by $\phi(\infty) = \Phi$ or, in other words,

$$A \int_{z_*}^{\infty} c(z)\, \mathrm{d}z = (1 - \Phi)^{1-m}. \tag{3.46}$$

The result of (3.45) shows that the porosity profile undergoes a transition across a critical position z_* with the solid fully reacted ($\phi \equiv 1$) for all $z < z_*$ and containing unreacted material for all $z > z_*$. The position z_* is equivalent to the front position that is supposed in Szymczak and Ladd [2013, 2014] as the position of the transition interface, allowing for their decomposition of the concentration transition to upstream and downstream regions with respect to z_*. The structure is illustrated in figure 3.7, where our numerical solution to (3.42)–(3.43) is shown as a solid curve for three different S. The critical position z_*, derived by using the concentration field from the numerical solution for $c(z)$ to evaluate the integral in predicted by (3.46) numerically using quadrature, is marked by a star.

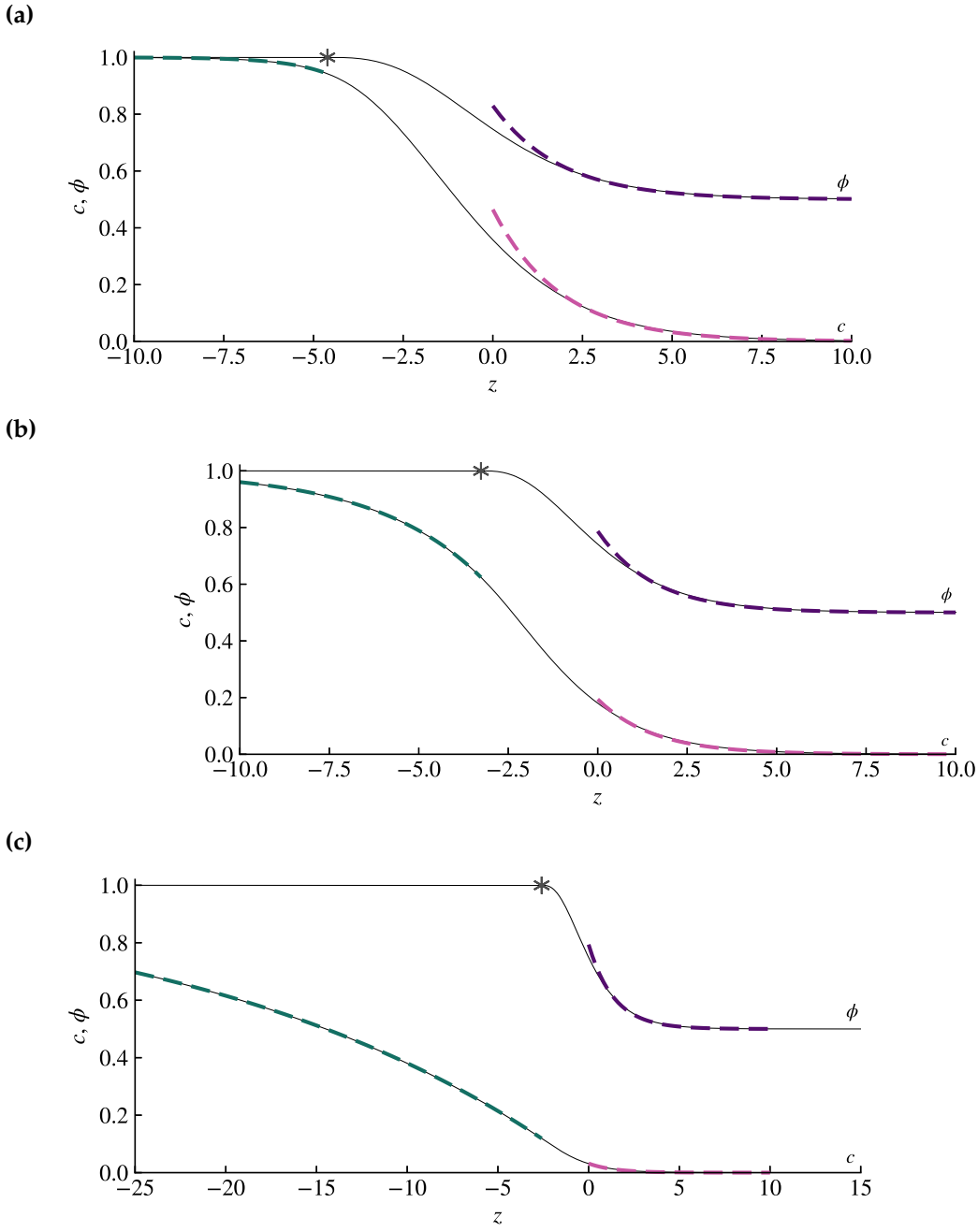

Figure 3.7: Solution to the travelling-wave system (3.42)–(3.43), subject to boundary conditions (3.44), giving concentration $c(z)$ and porosity $\phi(z)$ profiles. The critical spatial onset of the porosity transition predicted by (3.46) is shown as a star. The upstream asymptotic tail for the concentration predicted by (3.47) is shown green, and the downstream tails for the concentration and porosity in (3.51) are shown in purple and pink, respectively. The fixed parameter values are $B = 1$, $\nu = 1$, $\Phi = 0.5$ and $S =$ (a) 0.1, (b) 1 and (c) 10. We see here, that as S increases (moving down though the panels), the downstream tail shortens whilst the upstream tail extends. The region of transition not captured by the tails is a larger proportion of the transition for smaller S.

Tails of the concentration and porosity fields

Now that we can partition the domain about $z = z_*$, we can consider the tail behaviour of the concentration and porosity based on the knowledge of ϕ. Upstream for $z < z_F$ which includes the upstream limit $z \to -\infty$, the porosity is uniformly equal to unity in accordance with (3.45). Since the solid is fully reacted, the concentration profile $c(z)$ in this region is controlled purely by advection and diffusion, with the reduced form of (3.37) being $(1 - V)c' = c''$. Solving this equation, we obtain

$$c = 1 - \gamma_- e^{(1-V)z}, \qquad \phi \equiv 1 \qquad (z < z_*), \tag{3.47}$$

where γ_- is a constant of integration which is unknown and constraining its value requires the solution of the full model. With just γ_- fitted, (3.47) is overlaid in each panel of figure 3.7 as a dashed green curve, showing direct agreement with our numerical solution for $z < z_*$. This is the same as the upstream concentration profile derived by Szymczak and Ladd [2013] in the small acid capacity limit, where γ_- is derived based upon matching the downstream tail at the interface z_*.

Downstream ($z \to \infty$), the porosity converges to the unreacted value Φ, as specified by (3.38). The system (3.42)–(3.43) then simplifies asymptotically to a pair of linear first-order ordinary equations with constant coefficients given by

$$V\phi' = -BSf(\Phi)c, \tag{3.48}$$

$$\Phi c' + S^{-1}V(\phi - \Phi) = c(1 - V + \nu V(1 - \Phi)). \tag{3.49}$$

The solution is $c \sim \gamma_+ e^{-dz}$ and $\phi \sim \Phi + r\gamma_+ e^{-dz}$, where γ_+, r and d are constants, with $r = BSf(\Phi)/dV$ and

$$d = a\left(-1 + \sqrt{1 + \frac{f(\Phi)B}{\Phi a^2}}\right), \qquad \text{where } a = \frac{1 - V + \nu(1 - \Phi)V}{2\Phi}. \tag{3.50}$$

The asymptotic forms of the downstream tails are therefore

$$c \sim \gamma_+ e^{-dz}, \qquad \phi \sim \Phi + \frac{\gamma_+ BSf(\Phi)}{dV} e^{-dz} \qquad (z \to \infty), \tag{3.51}$$

where γ_+ is the unique unknown. With just γ_+ fitted, the predicted tails (3.51) are plotted in each panel of figure 3.7 as purple and pink dashed curves for the porosity and concentration, respectively, showing agreement with the full solution. Compared to the upstream tail (3.47), the decay scale d is likewise related to the travelling-wave speed $1-V$ via the prefactor a. In contrast, d depends strongly on the dimensionless number B. For $B \to \infty$, $d \sim f(\Phi)B/2\Phi a$ is linear in B. For $B \to 0$, $d \sim \sqrt{f(\Phi)B/\Phi}$ is proportional to $\sqrt{B}$. The results imply a predictable ratio in the amplitude of the downstream concentration and porosity tails, namely $r = (\phi - \Phi)/c \sim BSf(\Phi)/dV$, dependent on both B and S. For $f(\Phi) = 1$ and $S_* \to 0$, this recovers l_d equal to that derived by Szymczak and Ladd [2013]. In their work l_d is the prevailing length scale in the whole downstream region as $f(\phi) = 1$ through the region due to their simplified reaction rate, however this is not necessarily the case for a more complex reaction rate. Figures 3.7(a) and 3.7(b) both show regimes in which the regions not captured by these tails are of approximately the same magnitude as those captured, which we will seek to encompass in our regime analysis.

3.4 Regime analysis

The system of (3.42)–(3.44) describes the final structure of reaction fronts over a parameter space dependent on B, S, ν, Φ, and m. The time-dependent solutions (figure 3.5) demonstrated variations both in the absolute and relative magnitudes of the length scales on which the concentration and porosity profiles transition across this space. We now investigate: first, how the length scales are controlled by the underlying parameters; and second, the relative magnitude of the terms contributing to the governing transport equation. In each case, a key asymptotic reduction is identified, an associated reduced analytical theory developed, and finally classified within a unified regime diagram.

3.4.1 Relative sharpness

To measure the length scales on which the transitions in porosity and concentration across the reaction front take place, we define *transition thicknesses* by

$$l_\phi = z_\phi^+ - z_\phi^-, \qquad l_c = z_c^+ - z_c^-, \tag{3.52}$$

where $\phi(z_\phi^-) = \varepsilon\Phi + (1-\varepsilon)$ and $\phi(z_\phi^+) = (1-\varepsilon)\Phi + \varepsilon$ define the characteristic beginning and end, z_ϕ^- and z_ϕ^+, of the porosity transition, where ε is a small parameter. Further, we let $c(z_c^-) = 1-\varepsilon$ and $c(z_c^+) = \varepsilon$ define the corresponding start and end of the concentration transition. We will take $\varepsilon = 0.1$, for which (3.52) measure the length scales on which the transitions develop from 10% to 90% complete. The transition regions $[z_\phi^-, z_\phi^+]$ and $[z_c^-, z_c^+]$, with lengths l_ϕ and l_c, are illustrated respectively by blue and purple bars in figure 3.8 for $B = 0.01, 1$ and 100, and fixed parameters $\nu = 1$, $S = 1$, and $\Phi = 0.5$. For $B = 0.01$, $l_\phi \approx 280$ is similar to $l_c \approx 230$. For $B = 1$, the thicknesses $l_\phi = 4.7$ and $l_c = 8.3$ are smaller but with the concentration thickness relatively larger than the porosity thickness. For $B = 100$, $l_\phi \approx 0.3$ and $l_c \approx 6.6$, revealing a clear separation of length scales, with $l_\phi \ll l_c$. These trends are confirmed in figure 3.10, where l_ϕ and l_c are plotted as functions of B for $S = 0.01$ and 1.

The transition regions $[z_\phi^-, z_\phi^+]$ and $[z_c^-, z_c^+]$, with lengths l_ϕ and l_c, are illustrated respectively by blue and purple bars in figure 3.9 for $S = 0.1, 1$ and 10, and fixed parameters $\nu = 1$, $B = 1$, and $\Phi = 0.5$. Figure 3.9(b) is the same as figure 3.8(b) for easy comparison to $S = 0.1$ and $S = 10$. For $S = 0.1$, the thicknesses $l_\phi = 6.1$ and $l_c = 6.9$ are of the same magnitude with a sharpness of $\Sigma = 1.13$. For $S = 10$, $l_\phi \approx 4.1$ and $l_c \approx 46.6$, with a sharpness of 11.3, revealing a clear separation of length scales, with $l_\phi \ll l_c$. This shows that independently of B, S is able to alter the relative sharpness of the transition fields. This extends prior work [Szymczak and Ladd, 2013] which deduced that B controlled the relative length scales for $S \ll 1$.

To quantify the length scale separation more directly, we define the *relative sharpness*,

$$\Sigma = l_c / l_\phi, \tag{3.53}$$

forming the ratio of the concentration thickness to the porosity thickness. For the examples of figure 3.8, (a) $\Sigma = 0.83$, (b) 1.75 and (c) 21.3, showing that the relative sharpness increases with B. Figure 3.11 and figure 3.12 present contour plots of relative sharpness (3.53) over the full parameter space of (S, B) for $\Phi = 0.5$ and $\nu = 1, 0$ respectively. Figures 3.11 and 3.12 confirm that the sharp regime is ν independent. The $\Sigma = 10$ contour is

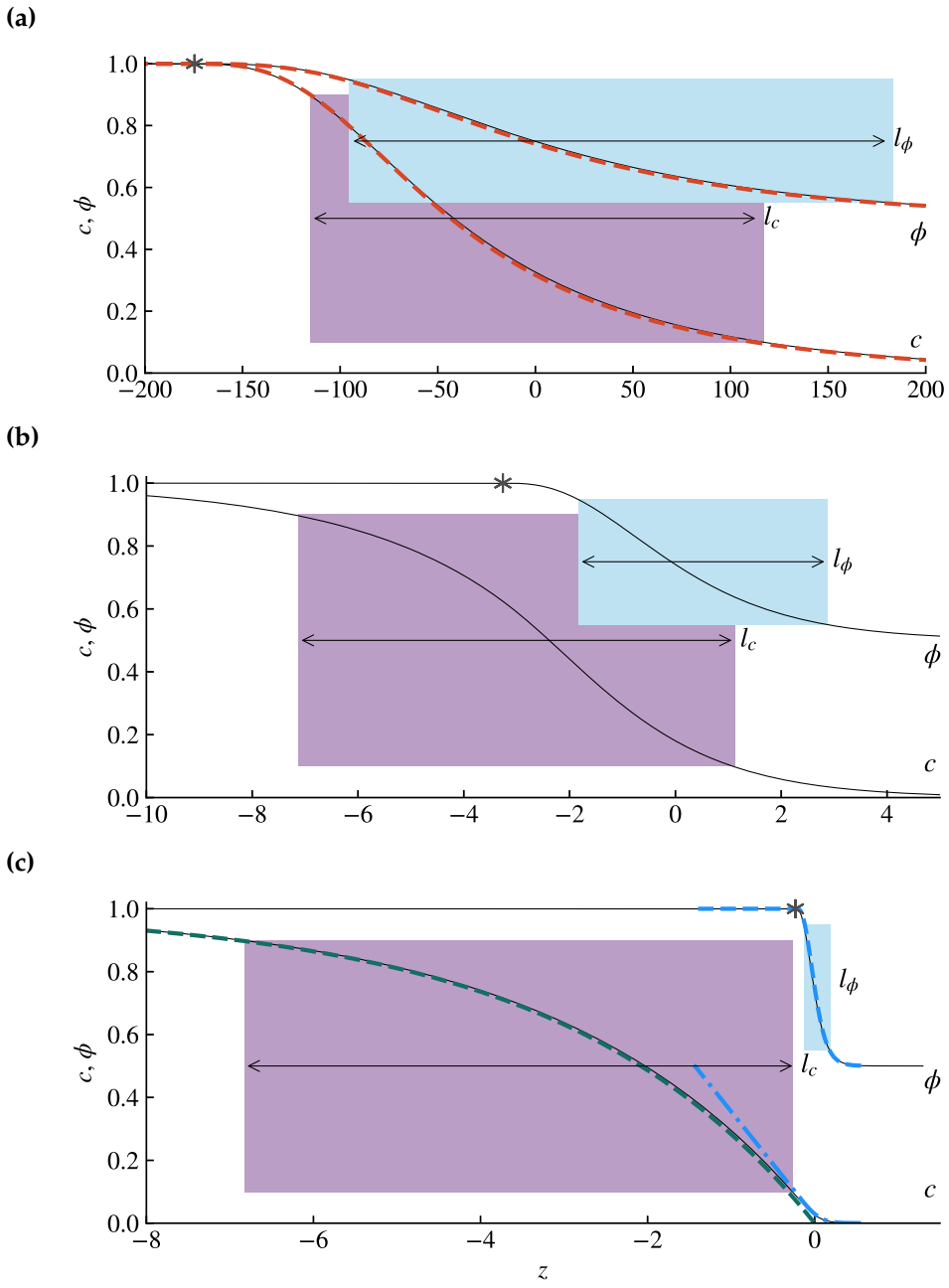

Figure 3.8: The travelling-wave solutions given by solving (3.42)–(3.44) for $\phi(z)$ and $c(z)$ for (a) $B = 0.01$, (b) $B = 1$, (c) $B = 100$, with $S = 1$, $\Phi = 0.5$ and $\nu = 1$. The transition regions, with thicknesses l_ϕ and l_c as defined by (3.52), are indicated by blue and purple rectangles in each case, illustrating their dependence on the dimensionless number B. The solutions form part of the larger regime diagram shown in figure 3.11. In (a), the asymptotic approximation for porosity (3.74) and concentration (3.75) are shown in red. In (c), the prediction of the advective-diffusive outer theory (3.56) is shown as a dashed green curve. The predictions of the reactive-diffusive inner theory (3.60)–(3.62) are shown as blue dashed lines. Stars indicate the critical onset of the porosity transition.

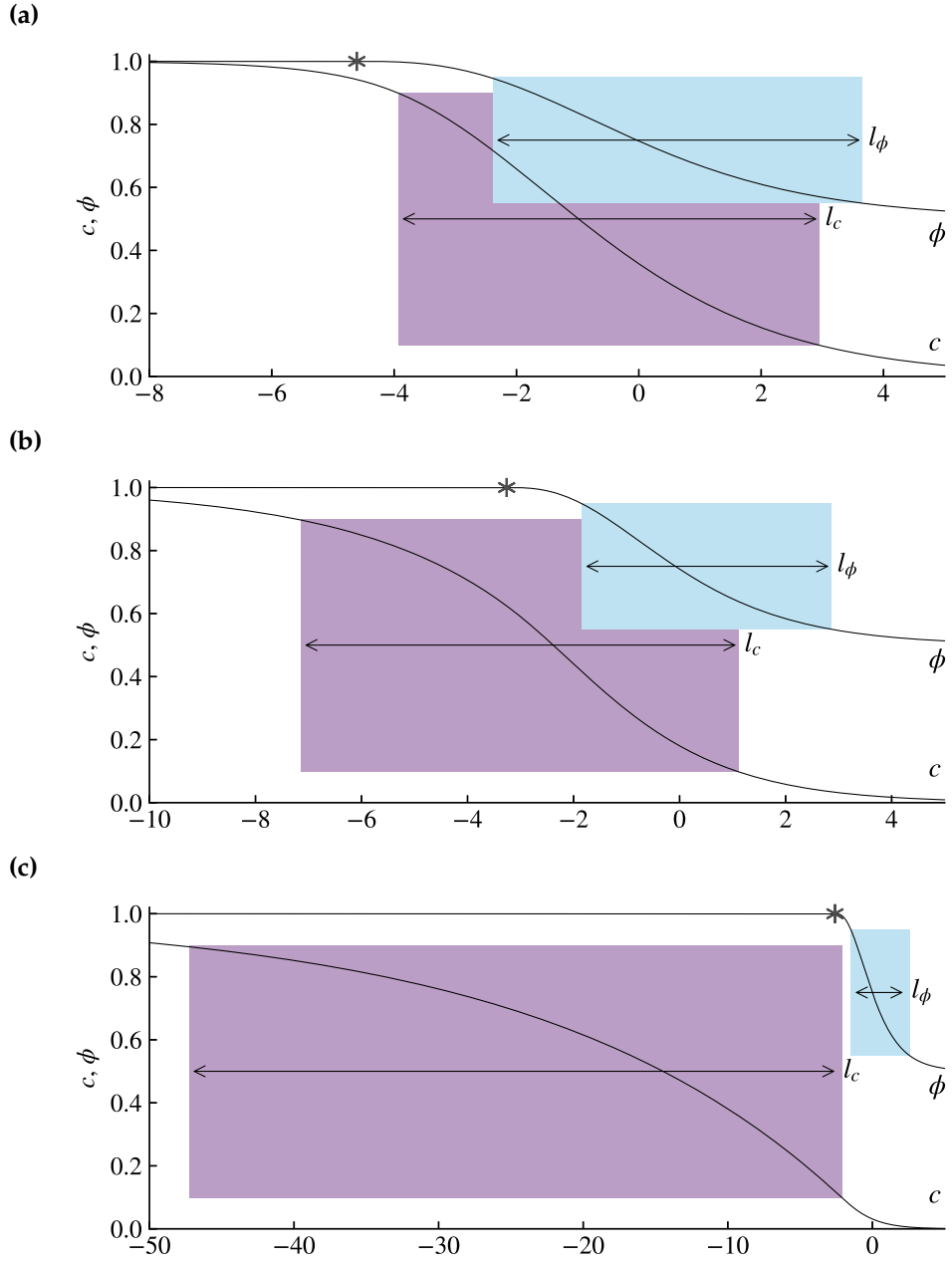

Figure 3.9: The travelling-wave solutions given by solving (3.42)–(3.44) for $\phi(z)$ and $c(z)$ for (a) $S = 0.01$, (b) $S = 1$ and (c) $S = 10$, with $B = 1$, $\Phi = 0.5$ and $\nu = 1$. The transition regions, with thicknesses l_ϕ and l_c as defined by (3.52), are indicated by blue and purple rectangles in each case, illustrating their dependence on the dimensionless number S. The solutions form part of the larger regime diagram shown in figure 3.11.

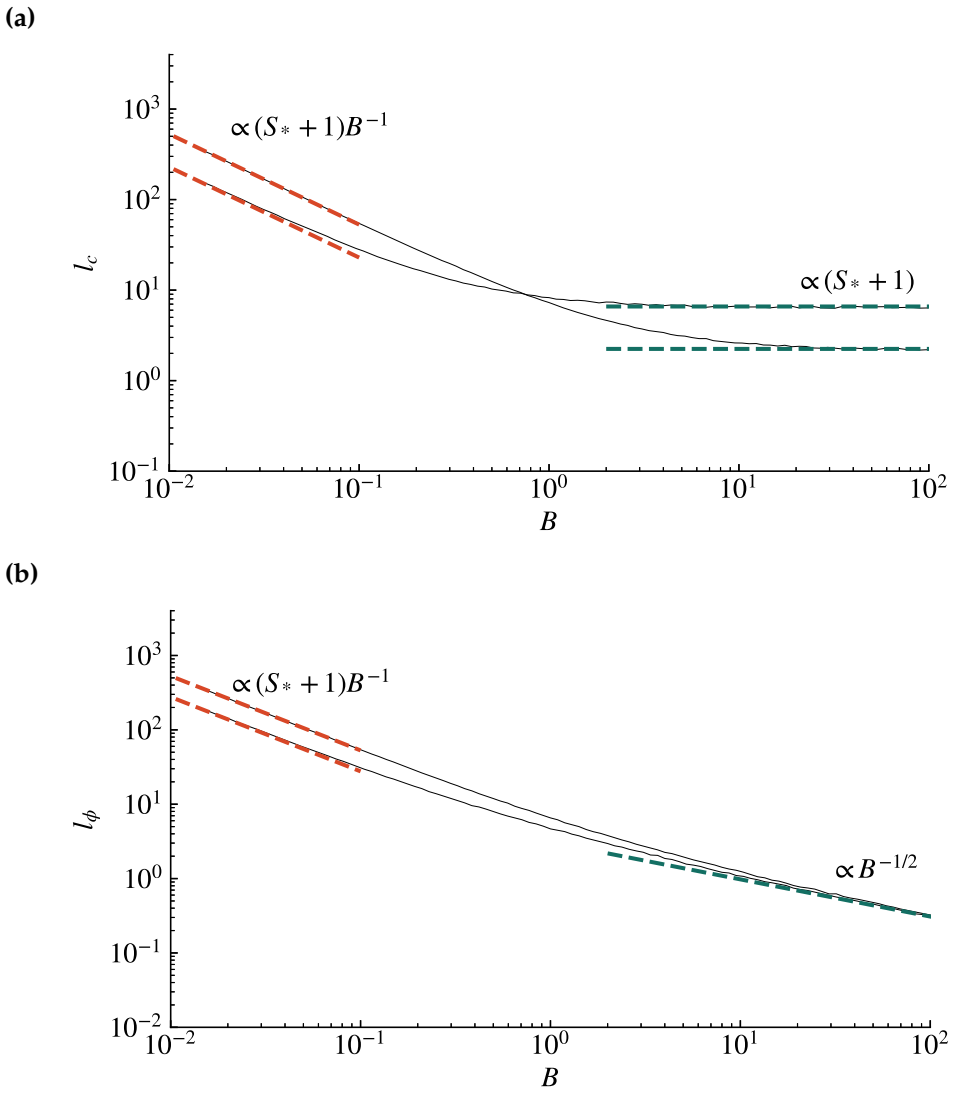

Figure 3.10: (a) Concentration transition thickness l_c and (b) porosity thickness l_ϕ as functions of B for fixed $\Phi = 0.5$, $\nu = 1$ and two different Stefan numbers, $S = 0.01$ and 1. The solutions were determined by solving (3.42)–(3.43) numerically and using the definitions of l_c and l_ϕ in (3.52) for $\varepsilon = 0.1$. The predictions of the sharp-interface asymptotic theory arising for $B \to \infty$, given by (3.57) and (3.66), are plotted as green dashed lines. The predictions of the diffusionless asymptotic theory arising for $B \to 0$ given by (3.80) are plotted as red dashed lines.

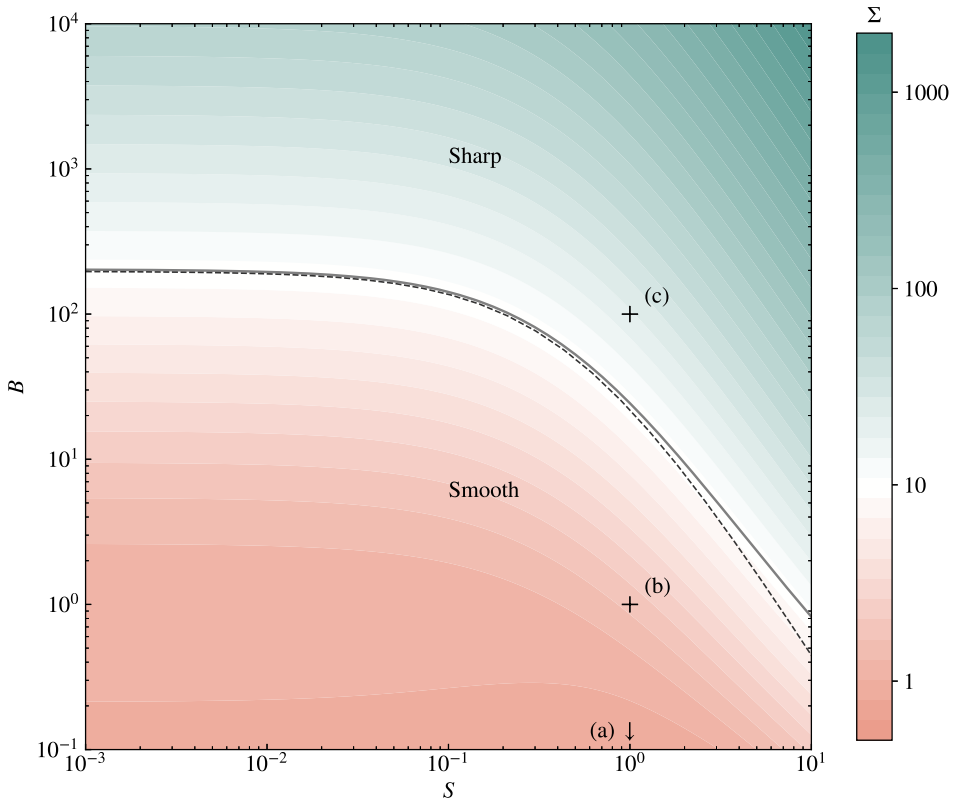

Figure 3.11: Contour plot of relative sharpness Σ defined by (3.53), plotted across the parameter space of B and Stefan number, (B, S), for constant dimensionless initial porosity $\Phi = 0.5$ and production ratio $\nu = 1$. Red and green indicate small and large relative sharpness, respectively. The contour of $\Sigma = 10$, characterising the separation between sharp and smooth reaction fronts, is indicated as a solid black line, showing a levelling as $S \to 0$, and a more complex dependence on Stefan number as $S \to \infty$. The contour for $\Sigma = 10$, namely, $\Omega \approx 124$ predicted by the asymptotic theory of the sharp regime (3.67) is shown as a dashed curve. Crosses indicate the positions of examples (b) and (c) from figure 3.8.

shown as a solid curve, providing a characteristic separation between a regime where the porosity transition is *sharp* versus those which are relatively smooth. The contours become independent of S for $S \lesssim 1$, implying a largely direct control of relative sharpness due to the parameter B in the limit $S \to 0$. For $S \gtrsim 1$, the relative sharpness contours are dependent on S, indicating a more complex dependence on both B and S.

3.4.2 The sharp regime

Figure 3.11 showed that for sufficiently large B, there can be a separation of scales between the porosity and concentration thicknesses, with $\Sigma \gg 1$. Informed by this, we seek to understand where this *sharp regime* arises based on the simplifying asymptotic property

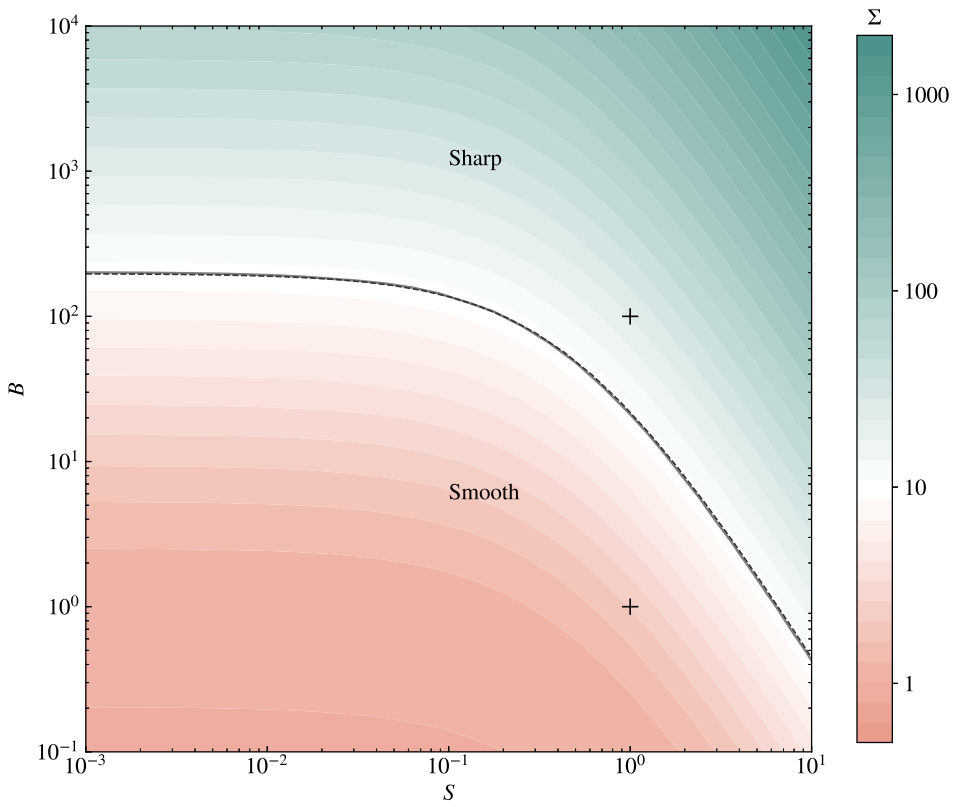

Figure 3.12: Contour plot of relative sharpness Σ defined by (3.53), plotted across the parameter space of B and Stefan number, (B, S), for constant dimensionless initial porosity $\Phi = 0.5$ and production ratio $\nu = 0$. Red and green indicate small and large relative sharpness, respectively. The contour of $\Sigma = 10$, characterising the separation between sharp and smooth reaction fronts, is indicated as a solid black line, showing a levelling as $S \to 0$, and a more complex dependence on Stefan number as $S \to \infty$. The contour for $\Sigma = 10$, namely, $\Omega \approx 124$ predicted by the asymptotic theory of the sharp regime (3.67) is shown as a dashed curve.

of a step-like porosity field. We begin by developing a simplified leading-order theory for $\Sigma \gg 1$ based on the assumption that, to first order,

$$\phi(z) \sim \begin{cases} 1 & (z < 0), \\ \Phi & (z > 0). \end{cases} \tag{3.54}$$

In this regime, the leading-order system reduces to a Stefan problem describing a travelling wave [cf. the basic states used in the studies of Chadam et al., 1986].The simplified form of (3.37), along with the relevant Stefan condition (appendix C), is then

$$(1 - V)\frac{\partial c}{\partial z} = \frac{\partial^2 c}{\partial z^2}, \qquad -S_* \frac{\partial c}{\partial z}(0) = V. \tag{3.55}$$

Solving (3.55) subject to $\lim_{x \to -\infty} c = 1$ and $c(0) = 0$, we obtain

$$c = 1 - e^{(1-V)z} \qquad (z < 0), \tag{3.56}$$

a classical travelling wave solution to the Stefan problem. The solution (3.56) is plotted as a green dashed curve in figure 3.8(c) for the case $B = 100$, showing good agreement with our numerically determined solution to the full steady-state system (3.42)–(3.43). We also recover the travelling wave velocity, equation (3.41), from the Stefan condition (3.55).

We note that (3.56) is consistent with the general form of the upstream tail (3.47) for the specific matching constant $\gamma_- = 1$.

Using (3.56) to evaluate the concentration thickness l_c defined by (3.52), we obtain the following prediction for the concentration thickness in the sharp regime,

$$l_c = b(1 - V)^{-1} = b(S_* + 1), \tag{3.57}$$

where $b = \log((1 - \varepsilon)/\varepsilon)$ is a prefactor dependent on the chosen tolerance ($b \approx 2.2$ for $\varepsilon = 0.1$ and $b \approx 4.6$ for $\varepsilon = 0.01$). The result shows that the dimensionless concentration thickness l_c ultimately becomes independent of B as $B \to \infty$, being controlled entirely by

the effective Stefan number S_*. The prediction (3.57) is plotted in figure 3.10(a) as a green dashed line, showing excellent agreement with the concentration thickness l_c predicted by our numerical solution to the full unsimplified model for $B \gtrsim 10$.

The leading-order concentration field (3.56) is a classical solution describing a solidifying or melting boundary. We now develop a novel asymptotic theory describing the leading-order solution for the smooth transitions inside the narrow region through which the dominant porosity transition takes place. From (3.56), we deduce that, in the approach into the transition region as $z \to 0$, the concentration profile $c \to 0$ with $c' \sim -(1-V)$. Thus, we propose an inner region of size $l_\phi \ll l_c$ in which the leading-order forms of porosity and concentration are governed by (3.42)–(3.43) but with the concentration condition $c \to 1$ as $z \to -\infty$ in (3.44) being replaced by the matching condition

$$c' \sim -(1-V) \qquad (z \to -\infty). \tag{3.58}$$

With this replacement, it is now possible to define a new set of scaled variables given by

$$z = \frac{1}{\sqrt{B}}\zeta, \qquad c = \frac{V}{\sqrt{B}S}C, \tag{3.59}$$

that absorbs the asymptotic parameter B, yielding a regularised inner system. Noting also that, under the scalings of (3.59), the right-hand side of (3.43), representing advection, is higher-order as $B \to \infty$, we obtain the leading-order reactive-diffusive inner system:

$$\phi_\zeta = -Cf(\phi), \tag{3.60}$$

$$\phi C_\zeta = -(\phi - \Phi), \tag{3.61}$$

where subscripts of ζ represent partial differentiation. The matching condition (3.58) and downstream condition become

$$\lim_{\zeta\to-\infty} C_\zeta = -(1-\Phi), \qquad \lim_{\zeta\to\infty} C = 0. \tag{3.62}$$

Remarkably, all parameters in the inner system have been absorbed with the exception of the porosity parameter Φ and the function $f(\phi)$. Hence, the form of the porosity

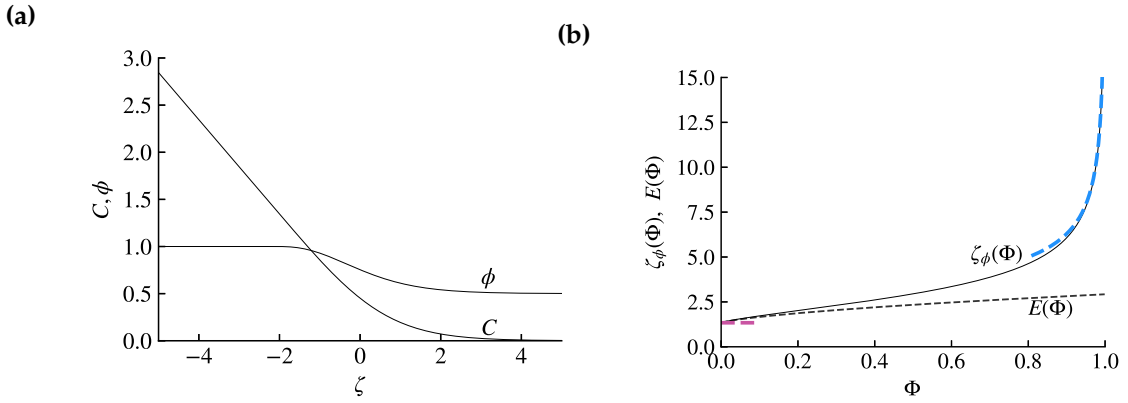

Figure 3.13: (a) The solution to the boundary-layer system (3.60)–(3.62) describing the transition in porosity and (scaled) concentration connecting the upstream advective-diffusive region of the sharp regime to the downstream unreacted state. (b) The general function $\zeta_\phi(\Phi)$ giving the coefficient to the porosity thickness predicted by the inner theory, determined by solving (3.60)–(3.62) over the full range of $0 \leq \Phi < 1$. The solution in the singular limit $\Phi \to 1$ determined below (3.65) is overlaid as a blue dashed curve. A pink dashed line highlights the lower bound $\zeta_\phi(0)$, calculated below (3.63). The function $E(\Phi)$ appearing in the prediction for relative sharpness (3.68) is plotted as a dotted curve, demonstrating its boundedness to values of order unity over all Φ.

transition is universal subject to these specifications. The solution, determined using the same numerical integrator as used for the full system, is plotted for $\Phi = 0.5$ in figure 3.13(a), showing that it successfully connects the upstream flux condition (3.58) to the downstream unreacted state. The solution is also overlaid as a blue dashed curve in figure 3.8(c), showing excellent agreement with the solution to the full model. From the solutions, we determine the scaled transition thickness $\zeta_\phi(\Phi) = \sqrt{B} l_\phi$. Figure 3.13(b) shows that the porosity transition thickens with Φ, and contains a singularity as $\Phi \to 1$.

For $\Phi = 0$, (3.61) simplifies to $C = -\zeta$ and, in turn, (3.60) integrates to yield

$$\phi = 1 - \left[1 - (\zeta/\zeta_*)^2\right]^{1/(1-m)}, \tag{3.63}$$

where $\zeta_* = \sqrt{2/(1-m)}$. The above yields the prediction for the porosity transition thickness $\zeta_\phi(0) = 1.338$, which is indicated on figure 3.13(b) as a dashed pink line.

The limit $\Phi \to 1$ forms a singular perturbation. Let $\Phi = 1 - \delta$ and $\psi = 1 - \phi$ and consider $\delta \to 0$. In this limit, $\phi \sim 1$ everywhere and the ϕ on the left-hand side of (3.61) can be approximated as unity. However, the ϕ in (3.60) must be retained because its difference

from Φ is leading-order. The resulting simplified system is

$$\psi_\zeta = C\psi^m, \qquad C_\zeta = -(\delta - \psi). \tag{3.64}$$

We can now absorb δ, and hence regularise the $\delta \to 0$ limit, by introducing the new variables $\zeta = \delta^{-m/2}\tilde{\zeta}$, $\psi = \delta\tilde{\psi}$, and $C = \delta^{(2-m)/2}\tilde{C}$. In terms of these variables, (3.64) transforms to the regularised parameterless system

$$\tilde{\psi}_{\tilde{\zeta}} = \tilde{C}\tilde{\psi}^m, \qquad \tilde{C}_{\tilde{\zeta}} = -(1 - \tilde{\psi}), \tag{3.65}$$

with $\tilde{C}_{\tilde{\zeta}}(-\infty) = -1$ and $\tilde{C}(\infty) = 0$. The unique solution to this system yields $\tilde{\zeta}_\phi \approx 2.92$ and hence $\zeta_\phi(\Phi) \sim 2.92\,(1 - \Phi)^{-m/2}$ as $\Phi \to 1$. The result is overlaid as a blue dashed curve in figure 3.13(b), showing that it correctly captures the singularity in $\zeta_\phi(\Phi)$ as $\Phi \to 1$.

With the function $\zeta(\Phi)$ determined, we express the transition thickness back in terms of the original dimensionless variables to yield the following general expression for the leading-order porosity transition thickness:

$$l_\phi \sim \frac{\zeta_\phi(\Phi)}{\sqrt{B}}. \tag{3.66}$$

The prediction of (3.66) is plotted alongside the numerically determined prediction to the full system in figure 3.10(b), showing excellent agreement. According to the result of (3.66), the porosity thickness decreases with B as $B^{-1/2}$, implying that diffusion sharpens the porosity transition. It is notable, upon contrasting (3.57) and (3.66), that l_c is dependent solely on S_* whilst l_ϕ is dependent solely on B and Φ, giving a clear separation of parametric controls on l_c and l_ϕ in this sharp regime. We note that the $B^{-1/2}$ scaling in (3.66) is consistent with the $B \to \infty$ limit of the general downstream tail (3.51).

Combining (3.57) and (3.66), we obtain the asymptotic prediction for the relative sharpness,

$$\Sigma \sim \frac{b}{\zeta_\phi(\Phi)}(1 + S_*)\sqrt{B}. \tag{3.67}$$

The result indicates that, in this sharp regime, the relative sharpness increases in proportion to $\sqrt{B}$, and hence larger diffusivity, larger reactivity and smaller flux result in a relatively sharper porosity transition. For $S_* \ll 1$, (3.67) predicts that Σ loses any dependence on Stefan number. This is consistent with the plateauing of the contours as $S \to 0$ shown in figure 3.11. For $S_* \gg 1$, the relative sharpness $\Sigma \propto S_*\sqrt{B}$, implying a dependence on both S_* and B, and explaining the curvature of the contours in figure 3.11. A key implication of these results is that diffusion is necessary to sharpen the porosity transition relative to the concentration transition.

The result of (3.67) can be written

$$\Sigma \sim \frac{b}{E(\Phi)}\sqrt{\Omega}, \tag{3.68}$$

where $E(\Phi) = \zeta_\phi(\Phi)\sqrt{f(\Phi)}$ is a function of Φ only, and

$$\Omega = f(\Phi)(1+S_*)^2 B \tag{3.69}$$

is a key dimensionless number. The function $E(\Phi)$ is plotted as a dotted curve in figure 3.13(b), showing that it is bounded to values of order unity ($1.3 < E(\Phi) < 3.0$). The boundedness is due to the $\sqrt{f(\Phi)} = (1-\Phi)^{m/2}$ factor regularising the singularity in $\zeta_\phi(\Phi)$ as $\Phi \to 1$ derived in the result below (3.65). Using the fact that E is order unity, from (3.68) we deduce that the sharp regime is internally consistent (i.e. it predicts that $\Sigma \gg 1$) if and only if $\Omega \gg 1$. We therefore determine that $\Omega \gg 1$ forms the key criterion for emergence of the sharp regime. From (3.68), we obtain the analytical prediction for the contours of Σ given by $\Omega = (\Sigma E(\Phi)/b)^2$. For $\Sigma = 10$, this prediction yields $\Omega \approx 124$, which is plotted as a dotted curve over the parameter space (S, B) in figure 3.11, showing excellent agreement with the contour predicted by the full unsimplified model.

3.4.3 Reactant dynamics

Our regime analysis has thus far focused on the diagnostic property of relative sharpness, with the result of revealing one key asymptotic simplification based on a separation of transitional length scales ($\Sigma \to \infty$) as $B \to \infty$. However, in the converse limit of $B \to 0$,

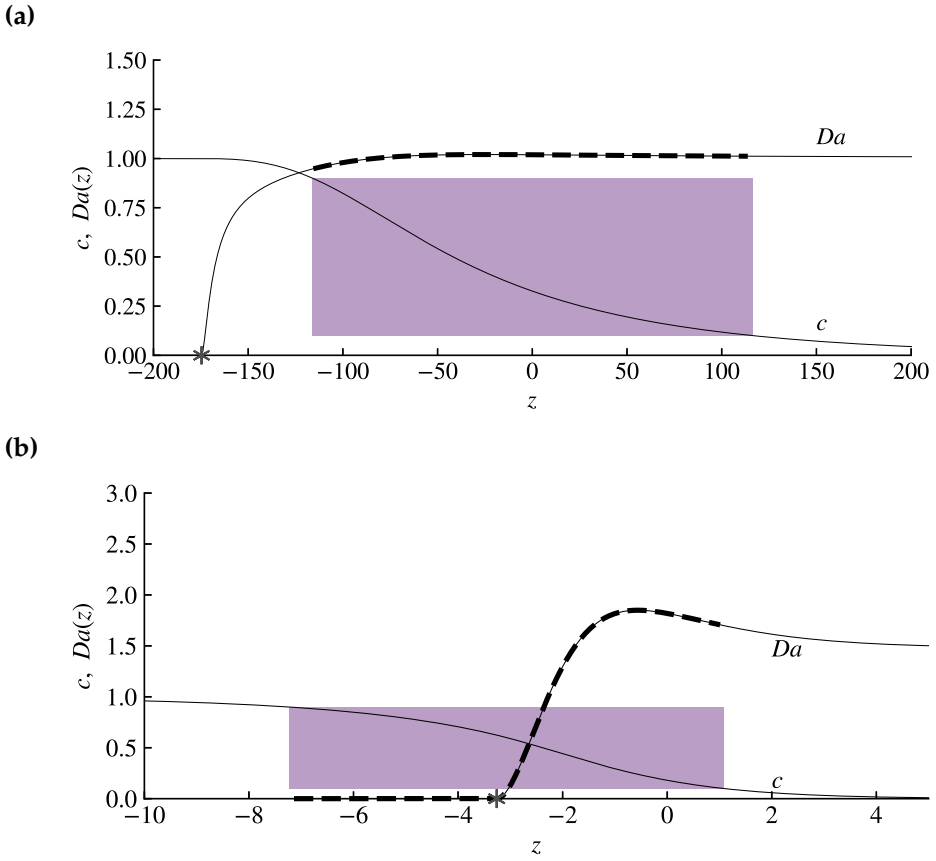

Figure 3.14: Profiles of the emergent Damköhler number, $Da(z)$, defined by (3.70) (solid, black) as functions of position z for (a) $B = 0.01$ and (b) $B = 1$, and fixed $S = 1, \Phi = 0.5, \nu = 1$, alongside the corresponding concentration profiles $c(z)$. Shaded rectangles illustrate the concentration transition thicknesses from z_c^+ to z_c^- defined below (3.52), which we use to calculate the representative inverse Péclet number (3.73). The corresponding parts of the curves of the Damköhler used to formulate (3.70) are shown by the thicker regions of the $Da(z)$ curves. The position of the beginning of the porosity transition, z_*, is indicated by a star in each case.

the relative sharpness saturates at values of order unity ($\Sigma \sim 1$) (figure 3.11), thus failing to reveal any direct simplifying asymptotic property based on length-scale separation. A natural question now is to identify and investigate the new simplifying asymptotic property emergent for $B \to 0$.

The leading-order regime for $B \to 0$ is in fact based, not on the relative scales of transition like $B \to \infty$, but a direct simplification of the dominant balances in the governing equation (3.16). To demonstrate this, we consider the relative roles of diffusion, advection and reaction in (3.16). We define the *emergent* Damköhler number as the ratio of the contributions to (3.35) due to the reactive and advective terms:

$$Da(z) = \frac{B(1 + S\nu c)R(c, \phi)}{\phi(u - V)c_z}, \tag{3.70}$$

with the z subscript denoting partial differentiation. Where $Da \approx 1$, advection and reaction form the dominant balance with negligible diffusion. Where $Da \approx 0$, reaction is negligible, and the dominant balance is given by advection and diffusion. Where $Da \gg 1$, advection is negligible and the dominant balance is formed between diffusion and reaction. Thus, all three possible dominant balances between advection, diffusion and reaction can be assessed by the single metric of (3.70).

Figure 3.14 shows the profile of $Da(z)$ for (a) $B = 0.01$ and (b) $B = 1$, with fixed $S = 1$, $\phi_0 = 0.5$ and $\nu = 1$. We see that $Da \equiv 0$ uniformly for $z < z_*$ since the reaction rate is identically zero in that region. The Damkhöler number Da increases for $z > z_*$ (through a peak in case (b)), before plateauing as (a) $Da \sim 1.0$ and (b) $Da \sim 1.5$ as $z \to \infty$. The plateau value reflects the balance of terms as the residual chemical is consumed ($c \to 0$). The value $Da \sim 1.0$ implies a balance between advection and reaction in case (a). The approach of $Da \sim 1.5$ in case (b) shows that reaction, diffusion and advection all remain comparable as $z \to \infty$, though the magnitudes of all the terms tend to zero.

To assess the importance of diffusion directly, we define the inverse Péclet number by

$$Pe^{-1}(z) = \frac{(\phi c_z)_z}{\phi(u - V)c_z}, \tag{3.71}$$

representing the ratio of diffusion to advection. Writing (3.37) in terms in terms of only derivatives of c and $R(c, \phi)$ yields

$$(\phi c_z)_z - \phi(u - V)c_z = B(1 + S\nu c)R(c, \phi), \tag{3.72}$$

which in accordance with (3.70) shows that the Péclet number is related to the Damkhöler number via $Da = 1 + Pe^{-1}$. Thus Pe^{-1} quantifies the deviation of the Damköhler number from a diffusionless balance $Da = 1$. In assessing the controlling dominant balance in the governing transport equation (3.16), we are specifically interested in its values within the concentration transition (indicated by purple bars in figure 3.14) through which the non-trivial variation in the concentration field is controlled . Thus, as a single metric to assess the dominant balance, we define the representative inverse Péclet number $\langle Pe^{-1} \rangle$ by the L_1-norm,

$$\langle Pe^{-1} \rangle \equiv \frac{1}{l_c} \int_{z_c^-}^{z_c^+} |Da(z) - 1| \, \mathrm{d}z. \tag{3.73}$$

Figure 3.15 and figure 3.16 present contour maps of $\langle Pe^{-1} \rangle$ over the parameter space (S, B), with $\Phi = 0.5$ and $\nu = 1, 0$ respectively. In both figures 3.15 and 3.16 for $B \to \infty$, we observe that $\langle Pe^{-1} \rangle \approx 1$, indicating that the concentration field is dominated by advection and diffusion, consistent with the recovery of (3.55) defining the sharp regime. The deviation from the asymptotic theory as S gets large is thought to be a consequence of $h(z, \phi, N)$ being weakly dependent on S and is more apparent for $\nu = 0$ suggesting that the asymptotic theory breaks down sooner as $\nu \to 0$. In the converse limit $B \to 0$, we see that $\langle Pe^{-1} \rangle \to 0$, indicating a broad region of the parameter space forming a *diffusionless* regime dominated by an advective-reactive balance.

3.4.4 The diffusionless regime

Upon neglecting diffusion, the travelling wave system (3.42)–(3.43) reads

$$-V\phi' = BSR(c, \phi), \tag{3.74}$$

$$c(1 - V + \nu V(1 - \phi)) = S^{-1}V(\phi - \Phi). \tag{3.75}$$

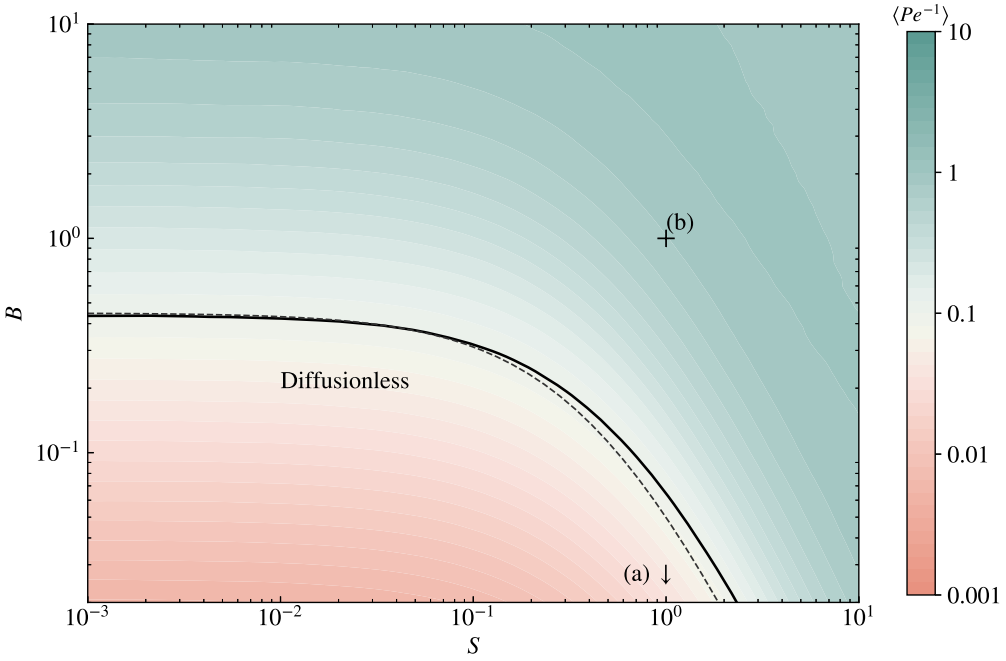

Figure 3.15: Contour plot of the representative inverse Péclet number $\langle Pe^{-1} \rangle$ defined by (3.73), plotted over the parameter space (S, B) for fixed $\Phi = 0.5$ and $\nu = 1$. The contour of $\langle Pe^{-1} \rangle = 0.1$ is indicated as a solid black line, which we choose as the threshold for the diffusionless regime. Our asymptotic prediction for this contour derived below (3.90) is shown as a dashed curve. The positions of examples (a) and (b) from figure 3.14 are indicated.

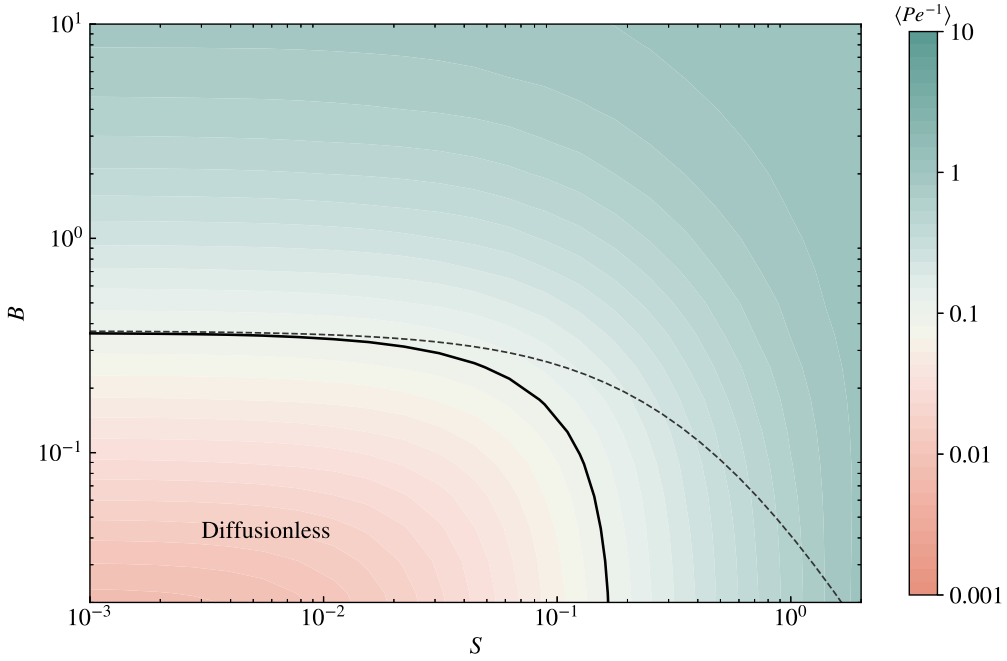

Figure 3.16: Contour plot of the representative inverse Péclet number $\langle Pe^{-1} \rangle$ defined by (3.73), plotted over the parameter space (S, B) for fixed $\Phi = 0.5$ and $\nu = 0$. The contour of $\langle Pe^{-1} \rangle = 0.1$ is indicated as a solid black line, which we choose as the threshold for the diffusionless regime. Our asymptotic prediction for this contour derived below (3.90) is shown as a dashed curve. The contour deviates from the asymptotic prediction as S gets large, likely due to the breakdown of the asymptotic regime here.

Rewriting (3.75) in favour of the reactive solid fraction, $\psi = (1-\phi)/(1-\Phi)$, we obtain the simpler equation

$$c = \frac{1-\psi}{1+N\psi}, \tag{3.76}$$

where $N = \nu S$ is referred to herein as the *production Stefan number*. Equation (3.76) provides a direct relationship between (reactable) solid fraction and reactant concentration. The denominator of (3.76) represents two different ways in which concentration is controlled. For $N = 0$, (3.76) reduces to $c = 1 - \psi$, representing the simple exchange between reactant and solid fraction. For $N > 0$, the additional $N\psi$ term represents the reduction in concentration owing to the increase in fluid solvent generated by reaction. The production Stefan number N controls the relative importance of this second effect.

With diffusion neglected, it is now possible to absorb almost all the parameters in the problem by introducing the scaled coordinate $z = \lambda\xi$, where

$$\lambda = \frac{V}{f(\Phi)BS_*}. \tag{3.77}$$

Substituting (3.76) into (3.74) and recasting in terms of ξ, we obtain the single equation

$$\psi_\xi = \frac{(1-\psi)F(\psi)}{1+N\psi}, \tag{3.78}$$

where $F(\psi) = f(\phi)/f(\Phi) = \psi^m$. Remarkably, all parameters have now been absorbed with the unique exception of the production Stefan number N. Thus, for a given value of N, all diffusionless one-dimensional reaction fronts are equivalent up to scaling.

Solutions to (3.76) and (3.78), $\psi(\xi)$ and $c(\xi)$, solved subject to our normalisation condition $\psi(0) = 1/2$, are shown in figures 3.17(a) and 3.17(b), for (a) $N = 0.1$ and (b) $N = 10$. The results show an approach to one distinguished profile in the limit of $N \to 0$ overlaid as pink dashed curves in figure 3.17(a), and a broadening of the porosity transition for $N > 1$ as in figure 3.17(b). The inferred concentration and porosity thicknesses, $\xi_c(N)$ and $\xi_\phi(N)$, can be calculated and depend solely on N and the form of the function $F(\psi)$. The thicknesses are plotted as functions of N in figure 3.17(c), showing that both are equal as $N \to 0$. As N is increased, ξ_c and ξ_ϕ progressively deviate from each other, exhibiting

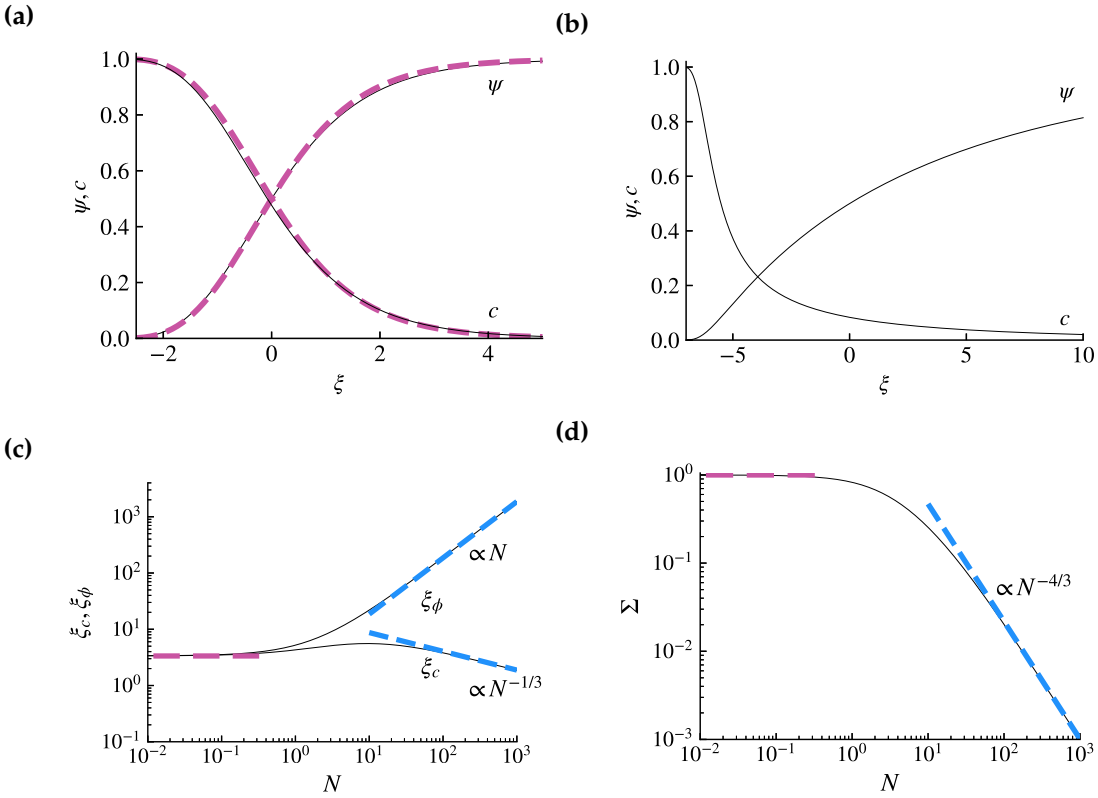

Figure 3.17: (a) The solid fraction $\psi(\xi)$ and concentration $c(\xi)$ predicted by (3.76) and (3.78) for $F(\psi) = \psi^m$ for $m = 2/3$ and $N = 0.1$. The predictions of the general $N \to 0$ limiting regime represented by the solution to (3.82) are plotted as pink dashed curves. (b) The corresponding solution for $N = 10$. (c) The functions $\xi_c(N)$ and $\xi_\phi(N)$ appearing in the transition lengths (3.80). (d) The relative sharpness $\Sigma(N)$. In panels (c) and (d), the asymptotic predictions of (3.83) and (3.87) are shown as pink and blue dashed curves.

different asymptotic dependences on N as $N \to \infty$. The concentration thickness becomes a decreasing function of N, while the porosity thickness increases with N.

With $\psi(\xi)$ determined by solving (3.78) for a given value of N and expressing it in terms of ϕ and z, we obtain

$$\phi = 1 - (1 - \Phi)\psi\left(\frac{z}{\lambda}\right), \tag{3.79}$$

yielding a general prediction of the shape of the porosity transition for a given value of N. The solutions for $\phi(z)$ and $c(z)$ predicted by the results of (3.79) and (3.76) are plotted as orange dashed curves in the example of figure 3.8(a) for which $B = 0.01$, showing excellent agreement with the numerically determined solution to the full model. With the general N-dependent functions $\xi_c(N)$ and $\xi_\phi(N)$ determined (figure 3.17(c)), and noting that $l_c = \lambda\xi_c$ and $l_\phi = \lambda\xi_\phi$, we obtain, with use of (3.41), the corresponding

general predictions for the dimensionless transition length scales:

$$l_c = \frac{\xi_c(N)}{f(\Phi)(1+S_*)B}, \qquad l_\phi = \frac{\xi_\phi(N)}{f(\Phi)(1+S_*)B}. \tag{3.80}$$

The predictions are plotted as orange curves in figure 3.10, showing excellent agreement with the numerical solutions to the full model in the relevant limit $B \to 0$. The dimensionless forms of the lengthscales l_c and l_ϕ are both inversely proportional to B, implying that they both decrease with reaction rate K and increase with fluid velocity U. This is in contrast to the sharp theory, where l_c becomes independent of B, as given by (3.57).

The corresponding relative sharpness $\Sigma = l_c/l_\phi$ in the diffusionless regime is predicted to be

$$\Sigma = \xi_c(N)/\xi_\phi(N), \tag{3.81}$$

which is shown as a black curve in figure 3.17(d). We see that Σ depends independently on the production Stefan number N, and forms a decreasing function of N. There is an approach of $\Sigma \to 1$ as $N \to 0$, indicating a simple upper bound on relative sharpness in the diffusionless regime of $\Sigma < 1$ across all N. For large N, the relative sharpness $\Sigma \to 0$ and the concentration profile becomes narrow relative to the porosity transition, the reverse of the regime considered in section 3.4.2.

We now consider the asymptotic sub-regimes in limits of N. For $N \to 0$, as typifies dissolution for example, (3.78) and (3.76) reduce to

$$\psi_\xi = (1-\psi)F(\psi), \qquad c = 1-\psi. \tag{3.82}$$

The latter implies a simple exchange between concentration and solid fraction, and hence both concentration and porosity transition on identical scales to leading order and $\Sigma = 1$. The solution to (3.82) is shown as a pink dashed curve in figure 3.17(a), confirming that it provides a limiting parameterless prediction for $N \ll 1$. The concentration and porosity thicknesses take the identical limiting value given by

$$\xi_c \sim \xi_\phi \sim 3.35, \qquad \Sigma \sim 1, \qquad (N \to 0), \tag{3.83}$$

which are overlaid in figures 3.17(b) and (c) as pink dashed lines, showing excellent agreement with the numerical results for $N \to 0$.

Double-decked structure for $N \to \infty$

In the converse limit of $N \to \infty$, the solution forms a more complex double-decked asymptotic structure, wherein the concentration transition is an order of N^{2-m} narrower than the porosity transition and the relative sharpness $\Sigma \to 0$. Each deck is an annulus centred around the point source located at $\eta = 0$. We recall that the denominator of (3.78), $1+N\psi$, represents two controls on concentration: one due to the consumption of reactant; the other, represented by $N\psi$, due to the generation of solvent. For $N \to \infty$, the system partitions into two decks. The outer deck is characterised by the dominance of the control by solvent production, $N\psi \gg 1$, with (3.76) and (3.78) yielding the outer equations

$$\psi_\xi = \frac{(1-\psi)\psi^m}{N\psi}, \qquad c = \frac{1-\psi}{N\psi}, \tag{3.84}$$

where $\psi(\infty) = 1$. Upon letting $\xi = NZ$ and $g(Z) = \psi(\xi)$, we obtain the parameterless equation $g_Z = (1-g)g^{m-1}$ with $g(\infty) = 1$. Solving this system numerically for the unique parameterless function $g(Z)$ with normalisation $g(0) = 1/2$, we obtain the universal form of the outer solution expressed in terms of the original variables as

$$\psi = g(N^{-1}\xi), \qquad c = N^{-1}(g(N^{-1}\xi)^{-1} - 1).$$

The outer solution describes the dominant transition of the solid fraction ψ, and can thus be used to determine the leading-order porosity thickness ξ_ϕ as $N \to \infty$. Using the solution $g(\zeta)$, we evaluate $N^{-1}\xi_\phi \approx 1.85$ for $\varepsilon = 0.1$, giving $\xi_\phi \sim 1.85\,N$.

For sufficiently negative ξ, the solid fraction $\psi \to 0$ and the assumption of $N\psi \gg 1$ underlying the outer breaks down once $\psi \sim N^{-1}$. The inner deck is characterised by the importance of both terms in the denominator of (3.78), with $\psi \sim N^{-1} \ll 1$, but is simplified by the negligibility of the ψ in the numerator:

$$\psi_\xi = \frac{\psi^m}{1+N\psi}, \qquad c = \frac{1}{1+N\psi}. \tag{3.85}$$

The rescalings $\xi = N^{-p}\zeta$ where $p = 1 - m$ (with $p = 1/3$ for $m = 2/3$) and $G(\zeta) = N\psi(\xi)$ render the inner system above parameterless, with $G_\zeta = G^m/(1 + G)$. Upon numerical integration, this equation yields the parameterless inner solution $G(\zeta)$. The universal form of the inner solution can then be expressed in terms of the original variables as

$$\psi = N^{-1}G(N^{-p}\xi), \qquad c = (1 + G(N^{-p}\xi))^{-1}.$$

The inner solution above describes the primary transition in the concentration over a scale N^{-p} that is narrow relative to the porosity transition ($N^{-p} \ll N$). Using the computed function $G(\zeta)$, we evaluate $N^p\xi_c \approx 18.8$, giving $\xi_c \sim 18.8\,N^{-p}$.

Between the two decks is an intermediate zone ($N^{-p} \ll \xi \ll N$) wherein both simplifying features of the decks apply, such that (3.78) and (3.76) reduce to the leading-order forms $\psi_\xi = N^{-1}\psi^{m-1}$ and $c = (N\psi)^{-1}$. Upon integrating these equations using separation, we obtain explicit solutions for $\psi(\xi)$ and $c(\xi)$ in this intermediate zone. These solutions are included below alongside a full summary of the asymptotic structure:

$$\begin{cases} \psi \to 0 & c \to 1 & (\xi \ll N^{-p}) \\ \psi \sim N^{-1}G\big(N^p\xi\big) & c \sim \big(1 + G\big(N^p\xi\big)\big)^{-1} & (\xi \sim N^{-p}) \\ \psi \sim \big((1+p)N^{-1}\xi\big)^{\frac{1}{1+p}} & c \sim \big((1+p)N^p\xi\big)^{-\frac{1}{1+p}} & (N^{-p} \ll \xi \ll N) \\ \psi \sim g\big(N^{-1}\xi\big) & c \sim N^{-1}(g(N^{-1}\xi)^{-1} - 1) & (\xi \sim N) \\ \psi \to 1 & c \to 0 & (\xi \gg N) \end{cases} \tag{3.86}$$

In summary, the outer deck is characterised by the dominance of the $N\psi$ terms in the denominators of (3.78) and (3.76), such that the concentration field in this deck is primarily controlled by the production of solvent, as opposed to the consumption of reactant. This deck contains the dominant variation in solid fraction, and thus controls ξ_ϕ to leading order. The inner deck is characterised instead by both terms in the denominators of (3.78) and (3.76), and controls the dominant concentration variation and hence ξ_c. For $m = 2/3$,

the analysis yields the following asymptotic predictions:

$$\xi_c \sim 18.8\, N^{-1/3} \qquad \xi_\phi \sim 1.85\, N \qquad \Sigma \sim 10.1\, N^{-4/3} \qquad (N \to \infty). \tag{3.87}$$

The results are overlaid as blue dashed curves in figures 3.17(c) and 3.17(d), showing excellent agreement with the numerical solutions to the full diffusionless system for $N \to \infty$.

Condition for self-consistency of the diffusionless regime

We now derive theoretically the condition for asymptotic self-consistency of the diffusionless regime, namely, the conditions for which it predicts that $Pe^{-1} \ll 1$. Inserting the scaled diffusionless solution given by (3.76) and (3.79) into (3.71), we obtain

$$Pe^{-1} = \Omega\, h(z, \Phi, N), \tag{3.88}$$

where $\Omega \equiv f(\Phi)(1 + S_*)^2 B$ is the same key parameter we derived in the context of the self-consistency of the sharp theory in (3.67), and

$$h(z, \Phi, N) = f(\Phi)\left(\frac{1 - (1-\Phi)\psi}{1 + N\psi}\left(\frac{\psi_{\xi\xi}}{\psi_\xi} - \frac{2N\psi_\xi}{1 + N\psi}\right) + \frac{(1-\Phi)\psi_\xi}{1 + N\psi}\right) \tag{3.89}$$

defines a function of z that depends on the parameters Φ and N only. Equation 3.85 defines ψ_ξ and by inspection of its form and the fact that $\psi \geq 0$ (figure 3.17(a)) we know that $\psi_{\xi\xi}/\psi_\xi$ cannot become undefined, and as such neither can $h(z, \Phi, N)$. Upon taking the norm of (3.88), we obtain the prediction for the characteristic inverse Péclet number:

$$\langle Pe^{-1} \rangle = \Omega H(\Phi, N), \qquad \text{where } H(\Phi, N) \equiv \big\langle h(z, \Phi, N) \big\rangle. \tag{3.90}$$

Thus, the representative inverse Péclet number in the diffusionless regime partitions into a product of the key parameter Ω and a specific function H dependent on (Φ, N) only. In accordance with (3.90), the contours of constant $\langle Pe^{-1} \rangle$ are predicted as $\Omega = \langle Pe^{-1} \rangle / H(\Phi, N)$. For the value $\Phi = 0.5$ used for the contour plot of figure 3.15 and $\langle Pe^{-1} \rangle = 0.1$, with the reference value $S = 0$ used to evaluate the function $H(0.5, 0) \approx 0.35$, we obtain the dif-

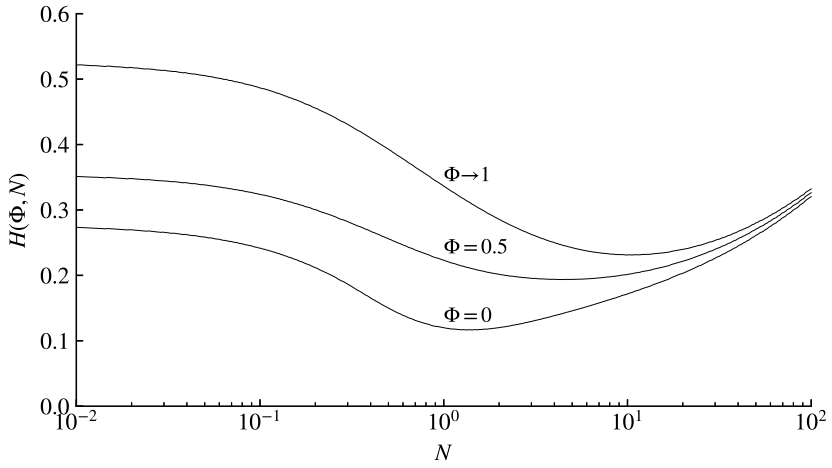

Figure 3.18: The function $H(\Phi, N)$ defined by (3.90) for $0 \leq \Phi < 1$ shown as functions of N, demonstrating its boundedness to values of order unity, $0.1 < H(\Phi, N) < 0.6$.

fusionless prediction for this contour as $\Omega \approx 0.29$. The predicted contour is plotted as a dashed curve in figure 3.15, showing excellent agreement with the numerical prediction of the full model. The slight discrepancy for $S > 1$ can be attributed to a weak dependence of H on N and hence S.

The general function $H(\Phi, N)$ is plotted as a function of N for $\Phi = 0, 0.5$ and $\Phi \to 1$, showing that it retains values of order unity for all $N < 10^2$, with $0.1 < H(\Phi, N) < 0.6$. It follows that the prediction for the inverse Péclet number (3.90) is generally characterised by $\langle Pe^{-1} \rangle \sim \Omega$, thus revealing that the parameter space is partitioned independently by the key parameter Ω. In conjunction with the finding that Ω also controls the emergence of the diffusionless regime via (3.67), we conclude that Ω provides a single independent number to demarcate between the sharp and diffusionless regimes. These two asymptotic regimes thus form the limits of a single spectrum bridging all possible reaction fronts.

3.5 Summary

Our analysis has revealed two asymptotic regimes which bound our model in two limits of the parameter space: the sharp and the diffusionless regimes. Which arises is controlled by the single dimensionless number

$$\Omega = \frac{f(\Phi)(1 + S_*)^2 KD}{U^2}, \tag{3.91}$$

	Sharp regime	Diffusionless regime
	$\Omega = f(\Phi)(1+S_*)^2\dfrac{KD}{U^2} \gg 1$	$\Omega = f(\Phi)(1+S_*)^2\dfrac{KD}{U^2} \ll 1$
l_c	$b\,(1+S_*)\,\dfrac{D}{U}$	$\dfrac{\xi_c(\nu S)}{f(\Phi)(1+S_*)}\dfrac{U}{K}$
l_ϕ	$\zeta_\phi(\Phi)\sqrt{\dfrac{D}{K}}$	$\dfrac{\xi_\phi(\nu S)}{f(\Phi)(1+S_*)}\dfrac{U}{K}$
Σ	$\dfrac{b}{\zeta_\phi(\Phi)}\sqrt{\dfrac{(1+S_*)^2KD}{U^2}} \propto \sqrt{\Omega}$	$\dfrac{\xi_c(\nu S)}{\xi_\phi(\nu S)} \sim \begin{cases} 1 & (\nu S \ll 1) \\ \propto (\nu S)^{-(1-m)} & (\nu S \gg 1) \end{cases}$

Table 3.3: Summary of the dimensional predictions for the structural components of reaction fronts in the (left) sharp regime (section 3.4.2) arising for $\Omega \gg 1$, and the (right) diffusionless regime (section 3.4.4) arising for $\Omega \ll 1$, where Ω is the key controlling dimensionless number given by (3.91). The secondary control is by the acid capacity S in the form of $S_* = S(1-\Phi)^{-1}$ in the sharp regime and by $N = S\nu$ in the diffusionless regime.

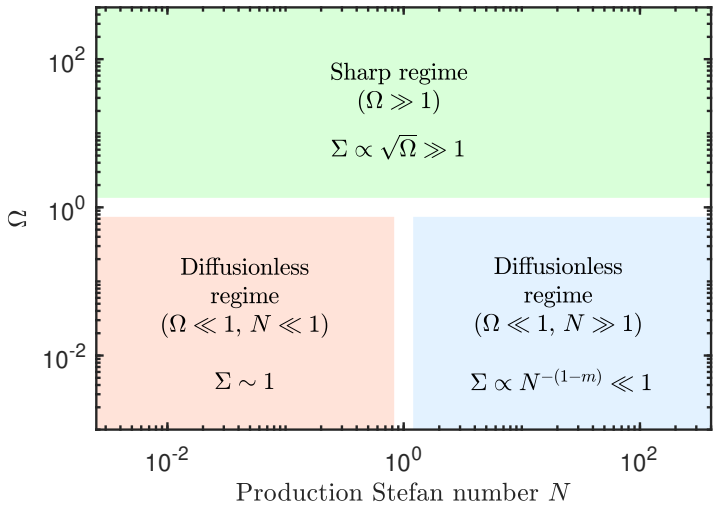

Figure 3.19: Schematic regime diagram illustrating the partitioning of the parameter space over the two key numbers (N, Ω), where Ω is defined by (3.91) and $N = \nu S$ is the production Stefan number. The three primary regimes are represented by the two columns of table 3.3 and the two N-dependent limits of the diffusionless regime. (Regime diagram produced by Sam Pegler.)

a combination of parameters encoding the relative strength of background flow U, diffusivity D, reactivity K, effective Stefan number S_*, and ratio of the unreacted to the fully unreacted porosity Φ within a given scenario. A full summary of the dimensional forms of our theoretical predictions for the transitional length scales and relative sharpness in each regime is provided in table 3.3. Figure 12 provides an accompanying regime diagram illustrating the partitioning of the parameter space in terms of the two key derived dimensionless numbers Ω and N.

In the sharp regime, the concentration transition thickness l_c is a function of diffusivity D and fluid velocity U, whilst l_ϕ is a function of diffusivity D and reactivity K. Both l_c and l_ϕ are increasing functions of diffusivity, but differ in their form: $l_c \propto D$ while $l_\phi \propto \sqrt{D}$, implying a stronger influence of diffusivity on concentration thickness than porosity thickness. The increase of l_c with D can be interpreted physically as being a result of larger diffusivity increasing how far the reactant is spread. Similarly l_ϕ being an increasing function of D can be interpreted in terms of the reactant being transported at a faster rate to react. The different dependences of l_c and l_ϕ on D give rise to a separation of length scales, with an increasingly sharp porosity transition occurring for larger diffusivities. This effect is seen in the relationship for Σ showing that it increases in proportion to $\sqrt{\Omega}$ and hence $\sqrt{D}$.

In the diffusionless regime, we see that l_c and l_ϕ have the same functional dependence on U/K as one another. Their difference to each other arises in the prefactors $\xi_c(N)$ and $\xi_\phi(N)$ which are functions of the production Stefan number $N = \nu S$ only. As a result the relative sharpness is controlled entirely by N, contrasting with the more complex dependence on each of D, U, K, S and Φ in the sharp regime. The proportionality of both l_c and l_ϕ to U reflects the fact that a larger flow rate U transports reactant over a larger distance before the reactant is consumed. Contrasting the regimes, it is first clear that D has no effect on either l_c or l_ϕ in the diffusionless regime. It is notable that the dependence of l_c on U is entirely opposite in the regimes. In the sharp regime, l_c is inversely proportional to U whereas in the diffusionless regime it is proportional to U. Thus, in sharp cases, increased flow narrows the concentration transition but in the diffusionless case it instead broadens the concentration transition. The limit of $N \to 0$

yields an asymptotic form of the diffusionless regime where $\Sigma \sim 1$, forming a fundamental upper bound on the relative sharpness of a porosity transition without diffusion. In the converse limit $N \to \infty$, the relative sharpness $\Sigma \propto N^{-4/3}$ highlighting that the l_c and l_ϕ prefactors diverge from one another as N increases. Relative sharpness Σ thus *decreases* with $N = S\nu$, in direct opposition to the corresponding trend in the sharp regime where $\Sigma \propto S$ as $S \to \infty$.

3.6 Conclusions

In this Chapter, we have made four primary developments. First, we developed and presented integrated forms of a generalised two-phase theory of reaction-front dynamics that allows for smooth transitions in porosity, diffusive transport of the reacting agent and the non-zero reactive production of fluid. This is a generalisation of the model presented in Szymczak and Ladd [2013].

Second, we identified a succession of transient regimes preceding the final travelling wave state, including advective-diffusive and reactive-diffusive regimes. Third, we demonstrated that reaction fronts generally partition into two fundamental regimes (the sharp and the diffusionless regime) depending on the value of a key number Ω defined by (3.91). Specifically we are able to quantify the value of Ω necessary to define each of the fundamental regimes, an extension to the work of Szymczak and Ladd [2013] which ascertained that B (and so Ω) was the controlling parameter for small S_*. Fourth, we developed asymptotic theories in these limiting regimes and used them to develop full analytical predictions for the transition length scales in each regime, summarised in table 3.3, and validated against the full model in figure 3.10. The inner theory of the relative sharp theory (section 3.4.2) reveals, for the first time, that the porosity transition thickness scales $l_\phi \propto \sqrt{B}$ in this regime.

The key parameter Ω yields a dimensionless number that directly measures whether the dynamics of a reactive two-phase flow will be characterised by primarily advective-diffusive transport with highly localised sharp porosity transitions, versus diffusionless dynamics with large-scale smooth porosity and concentration transitions on comparable

scales. Working beyond the small acid capacity limit of Szymczak and Ladd [2013] reveals the additional control of S_* on the controlling parameter Ω.

By considering conditions for asymptotic consistency, we showed that Ω independently partitions the parameter space between these two regimes, and thus Stefan-type and two-phase diffusionless theories are unified into a generalised theoretical framework for non-negligible acid capacity. The results reveal a physical mechanism whereby diffusion allows porosity transitions to relatively sharpen to scales much smaller than those of reactive transport.

The analyses reveal surprising differences in how the relative sharpness of a porosity transition is controlled. In the sharp regime, the relative sharpness increases with Stefan number and depends on the diffusivity, advective flux, kinetic rate factor and ratio of the unreacted to the fully unreacted porosity. In the diffusionless regime, the relative sharpness instead decreases with Stefan number, and is dependent only on a parameter we referred to as the production Stefan number, the product of the Stefan number and the production ratio.

Our results (table 3.3) present a toolkit for predicting dominant regimes and transition length scales in practice. Illustrative parameter values in a selection of examples (appendix A), including mantle dynamics, chemical weathering, and laboratory models involving flow through a dissolving or melting bead pack, indicate that both sides of the parameter space are realisable. Predominantly, previous analysis of reactive fronts and their stability is presented in either the sharp [e.g. Chadam et al., 1986] or diffusive limit [e.g. Hinch and Bhatt, 1990], holding for $S_* \ll 1$ for $B \gg 1$ and $B \ll 1$ respectively. [Szymczak and Ladd, 2013, 2014] bridge these regimes in a framework based upon the extent of concentration field ahead of and behind the porosity transition. In this work, we generalise the regimes to span S_*, identifying where S_* feeds into the controlling parameter which partitions the regimes. The prior spanning of the regime space [Szymczak and Ladd, 2013, 2014] assumed small acid capacity and $\nu = 0$ and the relaxation of these conditions allows us to apply our results more broadly, including to problems of melting for $\nu \neq 0$.

The results of this work are based on idealised one-dimensional flows fed at an ap-

proximately constant flux, which will limit general applicability. In two-dimensions, for example, the one-dimensional solutions are unstable to the reaction-infiltration instability subject to a critical condition. In this context, our solutions present either the stable asymptotic states or could be used as basic states for linear stability analysis of two-phase reaction fronts. Axisymmetry, as well as other three-dimensional geometries, are also likely to introduce interesting new considerations. Other idealisations include the assumption of a rigid medium, with elastic or viscous models of the host material having the potential for new effects. Another generalisation of the model could include more complex reaction kinetics, as well as an allowance for reactive agents in more than one component. There is thus significant scope for interesting new research directions based on these complications, for which the idealised one-dimensional case considered here provides a theoretical foundation.

3.7 Contribution of this Chapter

This Chapter has addressed the following research questions:

Research Question 1
How do reaction fronts evolve in fundamental geometries?

This Chapter has studied the evolution of reaction fronts from an initially reactant free and uniform porosity through to the steady travelling wave regime, spanning the parameter space (B, S). Section 3.3 details, for the first time, a comprehensive understanding of the timescales upon which 1D fronts transition from diffusion dominated through to fully developed and steady advective-diffusive-reactive reaction fronts. In the case of small B, this is via a time dependent advective-diffusive balancing regime and in the case of large B it is via a reactive-advective regime. The transition to steady travelling waves from initiation has been thoroughly documented, and develops a novel sharp interface model which relaxes the requirements of prior work such as Chadam et al. [1986] which requires small S_* to generate a sharp interface model.

Research Question 2

What controls the extent of chemical and porosity transitions in steadily propagating 1D fronts?

In the latter half of this Chapter, section 3.4 has studied the extent of chemical and porosity transitions in travelling wave fronts. We began with numerical exploration of the parameter space (B, S) to understand where asymptotic regimes appear and then derive these regimes and their conditions for consistency which are based on our novel parameter Ω, encompassing the effects of reaction model, transport dynamics and fluid reactivity into one diagnostic. In the large Ω limit, there is one 'sharp' regime which has the characteristic separation of scales between the concentration and porosity transitions. In the small Ω limit, the asymptotic regime hinges upon the balance of advection to reaction and the behaviour in this limit becomes dependent on the parameter $N = S\nu$ the production Stefan number, which quantifies the effect of dilution on the depletion of chemical concentration. The benefit of understanding these parametric controls is grounded in reality by the approximation of their magnitude in appendix A. Bridging these limits for general S, through a smooth porosity transition has developed new understanding of how previously studied work in the small S limit [Szymczak and Ladd, 2013] fit into the larger parameter space. The limiting regimes bridged by Szymczak and Ladd [2013] have been thoroughly explored in the new framework considering the total transitional length scale of porosity and concentration.

3.7.1 Implications for geosciences

The parameters estimated in appendix A suggest that in scenarios such as the Earth's lithosphere, Ω may vary between 10^{-3}–10^{6} which encompasses both limiting cases of the reaction front dynamics, from the sharp porosity transition, to the diffusionless transition. The consequence of this geologically is that we can begin to use this knowledge to understand the conditions in which a preserved stable reaction front developed. For example, for a reaction front with transitions in porosity and chemical concentration (of a reactant or product) of broadly the same magnitude, we could identify that $\Omega \ll 1$ is the parameter under which it developed. Similarly for a reaction front with an interfacial

porosity transition relative to the concentration transition, we could identify that $\Omega \gg 1$ is likely.

4

Axisymmetric reactive injection

In this Chapter, we present an analysis of reaction fronts formed by the injection of reactive fluid at a point source. This situation forms a fundamental configuration that differs from the 1D configuration of Chapter 3. In particular the flux of material supplied to the front is reduced as it moves away from the source, resulting in entirely different asymptotic regimes and mathematical treatments. This Chapter is the basis of a paper drafted for submission to the Journal of Fluid Mechanics under the title *Reactive injection into a porous medium*. The authors are D Bullamore and S. Pegler.

4.1 Introduction

The reaction of fluid with a porous medium, through either chemical or physical process, is a fundamental phenomenon that arises throughout the natural and industrial worlds. In this Chapter, we address the axisymmetric dynamics of reactive two-phase flows generated by the introduction of a reactant-laden fluid into a reactive porous medium at a point source. Chapter 3 studied the emergence of reaction fronts in a 1D system, effectively the steady flow of fluid from a planar boundary.

However there are many potential scenarios in which a local radial source of reactive fluid, for example a localised influx of warm water into a layer of snow [Grodzki and Szymczak, 2019], or intrusion of magma in a porous magma reservoir [Edmonds et al., 2019], will

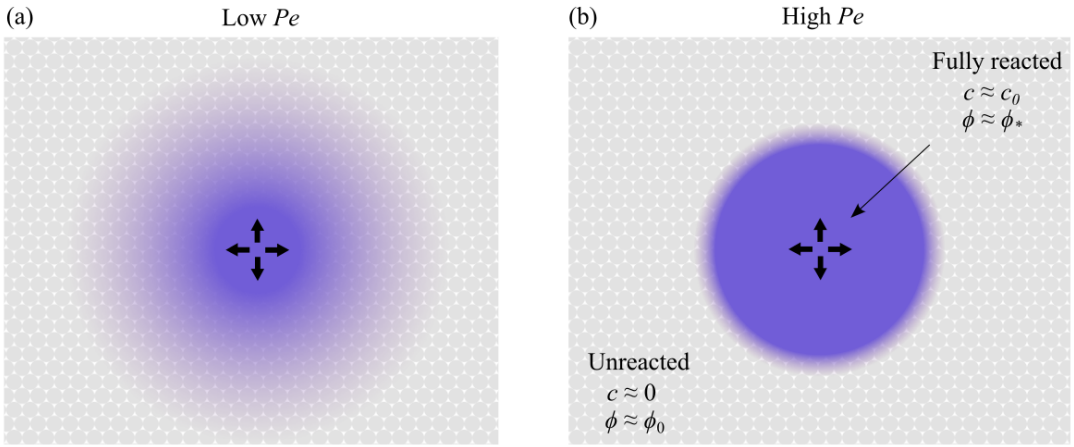

Figure 4.1: Schematic of the axisymmetric reaction injection configuration under consideration here, illustrating an example of (a) low Péclet number (primarily diffusive) dynamics, and (b) high Péclet (primarily advective) dynamics, following the injection of a reactive fluid into a porous medium. Colour indicates the strength of the concentration field.

drive a characteristically radial flow, forming a distinct fundamental configuration (figure 4.1). In such situations, the Darcy flux decays radially and, as we will demonstrate here, the transitional dynamics and asymptotic states differ fundamentally compared to the one-dimensional case. This new configuration thus presents a host of open questions in regards to the asymptotic states and transitional dynamics.

The most related previous work that includes an axisymmetric reactive flow is the study of Grodzki and Szymczak [2019] who focused on the reaction-infiltration instability of a radially spreading reactive flow under the assumption of a sharp porosity interface governed by a Stefan theory. In that analysis, fluid is supplied at the point source at a constant volumetric flux, generating a porosity front in the form of a sharp step which grows as $r \propto t^{1/2}$. In the small acid capacity limit, where the infiltrating fluid has the capacity to dissolve a small volume of the solid medium on a volume basis, the work assumes that the velocity and concentration fields remain approximately steady relative to the evolution of the reaction front, i.e. front velocity $\ll$ fluid velocity. The work further assumed a sharp porosity transition, wherein the domain is partitioned into a region of fully reacted material with variable reactant concentration determined by the balance of diffusion-advection and a region of unreacted material where $c = 0$ uniformly. These regions are separated by a boundary subject to a Stefan condition. Grodzki and Szymczak

[2019] go on to study the linear instability of a sharp reaction front growing fingers of fully reacted porosity intruding into an unreacted medium. There remains an open question as to how reaction fronts develop transiently without the restriction of these limits and what conditions on the flow ensure a sharp or diffusionless reaction front develops in the radial domain.

We present in section 2 our continuum two-phase theory and derive the axisymmetric system. Section 3 presents numerical solutions to the time-dependent equations, identifies the early time flow regimes and conducts a detailed regime analysis of the long-time states, with analytical theories of the limiting regimes. Section 4 summarises the key results for demarcating criteria of the two limiting regimes and their structural characteristics in dimensional form. Section 5 summarises how this fits with prior work on the radial geometry.

4.2 Model development

We consider a rigid porous medium, with porosity field $\phi(\boldsymbol{x}, t)$ where $\boldsymbol{x}$ is position and t is time, containing an incompressible interstitial fluid (figure 4.1). The fluid is assumed to react with the solid to change the local volume of both the fluid and solid, forming a two-phase system. Our basic system is as in Chapter 3,

$$\frac{\partial(\phi_* - \phi)}{\partial t} = -kR(c, \phi), \tag{4.1}$$

$$\frac{\partial \phi}{\partial t} + \boldsymbol{\nabla} \cdot (\phi \boldsymbol{u}) = \nu k R(c, \phi), \tag{4.2}$$

$$\frac{\partial(\phi c)}{\partial t} + \boldsymbol{\nabla} \cdot (\phi \boldsymbol{u} c) = \boldsymbol{\nabla} \cdot (D\phi \boldsymbol{\nabla} c) - k c_R R(c, \phi). \tag{4.3}$$

Equation (4.1) represents the conservation of solid volume, with the rate of decrease of the volume of the solid fraction, or reaction rate, denoted by $kR(c, \phi)$, where ϕ_* is the porosity of the solid after all reactable material is consumed and k is the kinetic rate constant of the reaction. The dimensionless empirical function $R(c, \phi)$ encodes the dependence of relative reaction rate on local concentration and porosity. Equation (4.2) represents mass conservation of fluid mass, where $\boldsymbol{u}(\boldsymbol{r}, t)$ is the interstitial fluid velocity. When solid is reacted, fluid is produced at a rate of $\nu R(c, \phi)$, where the production ratio

ν is a dimensionless constant representing the volume change on conversion from solid to fluid. Equation (4.3) represents mass conservation of the reactive component $c(\boldsymbol{x}, t)$, where D is the molecular diffusivity of the reactant and c_R is a consumption coefficient, representing the molar mass of reactant required to consume a unit volume of solid.

In general, closure would require a momentum conservation equation such as Darcy's law, $\phi \boldsymbol{u} = -(\kappa/\mu)\boldsymbol{\nabla} P$, where velocity is related to gradients in pressure P with parameters μ, the viscosity of the fluid, and κ, the permeability of the porous medium. However, for the axisymmetric systems we consider here, continuity will be determined to constrain the velocity field independently and hence there is no need to apply Darcy's law, nor any empirical relationship between permeability and porosity.

The addition of (4.1) and (4.2) eliminates $\partial\phi/\partial t$ and yields an equation for the divergence of the Darcy flux $\phi \boldsymbol{u}$

$$\boldsymbol{\nabla} \cdot (\phi \boldsymbol{u}) = (\nu - 1) k R(c, \phi), \tag{4.4}$$

representing the conservation of total mass of solid and fluid. The Darcy flux $\phi \boldsymbol{u}$ is thus non-locally related to the reaction rate across the flow.

Following Chapter 3, we model the reaction rate using

$$R(c, \phi) = c f(\phi), \tag{4.5}$$

where $f(\phi)$ is an empirical increasing function of porosity with the property that $f(\phi_*) = 0$, such that reaction ceases when the local reactable solid fraction is exhausted, and normalisation $f(0) = 1$. While the primary asymptotic regimes we document are independent of the specific form of $f(\phi)$, for our illustrative time-dependent simulations we adopt

$$f(\phi) = (1 - \phi/\phi_*)^m, \tag{4.6}$$

with $m = 2/3$, a value motivated by scaling volumetric solid fraction and pore-surface area [Aharonov et al., 1995].

4.2.1 Axisymmetric model

In axisymmetric systems, the velocity has a single component, $\boldsymbol{u} = u(r,t)\mathbf{e}_r$, and all variables depend solely on (r,t), where $r = \sqrt{x^2+y^2}$ is the radial coordinate. The system defined by (2.3)–(2.7) then reads

$$\frac{\partial \phi}{\partial t} = kR(c,\phi), \tag{4.7}$$

$$\frac{1}{r}\frac{\partial (r\phi u)}{\partial r} = (\nu - 1)kR(c,\phi), \tag{4.8}$$

$$\frac{\partial (\phi c)}{\partial t} + \frac{1}{r}\frac{\partial (r\phi u c)}{\partial r} = \frac{D}{r}\frac{\partial}{\partial r}\left(r\phi \frac{\partial c}{\partial r}\right) - kc_R R(c,\phi). \tag{4.9}$$

There are three spatial derivatives in the system: one in (4.7) and two in (4.9). Hence, the system requires a total of three boundary conditions on the dependent variables u and c. We specify two conditions on the concentration field given by

$$c(0,t) = c_0, \qquad \lim_{r\to\infty} c = 0, \tag{4.10}$$

where c_0 is a constant representing the mass concentration of reactant supplied at $r = 0$ and the latter implies that reactant is fully depleted far downstream. We impose the source condition

$$\lim_{r\to 0}(2\pi r\phi u) = Q, \tag{4.11}$$

where Q is the imposed ooint source flux centred on the point source. The initial conditions are

$$\phi(r,0) = \phi_0, \qquad c(r,0) = 0, \tag{4.12}$$

such that the system is initially free of reactant with uniform porosity ϕ_0. Equations (4.7)–(4.12) form a closed system comprising a coupled parabolic-elliptic differential system describing the evolution of the porosity and concentration fields.

The conservation of flux (4.8) can be integrated once to yield the influence of material production on u

$$r\phi u = \frac{Q}{2\pi} + \int_0^r (\nu - 1)kR(c,\phi)r \, \mathrm{d}r. \tag{4.13}$$

We remark that for $\nu = 1$, corresponding to the situation where the total volume of material is conserved, (4.8) simplifies to the simple local relationship $u = U/2\pi r$. Using this relationship to eliminate u from (4.9), we obtain

$$\frac{\partial(\phi c)}{\partial t} + \frac{Q}{2\pi r}\frac{\partial c}{\partial r} = \frac{1}{r}\frac{\partial}{\partial r}\left(rD\phi\frac{\partial c}{\partial r}\right) - kc_R R(c,\phi). \tag{4.14}$$

The governing equation for the reactive component is then given by a single purely parabolic equation, coupled to the porosity evolution (4.7).

4.2.2 Intrinsic scales and dimensionless model

Reading left to right, we refer to the respective terms of (4.9) after $\partial(\phi c)/\partial t$ as the advective term, the diffusive term and the reactive term. Scaling the advective and diffusive terms reveals a similarity variable in which $r^2 \sim t$ with no intrinsic scale. This similarity scaling is in contrast with the one-dimensional version of the system where scaling diffusion and advection reveals distinct time and length scales, owing to the decay of the advective flux with distance from the source. Scaling the reactive term with either the advective or diffusive term reveals a single intrinsic timescale $\tau_R = K^{-1} = \phi_*(kc_R)^{-1}$, representing the timescale on which reactive effects become important. Further, we can construct two intrinsic length scales $(Q/K\phi_*)^{1/2}$ and $(D/K)^{1/2}$, representing an advective-reactive balance and a diffusive-reactive balance, respectively.

The scales available in the system differ fundamentally from the one-dimensional case (Chapter 3) where there are two intrinsic time scales and three lengths scales. The difference arises because of the differing scalings that can be formed in view of the imposition of a two-dimensional radially decaying advective flux in the present case, as opposed to a one-dimensional flux. In particular, the differing intrinsic advective-diffusive scales in the present problem lead to entirely new self-similar regimes dependent on a prescribable Péclet number, a direct control that is absent in the one-dimensional problem.

We use the unique intrinsic time scale K^{-1} and, without loss of generality, the reactive-

diffusive length scale $\sqrt{D/K}$ to conduct a non-dimensionalisation. Thus, we let

$$r = \sqrt{\frac{D}{K}}\hat{r}, \quad t = \frac{1}{K}\hat{t}, \quad c = c_0\hat{c}, \quad \phi = \phi_*\hat{\phi}, \quad u = \frac{Q}{2\pi\phi_*}\sqrt{\frac{K}{D}}\hat{u}, \quad \hat{R} = c_0 R.$$

On dropping hats, (4.7)–(4.9) become

$$\frac{\partial \phi}{\partial t} = SR(c, \phi), \tag{4.15}$$

$$\frac{\lambda}{r}\frac{\partial \left(r\phi u\right)}{\partial r} = (\nu - 1)SR(c, \phi), \tag{4.16}$$

$$\phi\left(\frac{\partial c}{\partial t} + \lambda u\frac{\partial c}{\partial r}\right) = \frac{1}{r}\frac{\partial}{\partial r}\left(r\phi\frac{\partial c}{\partial r}\right) - (1 + S\nu c)R(c, \phi), \tag{4.17}$$

where $S = c_0/c_R$ is a Stefan number, $\lambda = Q/2\pi\phi_* D$is a Péclet number and $R(c, \phi) = cf(\phi)$. The boundary conditions on the fluid flux (4.11) and concentration (4.10) become

$$\lim_{r\to 0}(r\phi u) = 1, \qquad c(0, t) = 1, \qquad \lim_{r\to\infty} c = 0. \tag{4.18}$$

With $\Phi = \phi_0/\phi_*$, the initial conditions (4.12) become

$$\phi(r, 0) = \Phi, \qquad c(r, 0) = 0. \tag{4.19}$$

Along with $f(\phi)$, the dimensionless system above depends on four numbers:

$$\lambda = \frac{Q}{2\pi\phi_* D}, \qquad S = \frac{c_0}{c_R}, \qquad \Phi = \frac{\phi_0}{\phi_*}, \qquad \nu. \tag{4.20}$$

The parameter λ is a Péclet number, representing the ratio of the imposed flux to the diffusivity. The parameter S is a Stefan number, related to the acid capacity number $\gamma_a = S/(1 - \Phi)$ in acidisation contexts [e.g. Szymczak and Ladd, 2012], representing the relative concentration of reactant needed to consume the solid. The parameter Φ is the ratio of the initial porosity ϕ_0 to the maximum porosity ϕ_*. The production ratio ν is the ratio of the rate of increase of fluid volume to the rate of decrease of solid volume during reaction.

The system forms an advection-diffusion-reaction equation (4.17) that is two-way coupled

to the porosity evolution equation (4.15). The system differs from the one-dimensional system (Chapter 3) by the presence of the $1/r$ coefficients representing radial decay in the advective terms of (4.17), and in the divergence of the Darcy and diffusive fluxes in (4.16) and (4.17). These differences introduce fundamentally new regimes, parametric controls and transitional considerations. A key difference revealed immediately from the non-dimensionalisation is that the relative importance of advection to diffusion can be controlled directly by an *imposed* Péclet number λ. In the one-dimensional system, there is instead a dimensionless constant, labelled B, that independently encapsulates the relative effects of advective, diffusive and reactive controls together (Chapter 3).

4.2.3 Numerical scheme

In the same way as in Chapter 3, we use the method of lines to solve our system of equations numerically. This approach is restricted to the solution of the model with $\nu = 1$ imposed. We discretise the spatial derivatives in (4.15) and the dimensionless form of (4.14) using centred differences for the second-order derivative and an upwind derivative for the advective term. The resulting coupled dynamical system for $2 \leq i \leq n-1$ is

$$\frac{\mathrm{d}\phi_i}{\mathrm{d}t} = SR(c_i, \phi_i) \tag{4.21}$$

$$\frac{\mathrm{d}c_i}{\mathrm{d}t} = \frac{(\phi_i r_i - \phi_{i-1} r_{i-1})(c_i - c_{i-1})}{(\delta r)^2 \phi_i r_i} + \frac{c_{i+1} - 2c_i + c_{i-1}}{(\delta r)^2} - \frac{\lambda}{\phi_i r_i} \frac{c_i - c_{i-1}}{\delta r} - \frac{(1 + S\nu c_i) R(c_i, \phi_i)}{\phi_i}. \tag{4.22}$$

The node at $i = 1$ has fixed concentration $c = 1$ as the input boundary condition.

4.2.4 Validation of the numerical scheme in axisymmetry

As in the 1D case, we now validate that the numerical scheme converges towards the correct solution as the resolution is increased. Table 4.1 outlines the numerical simulations and meshes used to perform the mesh sensitivity analysis of our numerical model. Figure 4.2 plots (a) concentration and (b) porosity profiles at $t = 1$ for each mesh, with the curve corresponding to the finest mesh shown in (a) purple, and (b) blue; showing good agreement and convergence towards the finest mesh. Figure 4.3 plots the mean absolute

value of concentration (purple) and porosity (blue) as defined in (3.22) against time for the most refined case C3, and the same metric for the coarser meshes in black. In each case these demonstrate convergence as the mesh is refined. Further verification of results is provided in section 4.3 where analytical results are developed which agree with the numerical solution to the model.

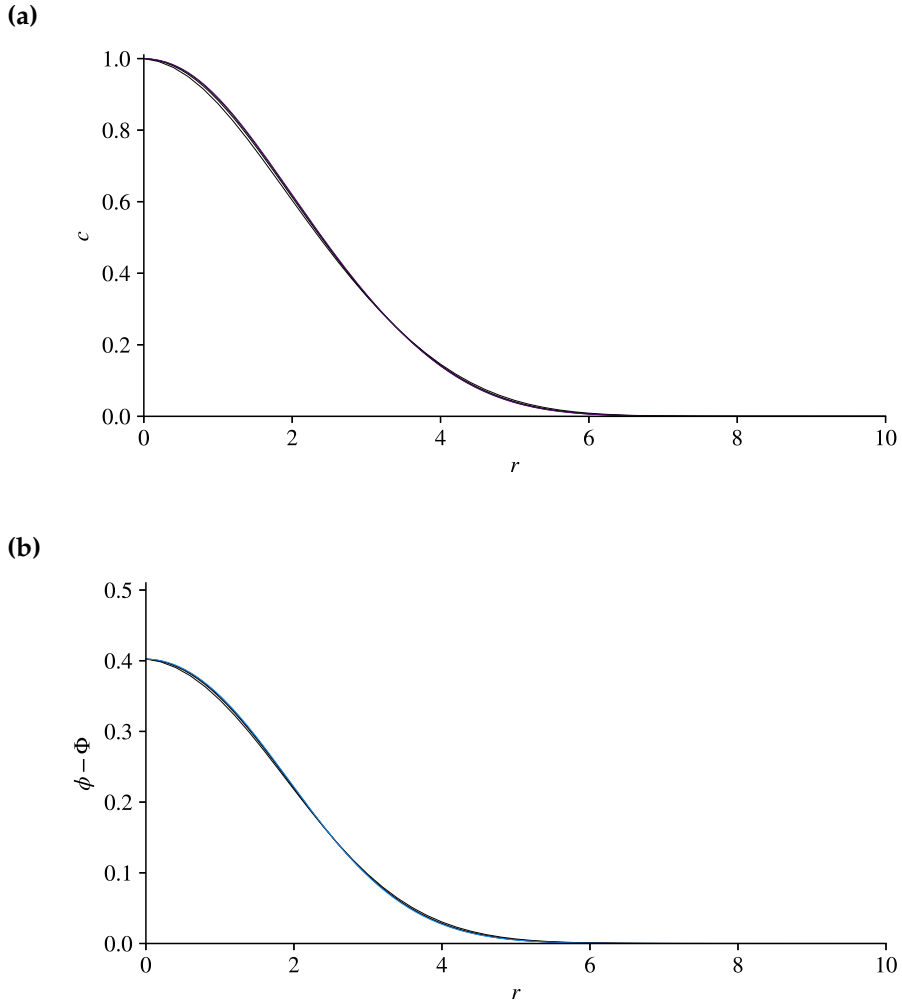

Figure 4.2: (a) concentration c and (b) ϕ for time $t = 1$ plotted for the cases C0, C1, C2 (all black), C3 (purple for concentration, blue for porosity), showing convergence towards the most refined (purple/blue) as the mesh is refined. Details of the meshes are given in table 4.1.

As explained in section 3.2.3 we rescale the domain periodically as the area of interest moves towards the far field boundary. This reduces the computational burden where the area of interest is local to the injection point.

ID	domain length, L	δr	λ	S	ϕ_0
C0	10	0.2	4	1	0.5
C1	10	0.1	4	1	0.5
C2	10	0.05	4	1	0.5
C3	10	0.025	4	1	0.5

Table 4.1: Table of simulation runs used in the grid sensitivity analysis of the radial method of lines.

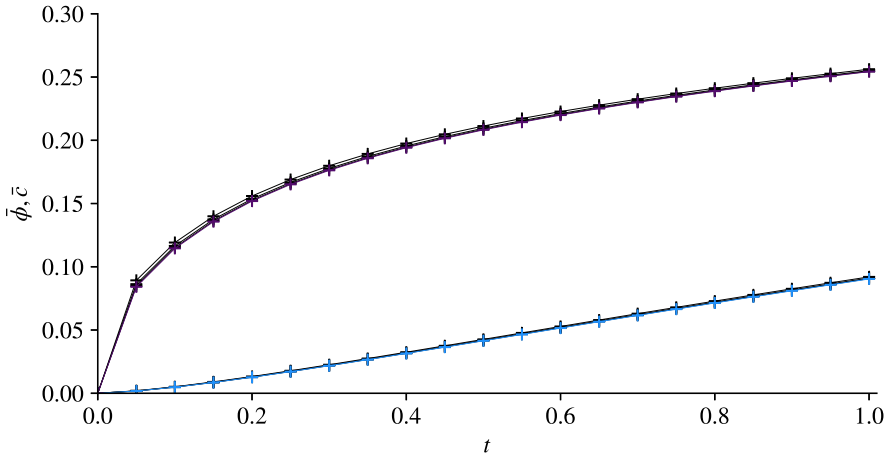

Figure 4.3: Profiles of mean $\bar{c}$ (purple) and $\bar{\phi}$ (blue), defined in (3.22) over time for the case C3. Overlaid for each is those variables cases C0, C1, C2 in black, demonstrating convergence of the results as the mesh is refined. Details of the meshes are given in table 4.1.

4.3 Theoretical analysis

4.3.1 Overview

To illustrate the key transient dynamics, we present a suite of time-dependent solutions to (4.15)–(4.17), using the numerical method developed in section 4.2.3.

Figure 4.4 presents the evolution of the spatial profile of the concentration, $c(r,t)$, and of the porosity, $\phi(r,t)$, at a progression of times for $\lambda = 0.1$ and $\lambda = 50$, both for fixed Stefan number $S = 1$, initial porosity $\Phi = 0.5$, production ratio $\nu = 1$ and reactive exponent $m = 2/3$.

We begin by considering the evolution of the small Péclet case, $\lambda = 0.1$ (figure 4.4(a)-4.4(b)), corresponding to predominantly diffusive dynamics. Figure 4.4(a) shows that the reactant concentration initially spreads into the domain with a characteristic convex

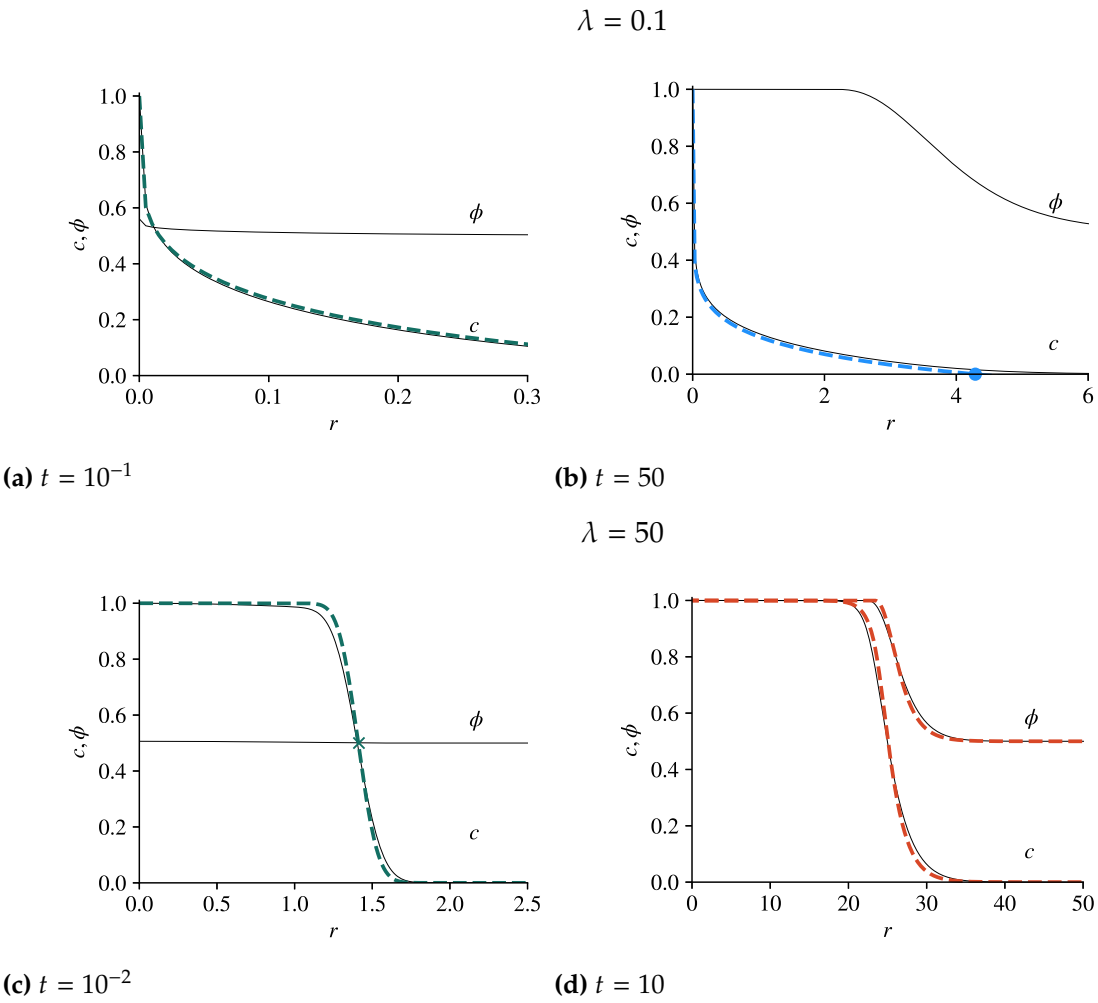

(a) $t = 10^{-1}$ **(b)** $t = 50$

(c) $t = 10^{-2}$ **(d)** $t = 10$

Figure 4.4: Representative time-dependent numerical solutions to (4.15)–(4.17) describing the evolutions of the concentration $c(r,t)$ and porosity $\phi(r,t)$ profiles, for (a)–(b) the low Péclet number case $\lambda = 0.1$ and (c)–(d) the high Péclet case $\lambda = 50$, each shown at progressive times. For both examples, we set the Stefan number $S = 1$, dimensionless initial porosity $\Phi = 0.5$, and production ratio $\nu = 1$. In (a) and (c), the early-time diffusive regime (4.33) is shown as a green dashed curve for concentration, showing reasonable agreement. A green cross on (c) indicates the asymptotic position of the concentration step (4.45). In (b), the concentration predicted by the sharp regime (4.72) is shown as a dashed blue curve showing good agreement as the porosity approaches sharpness. A blue dot on (b) indicates the 'sharp' location of the porosity transition given by (4.83). Panel (d) shows the predictions of concentration and porosity by the quasi-1D theory, given by (4.52)–(4.54), as a dashed orange curve showing good agreement.

profile which is typical of diffusion and porosity remains largely unchanged throughout the domain. By $t = 50$, (figure 4.4(b)), the concentration remains convex, but the porosity has developed into a sigmoidal form, connecting a fully reacted region ($\phi \approx 1$) to an unreacted region ($\phi \approx \Phi$). The average concentration in the domain has increased with time and is spread throughout the domain with an exponential tail.

The second illustrative case is $\lambda = 50$ (figure 4.4(c)-4.4(d)), corresponding to primarily advective transport dynamics. Figure 4.4(c) shows that at early times the concentration profile forms an approximate step profile, differing in fundamental form to the low Péclet scenario discussed above. At the later time $t = 10$, we see that the porosity departs from $\phi \approx \Phi$ and the concentration and porosity profiles are both localised to a region away from the origin.

We begin to analyse the characteristics of each case by considering the total mass of reactant in the domain at a given time

$$M(t) = \int_0^\infty \phi(\tilde{r}, t) c(\tilde{r}, t) \tilde{r} \, \mathrm{d}\tilde{r}. \tag{4.23}$$

Figure 4.5 shows the total mass of concentration in the system $M(t)$ (4.23) for (a) $\lambda = 0.1$ and (b) $\lambda = 50$ which both exhibit a largely $M(t) \propto t$ dependence on time. In each example, this is initially with one prefactor and transitions to a differing, smaller, prefactor at a timescale roughly coincident with the onset of evolving porosity.

As a general measure of the length scales on which the transitions in porosity and concentration across the flow take place, we define

$$l_c(t) = r_c^+(t) - r_c^-(t), \tag{4.24}$$

where $r_c^+(t)$ and $r_c^-(t)$ define the downstream and upstream extent of the relative surplus concentration

$$m(r) = \frac{M(r, t) - M_0(r, t)}{M(t)}, \tag{4.25}$$

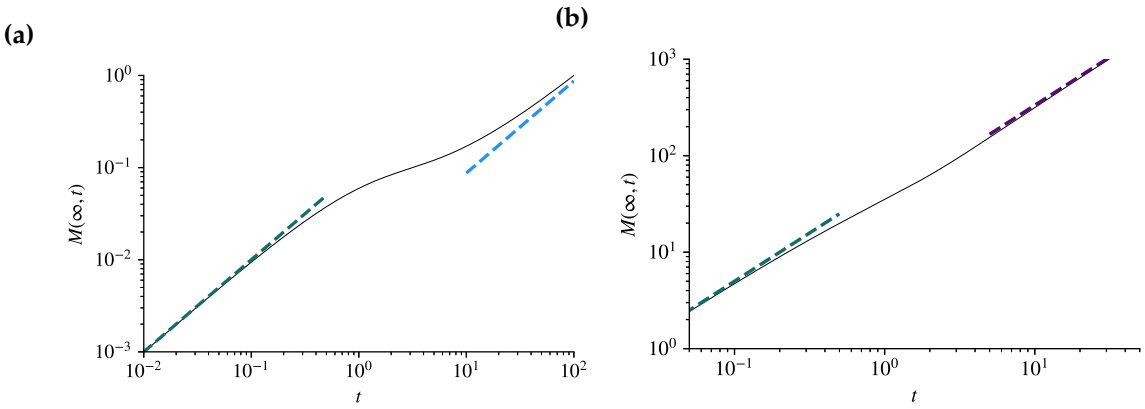

Figure 4.5: The mass of concentration in the domain $M(t)$ defined by (4.26) plotted against time, for fixed parameters $S = 1$, $\phi_0 = 0.5$, $\nu = 1$ and (a) $\lambda = 0.1$, (b) $\lambda = 50$. Overlaid on panel (a) is the early-time prediction of $M(t)$ (4.34) as a green dashed line and the late-time prediction of (4.79) as a blue dashed line, both showing excellent agreement. Overlaid on panel (b) is the early-time prediction of $M(t)$, (4.34) as a green dashed line, and the late-time prediction of $M(t)$ (4.75) as a purple dashed line, both showing good agreement with the numerical solution.

where

$$M(r,t) = \int_0^r \phi(\tilde{r},t)c(\tilde{r},t)\tilde{r}\,\mathrm{d}\tilde{r}, \qquad M_0(r,t) = \tfrac{1}{2}r^2\phi(r,t)c(r,t), \tag{4.26}$$

We define r_c^+ and r_c^- at a given t by $m(r_c^+) = 1-\varepsilon$ and $m(r_c^-) = \varepsilon$, where ε is a small parameter which we will take as $\varepsilon = 0.1$ for demonstration. These represent the relative extent of transition, with the transition 10% complete at r_c^- and 90% complete at r_c^+, and are presented as green dashed curves in figure 4.6, with l_c represented by the vertical distance between the two curves. Similarly, we define

$$l_\phi(t) = r_\phi^+(t) - r_\phi^-(t) \tag{4.27}$$

where $\phi(r_\phi^-) = \varepsilon\Phi + (1-\varepsilon)$ and $\phi(r_\phi^+) = (1-\varepsilon)\Phi + \varepsilon$ define the characteristic beginning and end, r_ϕ^- and r_ϕ^+, of the porosity transition. Figure 4.6 shows the evolution of r_ϕ^+ and r_ϕ^- as purple dashed curves, with l_ϕ represented as the vertical distance between the two.

Figure 4.6(a) shows the evolution of the locations $r_c^{+,-}$ and $r_\phi^{+,-}$, showing that initially porosity does not evolve and concentration is localised near to the origin (remaining $r_c^+ < 1$ up to $t \approx 0.1$) to the origin. After $t \approx 1$ we see a change in the time dependence of

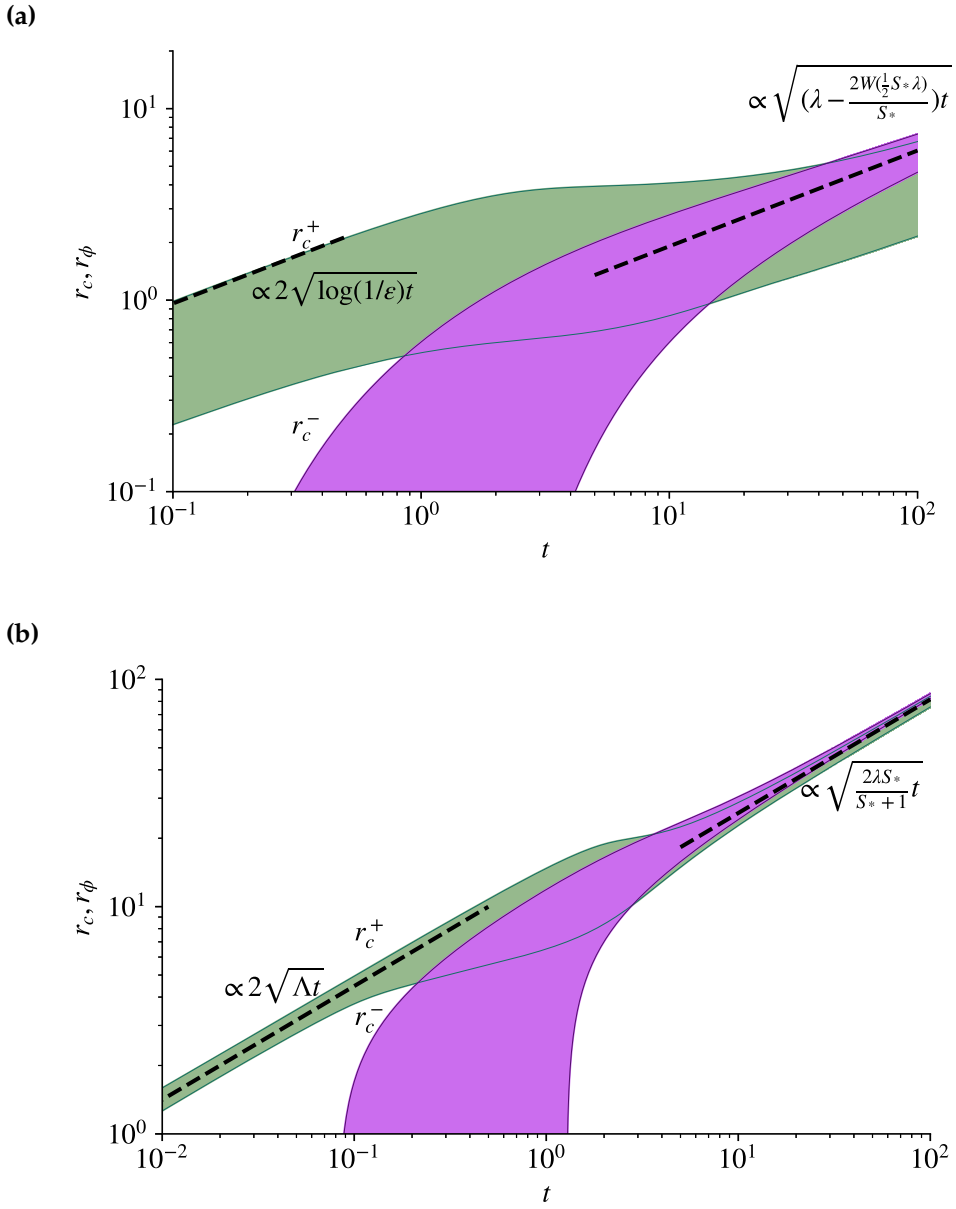

Figure 4.6: Plots of $r_c^{+,-}$ (green) and $r_\phi^{+,-}$ (purple) over time, for fixed parameters $S = 1$, $\phi_0 = 0.5$ and (a) $\lambda = 0.1$, (b) $\lambda = 50$ showing the evolution of the positions, defined in (4.24) and (4.27). Overlaid on panel (a) is the early time prediction of r_c^+, from (4.41) as a black dashed curve and the late time prediction of r_ϕ (4.78) showing good agreement as r_ϕ^+ and r_ϕ^- converge. Overlaid on panel (b) are the early time prediction of r_c below (4.45), about which r_c^+ and r_c^- are expected to lie , as a black dashed line, and also the late time prediction of r_ϕ (4.83) as a black dashed line showing good agreement with the numerical solution. The parameter ε is defined below (4.26), it is a small parameter defining the edge of the transition zone. The extent of region over which the transitions of porosity and concentration happen are shaded in purple and in green respectively.

$r_c^{+,-}$ and the evolution of the porosity transition emerges around $t \approx 3$, where r_ϕ^+ becomes non zero. After this point we see both the concentration and porosity lengths departing the origin, with the distance between r_ϕ^+ and r_ϕ^- reducing as time increases. Figure 4.6(b) also plots $r_c^{+,-}$ and $r_\phi^{+,-}$ against time. Similarly to figure 4.6(a), the extent of concentration exhibits a power-law dependence on time before the porosity begins to evolve. Once $t \sim 1$, the porosity transition emerges and departs from the origin, at this time $r_c+,-$ break from their previous power law behaviour as a new regime is established. By the later time of $t = 10$, we see porosity narrows with r_ϕ^+ and r_ϕ^- converging towards each other, reflecting an approach to a step transition moving with $t^{1/2}$. Both extents of concentration, $r_c^\pm$ follow the same power law behaviour but do not converge towards each other as quickly as their porosity analogues.

4.3.2 Early-time transportive regimes

At early times (figure 4.4(a) and figure 4.4(c)), we see two distinct regimes develop in the concentration profiles. For small $\lambda = 0.1$ (figure 4.4(a)), we observe a convex concentration profile extending further into the domain with time. In the case of large λ (figure 4.4(c)), the concentration profile is markedly different at the same early time scales, forming a sharp step in concentration, also with no porosity evolution. What the two have in common is that porosity remains close to its starting value $\phi \approx \Phi$ which suggests that reaction is not necessary in this regime. We can thus formulate an early advective-diffusive theory in which reaction is negligible.

The neglect of reaction simplifies (4.16) to

$$\frac{\partial \left(ru\phi\right)}{\partial r} \approx 0, \qquad (\Phi u r) \approx 1 \tag{4.28}$$

and therefore the advective term in (4.17) can be simplified to yield

$$\frac{\partial c}{\partial t} + \frac{\Lambda}{r}\frac{\partial c}{\partial r} = \frac{1}{r}\frac{\partial}{\partial r}\left(r\frac{\partial c}{\partial r}\right), \tag{4.29}$$

where $\Lambda = \lambda/\Phi$ we refer to as the *effective* Péclet number. Using a similarity variable

$\eta = t^{-1/2}r$ with $c = c(\eta)$, (4.29) becomes

$$\left(-\tfrac{1}{2}\eta^2 + \Lambda\right) c' = \left(\eta c'\right)', \tag{4.30}$$

with boundary conditions

$$\lim_{\eta\to 0} c = 1, \qquad \lim_{\eta\to\infty} c = 0. \tag{4.31}$$

By expanding the product on the right-hand side of (4.30), dividing the resulting equation by $\eta c'$ and integrating, we obtain

$$c' = -A\eta^{\Lambda-1}e^{-\eta^2/4}, \tag{4.32}$$

where A is a constant of integration. The above demonstrates a critical transition in the qualitative form of the solutions. The gradient of the concentration profile $\lim_{\eta\to 0} c' = -\infty$, with an integrable singularity, if $\Lambda < 1$, and a zero gradient $\lim_{\eta\to 0} c' = 0$ if $\Lambda < 1$, forming a critical qualitative difference across Péclet number $\Lambda = 1$.

Integrating (4.32) further, imposing conditions (4.31), and rewriting the integral in terms of the variable $u = \eta^2/4$, we obtain the exact solution,

$$c(\eta) = \frac{\displaystyle\int_{\eta^2/4}^{\infty} u^{\Lambda/2-1}e^{-u}\,\mathrm{d}u}{\displaystyle\int_{0}^{\infty} u^{\Lambda/2-1}e^{-u}\,\mathrm{d}u} \equiv \frac{\Gamma\left(\frac{1}{2}\Lambda, \frac{1}{4}\eta^2\right)}{\Gamma\left(\frac{1}{2}\Lambda, 0\right)}, \tag{4.33}$$

where $\Gamma(s,z) \equiv \int_z^\infty u^{s-1}e^u\,\mathrm{d}u$ is the upper incomplete gamma function. A selection of the solutions (4.33) for effective Péclet numbers $\Lambda = 0.1, 1$ and 10 is shown in figure 4.7(a), illustrating a characteristic variation from a convex curve for small Λ to a sigmoidal transition for large Λ. The special cases $\Lambda = 1$ and 2 admit the simple exact forms $c = \operatorname{erfc}(\eta/2)$ and $e^{-\eta^2/4}$, respectively; each is overlaid as a dashed curve in figure 4.7(a) and validating our numerical evaluations of (4.33). The characteristic position η_c^+, correspondent with r_c^+ (4.24), providing a measure of the extent of transport, is shown as a function of Λ in figure 4.7(b). As no material is consumed in the transportive regime, conservation of mass of

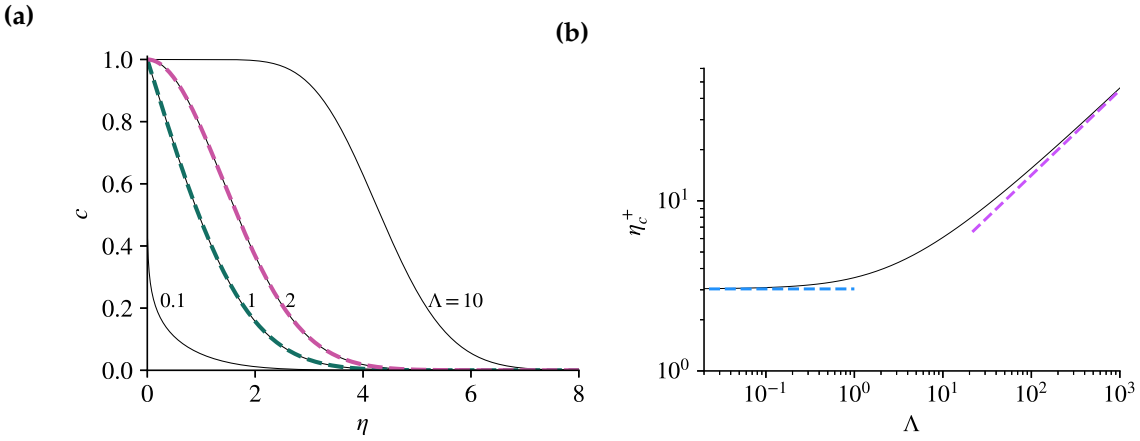

Figure 4.7: (a) The similarity solutions describing the early-time transportive regimes given by solving the system (4.33) for a selection of effective Péclet numbers $\Lambda = 0.1, 1, 2$ and 10. The exact solutions in the cases of $\Lambda = 1$ and 2 (below (4.33)) are shown as green and pink dashed lines respectively. (b) The characteristic extent of spreading, defined by the location η_c^+ where $m(\eta_c^+) = 0.1$, plotted against Λ. The $\Lambda \to 0$ asymptotic prediction given by (4.43) is shown as a blue dashed curve showing good agreement. The $\Lambda \to \infty$ prediction below (4.45), namely, $\eta_c = \sqrt{2\Lambda}$ is shown as a pink dashed curve showing good agreement.

reactant along with (4.26), we note that the total mass of reactant in the system

$$M(t) = \lambda t, \tag{4.34}$$

which is overlaid in figure 4.5 (a) and (b), as green dashed lines, providing validation in both cases.

Low Péclet number

At low Péclet number, we would typically expect flow to be diffusion-dominated, for which a question arises due to the non-integrability of (4.32) at the origin for $\Lambda < 1$. We anticipate that the diffusion-dominated solution would be fed by an infinite point source.

Proceeding heuristically to begin with the assumption that the dynamics are dominated by diffusion, (4.30) and its integrated form (4.32) reduce to

$$-\tfrac{1}{2}\eta^2 c' = \left(\eta c'\right)', \qquad c' = -A\eta^{-1}e^{-\eta^2/4}. \tag{4.35}$$

Integrating the above subject to the condition $\lim_{\eta\to\infty} c = 0$, we obtain

$$c = A\int_{\eta}^{\infty} \eta^{-1}e^{-\eta^2/4}\,\mathrm{d}\eta = \tfrac{1}{2}A\int_{\frac{1}{4}\eta^2}^{\infty} u^{-1}e^{-u}\,\mathrm{d}u = \tfrac{1}{2}AE\left(\tfrac{1}{4}\eta^2\right), \tag{4.36}$$

where A is a constant of integration, the second equality follows upon transforming the integration variable to $u = \eta^2/4$, and $E(z) \equiv \int_z^{\infty} u^{-1}e^{-u}\,\mathrm{d}u$ defines the exponential integral function.

Using the result that $E(z) \sim \log(1/z) - \gamma$, as $z \to 0$, where $\gamma \approx 0.577$ is Euler's constant [Abramowitz and Stegun, 1964], (4.36) predicts the near-source expansion

$$c \sim A\left(\log\left(\frac{1}{\eta}\right) - \frac{\gamma}{2}\right) \qquad (\eta \to 0). \tag{4.37}$$

The result above implies that the purely diffusive theory necessitates a singularity in the near-source limit. In view of this singularity, it is impossible for (4.36) alone to satisfy the input boundary condition (4.31), indicating that $\Lambda \to 0$ forms, as anticipated, a singular asymptotic problem. Physically, the incompatibility reflects the fact that an idealised point or vertical line source held at a *finite* concentration (or temperature) cannot prescribe a local diffusive gradient across its extent.

In order to complete the asymptotic theory and determine the unknown A, we must consider an inner asymptotic deck in the vicinity of $\eta = 0$ wherein advection intervenes to generate a finite concentration flux that is then matched to the diffusive solution (4.36). The near-source deck is defined by the inclusion of advection but the neglect of $-\eta^2/2$, which has its origin in the rate of change $\partial c/\partial t$. Thus, the neglect of this term can be interpreted as a quasi-steady balance, given by

$$\Lambda c' = (\eta c')'. \tag{4.38}$$

Integrating once subject to $c(0) = 1$ and then solving the resulting first-order linear differential equation, we obtain the inner solution given by

$$c = 1 - B\eta^{\Lambda} = 1 - Be^{\Lambda\log\eta}, \tag{4.39}$$

where B is a constant of integration. From (4.39), we see that the size of the inner deck, in which c is of order unity, is defined by where $e^{\Lambda \log \eta}$ decreases by an amount of order unity. Thus, the boundary-layer scale is $\eta \sim e^{-1/\Lambda}$, which is indeed small as $\Lambda \to 0$.

In order to match (4.39) and (4.36), we note that the outer limiting form of (4.39) is given by retaining the first two terms in its Taylor expansion, namely,

$$c \sim 1 - B(1 + \Lambda \log \eta) \qquad (\eta \gg e^{-1/\Lambda}). \tag{4.40}$$

Comparison with the inner limit of the outer deck (4.37) shows that a consistent matching requires $B = 1$ and $A = \Lambda$. In summary, the full composite leading-order solution is

$$c \sim \begin{cases} 1 - \eta^{\Lambda} & (\eta \ll e^{-1/\Lambda}), \\ \Lambda \log(1/\eta) & (e^{-1/\Lambda} \ll \eta \ll 1), \\ \frac{1}{2}\Lambda E\left(\frac{1}{4}\eta^2\right) & (\eta \sim 1), \\ 2\Lambda \eta^{-2} e^{-\eta^2/4} & (\eta \gg 1). \end{cases} \tag{4.41}$$

The outer solution, given by the third row of (4.41), is plotted as a dashed blue curve in figure 4.8 for $\Lambda = 0.1$, forming a concave solution with a Gaussian-like tail for $\eta \gg 1$. The prediction shows good agreement with the corresponding solution to the full, unsimplified transportive model given by (4.33).

A key implication of (4.41) is that, in the general context of a diffusive system fed by a point source, the prevailing outer solution given by the third row of (4.41) can be interpreted as a primarily diffusively spreading concentration field fed by an *effective* diffusive flux condition

$$\lim_{\eta \to 0}(-\eta c') = \Lambda. \tag{4.42}$$

The near-source condition (4.42) implies a logarithmic singularity as $\eta \to 0$, and hence there is a small region in $r \lesssim e^{-1/\Lambda}$ wherein the prediction $c > 1$ is unphysical, but which lies outside the prevailing region of interest wherein $c \sim \Lambda \ll 1$. The application of (4.42) in place of the inlet concentration condition (4.19) circumvents the need to resolve the very small advective-diffusive boundary layer over $\eta \sim e^{-1/\Lambda} \to 0$ in order to match

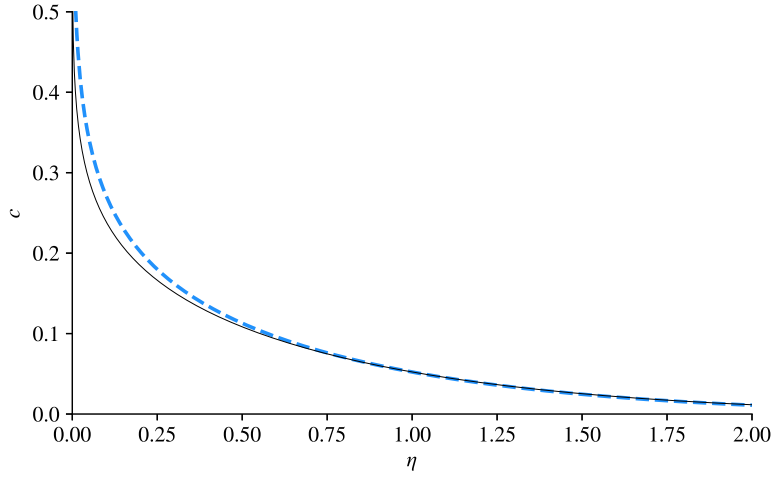

Figure 4.8: The transportive similarity solution given by the analytical solution (4.33) for a small effective Péclet $\Lambda = 0.1$, and production ratio $\nu = 1$ plotted against the similarity coordinate $\eta = rt^{1/2}$. The simplified diffusion-dominated asymptotic outer solution, given by the analytical solution in the third row of (4.41), representing a diffusive state solved subject to the effective singular matching condition (4.42) derived in the limit $\Lambda \to 0$, is overlaid as a blue dashed curve.

the Dirichlet boundary condition $c(\eta = 0) = 1$. Thus, we can reframe problems in the diffusion-dominated limit of $\Lambda \to 0$ by applying the following *diffusive* flux condition (4.42), a Neumann boundary condition.

Using the concentration profile (4.41) to evaluate the diagnostic (4.26), we recover the limiting characteristic extent of concentration (4.24),

$$\eta_+ = 2\sqrt{\log(1/\varepsilon)}. \tag{4.43}$$

This asymptotic prediction is shown as a dashed blue line in figure 4.7(b), showing good agreement with the numerical solution to the full transportive system in the relevant limit, $\Lambda \to 0$. The lack of dependence of (4.43) on λ reflects the dominantly diffusive control on the spread of reactant in this limit.

The limit of high Péclet number

Upon neglecting diffusion, (4.30) reduces to

$$\left(-\tfrac{1}{2}\eta^2 + \Lambda\right) c' = 0, \tag{4.44}$$

from which it follows that either $\eta = \sqrt{2\Lambda}$ or $c' = 0$. Thus, the leading-order early-time advection-dominated solution forms two uniform sections with an allowance for a single jump discontinuity in c at $\eta = \sqrt{2\Lambda}$. The unique solution that satisfies conditions (4.31) is therefore

$$c = \begin{cases} 1 & (\eta < \sqrt{2\Lambda}), \\ 0 & (\eta > \sqrt{2\Lambda}), \end{cases} \tag{4.45}$$

representing a cylindrical expansion of the concentration field advected radially with the flow, with scaled extent $\eta_+ = \sqrt{2\Lambda}$ where the concentration transitions from unity to zero. This prediction of η_+ is overlaid on figure 4.7(b) as a dashed pink curve, showing close agreement with the prediction of the full transportive system (4.33). The predicted position of both $r_c^{+,-}$, $r_c(t) = \sqrt{2\Lambda t}$ is indicated in figure 4.4(c) as a green cross and plotted as a function of time in 4.6(b) as a black dashed curve, each showing agreement with the numerical calculation of the location of the transition region at early times predicted by the full time-dependent model for $\lambda = 50$.

4.3.3 The intervention time scale of reactive effects

Given the use of the reactive timescale to non-dimensionalise our system in section 4.2.2, we anticipate that reaction becomes significant on a $t \approx O(1)$ timescale. In order to more directly assess when reaction intervenes from the dimensionless system, we look at the timescale on which reaction causes an $O(1)$ effect on c in (4.17),

$$\Phi \frac{\partial c}{\partial t} \sim (1 + S\nu c) c f(\Phi). \tag{4.46}$$

The characteristic value of c is that which is representative over the domain and so we evaluate c_* using the mass flux (4.26) and thus calculate a representative c_* across the domain. For $\lambda > 1$, the characteristic value is $c_* \approx 1$ and for $\lambda \ll 1$, it is $c_* = \Lambda$ arising from the effective diffusive flux condition (4.42). Thus $c_* = \min(1, \Lambda)$ will generally represent the concentration scale. From (4.46), we determine the reactive time scale

$$t_R = \frac{\Phi}{N_* f(\Phi)} \tag{4.47}$$

where $N_* = \max(1, Nc_*)$ and $c_* = \min(1, \Lambda)$. The parameter N quantifies the extent to which concentration is reduced by dilution during reaction, with ν quantifying solvent generation and S representing the relative volume of solid reacted, versus consumption. We now evaluate t_R for the two examples of figure 4.4. Both examples have fixed paramters $S = 1, \Phi = 0.5$ and $\nu = 1$, and for $\lambda = 0.1$ we get $t_R \approx 0.8$ for which figure 4.6(a) verifies the departure of both $r_c^{+,-}$ from the initial transportive scaling at around $t \approx O(10^{-1})$. For the second example $\lambda = 50, S = 1, \Phi = 0.5$ and $\nu = 1$, we get $t_R \approx 0.4$, which is again in keeping with figure 4.6(b). Thus, we expect that $t_R \approx O(1)$ for most parameters.

4.3.4 Quasi-one-dimensional travelling wave state for large Péclet number

For large Péclet numbers $\lambda \gg 1$, the flow enters a regime defined broadly by the property that both the concentration and porosity transitions remain localised near a single transition radius, which we denote by $r_N(t)$, where we define $\phi(r_N) = (1 + \Phi)/2$ (figure 4.4(d)). We propose that, in this regime, the flow simplifies asymptotically in two ways. Firstly, the dynamics can be treated as *quasi-one-dimensional*, meaning that the radial factors in (4.16) and (4.17) can be approximated uniformly by $r_N(t)$ across the transition region. Second, the dynamics over the transition region adjust over a relatively fast time scale relative to the variation in $r_N(t)$ such that the concentration and porosity profiles can be approximated as *quasi-steady* in the frame of the single transition radius, $r_N(t)$. As a result of both simplifications, the transition profiles form approximately steady travelling wave states that gradually vary over a slow time scale in response to the changing radial flux delivered towards the transition radius $r_N(t)$. We proceed heuristically by developing an asymptotic description of the system in these limits and subsequently validate the resulting predictions of the reduced model.

To demonstrate the emergence of these asymptotic properties, we proceed heuristically by first translating the system into the frame of a single transition region by defining $r = r_N(t) + \xi$, with ξ a moving coordinate. Assuming that we are far from the point

source, $r_N(t) \gg \xi$, the new system becomes

$$-\dot{r}_N(t)\frac{\partial \phi}{\partial \xi} = SR(c,\phi), \tag{4.48}$$

$$\lambda \frac{\partial(\phi u)}{\partial \xi} = (\nu - 1)SR(c,\phi), \tag{4.49}$$

$$\phi\left(-\dot{r}_N(t) + \lambda u\right)\frac{\partial c}{\partial \xi} = \frac{\partial}{\partial \xi}\left(\phi \frac{\partial c}{\partial \xi}\right) - (1 + \nu Sc)R(c,\phi), \tag{4.50}$$

with conditions

$$c \sim 1, \qquad u \sim q(t) = \frac{1}{r_N(t)} \qquad (z \to -\infty). \tag{4.51}$$

The rescaled system (4.48)–(4.50) has the same overall form as the one-dimensional system studied in (3.15)–(3.18) (Chapter 3). The key difference is that the prefactors $\dot{r}_N(t)$ involving a dependence on time t and the dimensionless flux delivered towards the front, $q(t) = 1/r_N(t)$, retain a time dependence, but are constant prescribed parameters in the one-dimensional theory. However, once $r_N(t) \gg 1$, these time scales vary increasingly more slowly compared to the adjustment time scale of the system, creating a quasi-steady regime. In other words, each solution to the travelling-wave system (4.52)–(4.54) for a given value of $\dot{r}_N(t)$ and $r_N(t)$ is instantaneously close to a steady state and evolves in response to a gradual change in these variables.

In order to render the system of (4.48)–(4.51) identical to the dimensionless ordinary differential equation system of Chapter 3 in terms of the dimensionless parameters and variables, we conduct a further rescaling by writing the front velocity $\dot{r}_N(t) = \lambda W q(t)$, the interstitial velocity $u = q(t)\tilde{u}$, and the stretched coordinate $\xi = q(t)\lambda z$. The system (4.48)–(4.50) then becomes

$$-W\frac{\partial \phi}{\partial z} = B(t)SR(c,\phi), \tag{4.52}$$

$$\frac{\partial(\phi \tilde{u})}{\partial z} = B(t)(\nu - 1)SR(c,\phi), \tag{4.53}$$

$$\phi\left(-W + \tilde{u}\right)\frac{\partial c}{\partial z} = \frac{\partial}{\partial z}\left(\phi \frac{\partial c}{\partial z}\right) - B(t)(1 + \nu Sc)R(c,\phi), \tag{4.54}$$

with conditions

$$c \sim 1, \qquad \tilde{u} \sim 1 \qquad (z \to -\infty), \tag{4.55}$$

where $B(t) = (\lambda q(t))^{-2} = (r_N(t)/\lambda)^2$ is a time-dependent form of the parameter B, which forms a specified constant in the one-dimensional theory. The rescaled travelling-wave system (4.52)–(4.55) is now structurally identical to the ordinary differential system in Chapter 3, as reviewed in Appendix C with the exception that the parameter $B(t)$ is dependent on time, as opposed to be being a specified constant. In accordance with the quasi-steady assumption of this regime, the parameter $B(t)$ varies on a slow time scale as compared to the adjustment time scale of the solution and the solution equals the instantaneous steady state for a given value of $B(t)$ to leading order.

By considering first integrals of the one-dimensional system (4.52)–(4.54), it was determined in Chapter 3 that the dimensionless travelling wave speed is a function of Stefan number alone, given by

$$W = \frac{S_*}{S_* + 1}, \tag{4.56}$$

a result that is consistent with global reactant conservation across the transition (Appendix C). Using the result above, recalling that $\dot{r}_N = \lambda W q(t)$ and $q(t) = 1/r_N(t)$, we obtain the following differential equation for the evolution of the leading-order position of the transition $r_N(t)$ given by

$$\dot{r}_N = \frac{\lambda S_*}{(1 + S_*) r_N}. \tag{4.57}$$

Integrating subject to the initial condition $r_N(0) = 0$ (or equivalently, neglecting the constant of integration for $r_N \gg r_N(0)$), we determine the leading-order solution

$$r_N(t) = \sqrt{\frac{2\lambda S_* t}{1 + S_*}}, \tag{4.58}$$

which gives a prediction for the position of both the concentration and porosity transitions within this quasi-one-dimensional regime. Thus, both transitions reside near the single position $r_c(t) \sim r_\phi(t) \sim r_N(t)$ that grows as $t^{1/2}$, with the leading-order transitions forming quasi-steady solutions in the frame of the moving position $r_N(t)$. The prediction of (4.58) is plotted as a black dashed curve in figure 4.6(b), showing good agreement with the prediction of the full time-dependent model at late times.

The analysis of the travelling-wave system (4.52)–(4.54) in Chapter 3 for a given value

of the parameter B revealed that the solutions exist on a parameter space that partitions into two regimes: the *sharp* regime and the *diffusionless* regime (Appendix C). In the sharp regime, there is a separation of scales between the concentration transition, with the length scale l_c, and the porosity transition, l_ϕ. The emergent sharpness,

$$\Sigma = l_c/l_\phi \tag{4.59}$$

quantifies the separation of the transition scales and we define $\Sigma \gg 1$ as 'sharp'. Figure 4.9 shows the evolution of Σ as a function of time for $\lambda = 50$. In the diffusionless regime, the concentration and porosity transition length scales are comparable but the dynamics are simplified by the negligibility of diffusion. The analysis shows that the sharp and diffusionless regimes are demarcated by the single dimensionless number,

$$\Omega(t) = f(\Phi)(1 + S_*)^2 B(t), \tag{4.60}$$

which incorporates together the effects of B, S and Φ. Our remapping of the quasi-one-dimensional axisymmetric system to the one-dimensional system (4.56)–(4.58) shows that the relationship between $B(t)$ and the parameters and variables of our axisymmetric non-dimensional model is

$$B(t) = \left(\frac{r_N(t)}{\lambda}\right)^2 = \frac{2S_* t}{\lambda(1 + S_*)}, \tag{4.61}$$

where the second equality follows with use of the prediction for the radial position of the front $r_N(t)$ given by (4.58). Thus, we determine that the parameter (4.60) satisfies

$$\Omega(t) = 2f(\Phi)S_*(1 + S_*)\lambda^{-1}t. \tag{4.62}$$

The parameter $\Omega(t)$ is, in the context of the quasi-one-dimensional regime of the axisymmetric configuration, therefore an increasing function of time, indicating that the quasi-one-dimensional state undergoes a gradual time-dependent transition through the parameter space of the one-dimensional theory from the diffusionless regime to the sharp regime.

To demonstrate this transition, figure 4.10 shows the time evolution of the concentration for $\lambda = 50$ from $t = 10$ through to $t = 100$ in increments of 10. The orange dashed line on figure 4.10 shows the the asymptotic diffusionless solution to (4.52)–(4.54), showing approximate agreement with the $t = 10$ solution. A purple dashed curve shows the sharp asymptotic solution to (4.52)–(4.54), which we can see the solution is approaching as time increases, confirming the evolution of the quasi-steady solution towards sharpness with time. There is a discrepancy at small c in which the tail of the concentration transition is not sharpening as much as the sharp 1D theory predicts, it is believed that this may be numerical in nature, likely excessive numerical diffusion, given that the theoretical results otherwise fit the numerical solution well.

The apparent quasi-1D regime allows us to therefore use the results of Chapter 3 to confirm the evolution of the radial system where it is applicable. Chapter 3 showed that in the sharp limit as $\Omega \gg 1$, $\Sigma \propto \sqrt{\Omega}$ and thus we expect this to be the case as the radial system after sufficient time. Substitution of (4.60) into those results generates a prediction of

$$\Sigma = \alpha \sqrt{\frac{2f(\Phi)S_*(1+S_*)t}{\lambda}}, \tag{4.63}$$

where α is a fitting parameter specific to the definition of the illustrative positions $r_c^{+,-}$ (4.24). In this case $\alpha = 0.54$ which is overlaid on figure 4.9 as a purple dashed curve, showing good asymptotic agreement with the numerically calculated sharpness. Furthermore, this allows us to generate a threshold time for sharpness, t_S by setting $\Omega(t_S) = \Omega_S$, a threshold value of Ω at which the solution is considered sharp, and we get

$$t_S = \frac{\Omega_S \lambda}{2f(\Phi)S_*(1+S_*)}, \tag{4.64}$$

which shows $t_S \propto \lambda$, the Péclet number and a more complex dependence on (S, Φ) which also have some control of t_S.

4.3.5 Final sharp regime

Whether the solution develops from large λ or small λ, the ultimate regime is one where the porosity transition has sharpened to an effective interface relative to the scale of the

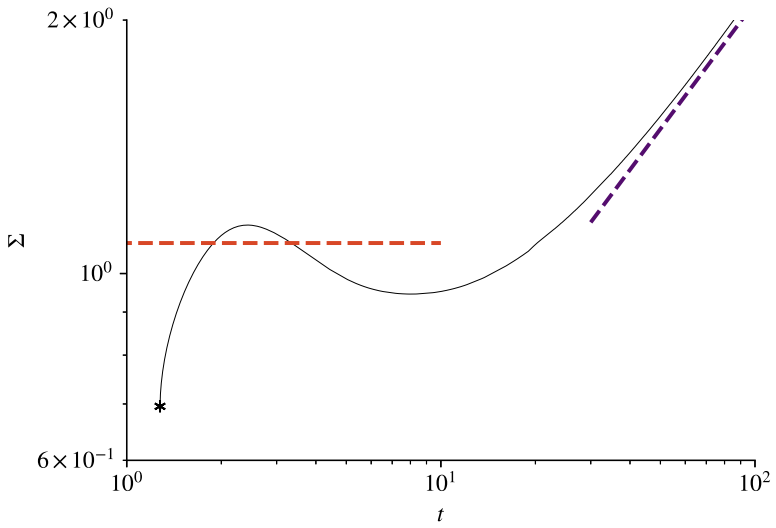

Figure 4.9: Sharpness (4.59) plotted as a function of time, for $\lambda = 50$, $S = 1$, $\Phi = 0.5$ and $\nu = 1$. Overlaid as an orange dashed curve is the prediction of the diffusionless limit (Appendix C) showing rough agreement at the early time of $t < 10$. Overlaid as a purple dashed curve is the prediction of (4.63) showing good agreement with the numerical solution at late times.

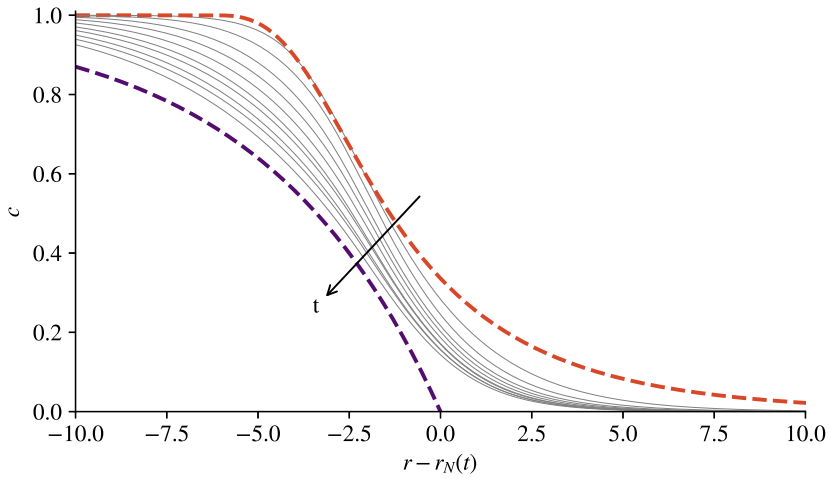

Figure 4.10: Solutions of the full radial system (4.15)–(4.17) (grey curves) for $\lambda = 50$, $S = 1$, $\Phi = 0.5$ and $\nu = 1$ at times of $t = 10, 20 \ldots 100$, with the direction of time indicated, subject to boundary and initial conditions conditions (4.18)–(4.19). The concentration profiles $c(r - r_N(t))$ are shown in the frame of $r_N(t)$, defined by the centre of the porosity transition, with $\phi(r_N) = (1 + \Phi)/2$. The asymptotic limiting forms of the quasi-1D travelling wave system (4.48)–(4.50) for $\Omega(t) = 1.5$ and 7.54 are overlaid as an orange (diffusionless) and purple (sharp) dashed curve respectively, illustrating the broadening of the concentration profile from the orange towards the purple line with time.

concentration profile. For $\lambda \gg 1$, this develops from the growing $B(t)$ in the quasi-1D regime which drives sharpening (Chapter 3). For $\lambda \ll 1$, the porosity step localises at $r = r_\phi$ away from the origin, whilst the concentration remains a convex function of radius spanning the domain.

Hence, we approximate the porosity as a Heaviside function, localised around the front location $r_\phi(t)$. We assume that all reactant is depleted at r_ϕ i.e. $c(r_\phi) = 0$.

$$\phi = \begin{cases} 1 & (r < r_\phi(t)), \\ \Phi & (r > r_\phi(t)). \end{cases} \tag{4.65}$$

This simplification allows us to directly integrate (4.16) upstream of r_ϕ to give

$$u = \frac{1}{r} \qquad (r < r_\phi(t)). \tag{4.66}$$

The governing equation (4.17) then simplifies to

$$\frac{\partial c}{\partial t} + \frac{\lambda}{r}\frac{\partial c}{\partial r} = \frac{1}{r}\frac{\partial}{\partial r}\left(r\frac{\partial c}{\partial r}\right) \qquad (r < r_\phi(t)), \tag{4.67}$$

with boundary conditions $c(0, t) = 1$ and $c(r_\phi, t) = 0$. The Stefan condition is

$$\dot{r}_\phi = -S_* \frac{\partial c}{\partial r}(r_\phi, t). \tag{4.68}$$

A scaling analysis of the system above reveals that the horizontal length scale in the system must scale as $r \sim t^{1/2}$, indicating that it supports similarity solutions of the form $c = c(\eta)$ with $\eta = t^{-1/2}r$. Recasting (4.67) in terms of these variables, we obtain the ordinary differential equation

$$\left(-\tfrac{1}{2}\eta^2 + \lambda\right) c' = \left(\eta c'\right)', \tag{4.69}$$

with boundary conditions

$$c(0) = 1, \qquad c(\eta_\phi) = 0, \qquad S_* c'(\eta_\phi) = -\tfrac{1}{2}\eta_\phi, \tag{4.70}$$

where η_ϕ is a free parameter to be determined. Equations (4.69)–(4.70) comprise a novel second-order similarity system describing a generalised Stefan problem allowing for both advection and diffusion of the reacting agent in a porous medium. The similarity solutions exist over a parameter space defined by two dimensionless numbers: the Péclet number λ and the effective Stefan number S_*. Owing to the uniformity of the porosity field in the region where the non-trivial transport occurs, the governing equation (4.69) is similar in form to that of the early-time transportive regime (4.33), with λ in place of Λ. The problem differs fundamentally in being subject to a Stefan condition with the solution existing over a finite domain $[0, \eta_\phi]$ with η_ϕ an unknown.

Integrating (4.69), we obtain

$$c' = -A\eta^{\lambda-1}e^{-\eta^2/4}, \tag{4.71}$$

where A is a constant. Integrating again subject to (4.70) and substituting $u = \eta^2/4$, we obtain the analytical solution

$$c = \frac{\displaystyle\int_{\frac{1}{4}\eta^2}^{\frac{1}{4}\eta_\phi^2} u^{\frac{1}{2}\lambda-1}e^{-u}\,\mathrm{d}u}{\displaystyle\int_{0}^{\frac{1}{4}\eta_\phi^2} u^{\frac{1}{2}\lambda-1}e^{-u}\,\mathrm{d}u} = \frac{I(\frac{1}{2}\lambda, \frac{1}{4}\eta^2, \frac{1}{4}\eta_\phi^2)}{I(\frac{1}{2}\lambda, 0, \frac{1}{4}\eta_\phi^2)}, \tag{4.72}$$

with function $I(a, b, c)$ defined by $I(a, b, c) = \int_b^c u^{a-1}e^{-u}\mathrm{d}u$, where η_ϕ satisfies the implicit algebraic equation

$$(\tfrac{1}{2}\eta_\phi)^{2-\lambda}e^{\eta_\phi^2/4}I(\tfrac{1}{2}\lambda, 0, \tfrac{1}{4}\eta_\phi^2) = S_*, \tag{4.73}$$

giving a relationship between the position of the porosity step η_ϕ, and the effective Stefan and Péclet numbers, S_* and λ.

To determine the solutions to (4.72)–(4.73), we first solve (4.73) using a numerical root finder `fsolve` and using the function `gammainc`, both from the python package `scipy` to evaluate $I(\frac{1}{2}\lambda, 0, \frac{1}{4}\eta_\phi^2)$. With η_ϕ in hand, we then evaluate (4.72) also using `gammainc`. Figure 4.11 presents both the profile $c(\eta)$ predicted by (4.72) and $\eta_\phi(\lambda)$ for selected S_*. In figure 4.11(a), we see that earlier observations of a convex concentration profile spanning the length of the flow remains characteristic of the diffusion-dominated limit of the Stefan problem. For large λ, the profile instead exhibits a steep *convex* sigmoidal profile with the

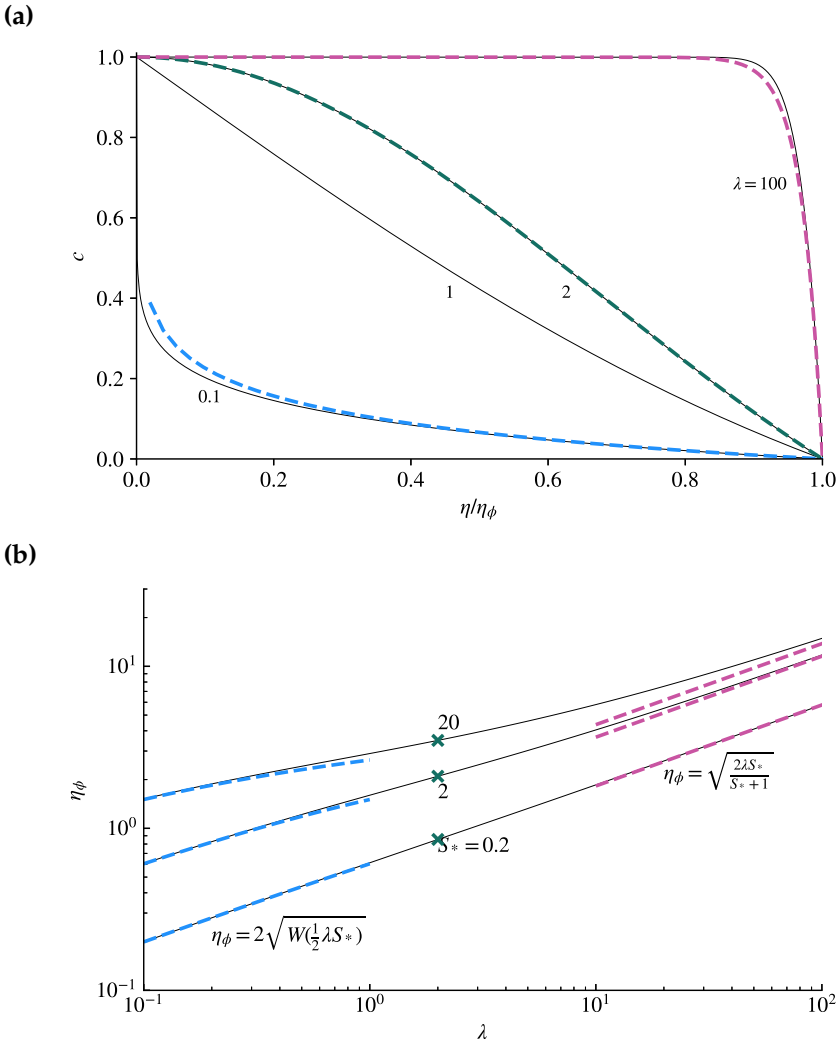

Figure 4.11: (a) concentration profiles for $\lambda = 0.1, 1, 2$ and 100 , and $S_* = 2$ by solving (4.72) and (b) η_ϕ plotted against λ for $S_* = 0.2, 2$ and 20 by solving (4.73). The solutions to (4.78), for the lower Péclet limit, are plotted on both (a) and (b) as blue dashed curves showing excellent agreement with the numerical solutions. The analytical solution to the sharp 1D regime is plotted as a pink dashed curve showing reasonable agreement at the nose ($\eta/\eta_\phi = 1$) in the $\lambda \gg 1$ limit (Appendix C). The exact solution (4.74) for $\lambda = 2$ is overlaid on (a) as a green dashed curve and on (b) indicated as green crosses for each S_* shown. The solutions to (4.83) for the high Péclet limit are overlaid as pink dashed curves on (b) showing agreement with the numerical results.

transition from $c \sim 1$ to $c(\eta_\phi) = 0$ localised close to the porosity transition.

Figure 4.11(b) shows the relationship between the position of the porosity transition η_ϕ and the Péclet number Λ for a selection of Stefan numbers $S_* = 0.2, 2$ and 20. The trends indicate a trend of increasing η_ϕ with λ, which is consistent with a larger mass flux of reactant producing a faster advancing reaction front. We also note the trend of increasing η_ϕ with S_* for given λ. At small Péclet , η_ϕ appears to take a non-power-law form and at large Péclet , η_ϕ takes a power law form of $\eta_\phi \propto \lambda^{1/2}$.

For $\lambda = 2$, there is an explicit analytical solution for all Stefan numbers given by

$$c = \frac{(1 + S_*)e^{-\frac{1}{4}\eta^2} - 1}{S_*}, \qquad \eta_\phi = 2\sqrt{\log(1 + S_*)}. \tag{4.74}$$

The result directly demonstrates the increase of η_ϕ with S_*, which is consistent with larger S_* resulting in relatively faster removal of solid volume as a result of the reaction. The prediction of (4.74) is indicated by green crosses in figure 4.11(b) at $\lambda = 2$ for the three values of S_* plotted, providing validation of the numerically evaluated predictions.

As defined earlier in (4.26), the total mass of reactant within the system is a useful diagnostic. The similarity form of this variable is defined by $M(t) = m(\lambda, S_*)t$, where

$$m = \int_0^{\eta_\phi} c(\eta)\eta \, \mathrm{d}\eta = \lambda - \frac{\eta_\phi^2}{2S_*}. \tag{4.75}$$

and the latter equality follows on noting that $\phi = 1$ between $[0, \eta_\phi]$ in the sharp theory, using the governing equation (4.69) in the form $\eta c = \left(\frac{1}{2}\eta^2 c - \lambda c + \eta c'\right)'$ to substitute for ηc in (4.75), and evaluating the boundary terms by applying the boundary conditions (4.70). Written this way we can clearly see the m has two constituent components: the input flux λ and a reactive consumption component.

The low Péclet number limit

For developing an asymptotic theory for low Péclet number, we begin by neglecting advection, for which the governing equation (4.30) reduces to

$$-\tfrac{1}{2}\eta^2 c' = (\eta c')'. \tag{4.76}$$

As for the low Péclet number theory of section 4.3.2, the near-source region will include a transitional layer through which the advective flux is converted to a diffusive flux over a small radius around the source. Thus, we can again replace the boundary condition $c(0) = 1$ in (4.31) by the matching condition $\lim_{\eta\to 0}(-\eta c') = \lambda$ to leading order. The full set of boundary conditions is then

$$\lim_{\eta\to 0}(-\eta c') = \lambda, \qquad c(\eta_\phi) = 0, \qquad S_* c'(\eta_\phi) = -\tfrac{1}{2}\eta_\phi. \tag{4.77}$$

The system (4.76)–(4.77) admits the analytical solution

$$c = \tfrac{1}{2}\lambda\left(E\left(\tfrac{1}{4}\eta^2\right) - E\left(\tfrac{1}{4}\eta_\phi^2\right)\right), \qquad \eta_\phi = 2\sqrt{W\left(\tfrac{1}{2}\lambda S_*\right)}, \tag{4.78}$$

where $E(z) \equiv \int_z^\infty u^{-1}e^{-u}\,\mathrm{d}u$ defines the exponential integral function, and $W(x)$ is the Lambert W-function defined as the solution to $We^W = x$. The prediction of (4.78) is shown as a blue dashed curve in figure 4.11(a). The prediction of η_ϕ in (4.78) is plotted for a selection of Stefan numbers $S_* = 0.2, 2$ and 20 as blue dashed curves in figure 4.11(b). Subsequently the prediction of the total reactant mass (4.75) becomes

$$M(t) = \lambda\left(1 - \frac{W(\frac{1}{2}\lambda S_*)}{\frac{1}{2}\lambda S_*}\right)t, \tag{4.79}$$

which is overlaid on figure 4.5(a) as a blue dashed curve showing agreement with the solution to the full model.

For large Stefan numbers, specifically $S_* \gg \lambda^{-1}$, the leading-order position of the porosity transition (4.73) simplifies to $\eta_\phi \sim 2\sqrt{\log(\lambda S_*/2)} \to \infty$ upon using the asymptote $W(x) \sim \log x$ as $x \to \infty$ [Abramowitz and Stegun, 1964]. This represents a regime in which the

concentration forms a Gaussian-like tail $c \sim 2\lambda\eta^{-2}e^{\frac{\eta^2}{4}}$. As a result of $\eta_\phi \to \infty$, upstream of the nose the interior of the flow approaches the purely transportive solution (4.41). For $S_* \ll \lambda^{-1}$, and noting that $W(x) \sim x$ as $x \to 0$, the nose $\eta_\phi \sim (2\lambda S_*)^{1/2}$ and $c \sim \lambda \log(\eta_\phi/\eta)$.

The high Péclet number limit

In considering this limit asymptotically, let us begin by writing the finite-interval gamma function in the form

$$I(\tfrac{1}{2}\lambda, a, b) = \int_a^b u^{\frac{1}{2}\lambda-1}e^{-u}\,\mathrm{d}u = \int_a^b g(u)e^{\psi(u)}\,\mathrm{d}u, \tag{4.80}$$

where $g(u) = 1/u$ and $\psi(u) = \frac{1}{2}\lambda \log u - u$. The above forms an integral of Laplace form [e.g. Bender and Orszag, 1978] for which the large-argument asymptotics ($\lambda \to \infty$) can be established using the techniques of Watson's lemma or Laplace's method, depending on whether the extremum of the function $\psi(u)$ over the integration interval $[a, b]$ lies on the boundary of the interval or interior to it (Appendix B).

The function $\psi(u)$ contains a local maximum where $\psi'(u_0) = \frac{1}{2}\lambda u_0^{-1} - 1 = 0$ given by $u_0 = \frac{1}{2}\lambda$. If $u_0 > b$, equivalent to $\eta_\phi < \sqrt{2\lambda}$, then the maximum u_0 lies exterior to the integration interval of (4.80), and hence the maximum of $\psi(u)$ within the integration interval lies on the boundary of the interval integration at $b = \frac{1}{4}\eta_\phi^2$. From Watson's lemma, it follows that the leading-order behaviour of the integral is given by a linearisation of the function $\psi(u)$ around the boundary point b, yielding the leading order expression

$$I(\tfrac{1}{2}\lambda, a, b) \sim g(b)\int_{-\infty}^b e^{\psi(b)+\psi'(b)(u-b)}\,\mathrm{d}u. \tag{4.81}$$

Evaluating the integral on the right-hand side, we obtain

$$I(\tfrac{1}{2}\lambda, a, b) \sim \left(\tfrac{1}{2}\lambda - b\right)^{-1} b^{\frac{1}{2}\lambda}e^{-b}. \tag{4.82}$$

Substituting $a = 0$ and $b = \eta_\phi^2/4$ into (4.73), and cancelling factors, we obtain the prediction

for the leading-order position of the porosity transition at large Péclet numbers,

$$\eta_\phi = \sqrt{\frac{2\lambda S_*}{1+S_*}}. \tag{4.83}$$

The result shows that the front advances proportionately to $\sqrt{\lambda}$, the Péclet number which is to be expected due to the fact that the fluid flux is proportional to $\sim \sqrt{\lambda}/r$. The front also advances proportionately to $\sqrt{\frac{S_*}{S_*+1}}$ revealing that in scenarios with low S_* the front moves relatively faster for given λ. This also reveals that there are two independent input controls on the front position in the regime. The result of (4.83) is plotted as a black dashed curve in figure 4.6(b), showing agreement in the relevant limit $\lambda \to \infty$.

Physically, we note that the property that $\eta_\phi < \sqrt{2\lambda}$ represents the physical requirement that the porosity transition occurs before the maximal extent of reactive transport. Mathematically, we note that, had we sought an asymptotic solution under the converse assumption that $u_0 < b$, then neither of the resulting asymptotic forms of I lead to consistent solutions for η_ϕ (Appendix B). The assumption of $u_0 > b$ is equivalent to $\eta_\phi < \sqrt{2\lambda}$, which we see is is self-consistent with the resulting solution (4.83).

The result of (4.83) is identical to the general asymptotic prediction of the quasi-1D regime (4.58). This equivalence applies because the quasi-1D theory approaches the sharp regime with time, corresponding to a regime in which both both the asymptotic properties of quasi-1D and sharp theory are satisfied concurrently. Knowing that the porosity tail at η_ϕ always lies behind the position $\sqrt{2\lambda}$, we consider the prediction of (4.72) in conjunction with (4.82) to yield $c(\eta)$ which is simply

$$c = 1, \qquad \eta < \eta_\phi, \tag{4.84}$$

describing a uniform concentration of unity upstream of η_ϕ to leading order.

4.3.6 General parameter-time regime diagram

A complete summary of the dimensional forms of our theoretical predictions is provided in table 4.2. Figure 4.12 provides an accompanying regime diagram illustrating the partitioning of the parameter space in terms of time and Péclet number λ. In the transportive

early regime, concentration is introduced into the domain with one of two characteristic appearances based on $\Lambda = \lambda/\Phi$, the effective Péclet number at early times, whilst porosity remains unchanged from its initial value $\phi \approx \Phi$. For large Λ the chemical is advected into the domain as a step function with extent controlled by the advective flux Q. For small Λ, the chemical is diffusively spread into the domain so the concentration remains $c \ll \lambda$ throughout the domain with extent controlled by diffusivity D. After a time $t_R \approx O(1)$, reaction intervenes and again, we see two different regimes emerge controlled by λ.

For $\lambda \ll 1$, the regime that emerges becomes sharp quickly, porosity is consumed entirely in the vicinity of the origin and develops a sigmoidal profile moving away from the origin, transitioning between $\phi = 1$ and $\phi = \Phi$ locally around a position. The concentration field varies over a region of roughly the scale $[0, r_\phi]$ and the regime is considered sharp by way of this delocalisation of the concentration field from the porosity transition.

For $\lambda \gg 1$, a quasi-1D regime emerges, wherein the concentration field set up by the transportive initial regime is localised as a sharp sigmoidal transition away from the origin. When reaction intervenes, the porosity is exhausted at the origin and begins to develop a sigmoidal profile which translates through the domain away from the origin. The porosity transition expands with a position proportional to the input flux Q and $t^{1/2}$. In this regime the concentration profile moves at the same rate as the porosity profile. The local extent of the concentration and porosity profiles is governed by the 1D travelling wave system (Chapter 3) at any given time, with time dependent $B(t)$. Owing to the properties of the travelling wave system, the initial quasi-steady regime exhibits *diffusionless* characteristics with small $B(t)$, and the concentration and porosity profiles vary over roughly that same length scale. As $B(t)$ grows the quasi-steady regime remains, but transitions towards a locally sharp front (Chapter 3). This occurs on a timescale t_S and at this time the sharpening of the reaction front over time develops in the (λ, t) space to yield an overlapping region, indicated in figure 4.12 in purple, where $t > t_S(\lambda)$ and $\lambda \gg 1$. At this time the quasi-1D theory becomes sharp and both the Stefan sharp regime and the quasi-1D theory are true.

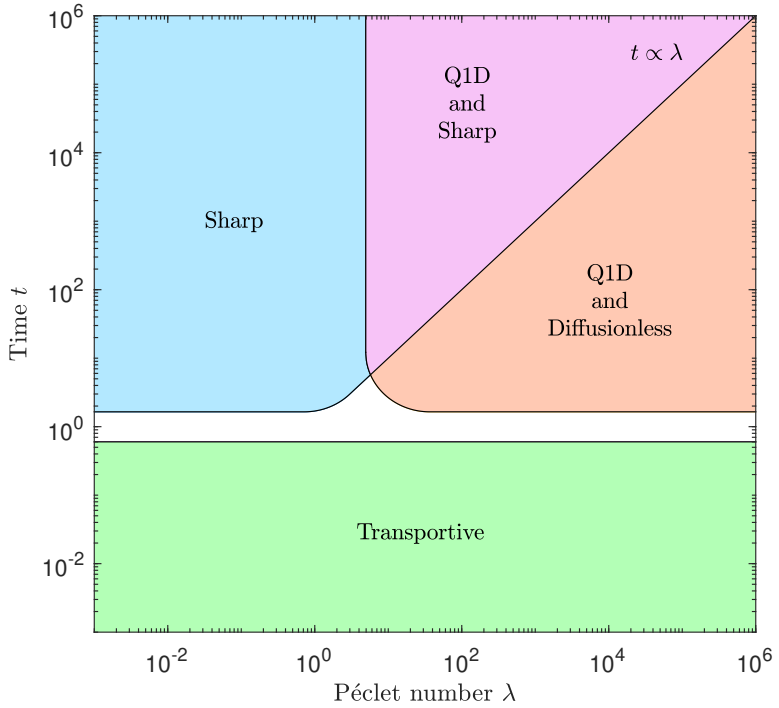

Figure 4.12: Schematic regime diagram illustrating the partitioning of the parameter space over (λ, t) where λ is a Péclet number defined as $\lambda = Q/(2\pi\phi_* D)$. Four primary regimes are represented by the early time transportive regime (green), the domain-scale sharp regime (blue), the quasi-1D (Q1D) and diffusionless regime (orange) and a regime where the quasi-1D (Q1D) and sharp regime overlap (purple) whose stability was previously studied by Grodzki and Szymczak [2019]; see text for further details (Regime diagram produced by Sam Pegler.)

<table>
<tr><th></th><th colspan="2">Small Péclet number</th><th>Large Péclet number</th></tr>
<tr><td>Early times</td><td colspan="2">$t \ll 1, (\Lambda \ll 1)$
$r_c = 2\sqrt{D \log\left(\frac{1}{\varepsilon}\right) t}$</td><td>$t \ll 1, (\Lambda \gg 1)$
$r_c = \sqrt{\frac{2Q}{\phi_0 \pi} t}$</td></tr>
<tr><td>Late times</td><td colspan="2">Sharp $t \gg 1, (\lambda \ll 1)$
$r_\phi \sim 2\sqrt{DW(\frac{1}{2}\lambda S_*)t}$</td><td>Quasi-1D $t \gg 1, (\lambda \gg 1)$
$r_c \sim r_\phi \sim \sqrt{\frac{QS_*}{\phi_* \pi (S_*+1)} t}$</td></tr>
<tr><td></td><td>$\lambda S_* \ll 1$
$r_\phi \sim (2D\lambda S_* t)^{1/2}$
$c \sim c_0 \lambda \log(r_\phi / r)$</td><td>$\lambda S_* \gg 1$
$r_\phi \sim 2\sqrt{D \log(\lambda S_*/2) t}$
$c \sim 2c_0 \lambda D t r^{-2} e^{\frac{r^2}{4t}}$</td><td>Diffusionless $1 \ll t \ll t_S$
$\Sigma \sim \min(1, S\nu^{-(1-m)})$

Sharp $t \gg t_S$
$\Sigma \propto \frac{b}{\zeta_\phi(\Phi)} \sqrt{\frac{(1+S_*)}{1} t}$</td></tr>
</table>

Table 4.2: Summary of the dimensional predictions of regimes of reaction fronts for the small Péclet number (left) , and the large Péclet number (right). Note that the early time behaviour is dependent on the effective Péclet number $\Lambda = \lambda/\Phi$ and the late time on the Péclet number λ; if $\Phi < \lambda < 1$, we observe large Péclet number early time behaviour followed by small Péclet number late time behaviour as the controlling porosity switches between Φ and 1 over time.

4.4 Summary & Discussion

Fundamentally we have discovered that in the radial geometry, the radial flux of reactant to the reaction front is not a parameter but a variable which evolves in time unlike in the 1D fronts we studied in Chapter 3. The consequence of this is that the ratio of diffusion to advection changes across the domain and controls the emergent reaction front dynamics. If advection is always small, the concentration profile remains pinned to the point source and spans the majority of the domain up to the porosity-front position. This sharp regime is inherently governed by radial dynamics. On the other hand, when advection is large enough, concentration of reactant is easily advected away from the point source. This means that the porosity and concentration profiles are locally controlled and as the radius increases, the front curvature becomes minimally important. The reaction front is quasi-1D. Further, the radial flux decays as the front radius increases and this leads to a change of balance between advection and diffusion. As this occurs, the reaction front transitions

from the diffusionless 1D dynamics (section 3.4.4) to the sharp 1D dynamics (section 3.4.2).

It is the sharp 1D dynamics, shown in figure 4.12 as a purple wedge, which have been previously explored by Grodzki and Szymczak [2019] as a basis for reactive infiltration to grow, in the small acid capacity S_* limit. The concentration field, which in the quasi-1D sharp regime reads

$$c = 1 - \exp\left((r - r_N)\frac{\lambda}{r_N(S_* + 1)}\right),$$

recovers their expression

$$c = 1 - \left(\frac{r}{r_N}\right)^{\lambda} \tag{4.85}$$

as used in their basic state, by taking $S_* \to 0$ and Taylor expanding the exponential, assuming $r - r_N$ is small.

4.5 Conclusions

In this Chapter, we have made three primary developments. First we have identified and mapped a succession of transient regimes preceding the final sharp similarity regime, including an initial transportive regime and a quasi-1D diffusive regime. Secondly we have shown that late time transient regime can be broadly partitioned into 2 overlapping regimes, depending on the Péclet number λ. Third we showed that in the large λ limit, given enough time, a sharp porosity interface can develop with minimal diffusive input. This is a marked departure from the 1D steady flux configuration studied in Chapter 3 where diffusion is critical to the development of sharp reaction fronts. This extends the current understanding of radial reaction fronts beyond the sharp quasi 1D model whose stability was investigated previously by Grodzki and Szymczak [2019] to include the early time dynamics, the inherently non-quasi 1D dynamics that arise for small λ, and the non sharp quasi 1D behaviour for large λ up to a transitional time scale.

We demonstrate how the 1D theory can emerge conditionally in a two-dimensional context, arising for large Péclet flows driven by the localisation of the concentration field which allows for a travelling wave expansion around a single transition radius as well as

bounding the parameter space in which it arises. Radial flow still matters, controlling the flux delivered into the transition region. However in the diffusive limit, the full radial structure becomes important for transport, with extent of concentration variation, l_c, being much larger than the extent of porosity variation l_ϕ. In the low Péclet limit, there are two asymptotic regimes: an early regime without the porosity step, and a late one with a porosity step.

Our results (table 4.2) provide a toolkit for predicting the dominant regime and transitional scales in practise.

The results of this work are based on idealised axisymmetric flows fed at a constant radial flux into a domain of uniform porosity, which may limit their general applicability to variable flux scenarios. For example, the axisymmetric solutions are unstable to the reaction-infiltration instability subject to a critical condition. In this context our solutions present either stable asymptotic states or can be used as basis states for linear stability analysis of reaction fronts fed by a point source. Other idealisations include the assumption of a rigid medium, with elastic or viscous response of the host material having the potential for new effects. A further generalisation of the model could include more complex reaction kinetics, as well as an allowance for more than one reactive agent in one or more components. There is thus significant scope for interesting new research directions based on these complications, for which the idealised axisymmetric case provides a theoretical foundation.

4.6 Contribution of this Chapter

This Chapter answers the following research questions:

Research Question 1
How do reaction fronts evolve in fundamental geometries?

This Chapter has studied the evolution of reaction fronts from an initially reactant-free medium with uniform porosity in the configuration of injection from a point source. For the first time, we present a detailed understanding of the timescales upon which ax-

isymmetric fronts transition from diffusion dominated through to their late time reaction fronts determined by the Péclet number λ. Critical to the radial geometry, we develop a mathematical understanding of the temporal regimes and the requirements that allow us to use the 1D dynamics for radial scenarios.

Research Question 3

How does a radially decaying flux influence reaction fronts versus a constant uniform flux?

In this Chapter we have addressed this question by developing an understanding of how reaction fronts driven by a locally injected source evolve. In particular, we find that the temporal evolution of such reaction fronts are controlled by the Péclet number λ. In the case of small λ, after an initially diffusive regime the reaction front enters a self similar reactive-diffusive regime in which the porosity front separates from the origin whilst the concentration front remains broad and spreads across the domain supplying reactant.

In the case of large λ, the initial regime is advective, before transitioning to a balanced advective-diffusive-reactive reaction front which is localised away from the origin in both porosity and concentration. Sufficiently far from the origin, the curvature of the reaction front becomes small and the reaction front locally recovers the 1D travelling wave theory in a quasi-steady manner. The novel parameter Ω, derived as a control on 1D fronts in Chapter 3, is an increasing function of time in this geometry and as such, the $\lambda \gg 1$ reaction fronts evolve towards sharp 1D dynamics in time.

4.6.1 Implications for geosciences

The governing parameter in radial reaction fronts is the Péclet number λ, which is the ratio of advective to diffusive transport. In geological environments advection can be arbitrarily large or small and as a consequence we would expect to see the full range of regime behaviours across the natural world. In appendix A, we calculate estimated values of λ for mantle flow, chemical weathering, salt dissolution and melting ice. We found that $\lambda \approx 10^{-2}$–10^{8} across these applications, all of which could arise in nature. We note that the exact conditions in which radial fronts would arise are not explored in this work.

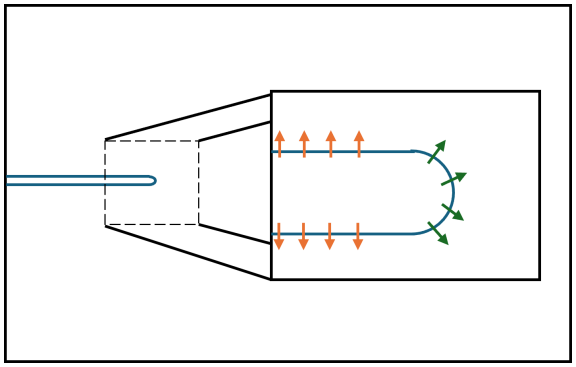

Figure 4.13: Schematic diagram of a crack tip showing the composite geometry which may. Regions of potential line-flux flow are indicated by orange arrows, and the region of radial flow is indicated by green arrows. The region between the two may have a combination of both resulting in a more complex flow behaviour.

Where a local source has produced a stable reaction front, we can use the observation of these regimes to understand the conditions under which it emerged. For example, the late time result of a sharp porosity transition irrespective of λ with concentration profile dependent on λ opens up the opportunity to analyse samples in view of this. Speculatively, it is possible that the new results of this Chapter in conjunction with the 1D analysis of Chapter 3 could be used to understand the generation of reaction fronts in the region of the tip of a fracture where the two geometries meet, which is depicted schematically in figure 4.13.

5

Reactive infiltration instability analysis of a planar reaction front: a quantitative application to geosciences

This Chapter presents an analysis of the linear instability of planar reaction fronts and conducts comparisons with geological observations. The instability of planar reaction fronts has been proposed as a driver of the growth of reactive fingers that are observed in geological media [e.g. Kelemen et al., 1995b]. Observations of finger like geological features are wide ranging, however there remain unanswered questions about the specific processes which control the formation of different geological features. In this Chapter, we begin to use the predicted preferred wavelength to understand where reactive infiltration may be responsible for these features. This Chapter is the basis of a paper being drafted for submission to the Geologist Magazine, under the working title *Reactive infiltration instability analysis of a planar reaction front: a quantitative application to geosciences*. The authors are D. Bullamore, S. Piazolo and S. Pegler.

5.1 Introduction

Across the natural world, there is often evidence of reactive fluid having flowed through a porous host and carved out fingers or channels within the host material. The evidence of this can be in the formation of karst topography [Merino and Banerjee, 2008, Szymczak and Ladd, 2011b], where there are holes in the medium at a range of scales caused by dissolution of the soluble rock; or in the presence of one particular, precipitated rock type which is different to the host rock, contributing to a mesoscale patterning of two types of rock. Fluid mechanically, these channels provide a 'path of least resistance' for the bulk transport of fluid between regions, when compared to the pervasive porous flow transport that is possible given the same material properties and pressure gradient. These channels may form due to any number of effects, such as brittle or ductile fracture of the host generating a void, or as we will study here by reactive flow.

Chapters 3 and 4 studied stable reaction fronts, in which porosity and concentration vary in only the imposed flow direction spatially and temporally. This Chapter relaxes the assumption of varying only in the flow direction to study how these steady reaction fronts evolve upon instability. This instability, driven by the reactive nature of the flow, can lead to the growth of fingers of preferential flow. Proposed by Chadam et al. [1986], Hinch and Bhatt [1990], Aharonov et al. [1995] amongst others, reactive infiltration instabilities are the generation of fingers caused by growing instability of planar flow fronts, focusing flow (and thus reaction) into localised features which result in concentrated regions of flow. Figure 5.1 shows a variety of patterns and relationships between reactive, reacted and unreacted components of geological features.

Earlier work such as Hinch and Bhatt [1990] was carried out in the diffusionless limit, motivated by industrial injection of acid into sandstone. In this work, the dispersion relationship is computed numerically. The characteristic profile in this limit is a positive growth rate for all wavenumbers m, approaching a maximum asymptotically as $m \to \infty$ which does not suggest a preferred wavelength but instead that the reaction front is unstable to all large wavenumber (small wavelength) instabilities. The work of Chadam et al. [1986] and subsequently Szymczak and Ladd [2011a] allow for diffusion of chemical

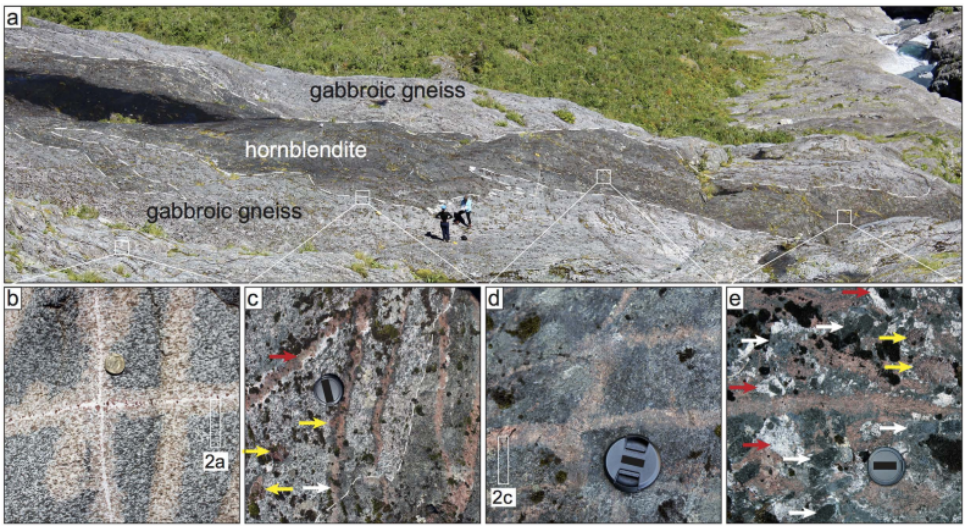

Figure 5.1: Figure demonstrating patterning found in regions of reactive fluid (now solidified hornblendite), with garnet reaction transition zones (GRT) in a host environment of gneiss. Features include (a) large O(10)m bodies of hornblendite, and then smaller features such as (b) grid pattern of melt veins with GRT zones, (c) Sharp interfaces of hornblendite and GRT, (d) grid pattern of garnierite within hornblendite. (Image Daczko et al. [2016])

species and study dissolution of a porous matrix in the small acid capacity limit.

We begin here by studying the linear stability of one asymptotic limit of the travelling wave 1D fronts explored in Chapter 3. We derive and present a general dispersion relation for fronts in the asymptotically sharp regime (derived in section 3.4.2) which relaxes the small acid capacity limit and reveals that the dispersion relation is fourth order. We use the dispersion relationship to quantitatively assess the occurrence of reactive infiltration instabilities in geological scenarios and present the dispersion relationship as a toolkit for understanding and comparing incidences of reactive infiltration in field observations. We show that the dispersion relation of Chadam et al. [1986] can be recovered in the small acid capacity limit of the dispersion relation and identify the strict asymptotic behaviour necessary for the validity of this dispersion relation. In the second half of this Chapter, we begin to use the dispersion relation as a tool for comparison of the theoretical prediction and observation of reaction fronts for five cases in geoscience. This is exploratory work which assesses whether the reactive infiltration instability, as modelled in this work, could be responsible for specific examples of patterning in geological media.

5.2 Stability of interfacial reaction fronts

This section details the 2D formulation of the sharp interface reaction front model. We consider the two-dimensional equations describing reactive dynamics of a fluid injected into a porous medium which generates a step in porosity. As defined in Chapter 2, the underlying governing equations are

$$\frac{\partial \phi}{\partial t} = kR(c, \phi), \tag{5.1}$$

$$\boldsymbol{\nabla} \cdot (\phi \boldsymbol{u}) = (\nu - 1)kR(c, \phi), \tag{5.2}$$

$$\frac{\partial (\phi c)}{\partial t} + \boldsymbol{\nabla} \cdot (\phi \boldsymbol{u} c) = \boldsymbol{\nabla} \cdot \left(D\phi \boldsymbol{\nabla} c \right) - c_R kR(c, \phi), \tag{5.3}$$

$$\phi \boldsymbol{u} = -\frac{\kappa}{\mu} \boldsymbol{\nabla} p, \tag{5.4}$$

For the general closure of the model we employ the permeability-porosity relation

$$\kappa = \kappa_0 \left(\frac{\phi}{\phi_0} \right)^n, \tag{5.5}$$

and a simple reaction model

$$R(c, \phi) = c f(\phi). \tag{5.6}$$

We adopt the same non-dimensional variables as given in section 3.2.2, with the addition of a pressure scaling for

$$x, y = \left(\frac{D}{U} \right) \hat{x}, \hat{y}, \quad t = \left(\frac{D}{U^2} \right) \hat{t}, \quad u = U\hat{u}, \quad c = c_0 \hat{c}, \quad \phi = \phi_* \hat{\phi}, \quad p = \frac{D\mu\phi_*}{\kappa_*} \hat{p}, \tag{5.7}$$

where $\kappa_* = \kappa(\phi_*)$ and μ is the fluid viscosity. Carrying out this scaling, dropping hats and translating the x co-ordinate into the frame of $z = x - Wt$, where W is the planar

reaction front speed yields the dimensionless system of equations:

$$-W\frac{\partial \phi}{\partial z} = BSR(c,\phi), \tag{5.8}$$

$$\boldsymbol{\nabla}\cdot(\phi \boldsymbol{u}) = (\nu-1)BSR(c,\phi), \tag{5.9}$$

$$-W\frac{\partial(\phi c)}{\partial z} + \boldsymbol{\nabla}\cdot(\phi \boldsymbol{u} c) = \boldsymbol{\nabla}\cdot\left(\phi \boldsymbol{\nabla} c\right) - BkR(c,\phi), \tag{5.10}$$

$$\phi \boldsymbol{u} = -\boldsymbol{\nabla} p, \tag{5.11}$$

We further specialise to the case of a sharp porosity interface at a position z_F (figure 5.2), and now the set of governing equations (5.8)–(5.11) are transformed as follows. The governing equation (5.10) reads

$$\frac{\partial c}{\partial t} - W\frac{\partial c}{\partial z} + \kappa_u \boldsymbol{\nabla} p \cdot \boldsymbol{\nabla} c = \boldsymbol{\nabla}^2 c, \qquad z < z_F, \tag{5.12}$$

forming an advection-diffusion equation describing the transport of fluid upstream of the porosity interface, we apply the boundary conditions,

$$c(z_F,t) = 0, \qquad \lim_{z\to-\infty} c \to 1. \tag{5.13}$$

Darcy's law reads

$$\phi \boldsymbol{u} = -\hat{\kappa}(\phi)\boldsymbol{\nabla} p \tag{5.14}$$

and Laplace's equation for pressure, arising from (3.2)

$$\nabla^2 p = 0 \qquad (z < z_f, \quad z > z_F) \tag{5.15}$$

holds on either side of the interface z_F but not across it. Pressure is continuous throughout the domain, with a jump in gradient at the interface $z = z_F$, to be given below. The porosity interface is defined by

$$\phi = \begin{cases} 1 & (z < z_F), \\ \\ \Phi & (z > z_F), \end{cases} \tag{5.16}$$

with the position $z_F(y,t)$ being the interface position. The front position $z = z_F(y,t)$ is

defined by the surface function

$$f = z - z_F(y,t), \tag{5.17}$$

where $f = 0$ on the front and the normal direction to the surface is thus

$$\boldsymbol{f}_N = \frac{\boldsymbol{\nabla} f}{|\boldsymbol{\nabla} f|}. \tag{5.18}$$

At the interface, we derive the 2D Stefan condition defining the interface velocity by conservation of chemical species in a pillbox which is parallel to the interface, [cf. Chadam et al., 1986]

$$\boldsymbol{f}_N \cdot \left(\frac{\partial \boldsymbol{z}_f}{\partial t} + W\hat{\boldsymbol{z}} \right) = -S_* \boldsymbol{f}_N \cdot \boldsymbol{\nabla} c. \tag{5.19}$$

The procedure for deriving this is the same as deriving equation (C.4) of Appendix C, with alterations including the addition of the interface normal vector $\boldsymbol{f}_N$ and the translation of the front to the z frame. The jump in pressure gradient, arising from conservation of fluid across the interface, is given by

$$\kappa_u \nabla p_u = \kappa_d \nabla p_d - \Delta \left(\frac{\dot{z}_F}{W} + \hat{\boldsymbol{z}} \right), \tag{5.20}$$

describing the jump in ∇P across the interface, where $\Delta = (1-\nu)(1-\Phi)W$. The permeabilities κ_u and κ_d are those of the upstream and downstream regions respectively. Assuming constant flux at the inlet boundary, the boundary conditions on the inlet pressure are given by

$$\kappa_u \nabla p = -1, \qquad p = P_0, \qquad (z = -Wt). \tag{5.21}$$

Now that we have the 2D governing system, we can study the stability of the 1D travelling wave by perturbing the 1D solution by a small amount, with dependence on z, y, t where z, y are the spatial co-ordinates and t is time. This is summarised in figure 5.2, the left panel of which shows a uniform 1D solution which is stationary in the z frame with the front depicted at $z = 0$. The right panels shows the perturbed 2D form, in which a sinusoidal perturbation may begin to grow, subject to the necessary conditions on parameters which will be sought here.

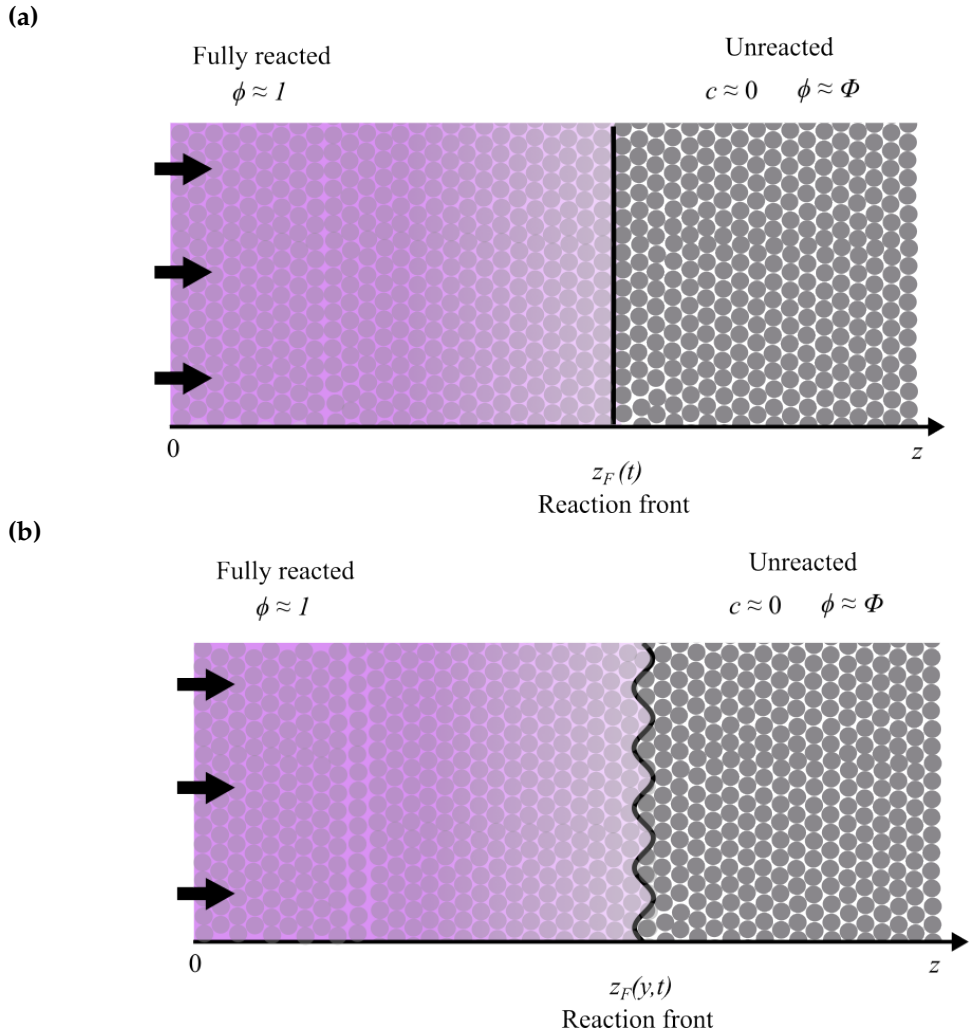

Figure 5.2: Schematic diagram of (a) a sharp interface 1D planar travelling wave, and (b) the growth of a linear instability from the 1D travelling wave.

The 1D basic state

The 1D state for concentration and porosity, derived earlier in section 3.4.2, for front location $z_F = 0$, reads

$$c_0 = 1 - e^{(1-W)z}, \quad z < 0 \tag{5.22}$$

$$\boldsymbol{z}_{F,0} = 0\mathbf{e}_z \tag{5.23}$$

$$\phi = \begin{cases} 1 & z < 0 \\ \Phi & z > 0. \end{cases} \tag{5.24}$$

The 1D pressure field, satisfying (5.14) and (5.15) is given by

$$p_{0,u} = P_0 - \frac{1}{\kappa_u}(z + Wt), \qquad (z \leq 0) \tag{5.25}$$

$$p_{0,d} = P_0 - \frac{1}{\kappa_u}Wt - \frac{1-\Delta}{\kappa_d}z, \qquad (z \geq 0) \tag{5.26}$$

a piecewise combination of the linear $p_{0,u}$ and $p_{0,d}$ which apply upstream and downstream respectively.

5.2.1 The perturbation equations

We perturb the basic states (5.22)–(5.26) by a small amount, $c_1(z, y, t)$, $p_{1,u}(z, y, t)$ and $p_{1,d}(z, y, t)$, and z_F by $z_{F1} = z_{F1}(y, t)\hat{\mathbf{z}}$. Substituting these into (5.12)–(5.20) and assuming small perturbations which allow us to discard any terms that are second order in the perturbation amplitude, we obtain

$$\frac{\partial c_1}{\partial t} - W\frac{\partial c_1}{\partial z} + \frac{\partial c_1}{\partial z} - \kappa_u \frac{\partial p_{1,u}}{\partial z}\frac{\partial c_0}{\partial z} = \frac{\partial^2 c}{\partial z^2} + \frac{\partial^2 c}{\partial y^2}, \qquad (z \leq 0), \tag{5.27}$$

$$\frac{\partial^2 p_{1,u}}{\partial z^2} + \frac{\partial^2 p_{1,u}}{\partial y^2} = 0, \qquad (z \leq 0), \tag{5.28}$$

$$\frac{\partial^2 p_{1,d}}{\partial z^2} + \frac{\partial^2 p_{1,d}}{\partial y^2} = 0, \qquad (z \geq 0), \tag{5.29}$$

$$\frac{\partial z_{F1}}{\partial t} + S_*(\frac{\partial c_1}{\partial z} + z_{F1}\frac{\partial^2 c_0}{\partial z^2}) = 0, \qquad (z = 0). \tag{5.30}$$

The equations (5.27)–(5.29) form a system of three coupled PDEs which describe the perturbations of pressure and concentration throughout the domain, and (5.30) is a perturbed boundary condition on the interface z_F. The boundary conditions on the system (5.27)–(5.29) are linearised to read

$$p_{1,u} \to 0, \quad z \to -\infty, \tag{5.31}$$

$$p_{1,d} \to 0, \quad z \to \infty, \tag{5.32}$$

$$p_{1,u} - p_{1,d} = (p'_{0,d} - p'_{0,u})z_{F1}, \quad z = 0, \tag{5.33}$$

$$c_1 \to 0, \quad z \to -\infty, \tag{5.34}$$

$$c_1 + c'_0 z_{F1} = 0, \quad z = 0. \tag{5.35}$$

We assume the ansatz form of the perturbations,

$$c_1 = \delta e^{\sigma t} \cos(my) C(z), \qquad p_{1,u} = \delta e^{\sigma t} \cos(my) P_u(z),$$
$$p_{1,d} = \delta e^{\sigma t} \cos(my) P_d(z), \qquad z_{F1} = \delta e^{\sigma t} \cos(my).$$

Substituting the above into (5.27)–(5.30) we obtain the ordinary differential system given by,

$$\sigma C(z) - WC'(z) + C'(z) + \kappa_u(1-W)e^{z(1-W)}P'_u(z) = C''(z) - m^2 C(z), \tag{5.36}$$

$$P''_u(z) - m^2 P_u(z) = 0, \tag{5.37}$$

$$P''_d(z) - m^2 P_d(z) = 0, \tag{5.38}$$

$$\sigma + S_*(C'(0)_{z=0} - (1-W)^2) = 0. \tag{5.39}$$

The boundary conditions on the perturbations thus become the conditions:

$$P_u \to 0, \quad z \to -\infty, \tag{5.40}$$

$$P_d \to 0, \quad z \to \infty, \tag{5.41}$$

$$P_u - P_d = (p'_{0,d} - p'_{0,u})\delta, \quad z = 0, \tag{5.42}$$

$$\kappa_u P'_u - \kappa_d P'_d = \frac{\Delta\sigma}{W}, \quad z = 0, \tag{5.43}$$

$$C \to 0, \quad z \to -\infty, \tag{5.44}$$

$$C = (1 - W), \quad z = 0. \tag{5.45}$$

Solving equation (5.37) and (5.38), we obtain the pressure fields in the upstream and downstream regions,

$$P_u = \alpha_1 e^{|m|z} + \alpha_2 e^{-|m|z}, \tag{5.46}$$

$$P_d = \alpha_3 e^{|m|z} + \alpha_4 e^{-|m|z}, \tag{5.47}$$

where $\alpha_1, \alpha_2, \alpha_3$, and α_4 are constants of integration. The boundary conditions (5.40) and (5.41), requiring the decay of the perturbations in the far field give $\alpha_3 = \alpha_2 = 0$. The boundary conditions on the interface (5.42) and (5.43) give

$$\alpha_1 - \alpha_4 = \frac{(\Delta + \beta - 1)}{\kappa_d}, \tag{5.48}$$

$$\alpha_1 = -\beta\alpha_4 - \sigma\frac{\Delta}{\kappa_u|m|W}, \tag{5.49}$$

where $\beta = \kappa_d/\kappa_u$ the ratio of permeability downstream and upstream of the interface. An underlying assumption in this work is that reaction increases porosity, so the value of β is constrained $0 < \beta < 1$. Thus, we obtain

$$\alpha_1 = -\left(\frac{\sigma\Delta}{\kappa_u|m|(1+\beta)W}\right) + \frac{\beta(1-\Delta-\beta)}{(1+\beta)\kappa_d}, \quad \alpha_4 = -\left(\frac{\sigma\Delta}{\kappa_u|m|(1+\beta)W}\right) - \frac{(1-\Delta-\beta)}{(1+\beta)\kappa_d}. \tag{5.50}$$

Integrating (5.36), we obtain the perturbation to the concentration field,

$$C = \alpha_5 e^{k_1 z} + \alpha_6 e^{k_2 z} + (1 - W)m\alpha_* e^{(m+1-W)z}, \tag{5.51}$$

with integration constants α_5 and α_6 where

$$k_{1,2} = \frac{1-W}{2}\left(1 \pm \sqrt{4\frac{(\sigma+m^2)}{(1-W)^2}+1}\right), \tag{5.52}$$

and

$$\alpha_* = \frac{(1-\Delta-\beta)+\frac{\sigma\Delta}{Wm}}{(\sigma-(1-W)m)(1+\beta)}. \tag{5.53}$$

The front velocity $W = S_*/(1+S_*)$ is strictly bounded $W < 1$ as $S_* > 0$ and as a consequence we can say that the exponential of k_2, the negative valued root must have a pre-factor $\alpha_6 = 0$ to satisfy (5.44) in the $z \to -\infty$ limit. Applying the boundary condition (5.45) for α_5 yields

$$\alpha_5 = (1-W)\,(1-m\alpha_*)\,, \tag{5.54}$$

which we can substitute into (5.39) for the full dispersion relationship

$$\frac{\sigma}{S_*}-(1-W)^2+\frac{(1-W)^2}{2}\,(1-m\alpha_*)\left(1+\sqrt{4\frac{(\sigma+m^2)}{(1-W)^2}+1}\right)+(1-W)m\alpha_*(m+1-W)=0. \tag{5.55}$$

Substituting back in the definition of α_* (5.53) yields the complete dispersion relation,

$$\begin{aligned}\left(\frac{\sigma}{S_*}-(1-W)^2\right)&(\sigma-(1-W)m)(1+\beta)\\ &+\frac{(1-W)^2}{2}\left(1-m\left((1-\Delta-\beta)+\frac{\sigma\Delta}{Wm}\right)\right)\left(1+\sqrt{4\frac{(\sigma+m^2)}{(1-W)^2}+1}\right)\\ &+(1-W)m\left((1-\Delta-\beta)+\frac{\sigma\Delta}{Wm}\right)(m+1-W)=0.\end{aligned} \tag{5.56}$$

The equation (5.56) is, to our knowledge, the first time the full variable Ω dispersion relation has been written down. The inclusion of the time derivative of concentration (5.12) gives rise to all but the first σ in (5.56), a marked difference from Chadam et al. [1986].

The implicit equation for growth rate σ depends on the permeability ratio β, the travelling wave speed W, the wavelength of perturbation m, and Δ the change in flux due to reaction. We can see by eye that this dispersion relation takes a similar functional dependence of

σ on m as that derived by Chadam et al. [1986] and repeated earlier in section 2.3.1. The coefficients of m and $\sqrt{1+4(\sigma+m^2)/(1-W)^2}$ here are functions of σ, reflecting the generalisation of the model away from the quasi-steady concentration profile derived in Chadam et al. [1986].

The equation (5.56) can be rearranged to form a 4th order polynomial for σ, yielding four potential growth rates for each parameter set including potentially complex growth rates. The study of each of these roots in turn and their implications for the problem at hand are beyond the scope of this work, nonetheless forming an interesting problem to be studied. At this point, we elect to take the limit of small σ in order to begin to analyse the behaviour of (5.56).

5.2.2 The small growth rate limit

In order to understand the primary behaviour of (5.56) it is instructive to take the limit of small σ, more specifically of $\sigma \ll (1-W)m, m^2$. As a result, we can neglect all but the first σ in (5.56) to, with some rearrangement, yield

$$\frac{\sigma}{W} = \left(\frac{(1-\Delta-\beta)}{(1-W)(1+\beta)}\right) m + \left(1+\frac{(1-\Delta-\beta)}{(1-W)(1+\beta)}\right)\frac{1-W}{2} - \left(1+\frac{(1-\Delta-\beta)}{(1-W)(1+\beta)}\right)\left(\sqrt{(m^2)+\frac{(1-W)^2}{4}}\right), \tag{5.57}$$

and we now define a new collection of parameters $\gamma = (1-\Delta-\beta)/(1+\beta)$. The parameter γ includes the contributions of both permeability ratio β and change in fluid flux Δ to the instability. We can then rewrite (5.57) for the simplified form

$$\sigma = \frac{W}{1-W}\left(\gamma m + (1-W+\gamma)\frac{1-W}{2} - (1-W+\gamma)\sqrt{(m^2)+\frac{(1-W)^2}{4}}\right), \tag{5.58}$$

which we can begin to manipulate to understand the conditions under which instability grows. Figure 5.3 demonstrates the characteristic shape of σ as a function of m for selected W, γ.

Recovering the results of Chadam et al. [1986] As outlined in section 2.3.1, the prior work of Chadam et al. [1986] produces a dispersion relation in the large solid density and small acid capacity limit which reads

$$\sigma = \frac{2}{(1+\beta)(1-\Phi)}(\alpha + (1-\beta)|m| - \sqrt{4m^2+\alpha^2}), \tag{5.59}$$

where $\alpha = -c_0' = (1-W)$. Our dispersion relation (5.58) is clearly of the same form as (5.59), aside from the generalisation of $\Delta \neq 0$, and $1 - W \neq 1$. Taking these two limits, we obtain

$$\sigma = \left(\frac{S}{(1-\phi)(1+\beta)}\right)\left(\left(1-\beta\right)m - \left(\sqrt{4(m^2)+(1-W)^2}\right) + (1-W)\right), \tag{5.60}$$

which is identical, subject to rescaling, to that presented in Chadam et al. [1986].

5.2.3 The large m asymptote

In order to understand the behaviour of σ as m varies, figure 5.3 plots σ against m for fixed W and varying γ as indicated. We note that γ is dependent on W, however this choice is made because the prefactors of W in the form of γ are $(1-\phi)(1-nu)$ which are typically small and here we are interested in the relationship between σ and m. In figure 5.3 we see that the growth rate approaches a linear function of m as m increases, which is found by considering the behaviour of (5.58) as $m \to \infty$ to yield the asymptote,

$$\sigma \sim W\left(\frac{1-W+\gamma}{2} - m\right), \tag{5.61}$$

which is overlaid as pink dashed curves in figure 5.3 for each case shown, demonstrating good agreement.

5.2.4 The maximum growth rate

The dimensionless maximum growth rate is calculated by first differentiating (5.58) to yield

$$\frac{1-W}{W}\frac{\partial\sigma}{\partial m} = \gamma - \frac{(1-W+\gamma)\,m}{\left(\sqrt{m^2+\frac{(1-W)^2}{4}}\right)}, \tag{5.62}$$

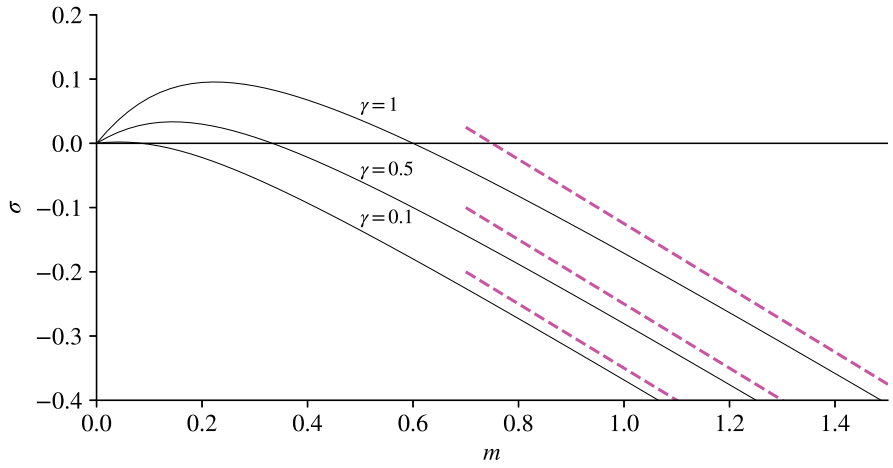

Figure 5.3: Plot of growth rate (5.57) against wavenumber m for $\gamma = 0.1, 0.5, 1$ as indicated, with fixed $W = 0.5$. The large m asymptote (5.59) is overlaid for each case as a pink dashed line, showing reasonable agreement as $m \gg 1$. Note that W and γ weakly covary, but W is fixed here for illustrative purposes.

for which the local maximum is found for $m = m_*$ defined as

$$m_* = \frac{\gamma}{2\sqrt{\left(1 + \frac{2\gamma}{1-W}\right)}}. \tag{5.63}$$

The corresponding σ_* is given by

$$\sigma_* = \frac{W}{2}\left(1 - W + \gamma - \sqrt{(1-W)(1-W+2\gamma)}\right). \tag{5.64}$$

Figure 5.4 plots (a) m_* and (b) the corresponding σ_* against β for $W = [0.1, 0.5, 0.9]$ respectively. Figure 5.4(a) shows that the optimal wavenumber m_* is an decreasing function of β for all W and that it is also a decreasing function of W, which we can see as well in the form of (5.63). Typically $0 < \beta < 1$ as this is reflects the assumption that reaction increases permeability, which constrains $0 < m_* < 1/2\sqrt{3}$. The corresponding maximum growth rate, σ_*, plotted in figure 5.4(b), is an increasing function of W.

Critical condition for stability A reaction front is unstable if there exists a wavenumber and growthrate (m, σ) for which $\sigma > 0$. In the case of our dispersion relation (5.57), the critical condition for this is $\gamma = 0$, at which m_* the fastest growing wavenumber has

(a)

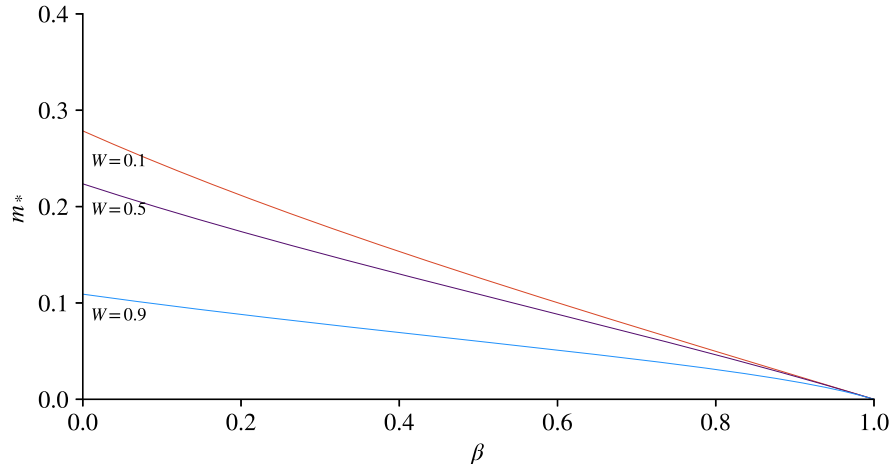

(b)

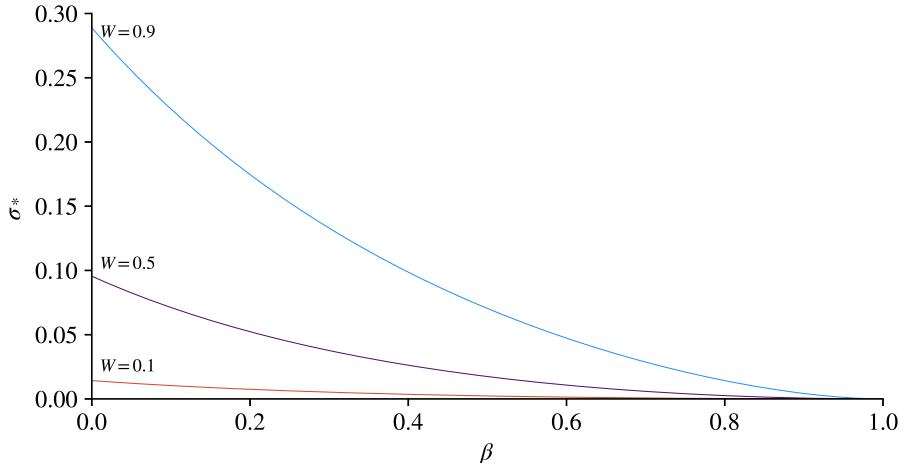

Figure 5.4: (a) Preferred wavenumber m_* and (b) corresponding maximum growth rate σ_* against β for $W = 0.1, 0.5, 0.9$ and $\nu = 1$.

growth rate $\sigma_* = 0$. Given the definition of γ, stability is governed by the value of

$$\frac{\kappa_d}{\kappa_u} + (1-\nu)(1-\Phi)W, \tag{5.65}$$

where

$$\frac{\kappa_d}{\kappa_u} + (1-\nu)(1-\Phi)W \quad \begin{cases} \geq 1 & \text{stable,} \\ < 1 & \text{unstable.} \end{cases} \tag{5.66}$$

Thus, stability could arise if this function is greater than one. This would occur only if the permeability increase due to reaction is small enough ($\beta \approx 1$) and if the production ratio $\nu > 1$, such that the second term of the left hand side is negative. This is largely impractical as this term is the product of $(1-\nu)$ and two other parameters which are $O(10^{-1})$ in most circumstances, hence the reactive infiltration instability is practically always unstable in the interfacial regime. In the case of $\Delta \to 0$, instability is automatic.

5.3 Quantitative evidence of the reactive infiltration instability in geological settings

In this section, we consider geological scenarios in which the reactive infiltration instability could explain the growth of fingers and use the relationship derived for m_* to consider whether our model can predict reactive infiltration instability in these scenarios at the wavelength they are observed. The scenarios we will consider are the size of features generated by both melt and hydrous flow in the lithosphere and in experiments. We note that in the field, there is a challenge to constrain the parameters which control flow and therefore all estimates in this section ought to be taken as order of magnitude approximations, rather than precise calculation. The use of the preferred wavenumber m_* to assess these scenarios has significant limitations, as instability is generated by non-linear interactions which are likely to evolve beyond the scope of the linear stability predictions due to competition between fingers [e.g. Szymczak and Ladd, 2006]. Further work will be necessary to constrain the parameters used to predict wavenumber m_* for field observation, in order to ascertain whether the reaction infiltration instability alone

can explain these features.

One example of features thought to derive from melt-based reactive infiltration instabilities are tabular dunites, composed of solidified pure olivine, which are the remnants of the high porosity solid through which melt may have flowed in the upper mantle [Braun and Kelemen, 2002]. Another scenario in which melt flow may be responsible is in the reaction fronts observed in geological samples found in New Zealand, where flow from the sides of a vein, or dyke, has driven reaction in the porous host. We also consider the pattern formation in experimental work carried out with both melt and hydrous fluid infiltration of a prepared sample [Pec et al., 2017, Koehn et al., 2021].

What is universal to these scenarios is a fluid flowing through a porous crystalline host rock and reacting with that rock leading to the transfer of material between the two phases. This transfer of material leaves a measurable reaction front between the initial and reacted host materials. In order to calculate dimensional preferred wavelengths for scenarios, we need to approximate the parameters of flow. The non-dimensional wavenumber m_* (5.63) can be converted to wavelength λ_* and presented in dimensional units, multiplying by the length scaling D/U (section 4.2.2) to yield

$$\lambda_* = \frac{4\pi D\sqrt{1+2\frac{\gamma}{1-W}}}{\gamma U}. \tag{5.67}$$

The dimensional timescale of instability, the inverse of σ_* (5.64), is given by

$$t_* = \frac{D}{U^2\sigma_*} = \frac{2D}{WU^2(1-W+\gamma-\sqrt{(1-W)(1-W+2\gamma)}}. \tag{5.68}$$

Firstly, let us consider what wavelengths of instability would be observable in a geological sample. In our idealised model, the grain scale is assumed to be much smaller than the Darcy scale and thus the wavelength of instability. In applying our results, we must consider the predicted wavelength relative to the grain or pore scale of the porous medium, g, and also the geometric scale of the sample, denoted as L.

If $\lambda_* \ll g$ then the model predicts fastest growing modes that are much smaller than the grain scale. A consequence of this is that fingers are unobservable due to being smaller

than the grain scale. We speculate that this would present as mixing across the interface rather than fingers. If $g < \lambda_* < L$, we would expect to see fingers of the appropriate wavelength as the model predicts. If λ_* is in the range of being observable by eye, indeed we would expect to see them by eye. If λ_* is smaller than we can see by eye, then fingers could be observed if facilitated by microscopy.

Finally, if $\lambda_* > L$ the sample itself is smaller than, or on the scale of, one such finger. In this instance the interaction of the fluid flow being constrained by sample size would be likely to interfere with the instability. Summarily, although mathematically reaction fronts are always unstable to reactive infiltration instability, we can use λ_* and knowledge of the scales of the physical system being studied to say whether or not we would expect to observe reactive infiltration instability fingers. Table 5.1 outlines 5 exemplar geoscience examples of reaction fronts, with some instability, which we will now discuss in turn. Broadly the first separation of these cases is into type 1 (aqueous) and type 2 (melt), delineating the fluid that generated the reaction front. The cases are then sorted alphabetically by type: field observations and then experimental studies.

	Source	λ_* predicted (m)	λ (m) measured
Case 1: Hydrous flow			
1A: Reaction Rim in the field	Piazolo [2025]	3×10^{-6}–10^{-4}	0, and 0.5–1×10^{-2}
1B: Experimental and numerical infiltration	Koehn et al. [2021]	1.3–2.6×10^{-4}	1.2–2.6×10^{-4}
Case 2: Melt flow			
2A: Infiltration from a melt vein	Piazolo [2025], Daczko and Halpin [2009]	0.5–5×10^{-2}	2.6–3.0×10^{-2}
2B: Dunite channels in the field	Piazolo [2025]	0.5–50×10^{-2}	3–10×10^{-2}
2C: Experiments in melt infiltration	Pec et al. [2017]	$O(10^{-6})$	1–5×10^{-3}

Table 5.1: Cases of potential reaction infiltration fingers in geoscience. Type 1 cases are generated by the flow of hydrous fluids, type 2 are generated by the flow of melt. Here for summary we report the predicted range of wavelengths by our model, and the range of measured wavelengths in the sample.

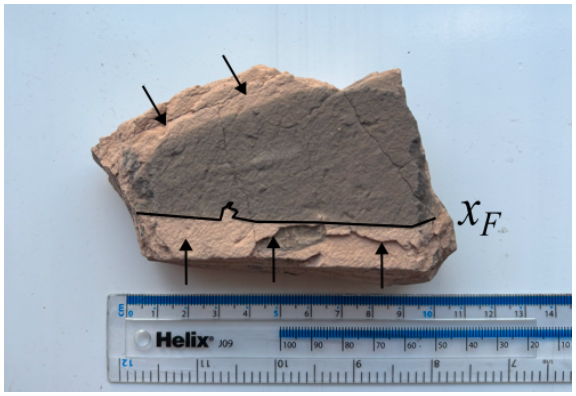

Figure 5.5: Image of a rock sample which features a reaction front generated by hydrous flow. (The rock is a sample of mudstone from Cyprus. Brittle fractures along the edges of this sample provide access for fluid which then flows into the rock fabric perpendicular to the fractures (indicated with black arrows). The reaction front is located at the interface between the two colours of rock, the reaction front at the bottom of this image is overlined in black. The reaction front is broadly smooth at the scale of the grain size (sub-mm), there is one particular deviation with wavelength 0.5 – 1 cm.

5.3.1 Case 1A: Hydrous flow in the geological setting

Hydrous dissolution of rocks such as limestone has long been thought to explain the existence of caves in Karst topography, having been proposed as early as the 1830s in the works of Lyell and Thirria [Klimchouk et al., 2000]. Despite early work, [White and Longyear, 1962] suggesting that the existence of caves could not be explained by dissolution as they ought to be arrested on the order of cm, several calculations in the 1990s such as those by [Groves and Howard, 1994] have shown that the dissolution of large amounts of rock (leading to a deep conduit) is possible. These early works studied the one dimensional dissolution of limestone however more recently, Szymczak and Ladd [2011b] performed analysis which focused on the case of dissolution by ground water which enters limestone at a single fracture and predicted that the reactive infiltration instability could generate fingers at the scale of karst topography. Their work studied went on to study the non-linearity of the fingers that form in this geometry.

In this work, we instead look at an example of hydrous fluid in crustal rock which does not give rise to caves but to a change in host material composition as fluid flows through it. Figure 5.5 shows a field example of a reaction front driven by aqueous fluid, which changes the colour of the host material from grey to pink as it reacts. We do not know

many parameters about this scenario, but we expect that the initial and final porosity are low. We generate a prediction of the expected wavelength of instability by assuming that porosity is doubled by reaction, increasing the permeability 4-fold ($\beta = 0.25$), and that $W \ll 1$ i.e. the reaction front advances much slower than the fluid flow [Piazolo, 2025]. These combine to yield $m_* = 0.20$. The diffusivity of minerals in water is $O(10^{-9})$ m^2 s^{-1} [Zhang, 2010] and we would expect hydrous flow to occur around $U \approx 0.1 - 10 \times 10^{-5}$ m s^{-2} [Koehn et al., 2021]. These parameters predict instability of wavelength $\lambda_* \approx 3 - 300$ μm, which is clearly below the scale on which we can expect to see instability by eye. For some samples, this may also be on the scale of the pores of the host. The fact that the instability is of this small size could explain why we see fingers in experiments with coarse grains but not in fine grains in the field. There is a small intrusion of the altered rock beyond the smooth reaction front we see in figure 5.5 (labelled), which could be attributed to heterogeneity in the initial composition of the sample making flow in this area preferential. The wavelength of this finger is plotted in figure 5.7 showing that this does not seem to be a reactive infiltration finger.

5.3.2 Case 1B: Hydrous fluid flow in crustal rock: modelling and experiments

Hydrous fluids flowing in crustal rock have important implications for reservoir development, ore formation and weathering [Koehn et al., 2021]. In prior work, Koehn et al. [2021] carried out experiments and numerical modelling to understand the parameters controlling the emergence of reaction front roughness in hydrous flow. This work divides the reaction fronts that emerge into categories of 'smooth', 'irregular' and 'rough' fronts. This work simulates the infiltration of a square of granular aggregate by a fluid with concentration c at constant fluid flux along the boundaries. The reactant c is consumed as the reaction progresses and the evolution of the concentration distribution in the fluid is the measure of 'reaction'. Their numerical modelling considers a porous medium consisting of a network of porous grains and higher permeability grain boundaries and the fronts are categorised as smooth, irregular or rough. In the framework of this work, the three categories mean the following: 'smooth' means that the reaction front is approximately planar and moves through the grains, 'irregular' means that the reaction front is not planar and has fingers emerging on the porous scale; and finally 'rough' means that

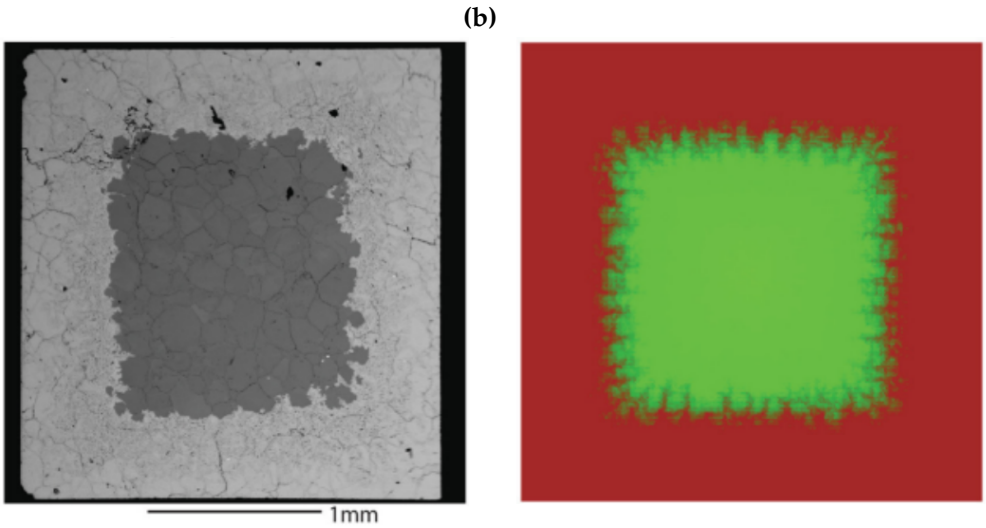

Figure 5.6: Images of (a) experimental and (b) numerical fingers, in the irregular regime, as modelled by Koehn et al. [2021].

where the reaction is localised to the grain boundaries. The irregular front is where our reactive infiltration instability model is most applicable and images of their experimental and numerical reaction fronts is shown in figure 5.6.

Measuring the fingers shown in the reaction fronts in figure 5.6(b), we measure that the finger wavelength ranges between 0.12–0.17mm with a mean wavelength $\lambda = 0.15$mm averaged over the four orthogonal fronts. Image analysis of the experimental results of Koehn et al. [2021] returns approximate wavelengths between 0.19–0.26 mm. Using their reported parameters, $U \approx 1 - 2 \times 10^{-5}$m/s (Koehn et al. [2021], figure 8e), with $D \approx 10^{-10}$ m^2 s^{-1}. Koehn et al. [2021] state that the porosity increase by reaction is $\phi_0 = 0.01 \rightarrow \phi_* = 0.02$, giving $\gamma \approx 0.78$ using the Carman-Kozeny relationship for permeability (as used in their numerical implementation), which predicts $\lambda_* = 0.13 - 0.26$ mm in good agreement with their numerical results. This predicted wavelength is plotted in figure 5.7 correlated against the measured experimental (green squares) and numerical (purple triangles) wavelengths. The result shows order of magnitude agreement, within the predicted range of wavelengths for each of the reaction fronts. The variation of the wavelengths is likely due to contributions of heterogeneity that are not accounted for in our model which are built into the numerical model of Koehn et al. [2021]. There is further work required to understand the interplay of heterogeneities and emergent fingers.

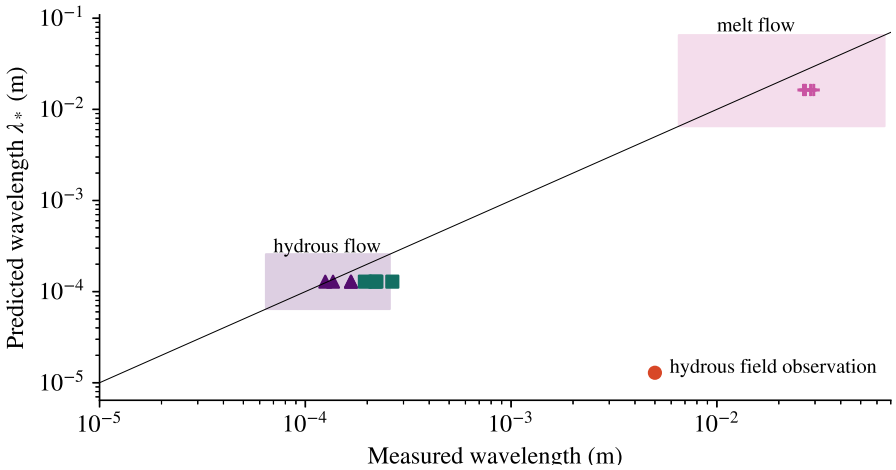

Figure 5.7: Measured wavelengths from each front of the images in (case 1B) figure 5.6 vs predicted wavelength from the model (purple triangles - numerical, green squares - experimental). Shaded boxes indicate the expected range of wavelengths for each of case 1B (purple) and case 2A (pink). Pink crosses indicate the field observations of case 2A (shown in figure 5.8). A red circle indicates the approximate wavelength of a finger we see figure 5.5 (Case 1A).

5.3.3 Case 2A: Melt flow in the lithosphere

Figure 5.8 provides images of two samples taken from the South Island of New Zealand near Lake Grave [Daczko and Halpin, 2009]. In the figure, we can see a vein of white granodioritic rock through the centre of the sample, which provides a high flux of melt into the sample. From the sides of this vein, fluid is driven into the host rock reacting to produce the pink garnet reaction zone that we can see and is the 'reacted material' (as shown schematically in figure 5.2). It is clear to see that the reacted zone does not have a planar interface with the host rock, but instead has undulations indicative of the growth of melt fingers. These are measured to have wavelengths of between 2.6–3.0 cm (measured per reaction front) with an average wavelength of 2.8cm.

Whilst the specific parameters governing the flow that this sample underwent in the lower crust are unknown, we can use approximate values and ranges from existing literature to predict the emergent length scale of reactive infiltration. Scott and Stevenson [1986] give us an expected upwelling flux of magma of $30 - 300$ cm yr^{-1} in porous rocks based upon the pressure gradients generated by the buoyancy of melt flowing in the lithosphere, which we use as an appropriate flux in this scenario after discussion with colleagues

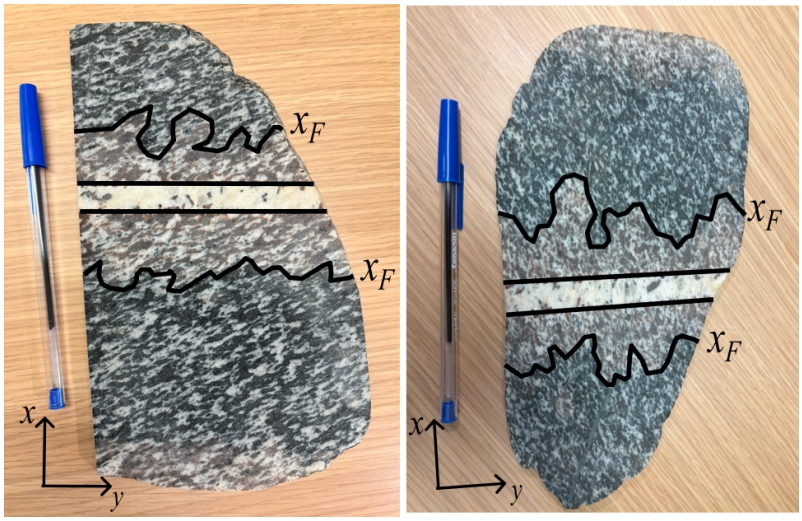

Figure 5.8: Images of rock samples from the South Island of New Zealand, showing evidence of melt fingers in a reaction front driven from a vein. The reaction fronts are overlined in thick black lines (labelled x_F), as are the inflow boundaries from the melt vein. Pen for scale.

[Piazolo, 2025]. Zhang [2010] propose that the average diffusivity of mineral species in melt is $D \approx O(10^{-11})$ m^2 s^{-1}. It is physically reasonable to expect that $W \ll 1$ in this scenario, and whilst we cannot exactly quantify W and thus Δ this allows us to approximate $\Delta \ll 1$. We expected that the initial porosity is approximately 0.05, and can be increased due to reaciton by a factor of 2 to around 0.1 in the reacted layer. Using the simple power-law permeability porosity model $\kappa = \kappa_0\phi^2/\phi_0^2$, these estimates yield $\beta \approx 0.25$. Combining these parameters into (5.63) we can then predict that $\lambda_* = 0.5$–5 cm, in keeping with those samples in figure 5.8. The wavelengths of the fingers shown in figure 5.8, calculated earlier, are plotted as pink crosses in figure 5.7 showing good order of magnitude agreement with the theoretical prediction. As the non-dimensional m_* is bounded by a maximum of $(2\sqrt{3})^{-1}$, the minimum expected $\lambda_* = 1.9$ mm for the application of lithospheric melt flow.

To our knowledge, the application of linear stability results to reaction fronts driven by lithospheric melt infiltration from a vein have not been studied before. The general study of the properties of these areas of reacted rock, figure 5.8, by e.g. Daczko and Halpin [2009] tend to focus on variations in the chemical composition of the reacted region, and demonstrate links between the degree of reaction in the reacted region and their interaction with migrating melt. Other bodies of work that study these regions also

tend to study the effect of changed composition of melt veins and reacted regions on the response of these structures to subsequent deformation [Smith et al., 2015]. We can expect that where these deformations occur, the initial reaction front may be obscured. The pattern of the reaction front, where not subsequently deformed, (overlined in black in figure 5.8) remains to be explored further.

5.3.4 Case 2B: Dunite melt channels

Tabular dunites are well studied geological structures that grow in the mantle. As such these are a departure from the previous case we have discussed, because their growth occurs in a much more dynamic porous host [Kelemen et al., 1995a]. As outlined in section 2.1.2, tabular dunites grow in mantle sections of ophiolites, and are typically elongated bodies contained within surrounding host harzburgite and lherzolite mantle rock. These bodies are thought to be the preserved host rock of melt channels, marking the structure of a previous high porosity channel system which provide a means of high melt extraction within the mantle under mid ocean ridges. Their presence helps to explain a geological phenomenon known as mid-ocean ridge basalt extraction. Mid-ocean ridge basalts are usually undersaturated in orthopyroxene, suggesting a high flux bulk migration through the mantle [Kelemen et al., 1995a] rather than slow percolation through the porous host.

Whilst the exact contributions of reactive infiltration instability, fracturing of the host and stress-driven melt segregation remains unknown, these dunite bodies represent an import feature of melt migration in the lithosphere. The scales on which dunites are observed vary greatly, for example field observation by Braun and Kelemen [2002] of the Oman Ophiolite measured dunites of widths between 3mm and 100 m, and their work suggests that dunites up to 3.5km wide may exist. They compared their findings with the predictions of Aharonov et al. [1995], Spiegelman and Kelemen [2001] for wavelength of reaction infiltration instability in pervasive flow, which predicts a wavelength of 1 km. This is outside of their observed range. Further work by Rees Jones and Katz [2018] which extends Aharonov et al. [1995] by extending the analysis to systematically map the parameter space, predicts wavelengths of between 1.5cm and 55m in dunites, which is consistent with the observations of Braun and Kelemen [2002]. There is an extent to which

matching simple theoretical predictions like ours to geological events is hard because the exact conditions under which geological features form are unknown.

Here, we illustrate one potential case of a dunite formed by the reactive infiltration instability in figure 5.9 which shows a melt vein photographed in the Troodos ophiolite in Cyprus. The melt vein is well developed and has some irregularities but has a broad channel width/wavelength of around $3-10$ cm. Taking the parameters used to study the melt generated fingers shown in 5.8, with the approximate upwelling rate of mantle $U \approx 3{-}300\,\mathrm{cm\,yr^{-1}}$ [Scott and Stevenson, 1986] yields a predicted wavelength of $O(0.5{-}50)$ cm, which this channel lies within. It therefore seem plausible that small scale dunite channels could be formed by the reactive infiltration instability.

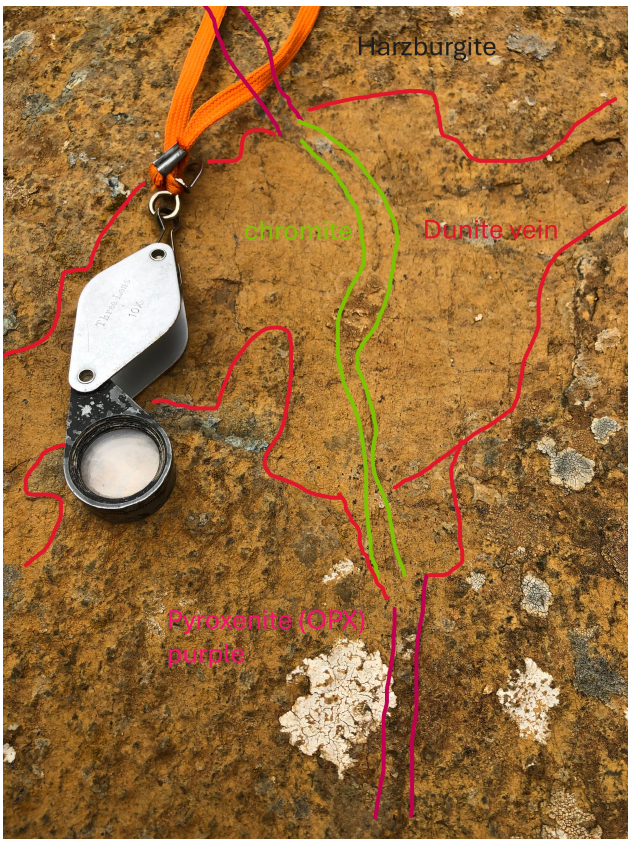

Figure 5.9: Image of a small dunite vein (Troodos ophiolite, Cyprus), showing a developed vein of Dunite roughly horizontally through the image, within a harzburgite host. Chromite and Pyroxenite are thought to be remnants of the reactive melt, whilst dunite is the region of host rock altered by flow. Hand lens for scale (approx 2-3 cm in diameter). (Image Piazolo [2025])

However, it is important to remember that there is a wide range of scales on which dunites are observed in nature and therefore it is unlikely that this simple mechanism can be used

to explain the features of most observed dunites. As we have mentioned, prior work that has focused on understanding how reactive infiltration could effect the scales that emerge in dunites [Aharonov et al., 1995, Rees Jones and Katz, 2018, Rees Jones et al., 2021] have found a wide range of wavelengths of instability which may occur across the parameter space. Importantly Rees Jones et al. [2021] explore how compaction and shearing of the porous host, relevant due to the fact that the upper mantle is not a rigid medium as our model assumes, can alter the preferred wavelength of the instability. There are other factors such as dynamic pressure gradients [Kelemen et al., 1997], flow anisotropy and anisotropy of the porous host due to the texture and alignment of the host crystals [Blackman and Kendall, 1997], and many other effects more could contribute to the varied scales of dunite features that are observed around the world. We therefore conclude that dunite features on the whole are more complexly produced than we are able to predict using a simple preferred wavelength of reactive infiltration.

5.3.5 Case 2C: Experimental reactive infiltration instabilities

A key experimental investigation into melt extraction, Pec et al. [2017] develop a set of experiments that study the generation of focused melt fingers in a porous medium comprising of olivine (10 μm mean particle size), clinopyroxene (3 μm mean particle size) and an alkali basalt powder, with an infiltrating fluid of alkali basalt melt. In figure 5.10 we plot the reported wavelengths of their experiments as green crosses. On the y axis of this plot, we show the predicted wavelength λ_* which is correspondent with the parameters reported for each of these experimental results using the D and U reported in their work. A black line indicates the line $y = x$, and we see clearly that there is a large order of magnitude discrepancy between the two. The parameter Δ is not reported in the work of Pec et al. [2017], so we choose to plot orange crosses for $\Delta = 0$.

The discrepancy between our predicted wavelength and Pec et al. [2017] suggest that this linear stability model is not able to capture some aspects of their experimental setup. We note that broadly the discrepancy is $O(10^3)$ and there are a few potential contributing factors. As noted in Pec et al. [2017], the emergence of fingers in their experiments are generally consistent with the reaction infiltration instability however, matching theoretical

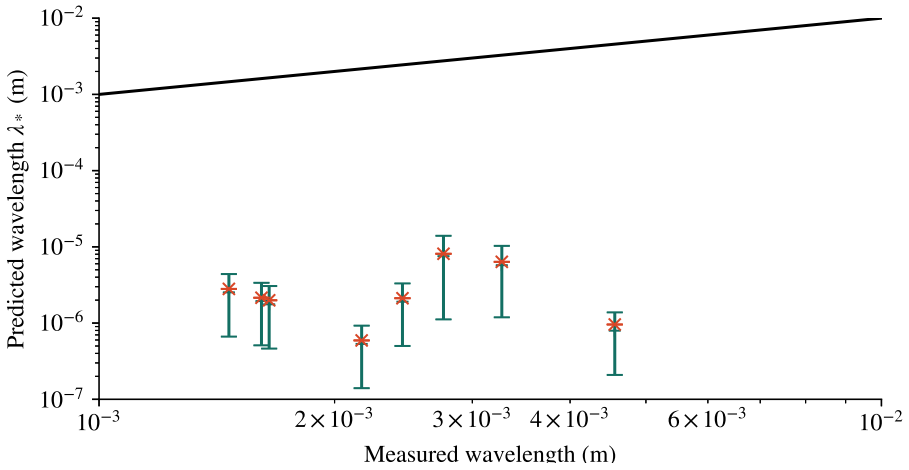

Figure 5.10: Reported finger wavelengths observed in experiments of Pec et al. [2017] (orange crosses), versus the predicted wavelength based on our model. A black line indicates the anticipated correlation.

prediction remains to be done. Our work here is not able to reconcile the two either.

Firstly, the parameters supplied by Pec et al. [2017] for their experiments suggest that their experiments are in the moderate Ω regime as they report $O(10^{-4}) < B < O(1)$, which is clearly a low Ω for the sharp interface theory to be applicable. Achieving large B experimentally is unlikely as this generally requires very long geological timescales for flow. Secondly, Pec et al. [2017] rightly note that their experiments are in small samples where dispersion rather than diffusivity is likely to be the leading order control of mixing throughout the fluid. This is something that our basic model does not account for and may be able to explain some of the discrepancy. Furthermore, our governing model also assumes a rigid porous medium, and as Pec et al. [2017] note, the observed melt channels are formed of pure melt (the maximum porosity is $\phi_* = 1$) and it is very likely that there are compaction and decompaction effects taking place in their experimental set up as the samples are small compared to the compaction length of the host rock.

We note that in later work, Pec et al. [2020] repeated their experimental process for synthetic samples of varying, but known, chemical composition to investigate the effect of specific lithologies on the propensity for melt flow channels to form. Their work found a strong influence of the composition of the host rock, which suggests that understanding the generation of dunites by reactively formed channels may require a more complex

underlying model which accounts for the distribution of different minerals in the host material. This leads us to conclude that the reaction infiltration instability, as modelled in our work, is not likely to be able to capture the dynamics which control the reactive fingers in this case.

5.4 The dispersion relation as a tool for understanding growth of fingers and inference in geology.

In section 5.3, we have begun to use known parameters and timescales in order to predict the wavelength of reactive infiltration instability fingers in samples and experiments for different geological scenarios. This allows us to begin to consider what the linear stability results can tell us about the process that geological samples have undergone. The use of this relation as a tool does require further investigation and understanding of when it is appropriate to use.

5.4.1 What does wavelength tell us about flux, for a given reaction?

Our dimensional expression (5.67) for the wavelength proposes, as shown in figure 5.11, that the preferred wavelength is inversely proportional to flux U and as such this allows us to begin to make comparison of scenarios such as those discussed in section 5.3.3. Where we anticipate γ to be broadly equal in scenarios, we can identify that those cases of larger wavelength fingers would form in the case of small U given the small variance in D expected between cases. Typical values of D could span $O(10^{-11})$ in melt through to $O(10^{-9})$ in hydrous (water based) geological fluids [Zhang, 2010], therefore we plot for these two cases in figure 5.11.

5.4.2 What could observed wavelength tell us about timescales?

In the case of observable fingers, we presume that their observed wavelength is (approximately) the preferred wavelength λ_*. With an idea of D, U, γ, W we can then infer the approximate timescale on which a finger grows. Figure 5.12 shows how the timescale of instability varies with preferred dimensional wavelength for typical melt and hydrous fluids. What we see in figure 5.12 is that the timescale increases with the square of the

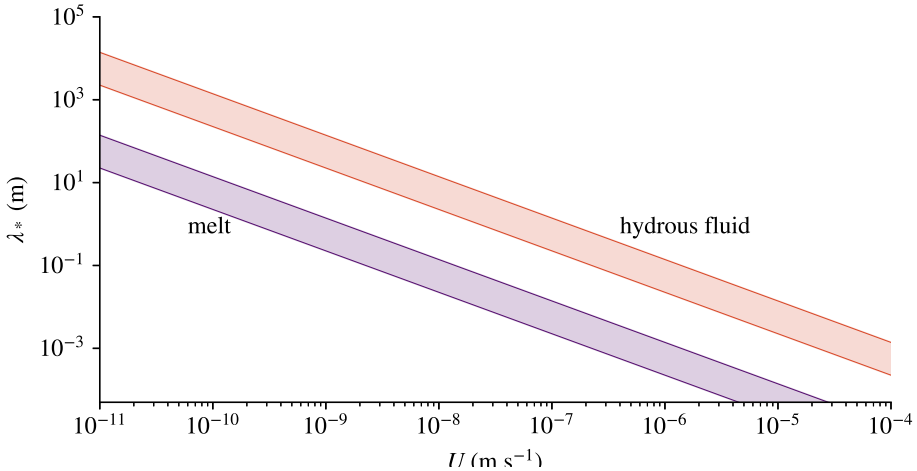

Figure 5.11: Dimensional wavelength, λ_* plotted against the flux to diffusivity ratio U/D which allows us to infer the flux in geological observation where γ and D are known. Plotted here for each fluid for $0.1 < \gamma < 1$.

wavelength, i.e. given the same reactive parameters (γ, W, ϕ_0) we expect that comparing fingers with a wavelength ratio of two suggests that the larger wavelength fingers take four times as long to grow to the same small intrusion length.

5.5 Summary

Our analysis in this Chapter has derived a generalised dispersion relation (5.56) for the linear instability of planar reaction fronts in the *sharp* regime, which is one end member of the stable planar front parameter space. We have shown that in the small acid capacity and small growth rate limits, the dispersion relation derived by Chadam et al. [1986] is recovered in our model, clarifying how the two systems are related. In the limit of small growth rate σ, but without the small acid capacity limit, we have found that the stability of reaction fronts is governed by a single parameter

$$\gamma = \frac{1 - (1-\nu)(1-\Phi)W - \beta}{1+\beta}. \tag{5.69}$$

Practically, given $0 < \Phi, W < 1$ and $\nu \lessapprox 2$, $\gamma > 0$ which suggests that sharp planar fronts in a rigid medium always becomes unstable. Compaction, as studied by Hesse et al. [2011], Rees Jones and Katz [2018] can act to suppress the reactive infiltration instability.

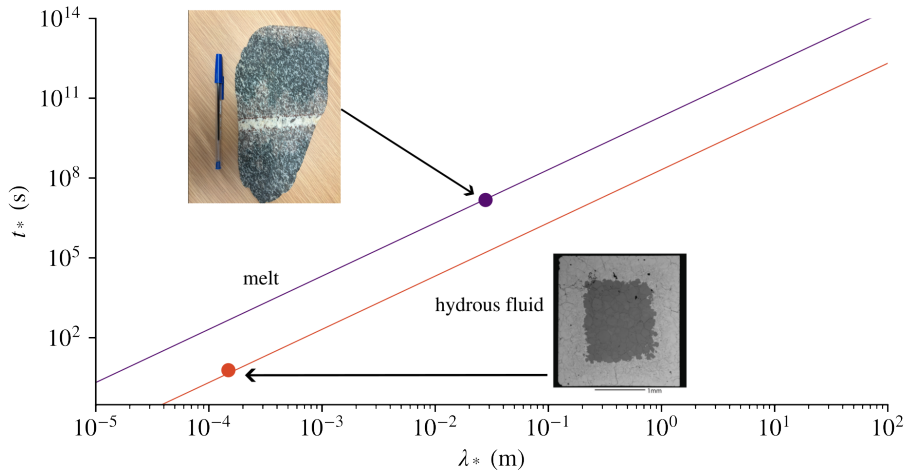

Figure 5.12: The timescale of instability growth versus the preferred wavelength, for melt (purple) and hydrous fluid (orange) assuming $D_{melt} \approx 10^{-11}$ and $D_{hydrous} \approx 10^{-9}$. The effect of γ and W on t_* is minimal and therefore this is a broad representation for $0.1 < \gamma < 1$.

The dimensional wavelength correspondent to the maximum growth rate is given by

$$\lambda_* = \frac{4\pi D\sqrt{1 + 2\frac{\gamma}{1-W}}}{\gamma U}. \tag{5.70}$$

This relationship tells us that higher diffusion D broadens infiltration fingers whilst increased advective flux U, narrows the fingers. This now gives us a tool with which to study reaction fingers.

In the latter portion of this Chapter, we compare the predictions of our model with observations from numerical modelling, experiments and field observation. We found that we are able to predict good order of magnitude agreement with field observations of garnet reaction zones (pictured in figure 5.8) and with the numerical modelling of Koehn et al. [2021] (figure 5.6). Experimental work by Pec et al. [2017] fits our theory less well, and requires further study of additional physical effects such as relaxation of the rigid porous medium that we model throughout this work.

5.6 Contributions of this Chapter

Research Question 4

How does the stability of 1D reaction fronts inform understanding of reactive fronts in geological porous media?

In this Chapter, we have derived a novel dispersion relation for the growth of a linearly unstable front from our general diffusion-limited model, allowing for any Stefan number S_*, and shown that it agrees with Chadam et al. [1986] in the small Stefan number (acid capacity) limit. We begin to use the small S_* limit of this dispersion relation as a tool to quantitatively understand the wavelength of various geological fingers, predicting the expected wavelength for five cases of reactive fingers across the geological field and experiments to understand where the dispersion relation is useful. A key result here has been to begin to develop an understanding of the scenarios in which the model is and is not sufficient on an order of magnitude basis. In particular, the analysis proposes that hydrous fluids tend not to produce reactive fingers in their flow through geological material as the theory predicts pore scale fingers, which do not manifest as reaction fingers. We are also able to motivate future work which can extend this framework to encompass additional physical effects at a later date, given the clear disagreement between some reactive fingers in geosciences and our model.

Tentatively we have used the broad agreement between some field observations and our theory, to begin to consider using the linear stability results as a diagnostic toolkit for understanding the approximate conditions under which such features formed. The simple relationships (figures 5.11 and 5.12) provide an easy way to compare observed reactive fingers based upon their wavelength in order to make comparisons of fluid flux and of the infiltration timescale. There is broad agreement between the predictions of the linear stability and early fingers in section 5.3.3, suggesting that the linear stability could be used for scenarios such as these fingers which are close to their source and have not experienced non-linear feedback. There is future work to be done, in order to develop theoretical predictions which can explain more instances of reactive infiltration such as those experiments carried out by Pec et al. [2017], where the inclusion of additional

physics such as dispersion in porous media, rather than diffusion, and relaxing the rigid medium assumption may be necessary. Studying the full behaviour of the dispersion relation derived in this Chapter also remains to be done.

6

Development and application of a numerical solver for studying reactive infiltration in two dimensions

This Chapter focuses on the development of a numerical solver for studying reactive infiltration in 2D. The numerical method, which uses the method of lines with the method of false transients as an extension of the numerical methods used earlier in this thesis, is validated. Initial numerical results provide support for the linear stability analysis in Chapter 5.

6.1 Introduction

Throughout this thesis so far, we have focused on simple one dimensional geometries in order to study the simplified development of stable reaction fronts and their evolution with time. Chapter 5 moved away from the stable reaction front by conducting a linear stability analysis of the stable front in the diffusion-limited regime to understand how instability grows from the planar front. In this Chapter, we move further from the stable and uniform reaction front by solving the governing system in a 2D domain with applied pressure gradient to provide an initial flow field. This allows us to study the

growth of reactive fronts more complex than the 1D planar front. The motivation for the development of this solver is to be able use it to test the preferred wavelength predicted by the stability analysis, to test the wavelengths to which reaction fronts are stable or unstable, and also to study the effects of different background porosity profiles on the reaction front which develops. This Chapter presents incomplete work which builds on that which has been completed in this thesis and could be further developed. We develop, validate and begin to use a numerical solver for the evolution of a 2D porous medium under an initially linear pressure gradient.

6.2 Two dimensional problem formulation

In a two-dimensional domain, the velocity has 2 components $\boldsymbol{u} = u(x, y, t)\mathbf{e}_x + v(x, y, t)\mathbf{e}_y$ and all variables are functions of position $\boldsymbol{x} = x\mathbf{e}_x + y\mathbf{e}_y$. The system defined by (2.3)–(2.7) then reads

$$\frac{\partial(\phi_* - \phi)}{\partial t} = -kR(c, \phi), \tag{6.1}$$

$$\frac{\kappa(\phi)}{\mu}\left(\frac{\partial^2 p}{\partial x^2} + \frac{\partial^2 p}{\partial y^2}\right) = -(1 - \nu)kR(c, \phi), \tag{6.2}$$

$$\frac{\partial(\phi c)}{\partial t} + \frac{\partial(\phi u c)}{\partial x} + \frac{\partial(\phi v c)}{\partial y} = \frac{\partial}{\partial x}\left(D\phi\frac{\partial c}{\partial x}\right) + \frac{\partial}{\partial y}\left(D\phi\frac{\partial c}{\partial y}\right) - c_R kR(c, \phi), \tag{6.3}$$

$$\phi u = -\frac{\kappa(\phi)}{\mu}\frac{\partial p}{\partial x}, \quad \phi v = -\frac{\kappa(\phi)}{\mu}\frac{\partial p}{\partial y}. \tag{6.4}$$

We specify initial conditions on c and ϕ assuming that the domain is initially reactant free

$$c(\boldsymbol{x}, t = 0) = 0, \quad \phi(\boldsymbol{x}, t = 0) = \Phi(x, y), \tag{6.5}$$

where Φ is some distribution function of the position x, y. For model validation and verification, we will assume that $\Phi(x, y) = \Phi$ a constant. We also impose boundary conditions on c and p. Firstly, we propose a domain in which there is inflow from the

$x = 0$ boundary, with periodic y boundary conditions

$$\frac{\partial f}{\partial y}_{y=0} = \frac{\partial f}{\partial y}_{y=L}, \tag{6.6}$$

for $f = c, p, \phi$. We set the an inlet boundary on $x = 0$, with a pressure P_0 and

$$c(x = 0) = 1, \quad p(x = 0) = P_0, \quad \frac{\partial p}{\partial x}(x = 0) = -1/\kappa(\phi). \tag{6.7}$$

In the far field, we propose that the pressure gradient becomes linear, and the concentration tends to 0

$$\frac{\partial p}{\partial x} = -p'_\infty, \quad c(x \to \infty) \to 0. \tag{6.8}$$

We initialise pressure to satisfy (6.2), the simplest version of which is that pressure is a linear function of x and independent of y

$$p(\boldsymbol{x}, t = 0) = P_0 \left(1 - \frac{x}{L}\right). \tag{6.9}$$

6.2.1 Requirements for closure of the model

In two dimensions, as opposed to one dimension, we require a model for the relationship between permeability and porosity to calculate κ, the permeability of the porous medium. In this Chapter of work we use a simple power-law relationship

$$\kappa(\phi) = \kappa_*(\phi/\phi_*)^n, \tag{6.10}$$

which is consistent with other work e.g. Rees Jones and Katz [2018], and for the numerical results presented in this Chapter we use $n = 2$. As in previous chapters, the chemical reaction rate used is

$$R(c, \phi) = c(1 - \phi)^m, \tag{6.11}$$

where $m = 2/3$.

6.2.2 Dimensionless model

Without loss of generality, we use the advective-diffusive scalings represented by the first row of table 3.1 to conduct a non-dimensionalisation. Thus, we let

$$x, y = \left(\frac{D}{U}\right)(\hat{x}, \hat{y}), \quad t = \left(\frac{D}{U^2}\right)\hat{t}, \quad u = U\hat{u}, \quad v = U\hat{v} \quad c = c_0\hat{c}, \quad \phi = \phi_*\hat{\phi}, \quad p = \frac{D\mu\phi_*}{\kappa_*}\hat{p}.$$

On dropping hats, (6.1)–(6.4) become

$$\frac{\partial\phi}{\partial t} = BSR(c, \phi), \tag{6.12}$$

$$\frac{\partial^2 p}{\partial x^2} + \frac{\partial^2 p}{\partial y^2} = \frac{(1-\nu)BS}{\kappa(\phi)}R(c, \phi), \tag{6.13}$$

$$\frac{\partial(\phi c)}{\partial t} + \frac{\partial(\phi \boldsymbol{u} c)}{\partial x} + \frac{\partial(\phi \boldsymbol{u} c)}{\partial y} = \frac{\partial}{\partial x}\left(\phi\frac{\partial c}{\partial x}\right) + \frac{\partial}{\partial y}\left(\phi\frac{\partial c}{\partial y}\right) - BR(c, \phi), \tag{6.14}$$

$$\phi u = -\kappa(\phi)\frac{\partial p}{\partial x}, \quad \phi v = -\kappa(\phi)\frac{\partial p}{\partial y}, \tag{6.15}$$

where $B = KD/U^2$ is a dimensionless number, $S = c_0/c_R$ is a Stefan number, $\kappa(\phi) = \phi^2/\phi_*^2$ is the functional dependence of permeability on porosity and $R(c, \phi) = cf(\phi)$, with $f(\phi) = (1-\phi)^m$.

6.3 Numerical scheme

First, we set up the numerical scheme which will be used to investigate flow in a 2D domain. This domain is a rectangle, depicted in figure 6.1, with horizontal extent L_x and vertical extent L_y. In the results we present, there is initially a pressure field which varies linearly in the horizontal direction to satisfy (6.13) which for $\nu = 1$ requires $\nabla^2 p = 0$. The pressure is assumed to be uniform in y initally.

As in the 1D case, section 3.2.3, we represent the domain as discrete nodes indexed i in the horizontal and now also k in the vertical for a matrix of size $n \times k$ for each of concentration c, porosity ϕ, and pressure p. Figure 6.2 depicts the arrangement of nodes relative to each other with their indices shown.

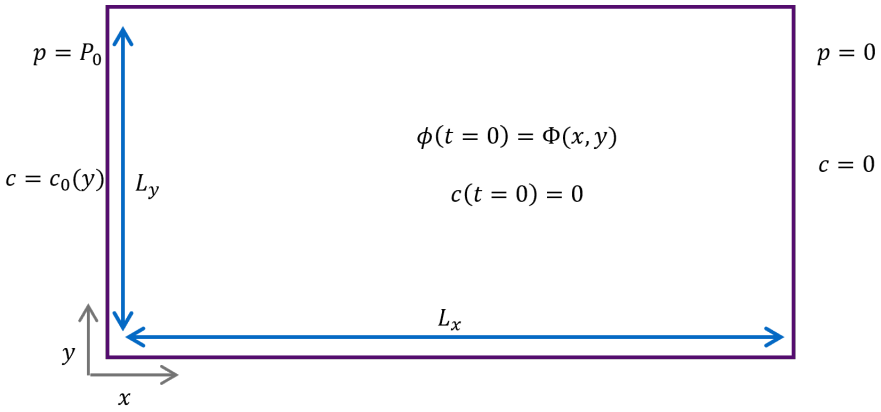

Figure 6.1: Schematic of a 2D numerical domain, initialised with uniform porosity and reactant concentration, showing inlet and outlet boundary conditions and domain dimensions.

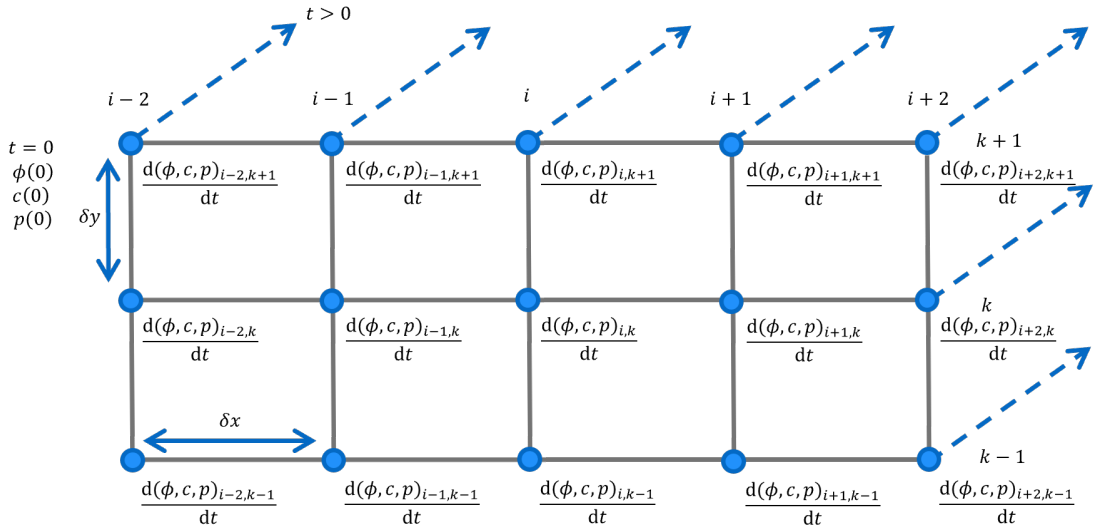

Figure 6.2: Representation of the 2D assignment of index notation to nodes in the 2D solver.

The solution at each point is marched forwards in time with an adaptive time stepping solver, whilst spatial derivatives are calculated as first order finite differences, upwind in x and centred in y. The use of this time-stepping arrangement requires us to implement a method which solves pressure in time also, as we note that (6.13) does not have a time derivative.

6.3.1 The method of false transients

The method of false transients [Mallinson et al., 1973] is a technique for converting an elliptical equation into parabolic equation by the addition of a false transient term. In the case of our model, it is necessary to convert the elliptic equation for pressure,

$$\frac{\partial^2 p}{\partial x^2} + \frac{\partial^2 p}{\partial y^2} = \frac{(1-\nu)BS}{\kappa(\phi)} R(c,\phi), \tag{6.16}$$

into one that can be solved with a time marching formulation by the addition of a false transient $\frac{\partial p}{\partial t}$ term,

$$\frac{\partial^2 p}{\partial x^2} + \frac{\partial^2 p}{\partial y^2} = \frac{(1-\nu)BS}{\kappa(\phi)} R(c,\phi) + \alpha^{-1}\frac{\partial p}{\partial t}. \tag{6.17}$$

We then rearrange to solve

$$\alpha^{-1}\frac{\partial p}{\partial t} = \frac{\partial^2 p}{\partial x^2} + \frac{\partial^2 p}{\partial y^2} - \frac{(1-\nu)BS}{\kappa(\phi)} R(c,\phi), \tag{6.18}$$

in time, which reduces to satisfy (6.13) in the limit of large α. Figure 6.3 verifies that this is the case, showing p at $t = 0.2$ and $t = 1$ for $\alpha = 3, 10, 30, 100$ as thin black lines. These converge towards the $\alpha \to \infty$ solution, shown at each time as thick orange dashed curves as α increases.

6.3.2 Numerical validation of 2D scheme

We must also confirm that the 2D scheme is able to reproduce the 1D dynamics of the model, such that we can be confident in the emergence of 2D effects. To do so, we impose a vertically uniform initial condition under horizontal pressure gradient and plot horizontal profiles of concentration and porosity for comparison to the 1D solutions. Figure 6.4 shows horizontal slices of the 2D solutions as thin black curves, overlaid with

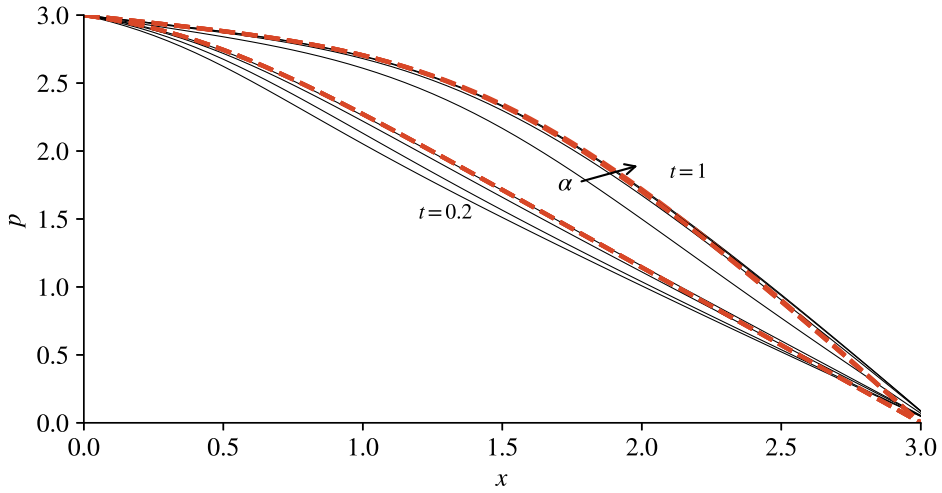

Figure 6.3: The pressure profile by solving (6.12), (6.14) and (6.18) across sample domain for $\nu = 1$, $B = 1$, $S = 1$ and $\phi_0 = 0.5$ for $\alpha = 3, 10, 30, 100$ (black curves) at $t = 0.2$ and $t = 1$ (indicated), demonstrating that the method of false transients relaxes towards the expected solution of the 1D system solved in Chapter 3, plotted for each time step as an orange dashed curve.

thick dashed curves of (a) porosity and (b) concentration at times $t = 0.1 - 1$ showing good agreement of the 1D and 2D models.

6.4 Exploration of two dimensional reaction fronts

In two dimensions, we can study the growth of reaction fronts which are not constrained to the planar, stable, reaction fronts that were studied in Chapters 3 and 4. This is the primary focus of this Chapter and allows us to validate the dispersion relation that is derived in Chapter 5. We can also begin to study the effect of geometrical constraints on the reaction front dynamics, imposing heterogeneity on the initial porosity of the medium.

6.4.1 Emergent dynamics in two dimensions

So far, we are able to verify the stable wavenumbers that are predicted by the dispersion relation (5.58). We model power-law permeability (6.10) ($\kappa = \kappa_0(\phi/\phi_0)^n$) with exponent $n = 2$ and the initial condition $\phi_0 = 0.5$ for $\nu = 1$ yields $\gamma = 0.6$ and $W = 2/3$ for $S = 1$, for which $m_* = 0.14$ (the wavenumber correspondent with the maximum growth rate) and stable wavenumbers are $m \gtrsim 0.37$. We initialise a 2D domain with the linearly perturbed

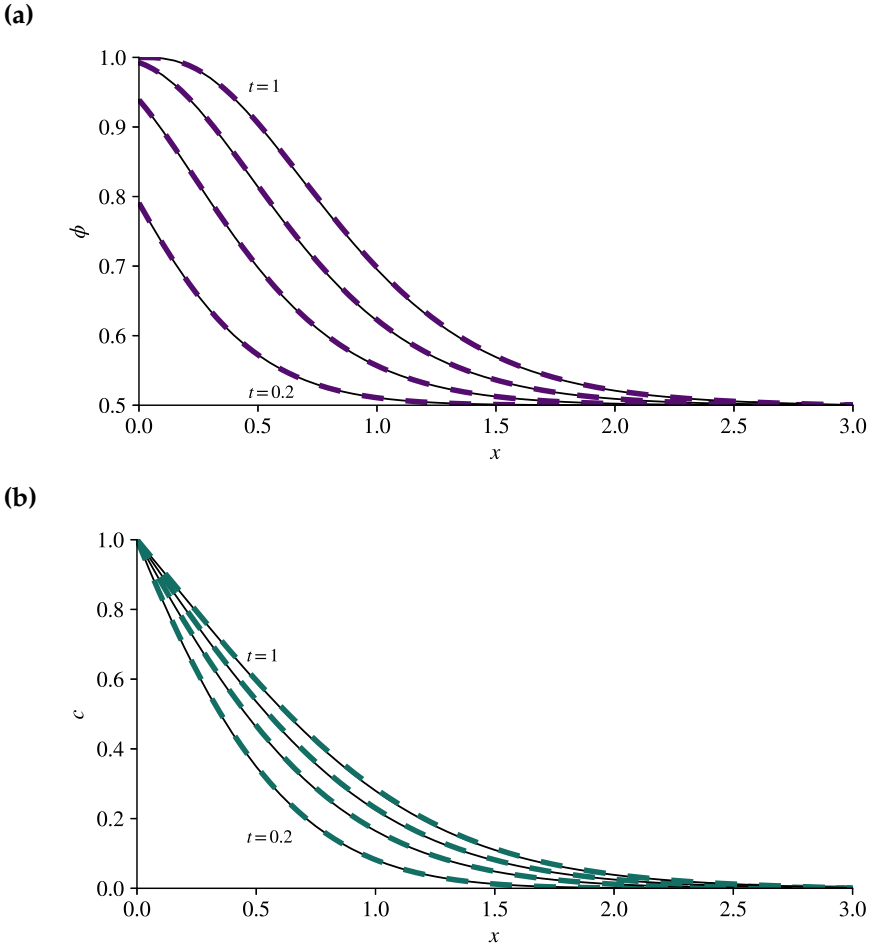

Figure 6.4: (a) Porosity and (b) concentration profiles at times $t = 0.2, 0.4..$ 1 as a black curve. Profiles are generated by the solution of (6.12), (6.14) and (6.18) for parameters $\nu = 1$, $B = 1$, $S = 1$, $\phi_0 = 0.5$ and $\alpha = 100$. A dashed purple (porosity) curve and a green curve (concentration) plotted at each time shows good agreement of the 2D numerical solution with the 1D.

solution (Chapter 5) as shown in figure 6.5. The wavenumber of the applied perturbation is $m = 1$, giving a growth rate of $\sigma = -0.385$. In this instance we would expect for the sinusoidal interface to decay in amplitude with a rate of $\exp \sigma t$. We run the solver for $B = 10$, 30 and 100 ($\Omega \approx 25$, 75 and 252) and $\alpha = 200$, saving the output at time steps of $\delta t = 0.01$.

Figure 6.6 shows contours of porosity (left) and concentration (right) at times $t = 0.15, 0.3,$ and 0.45 where broadly we see a few things that we would anticipate happening. As a continuum model, our solver does not maintain the sharp porosity front of the $\Omega \to \infty$ solution that we use as the initial condition, therefore we expect that in the first few times step, we should see the adjustment of the numerical solution towards the $B = 100$ ($\Omega = 252$) solution, for both the underlying basic state and the $m = 1$ perturbation (i.e. the x dependence of the perturbation will change). As such, looking at the left hand panels of figure 6.6, the interface between fully reacted (green) and unreacted (orange) regions broadens as the solution time increases. Secondly, looking at both panels, we see that the amplitude of the perturbation (i.e. the deviation from 1D flow) appears to be decreasing, smoothing out the y-variation in both fields - this is predicted by the linear stability theory which predicts that the perturbation should decay exponentially with the form $e^{-0.385t}$.

As the solver relaxes the sharp interface, we cannot directly apply the structure functions $f(z)$ that were derived in Chapter 5 for the analysis of the numerical results. Based on the stability analysis we expect that the variables porosity ϕ, concentration c, and pressure p take the general form

$$F(x, y, t) = F_0(x, t) + \delta e^{\sigma t} \cos(my) F(x) \tag{6.19}$$

where $F_0(x, t)$ is the unperturbed planar front evolving in time. We run the numerical solver on the same grid for both the unperturbed and perturbed modes to isolate the perturbation $\delta e^{\sigma t} \cos(my) F(x)$. We can then compute the maximum value of this perturbation across the domain for concentration and evaluate its temporal evolution. This amplitude is plotted in figure 6.7 as black crosses at each time step and demonstrates reasonable agreement with the linear stability theory which is overlaid as a purple curve.

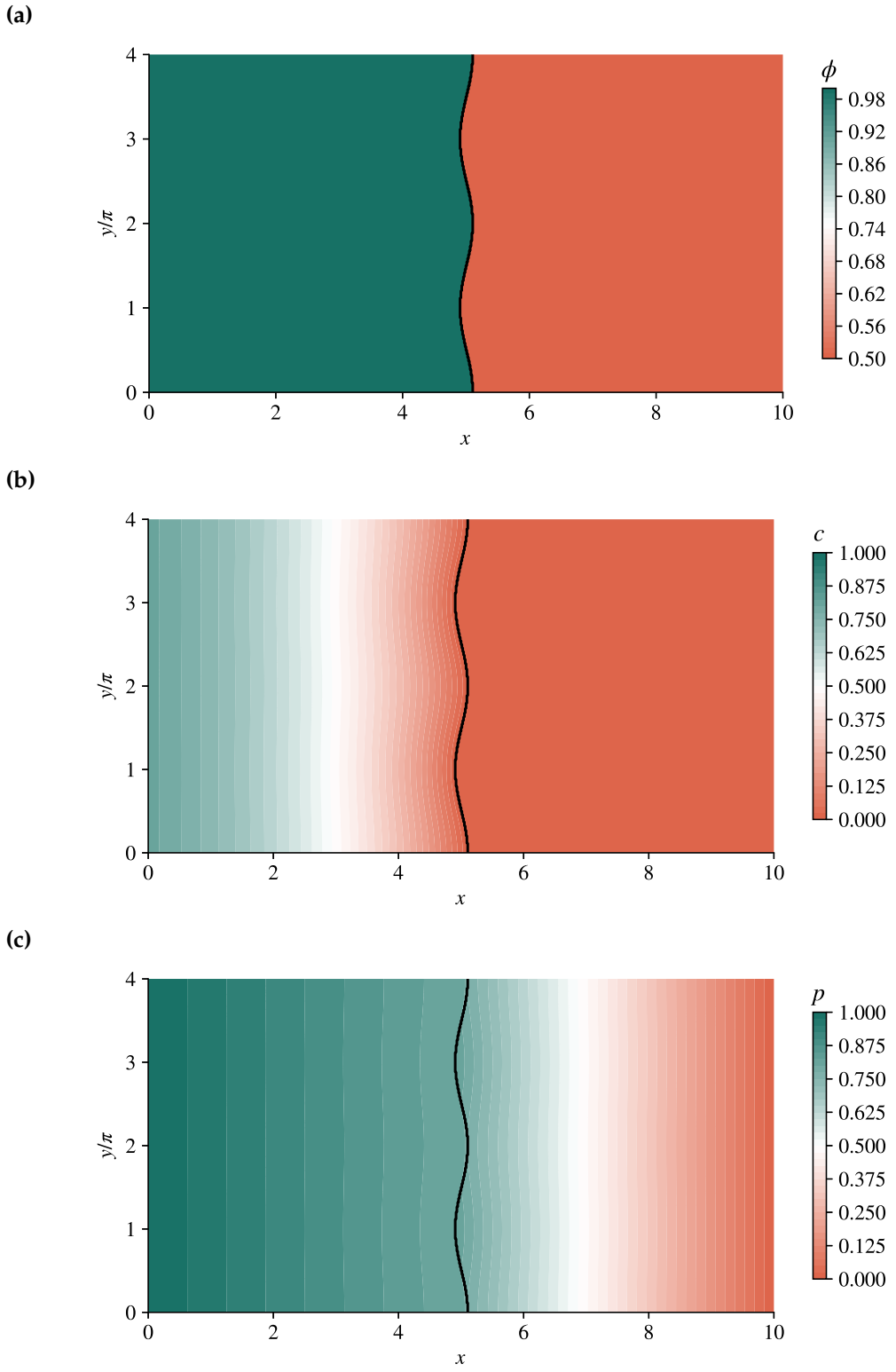

Figure 6.5: Initial conditions for emergent dynamics run for (a) porosity, (b) concentration and (c) pressure (scaled between 0 and 1). The initial condition is the linearly perturbed sharp interface solution for wavenumber $m = 1$. The y axis is scaled by π. The interface position x_F (cf. figure 5.2) is shown on each panel as a black curve.

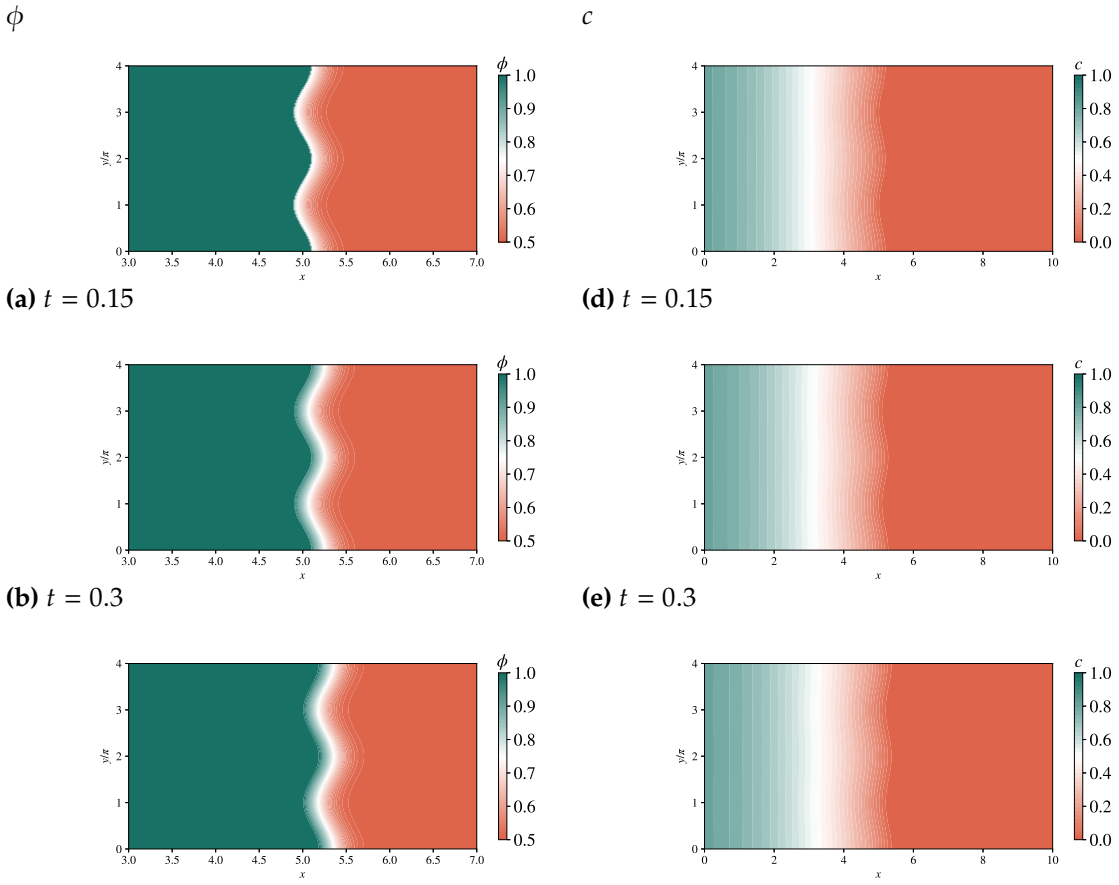

(a) $t = 0.15$ **(d)** $t = 0.15$

(b) $t = 0.3$ **(e)** $t = 0.3$

(c) $t = 0.45$ **(f)** $t = 0.45$

Figure 6.6: Numerical solutions of (6.12), (6.14), and (6.18) describing the evolutions of the (a)-(c) porosity $\phi(x,t)$ and (d)-(f) concentration $c(x,t)$ profiles, at times $t = 0.15, 0.3, 0.45$, from the initial conditions shown in figure 6.5. We set the Stefan number $S = 1$, dimensionless initial porosity $\Phi = 0.5$, $B = 100$, and production ratio $\nu = 1$. In (a) and (d), we see the linear perturbation is still strong, and the porosity step is becoming non-sharp. In (b) and (e) there has been further smoothing of both the porosity step and of the perturbation throughout the domain, these effects continue in panels (c) and (f).

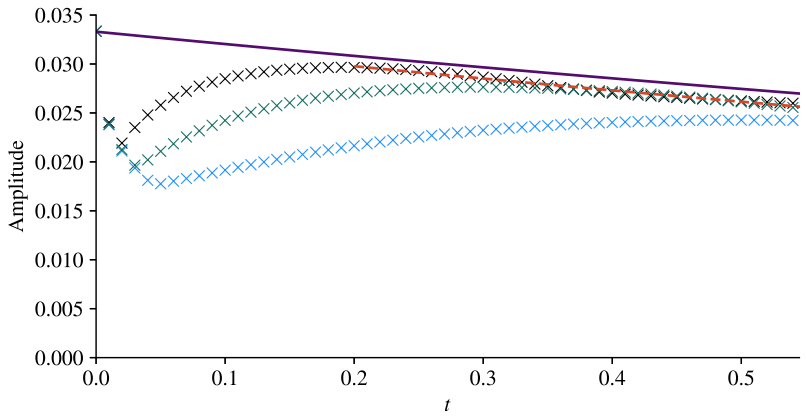

Figure 6.7: Amplitude of the perturbation of the concentration field as a function of time, plotted as black crosses for $B = 100$, green for $B = 30$ and blue for $B = 10$. Overlaid as a purple curve is the decay curve predicted by the linear theory (5.57), showing reasonable agreement in the decaying region for $B = 100$. The red dashed curve is fitted to the numerical data for $B = 100$ in the plotted region and has $\sigma = -0.43$, with is within 15% of the prediction of the linear theory. It is likely that the lack of agreement with the smaller B decay curves is due to deviation from the sharp interface model.

Figure 6.7 also plots the same metric for two simulations with $B = 30$ (green crosses) and $B = 10$ (blue crosses). Comparing the trend of the perturbation for each case, we see that the initial relaxation towards the smooth interface takes longer for smaller B, which one would expect, and that the decay of the perturbation is further from the prediction of the linear theory as B decreases. Intuitively, we can see that this is expected behaviour because the linear theory is derived for $B \to \infty$, and consequently we would expect that it breaks down for sufficiently small B. The discrepancy between the $B = 100$ decay rate and the $B \to \infty$ could also be being influenced by the false transient term, as here $\alpha = 300$ was used, which is larger than B but not necessarily large enough to satisfy $\nabla^2 p = 0$ sufficiently well. The requirement on the exact size of α with respect to B remains to be investigated at the time of submitting this thesis.

6.4.2 Geological evidence of stabilisation due to reactive infiltration

The situation that we have begun to model in this Chapter firstly provides numerical validation of the dispersion relation used in Chapter 5. The initial conditions (figure 6.5) can be thought of as being analogous to a scenario in which reaction fronts begin to emerge in heterogenous media. In this scenario, we would expect initial flow to be focused

in areas of high permeability before being smoothed out by the reaction front growth. Figure 6.8 presents images of garnet reaction zone development from the South Island of New Zealand (cf. figure 5.8) Daczko and Halpin [2009]. We can interpret the different patterns that emerge in these reaction fronts as being related to the timescale over which they have evolved. In field observation, we cannot directly study the evolution of one reaction front in time but must compare reaction fronts that emerge in similar settings.

Reaction fronts which are close to their melt vein (figure 6.8, bottom right) were likely arrested early in their development due to annealing of the melt rock in situ [Smith et al., 2015], or due to exhausting the melt available. Daczko and Halpin [2009] proposed that the supplying melt vein may narrow and close/collapse due to deformation after some amount of melt has passed through, resulting in the reacted GRZ texture appearing in only the immediate vicinity of the melt veins path. These early reaction fronts show perturbations of small wavelengths, (high wavenumber) whereas reaction fronts further from their melt supply (i.e. a larger reacted zone) tend to have smaller perturbations and some longer wavelength variability. This smoothing of the initial perturbations is likely driven by the linear decay of these wavelengths by reactive infiltration, as is seen in the numerical results presented in figure 6.6 for short times.

6.5 Contributions of this Chapter

Research Question 1
How do reaction fronts evolve in fundamental geometries?

This Chapter provides novel numerical support for the linear stability analysis of Chapter 5. We employ the method of lines for the 2D solution of the governing system which underpins all of the analysis in this thesis and validate the novel method of false transients for pressure. Initial results are presented, to explore the emergent dynamics and dynamics which are set by initial conditions, which provide a basis for multiple directions in future research.

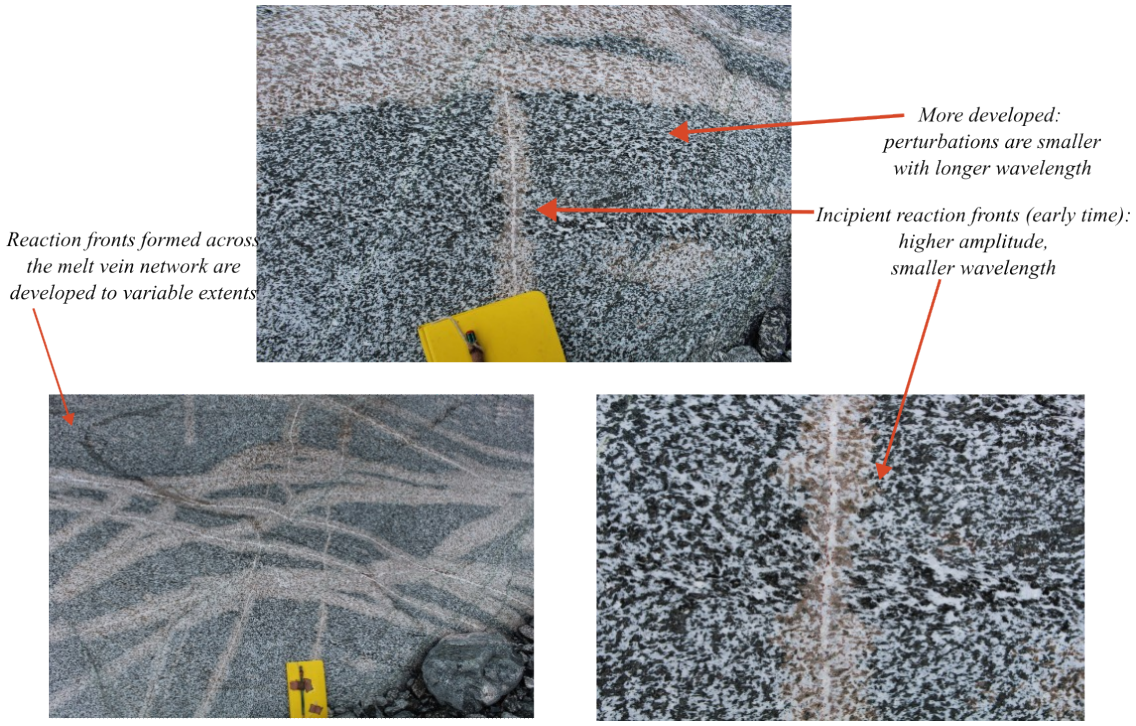

Figure 6.8: Images of reaction fronts generated from melt veins, taken in the South Island of New Zealand [Smith et al., 2015]. These images show that there are initial fingers of reaction, where the reaction front is localised near the melt vein, and in some scenarios where the reaction front has moved further from the inlet of melt, these fingers have decayed to a smooth interface. This can be interpretted as being analogous to the decay of the numerical perturbation, shown in figure 6.6. Images: Piazolo [2025].

Research Question 4

How does the stability of 1D reaction fronts inform understanding of reactive fronts in geological porous media?

In this Chapter, we present an example from geology of a situation in which it seems that initial perturbations to the planar front are smoothed over time. We are able to numerically model a similar scenario in which a linear perturbation to the planar front decays in time in our 2D model. This presents an opportunity for future work in which we can begin to use the 2D model in order to explore and predict the generation of more complex features than the linear stability analysis is capable of.

6.6 Future direction of this work

In this Chapter we have developed a numerical solver based on the method of lines which is able to solve our non-linear partial differential system in a 2D box domain. We have validated the method of lines with the use of false transients and verified that the 2D implementation can recover the expected 1D planar fronts from a stable initial condition. We have then explored use of the solver to model the emergent linear dynamics of reactive fingers which can grow from the instability of the reaction front, beginning by confirming that stable wavenumbers decay towards the stable front. We have as explored the use of the 2D solver to study the effect of porosity variation in the initial porous medium. This creates a wealth of opportunity for exploring the long time dynamics of the reactive system. The most pressing areas of interest to explore are the non-linear and unstable dynamics of finger growth.

Currently, the limiting factor in doing this is the computational efficiency of the numerical code. This code requires further optimisation to run faster, and the most logical first step is parallelisation of the python code, which is outwith the scope of this work. It would then be possible to get meaningful results for understanding the growth of fingers beyond the timescale that the linear regime can predict. If parallelisation of this code does not produce results for a long enough time, then it is now sensible to explore the use of other numerical tools e.g. FEniCs, a finite element based solver or Daedalus, a spectral element

method; both of which are open source codes that we have begun to investigate for the solution of this system of equations.

7

Discussion and conclusions

In this Chapter, I discuss the contributions of this thesis as a whole and discuss how the work could be developed in the future. The research questions of section 1.1 are discussed in view of the whole thesis.

7.1 Discussion

Motivated by the desire to understand patterns in geoscience which have an overarching characteristic of being formed by the flow of a fluid into a porous host rock, this thesis has developed mathematical models of reaction fronts in porous media. Chapters 3 and 4 both explore the steady evolution of reaction fronts in porous media.

In this section I discuss the contributions of the thesis, in terms of the original research questions.

Research Question 1
How do reaction fronts evolve in fundamental geometries?

In this work, I study the evolution of stable reaction fronts in one dimension and in axisymmetry. In Chapter 3 I develop an understanding of how reaction fronts evolve in time across the spectrum of the parameter $B = KD/U^2$, where K is the reactivity of the fluid, D is the diffusivity of the reactive species in the fluid, and U is the flowrate.

The parameter B is effectively the ratio of Damköhler to Péclet number, and in the early time controls their early time evolution through transportive regimes in section 4.3.2. We further study how their late time steady state emergence develops as a function of

$$\Omega = B(S_* + 1)^2 f(\Phi) = B(S_* + 1)^2 f(\Phi),$$

where S_* is the Stefan number and $f(\Phi)$ is a constant derived from the reaction rate dependence on porosity for Φ the initial porosity, partitioning the parameter space into clear asymptotic regimes.

These regimes are the limiting regions from existing models of Chadam et al. [1986] and Hinch and Bhatt [1990] (previously unified for small S_* by Szymczak and Ladd [2013]); and we quantify the values of Ω required to achieve each regime. The requirements on Ω, and the transition scales summarised in table 3.3 provide a toolkit for understanding the conditions under which a stable front has developed.

In Chapter 4 I study the development of reaction fronts in axisymmetry, and develop a novel understanding of the temporal evolution of these across the primary parameter λ before studying closely the late time behaviour for λ, the Péclet number and S, the Stefan number, to produce a regime diagram of axisymmetric behaviour. Prior work on radial geometry, Grodzki and Szymczak [2019], focuses on the instability of the quasi-1D sharp reaction front in axisymmetry. The contributions in this work clarify the parameters required for this to be applicable and study the regions that arise outwith these requirements.

Research Question 2

What controls the extent of chemical and porosity transitions in steadily propagating 1D fronts?

The control of chemical and porosity transition in steady 1D fronts is governed by Ω which contains contributions from B, S, Φ and the reaction rate function. Chapter 3 details this clearly and partitions the parameter space based on Ω, providing physical understanding of the emergent dynamics. The emergent limiting regimes, the sharp regime for $\Omega \to \infty$

and the diffusionless regime for $\Omega \to 0$ reveal that whilst the regimes emerge dependent only on the single parameter Ω, the controlling characteristic differs.

The emergent limiting regimes, the sharp regime for $\Omega \to \infty$ and the diffusionless regime for $\Omega \to 0$ are developed along with the conditions on their self consistency. This work uses a new approach to assessing the transitional length scales of porosity and concentration, extending the previous work of Szymczak and Ladd [2013, 2014] to extend understanding of the control of these regimes beyond B to Ω, we include variable production ratio ν and non-negligible Stefan number S_* to understand how these parameters provide additional control of the emergent regimes.

Research Question 3

How does a radially decaying flux influence reaction fronts versus a constant uniform flux?

Chapter 4 addressed this question by developing an understanding of how reaction fronts driven by a locally injected source evolve. In particular, I find that the temporal evolution of such reaction fronts are controlled by the Péclet number λ. In the case of small λ, after an initially diffusive regime the reaction front enters a self similar reactive-diffusive regime in which the porosity front separates from the origin whilst the concentration front remains broad and spreads across the domain supplying reactant. In this regime, the relative locations of the two transitions separate as well as their length scales.

In the case of large λ, the initial regime is advective, before transitioning to a balanced advective-diffusive-reactive reaction front which is localised away from the origin in both porosity and concentration. Sufficiently far from the origin, the curvature of the reaction front becomes small and the reaction front locally recovers the 1D travelling wave theory in a quasi-steady manner. The novel parameter Ω, derived as a control on 1D fronts in Chapter 3, is an increasing function of time in this geometry and as such, the $\lambda \gg 1$ reaction fronts evolve towards sharp 1D dynamics in time. This is a regime whose stability was previously studied by Grodzki and Szymczak [2019], and here we have bounded the emergence of this regime in the (λ, t) space.

Research Question 4

How does the stability of 1D reaction fronts inform understanding of reactive fronts in geological porous media?

In Chapter 5, I studied the linear stability of 1D reaction fronts in the diffusion dominated limit. Using the dispersion relation that I developed, I have demonstrated that it is physically reasonable to propose that fingers which are observed in two-phase rocks are formed by the reactive infiltration instability. The results of the large Ω stability analysis, which are correspondent with those of Chadam et al. [1986], show good order of magnitude agreement with some wavelengths that are observed in unstable fingers in geosciences, presented in the latter half of Chapter 5. There remain fingers (e.g. those formed in experiments by Pec et al. [2017]) that I am unable to reconcile with the analysis. There are multiple reasons that this could be true, whether the reported (calculated) flowrates in this work are correct in combination with the diffusivity stated, the instability which drives these fingers forms from a different basic state, or if there is additional physics such as the compaction of the porous medium which could be included in the model to more accurately predict the wavelength. Fundamentally, there are many competing factors that can contribute to the size of reactive fingers in geosciences and our results provide some insight into how these may be controlled but cannot capture all physical effects due to the limited physics included in our underlying model.

In Chapter 6, I presented a 2D non-linear numerical model for the governing system throughout this thesis. The development of this model allows us to begin to study reaction fronts and their instability beyond the analytical results provided in the earlier chapters. This ongoing work provides an exciting opportunity to study fingers beyond their initial instability, to explain more complex patterns that are seen in geosciences. The simple numerical results presented in figure 6.7, in conjunction with figure 6.8, already provide a reasonable explanation for why reaction fronts with initial perturbations (driven by initial heterogeneity) seem to evolve to a smooth more planar interface when they are able to mature, owing to the negative growth rate of small wavelength instabilities.

7.2 Limitations

This thesis set out to begin to understand the development of reaction fronts in porous media. From the outset, I focus on simplified theoretical modelling to develop asymptotic regimes and analytical results. As outlined throughout, contributions are made in unification of physical effects in order to understand how regimes fit together and partition the parameter space. Limitations of the chemistry of the model are that the reaction dynamics studied depend on the presence of a single reactant in the fluid, and the presence of reactable solid. This could be extended to include more than one reactant, products and equilibrium dynamics.

Physically, the model assumes that the porous medium is rigid and undeformed under the pressure of flow. This is a simplification for which relaxation would clearly affect the dynamics of the reaction fronts that form. One could speculate for example that gravity would act to compress a granular porous medium as it is consumed, restricting the flow to some extent.

In application to geological settings, this work is limited to two primary scenarios: stable reaction fronts which are supplied by a (roughly) constant source, and unstable planar reaction fronts also supplied by a constant source. The applicability to more complex geometries is therefore limited. This could be improved by further modelling and numerical solution of the conservation model.

In the background to this thesis, we noted that there are two paradigms for the study of reactive infiltration in porous media that are both relevant to the understanding of how reactive infiltration effects geological structures. This thesis focused on laying groundwork for the continued study of the reaction front paradigm, and of course there are going to be scenarios to which the pervasive flow framework and results are better suited. The development of both complementary avenues will provide the richest understanding of reactive infiltration in geological settings.

7.3 Future work

This thesis has predominantly focused on the control of stable one dimensional reaction fronts, and the initial linear instability of one limit of the planar reaction front. In Chapter 5, as in prior work by Szymczak and Ladd [2013], I have come to expect that one dimensional reaction fronts can be unstable for a large proportion of the studied parameter space. The consequences of this are that the planar sharp-interface solutions (Chapter 3) exist for a short time in real life scenarios, but they are still important for understanding and studying the dynamics which emerge in instability. Chapter 5 begins to address the long term instability through the study of initial growth of instability and further work modelling the non-linear feedback of this instability would greatly enhance the understanding of reactive-infiltration instabilities. The further study of this effect in deformable porous media and with more complex chemistry would no doubt elucidate rich insights in occurrences of reactive infiltration instabilities. Chapter 6 outlines the development of a 2D solver which can solve the model presented here with more complex domains and/or initial conditions in order to explore their effects on the reaction front that forms. Future work here can take one of two routes: to study the emergent dynamics of the reactive infiltration instability or to study the effect of infiltration in a non-uniform porous medium.

In Chapter 5, I began to use the results of the linear stability analysis to assess the reactive infiltration instability in geological applications. This shows good applicability in some scenarios, with further investigation required for others, providing a rich basis for future work on applying the relationships derived in this thesis for a wide variety of reaction fronts in porous media. This could include, but is not limited to, hydrothermal reactions, nuclear waste and more instances of aqueous, hydrous and melt flows in the Earth's crust. There is a rich opportunity in considering how the results of Chapters 3 and 4 can be combined to understand the dynamics of reaction fronts in more complex geometries which may result in a combination of steady and unsteady fluxes.

7.4 General conclusions

This thesis has developed understanding of reaction front development in the steady planar and axisymmetric configurations. In planar flow, it has extended understanding of the controlling parameter from

$$B = \frac{KD}{U^2}$$

to the new parameter

$$\Omega = \frac{KD}{U^2}(S_* + 1)^2 f(\Phi),$$

which controls the transition between the two limiting regimes of the sharp porosity transition and the diffusionless regime. We also quantified precisely the magnitude of Ω necessary to enter into each of the limiting regimes. This simple metric is ideal for understanding the regime behaviour of planar fronts. Following on, the axisymmetric analysis has revealed that in this configuration the front regime becomes universally sharp in porosity, but the way in which it does so is governed by the Péclet number, quantifying the contributions of advection vs diffusion in the system. Finally, the work moved on to study the linear instability of the sharp planar front and found that the front is unstable for the majority of fronts. This has been applied to geological observations of reactive instabilities, providing some order of magnitude evidence of the reactive infiltration instability in geoscience applications. There remains a wealth of additional factors that could contribute to the scale of reactive fingers in geosciences, that are not captured by the mathematical model underpinning this work.

This work provides a thorough basis from which to study the 2D non-linear dynamics of reaction fronts, using the numerical method outlined in Chapter 6 to explore dynamics which emerge from those studied here. The qualitative evidence provides a useful basis on which to continue to study these dynamics for applications in geoscience.

Bibliography

M. Abramowitz and I. A. Stegun, editors. *Handbook of Mathematical Functions*. Number 9780486612720 in Applied Mathematics Series 55. NBS, Washington, DC, USA, 1964.

E. Aharonov, J. A. Whitehead, P. B. Kelemen, and M. Spiegelman. Channeling instability of upwelling melt in the mantle. *Journal of Geophysical Research*, 100(B10), 1995. ISSN 01480227. doi: 10.1029/95jb01307.

P. Atkins, J. de Paula, and J. Keeler. *Atkins' Physical Chemistry*. Oxford University Press, Oxford, 12th edition edition, 2022.

N. Beaudoin, A. Hamilton, D. Koehn, Z. K. Shipton, and U. Kelka. Reaction-induced porosity fingering: Replacement dynamic and porosity evolution in the KBr-KCl system. *Geochimica et Cosmochimica Acta*, 232:163–180, 7 2018. ISSN 00167037. doi: 10.1016/j.gca.2018.04.026.

C. M. Bender and S. A. Orszag. *Advanced mathematical methods for scientists and engineers*. Number 007004452X in International series in pure and applied mathematics. McGraw-Hill, New York ;, 1978.

D. Blackman and J.-M. Kendall. Sensitivity of teleseismic body waves to mineral texture and melt in the mantle beneath a mid-ocean ridge. *Philosophical Transactions of the Royal Society A: Mathematical, Physical and Engineering Sciences*, 355:217 – 231, 1997. ISSN 1364-503X.

T. Bo, R. F. Katz, O. Shorttle, and J. F. Rudge. The Melting Column as a Filter of Mantle Trace-Element Heterogeneity. *Geochemistry, Geophysics, Geosystems*, 19(12):4694–4721, 2018. ISSN 15252027. doi: 10.1029/2018GC007880.

M. G. Braun and P. B. Kelemen. Dunite distribution in the Oman Ophiolite: Implications

for melt flux through porous dunite conduits. *Geochemistry, Geophysics, Geosystems*, 3 (11):1–21, 11 2002. ISSN 1525-2027. doi: 10.1029/2001gc000289.

H. S. H. S. Carslaw and J. C. J. C. Jaeger. *Conduction of heat in solids*. Clarendon Press, Oxford, second edition. edition, 1959. ISBN 0198533039.

J. Chadam. Reactive flows in porous media: the reaction infiltration instability. In J. Douglas Jr and U. Hornung, editors, *Flow in Porous Media*, pages 51–58. Springer Basel AG, 1993. ISBN 9783034896825.

J. Chadam, D. Hoff, E. Merino, P. Ortoleva, and A. Sen. Reactive Infiltration Instabilities. *IMA Journal of Applied Mathematics*, 36:207–221, 1986. doi: https://doi.org/10.1093/imamat/36.3.207.

D. B. Clark and R. E. Thompson. Acid Rain, pH & Acidity: A Common Misinterpretation. *The American Biology Teacher*, 51(1):11–13, 1989.

L. A. Coogan, A. D. Saunders, P. D. Kempton, and M. J. Norry. Evidence from oceanic gabbros for porous melt migration within a crystal mush beneath the Mid-Atlantic Ridge. *Geochemistry, Geophysics, Geosystems*, 1(9), 9 2000. ISSN 15252027. doi: 10.1029/2000GC000072.

N. R. Daczko and J. A. Halpin. Evidence for melt migration enhancing recrystallization of metastable assemblages in mafic lower crust, Fiordland, New Zealand. *Journal of Metamorphic Geology*, 27(2):167–185, 2009. ISSN 02634929. doi: 10.1111/j.1525-1314.2009.00811.x.

N. R. Daczko, S. Piazolo, U. Meek, C. A. Stuart, and V. Elliott. Hornblendite delineates zones of mass transfer through the lower crust. *Scientific Reports*, 6, 8 2016. ISSN 20452322. doi: 10.1038/srep31369.

M. Edmonds, K. V. Cashman, M. Holness, and M. Jackson. Architecture and dynamics of magma reservoirs, 2019. ISSN 1364503X.

D. L. Feltham, N. Untersteiner, J. S. Wettlaufer, and M. G. Worster. Sea ice is a mushy layer. *Geophysical Research Letters*, 33(14), 7 2006. ISSN 00948276. doi: 10.1029/2006GL026290.

D. Giordano, J. K. Russell, and D. B. Dingwell. Viscosity of magmatic liquids: A model. *Earth and Planetary Science Letters*, 271(1-4):123–134, 7 2008. ISSN 0012821X. doi: 10.1016/j.epsl.2008.03.038.

P. Grodzki and P. Szymczak. Reactive-infiltration instability in radial geometry: From dissolution fingers to star patterns. *Physical Review E*, 100(3):33108, 2019. ISSN 24700053. doi: 10.1103/PhysRevE.100.033108.

C. G. Groves and A. D. Howard. Early development of karst systems: 1. preferential flow path enlargement under laminar flow. *Water Resources Research*, 30(10):2837–2846, 1994. doi: https://doi.org/10.1029/94WR01303. URL `https://agupubs.onlinelibrary.wiley.com/doi/abs/10.1029/94WR01303`.

A. C. Hack and A. B. Thompson. Density and viscosity of hydrous magmas and related fluids and their role in subduction zone processes. *Journal of Petrology*, 52(7-8):1333–1362, 1 2011. ISSN 14602415. doi: 10.1093/petrology/egq048.

W. M. Haynes. *CRC Handbook of Chemistry and Physics*. CRC Press, 2016. doi: 10.1201/9781315380476.

M. A. Hesse, A. R. Schiemenz, Y. Liang, and E. M. Parmentier. Compaction–dissolution waves in an upwelling mantle column. *Geophysical Journal International*, pages 1057–1075, 2011. doi: 10.1111/j.1365-246X.2011.05177.x.

I. J. Hewitt. Modelling melting rates in upwelling mantle. *Earth and Planetary Science Letters*, 300(3-4):264–274, 2010. ISSN 0012-821X. doi: 10.1016/j.epsl.2010.10.010.

E. J. Hinch and B. S. Bhatt. Stability of an acid front moving through porous rock. *Journal of Fluid Mechanics*, 212:279–288, 1990. ISSN 14697645. doi: 10.1017/S0022112090001963.

A. W. Hofmann. *Chapter 9. Diffusion in Natural Silicate Melts: A Critical Review*, pages 385–418. Princeton University Press, Princeton, 1980. ISBN 9781400854493. doi: 10.1515/9781400854493.385.

B. K. Holtzman, N. J. Groebner, M. E. Zimmerman, S. B. Ginsberg, and D. L. Kohlstedt. Stress-driven melt segregation in partially molten rocks. *Geochemistry Geophysics Geosystems*, 2003. doi: 10.1029/2001GC000258.

K. T. Johnson and H. J. Dick. Open system melting and temporal and spatial variation of peridotite and basalt at the Atlantis II fracture zone. *Journal of Geophysical Research*, 97 (B6):9219–9241, 1992. ISSN 01480227. doi: 10.1029/92JB00701.

R. F. Katz and S. M. Weatherley. Consequences of mantle heterogeneity for melt extraction at mid-ocean ridges. *Earth and Planetary Science Letters*, 335-336:226–237, 2012. ISSN 0012-821X. doi: 10.1016/j.epsl.2012.04.042.

P. B. Kelemen, H. J. Dick, and J. E. Quick. Formation of harzburgite by pervasive melt/rock reaction in the upper mantle. *Nature*, 358(6388):635–641, 1992. ISSN 00280836. doi: 10.1038/358635a0.

P. B. Kelemen, N. Shimizu, and V. J. M. Salters. Extraction of mid-ocean-ridge basalt from the upwelling mantle by focused flow of melt in dunite channels. *Nature*, 375(6534), 1995a. doi: 10.1038/375747a0.

P. B. Kelemen, J. A. Whitehead, E. Aharonov, and K. A. Jordahl. Experiments on flow focusing in soluble porous media , with applications to melt extraction from the mantle. *Journal of Geophysical Research*, 100:475–496, 1995b.

P. B. Kelemen, G. Hirth, N. Shimizu, M. Spiegelman, and H. J. Dick. A review of melt migration processes in the adiabatically upwelling mantle beneath oceanic spreading ridges. *Philosophical Transactions of the Royal Society A: Mathematical, Physical and Engineering Sciences*, 355(1723):283–318, 02 1997. ISSN 1364-503X. doi: 10.1098/rsta.1997.0010. URL `https://doi.org/10.1098/rsta.1997.0010`.

J. Khinast, G. F. Krammer, C. Brunner, and G. Staudinger. Decomposition of limestone: The influence of CO2 and particle size on the reaction rate. *Chemical Engineering Science*, 51(4):623–634, 1996.

A. Klimchouk, D. Ford, A. Palmer, and D. Wolfgang. *Speleogenesis: Evolution of Karst Aquifers*, volume 240, page 527. 12 2000. doi: 10.1016/S0022-1694(00)00341-3.

D. Koehn, S. Piazolo, N. E. Beaudoin, U. Kelka, L. Spruženiece, C. V. Putnis, and R. Toussaint. Relative rates of fluid advection, elemental diffusion and replacement govern

reaction front patterns. *Earth and Planetary Science Letters*, 565, 7 2021. ISSN 0012821X. doi: 10.1016/j.epsl.2021.116950.

L.-C. Kuo and R. J. Kirkpatrick. Kinetics of crystal dissolution in the system diopside-forsterite-silica. *American Journal of Science*, 285(1):51–90, 1 1985. doi: 10.2475/ajs.285.1.51.

N. Li, Y. C. Tou, Y. Deng, J. Li, R. F. Liang, and R. D. An. Heat transfer at ice-water interface under conditions of low flow velocities. *Journal of Hydrodynamics*, 28(4):603–609, 8 2016. ISSN 10016058. doi: 10.1016/S1001-6058(16)60664-9.

Y.-H. Li and S. Gregory. Diffusion of ions in sea water and in deep-sea sediments. *Geochimica et Cosmochimeca Acts*, 38:703–714, 1974.

Y. Liang, A. R. Schiemenz, M. A. Hesse, E. M. Parmentier, and J. S. Hesthaven. High-porosity channels for melt migration in the mantle: Top is the dunite and bottom is the harzburgite and lherzolite. *Geophysical Research Letters*, 37(15):1–5, 2010. ISSN 00948276. doi: 10.1029/2010GL044162.

C. J. Lissenberg, C. J. MacLeod, K. A. Howard, and M. Godard. Pervasive reactive melt migration through fast-spreading lower oceanic crust (Hess Deep, equatorial Pacific Ocean). *Earth and Planetary Science Letters*, 361:436–447, 1 2013. ISSN 0012821X. doi: 10.1016/j.epsl.2012.11.012.

F. J. Lucia. *Origin and petrophysics of dolostone pore space*. Geological Society of London, Jan. 2004. ISBN 978-1-86239-166-6. doi: 10.1144/GSL.SP.2004.235.01.06.

G. D. Mallinson, G. De, and V. Davis. The Method of the False Transient for the Solution of Coupled Elliptic Equations. Technical report, 1973.

D. McKenzie. The generation and compaction of partially molten rock. *Journal of Petrology*, 25(3):713–765, 1984. ISSN 00223530. doi: 10.1093/petrology/25.3.713.

E. Merino and A. Banerjee. Terra rossa genesis, implications for karst, and eolian dust: A geodynamic thread. *Journal of Geology*, 116(1):62–75, 1 2008. ISSN 00221376. doi: 10.1086/524675.

C. R. Meyer and I. J. Hewitt. A continuum model for meltwater flow through compacting snow. *Cryosphere*, 11(6):2799–2813, 12 2017. ISSN 19940424. doi: 10.5194/tc-11-2799-2017.

P. O. Moslet. Field testing of uniaxial compression strength of columnar sea ice. *Cold Regions Science and Technology*, 48(1):1–14, 4 2007. ISSN 0165232X. doi: 10.1016/j.coldregions.2006.08.025.

M. Pec, B. K. Holtzman, M. E. Zimmerman, and D. L. Kohlstedt. Reaction Infiltration Instabilities in Mantle Rocks : an Experimental Investigation. *Journal of Petrology*, 58(5):979–1004, 2017. doi: 10.1093/petrology/egx043.

M. Pec, B. K. Holtzman, M. E. Zimmerman, and D. L. Kohlstedt. Influence of Lithology on Reactive Melt Flow Channelization. *Geochemistry, Geophysics, Geosystems*, 21(8):1–20, 2020. ISSN 1525-2027. doi: 10.1029/2020gc008937.

S. Piazolo. personal communication, 2025.

D. Poulikakos and M. Kazmierczak. Melting of an ice surface in porous medium. *Journal of Thermophysics and Heat Transfer*, 2:352–358, Oct. 1988.

A. Putnis. Fluid-Mineral Interactions: Controlling Coupled Mechanisms of Reaction, Mass Transfer and Deformation. *Journal of Petrology*, 62(12), 12 2021. ISSN 14602415. doi: 10.1093/petrology/egab092.

D. W. Rees Jones and R. F. Katz. Reaction-infiltration instability in a compacting porous medium. *Journal of Fluid Mechanics*, 852:5–36, 2018. ISSN 14697645. doi: 10.1017/jfm.2018.524.

D. W. Rees Jones, H. Zhang, and R. F. Katz. Magmatic channelization by reactive and shear-driven instabilities at mid-ocean ridges: A combined analysis. *Geophysical Journal International*, 226(1):582–609, 7 2021. ISSN 1365246X. doi: 10.1093/gji/ggab112.

A. R. Schiemenz, Y. Liang, and E. M. Parmentier. A high-order numerical study of reactive dissolution in an upwelling heterogeneous mantle-I. Channelization, channel lithology and channel geometry. *Geophysical Journal International*, 186(2):641–664, 2011. ISSN 0956540X. doi: 10.1111/j.1365-246X.2011.05065.x.

D. R. Scott and D. J. Stevenson. Magma ascent by porous flow. *Journal of Geophysical Research: Solid Earth*, 91(B9):9283–9296, 8 1986. ISSN 0148-0227. doi: 10.1029/jb091ib09p09283.

R. H. Sibson. Structural permeability of fluid-driven fault-fracture meshes. *Journal of Structural Geology*, 18(8):1031–1042, 1996.

S. J. Sim, M. Spiegelman, D. R. Stegman, and C. Wilson. The influence of spreading rate and permeability on melt focusing beneath mid-ocean ridges. *Physics of the Earth and Planetary Interiors*, 304:106486, 2020. ISSN 0031-9201. doi: https://doi.org/10.1016/j.pepi.2020.106486. URL `https://www.sciencedirect.com/science/article/pii/S003192011930202X`.

B. Simon. Dissolution rates of NaCl and KCl in aqueous solution. *Journal of Crystal Growth*, 52:789–794, 1981.

J. R. Smith, S. Piazolo, N. R. Daczko, and L. Evans. The effect of pre-tectonic reaction and annealing extent on behaviour during subsequent deformation: Insights from paired shear zones in the lower crust of Fiordland, New Zealand. *Journal of Metamorphic Geology*, 33(6):557–577, 8 2015. ISSN 15251314. doi: 10.1111/jmg.12132.

M. Spiegelman. Physics of melt extraction: theory, implications and applications. *Philosophical Transactions - Royal Society of London, A*, 342(1663):23–41, 1993. ISSN 0962-8428. doi: 10.1098/rsta.1993.0002.

M. Spiegelman and P. B. Kelemen. Causes and consequences of flow organization during melt transport : The reaction infiltration instability in compactible media at the Weizmann Science , problem to viscously deformable media , appropriate to the mental Sciences and through a series of theoretic. *Journal of Geophysical Research: Solid Earth*, 106:2061–2077, 2001.

M. Spiegelman and P. B. Kelemen. Extreme chemical variability as a consequence of channelized melt transport. *Geochemistry Geophysics Geosystems*, 4(July), 2003. doi: 10.1029/2002GC000336.

M. Spiegelman, D. A. May, and C. R. Wilson. On the solvability of incompress-

ible stokes with viscoplastic rheologies in geodynamics. *Geochemistry, Geophysics, Geosystems*, 17(6):2213–2238, 2016. doi: https://doi.org/10.1002/2015GC006228. URL https://agupubs.onlinelibrary.wiley.com/doi/abs/10.1002/2015GC006228.

L. Spruzeniece. *Fluid-Rock Interaction: From simple single crystals to complex natural systems*. PhD thesis, Macquarie University, Sydney, 2016.

P. Szymczak and A. J. C. Ladd. A network model of channel competition in fracture dissolution. *Geophysical Research Letters*, 33(5), 2006. doi: https://doi.org/10.1029/2005GL025334. URL https://agupubs.onlinelibrary.wiley.com/doi/abs/10.1029/2005GL025334.

P. Szymczak and A. J. C. Ladd. Wormhole formation in dissolving fractures. *Journal of Geophysical Research: Solid Earth*, 114(6):1–22, 2009. ISSN 21699356. doi: 10.1029/2008JB006122.

P. Szymczak and A. J. C. Ladd. Instabilities in the dissolution of a porous matrix. *Geophysical Research Letters*, 38, 2011a. doi: 10.1029/2011GL046720.

P. Szymczak and A. J. C. Ladd. The initial stages of cave formation: Beyond the one-dimensional paradigm. *Earth and Planetary Science Letters*, 301(3-4):424–432, 1 2011b. ISSN 0012-821X. doi: 10.1016/J.EPSL.2010.10.026.

P. Szymczak and A. J. C. Ladd. Reactive-infiltration instabilities in rocks . Fracture dissolution. *Journal of Fluid Mechanics*, pages 239–264, 2012. doi: 10.1017/jfm.2012.174.

P. Szymczak and A. J. C. Ladd. Inter-acting length scales in the reactive-infiltration instability. *Geophys. Res. Lett*, 40:3036–3041, 2013. doi: 10.1002/grl.50564.

P. Szymczak and A. J. C. Ladd. Reactive-infiltration instabilities in rocks . Part 2 . Dissolution of a porous matrix. *Journal of Fluid Mechanics*, pages 591–630, 2014. doi: 10.1017/jfm.2013.586.

A. J. Turner, R. F. Katz, M. D. Behn, and T. Keller. Magmatic Focusing to Mid-Ocean Ridges: The Role of Grain-Size Variability and Non-Newtonian Viscosity. *Geochemistry, Geophysics, Geosystems*, 18(12):4342–4355, 2017. ISSN 15252027. doi: 10.1002/2017GC007048.

O. Vanderhaeghe. Migmatites, granites and orogeny: Flow modes of partially-molten rocks and magmas associated with melt/solid segregation in orogenic belts. *Tectonophysics*, 477(3-4):119–134, 11 2009. ISSN 0040-1951. doi: 10.1016/J.TECTO.2009.06.021.

V. Vitagliano and P. Lyons. Diffusion coefficients for aqueous solutions of sodium chloride and barium chloride. *Journal of the American Chemical Society*, 78, 04 1956. doi: 10.1021/ja01589a011.

R. F. Weinberg. Mesoscale pervasive felsic magma migration: alternatives to dyking. *Lithos*, 46(3):393–410, 3 1999. ISSN 0024-4937. doi: 10.1016/S0024-4937(98)00075-9.

R. F. Weinberg and K. Regenauer-Lieb. Ductile fractures and magma migration from source. *Geology*, 38(4):363–366, 2010. ISSN 00917613. doi: 10.1130/G30482.1.

W. White and J. Longyear. Some limitations on speleogenetic speculation imposed by thehydraulicsofgroundwater flow in limestone. *Nittany Grotto Newl*, 10:155–167, 1962.

B. Williams, J. Gidley, R. Schechter, and S. of Petroleum Engineers of AIME. *Acidizing Fundamentals*. Henry L. Doherty Series. Henry L. Doherty Memorial Fund of AIME, Society of Petroleum Engineers of AIME, 1979. ISBN 9780895202055.

M. G. Worster. Solidification of an alloy from a cooled boundary. *J. Fluid Mech*, 167: 481–501, 1986.

Y. Zhang. Diffusion in minerals and melts: Theoretical background. *Reviews in Mineralogy and Geochemistry*, 72:5–59, 2010. ISSN 15296466. doi: 10.2138/rmg.2010.72.2.

Y. Zhang, D. Walker, and C. E. Lesher. Diffusive crystal dissolution. *Contrib Mineral Petrol*, 102:492–513, 1989.

A

Approximating parameters in geological and toy-model settings

This appendix derives illustrative parameter ranges in a selection of applications, which we summarise in table A.1. For melt intrusion in the mantle, fluid magma dissolves solid pyroxene, creating a two-phase reactive flow with mass transfer from solid to liquid. The kinetic constant $k \approx 10^{-12}$–10^{-8} $\mathrm{m^3\,mol^{-1}\,s^{-1}}$ [Kuo and Kirkpatrick, 1985, Zhang et al., 1989] spanning mixed and minimally mixed basalts. The diffusivity of the dissolved species is $D = 10^{-12}$–10^{-10} $\mathrm{m^2\ s^{-1}}$ [Hofmann, 1980]. Melt flux $Q \sim 10^{-8}$–10^{-12} $\mathrm{m\ s^{-1}}$, based on estimates of Aharonov et al. [1995] and Scott and Stevenson [1986]. Studies of mantle dynamics have assumed $\nu = 1$ and Stefan numbers of $S = c_0/c_R \sim 0.1$ for depths of ~ 100 km [e.g. Aharonov et al., 1995, Rees Jones and Katz, 2018]. Analysis of two-phase rock samples yield $\phi_* \approx 10^{-2}$–10^{-1} and $\phi_0 \approx 10^{-3}$–10^{-2} [Johnson and Dick, 1992]. Combining k, c_R and ϕ_*, we obtain $K \sim 10^{-10}$–10^{-1} $\mathrm{s^{-1}}$. Using these values, we estimate possible ranges in the dimensionless parameters of $B \sim 10^{-10}$–10^{6}, $S \sim 0.1$, and $\Phi \sim 0.01$–0.1. For the radial case where λ is the controlling parameter, we estimate $\lambda \sim 10^{-2}$–10^{6}.

A common example of chemical weathering is the dissolution of limestone by carbonic acid to produce calcium bicarbonate. In this instance, calcium bicarbonate is produced;

	Mantle	Chemical weathering	Salt dissolution	Melting ice
K (s^{-1})	10^{-10}–10^{-1}	10^{-5}–10^{-2}	10^{-2}–10^{-1}	10–10^{2}
D ($m^2\,s^{-1}$)	10^{-12}–10^{-10}	10^{-9}	1.5×10^{-9}	1.5×10^{-7}
Q ($m\,s^{-1}$)	10^{-12}–10^{-8}	10^{-8}–10^{-2}	10^{-3}–10^{-1}	10^{-3}–10^{-1}
c_0 (mol m^{-3})	$\sim 0.1\,c_R$	0–10^{3}	0–6.1	
c_R (mol m^{-3})		3×10^{4}	37	
ϕ_0	10^{-3}–10^{-2}	0.1–0.5	0.25–0.5	0–0.2
ϕ_*	10^{-3}–10^{-1}	0.2–0.5	1	1
B	10^{-11}–10^{6}	10^{-10}–10^{3}	10^{-9}–10^{-4}	10^{-4}–10^{1}
S	~ 0.1	0-0.03	0-0.16	0–6
Φ	0.01–0.1	0.5–0.9	0.1	0–0.2
ν	1	0	0.02	0.92
Ω	10^{-4}–10^{5}	10^{-10}–10^{2}	10^{-9}–10^{-5}	10^{-3}–10^{3}
N	0.1	0	0	0–6
λ	10^{-3}–10^{6}	1–10^{5}	10^{5}–10^{8}	10^{3}–10^{6}

Table A.1: Table of illustrative parameter values for four example scenarios described in this appendix. In the case of c_R for mantle, the ratio of c_0 to c_R, approximated from Aharonov et al. [1995] is stated instead of exact values. In the case of melting ice, the surrogates for c_0 and c_R are the sensible heat stored in the fluid and the latent heat required to melt ice, each with units of J m^{-3}. These entries are left blank and the determination of the given range of Stefan numbers in this case is detailed in the appendix.

therefore the reactive term takes the opposite sign. The kinetic rate factor is $k \approx 10^{-9}$–10^{-7} $\mathrm{m^3\ mol^{-1}\ s^{-1}}$ in ideal conditions [Khinast et al., 1996]. The product (calcium bicarbonate) has a diffusivity in water of $D \approx 10^{-9}$ $\mathrm{m^2\ s^{-1}}$ [Li and Gregory, 1974]. The lower bound for flux $Q \approx 10^{-8}$ $\mathrm{m\ s^{-2}}$ based on field measurement of rainfall, the upper bound for flux $Q \lesssim 10^{-2}$ $\mathrm{m\ s^{-2}}$ based on forced flow. The average concentration of fully saturated calcium bicarbonate in water is $c_0 \approx 10^3$ $\mathrm{mol\ m^{-3}}$ [Clark and Thompson, 1989]. In this case, $c_R \approx 3 \times 10^4$ $\mathrm{mol\ m^{-3}}$, which is the concentration produced by dissolving one unit volume of solid calcium bicarbonate. Values of $\phi_0 \approx 0.05$–0.5 [Lucia, 2004] and $\phi_* \approx 0.2$–1 reflect the large variation in overall rock composition from partial to pure calcium carbonate. Combining k, c_R and ϕ_*, we obtain $K \sim 10^{-5}$–10^{-2} $\mathrm{s^{-1}}$. The dissolution of calcium carbonate leads to a negligible increase in fluid volume upon dissolution, $\nu \approx 0$. Using the ranges of parameters above, we estimate $B \sim 10^{-10}$–10^{2}, $S \sim 0$–0.03, and $\Phi \sim 0.5$–0.9. For the radial case where λ is the controlling parameter, we estimate $\lambda \sim 1$–10^5.

For an illustrative physical example of dissolving a bed of salt granules, we use the chemistry of sodium chloride for which $D \approx 1.5 \times 10^{-5}$ $\mathrm{m^2\ s^{-1}}$ [e.g. Vitagliano and Lyons, 1956, Simon, 1981]. For the laboratory scale, we take $Q \lesssim 0.1$ $\mathrm{m\ s^{-1}}$. Sodium chloride has a density of 2.2 $\mathrm{g\ cm^{-3}}$ and a loose packed density of 1.1 $\mathrm{g\ cm^{-3}}$ [Haynes, 2016] giving $\phi_0 \approx 0.5$. Spherical packing gives a minimum of $\phi_0 = 0.25$. Allowing for differing mixtures of reactable pure salt and an unreactable solid (e.g. interspersed sand grains), $\phi_0 < \phi_* < 1$. Aqueous solutions of sodium chloride have concentrations over the range of $c_0 \approx 0$–6.1 $\mathrm{mol\ m^{-3}}$ and the molarity of solid sodium chloride is $c_R \approx 37$ $\mathrm{mol\ m^{-3}}$ [Haynes, 2016]. Combining k, c_R and ϕ_*, we obtain $K \sim 10^{-2}$–10^{-1} $\mathrm{s^{-1}}$. Using the ranges of parameters above, we estimate $B \sim 10^{-9}$–10^{-4}, $S \sim 0$–0.16, and $\Phi \sim 0.1$. For the radial case where λ is the controlling parameter, we estimate $\lambda \sim 10^5$–10^8.

In a scenario of melting porous ice, the rate constant k for transfer of heat from water to ice is the heat transfer coefficient. The governing equation for heat in the fluid is given by

$$\frac{\partial \phi c_p T_f}{\partial t} + \boldsymbol{\nabla} \cdot (\rho \boldsymbol{u} \rho c_p T_f) = \boldsymbol{\nabla} \cdot (D \phi \boldsymbol{\nabla} T_f) - k c_R(T_f) f(\phi) \tag{A.1}$$

where $c_p T_f$ is the fluid temperature which is analogous to c, c_p is the specific heat capacity of water, and c_R is the latent heat capacity of ice. This assumes that the host ice is at 0∘ celcius for simplicity. In the event of colder ice, the reactive consumption term would become more complex and we would also need to conserve heat in the solid host which is beyond the scope of this work. Experiments by Li et al. [2016] give $k \approx 1.1 \times 10^{-3}$ m^{-3} s^{-1}. The thermal diffusivity of water is $D \approx 0.15 \times 10^{-6}$ m^2 s^{-1}. We take $Q \lesssim 0.1$ m s^{-1}, allowing for fast and slow percolation rates. The fast percoluation rate is calculated as we did for dissolving salt, by an upper bound of the velocity of water driven by 0.1 m of hydrostatic pressure. Field testing of porous sea ice [Moslet, 2007] suggest a range of $\phi_0 \approx$ 0–0.2 is appropriate for sea ice and we anticipate similar values for porous fresh water ice. In the case of sea ice, the exact reaction would of course be more complex than is outlined here due to saline and salt dissolution effects. The maximum porosity $\phi_* = 1$ for pure ice. For melting, the analogue of c_0 for incoming warm water is the enthalpy, equal to the integral of specific heat capacities with respect to temperatures between the melting temperature of the porous solid and the temperature of the incoming fluid. For water introduced into the medium with temperatures between 0–100°C, we obtain $c_0 =$ 0–10^5 J m^{-3} where c_0 increases with fluid temperature. Assuming the ice is at 0°C, the latent heat required to melt 1 m^3 of ice is $c_R \approx 70 \times 10^3$ J m^{-3}. Combining k, c_R and ϕ_*, we obtain $K \sim$ 10–10^2 s^{-1}. Using the ranges of parameters above, we estimate $B \sim 10^{-4}$–10^1, $S \sim$ 0.01–6, and $\Phi \sim$ 0–0.2. For the radial case where λ is the controlling parameter, we estimate $\lambda \sim 10^3$–10^6. Large S is correspondent to hot water and therefore not typical in the natural environment.

B

Asymptotics of the finite-interval Gamma function

The integral which features in the late time sharp solutions is written

$$I(\tfrac{1}{2}\lambda, a, b) = \int_a^b u^{\frac{1}{2}\lambda - 1} e^{-u}\, \mathrm{d}u = \int_a^b u^{-1} e^{\psi(u)}\, \mathrm{d}u, \tag{B.1}$$

where $\psi(u) = \frac{1}{2}\lambda \log u - u$. The above forms an integral of Laplace form for which the large-argument asymptotics ($\Lambda \to \infty$) can be established using the techniques of Watson's lemma and Laplace's method, dependent on whether the extremum of the function $\psi(u)$ over the integration interval $u \in [a, b]$ lies on the boundary of the integration interval or interior to it. The function $\psi(u)$ contains a single turning point u_0 at $\psi'(u_0) = 0$ given by $u_0 = \lambda/2$. Thus, the relevant representation of $\psi(u)$ for determining the asymptotic expansion of I in these respective cases is:

$$I(\tfrac{1}{2}\lambda, a, b) \sim \begin{cases} g(a) \displaystyle\int_a^\infty e^{\psi(a) + \psi'(a)(u-a)}\, \mathrm{d}u & (a, b > u_0) \\ g(u_0) \displaystyle\int_{-\infty}^\infty e^{\psi(u_0) + \frac{1}{2}\psi''(u_0)(u-u_0)^2}\, \mathrm{d}u & (a < u_0 < b), \\ g(b) \displaystyle\int_{-\infty}^b e^{\psi(b) + \psi'(b)(u-b)}\, \mathrm{d}u & (a, b < u_0). \end{cases} \tag{B.2}$$

where $g(u) = 1/u$. Noting that $\psi' = \frac{1}{2}\lambda u^{-1} - 1$ and $\psi'' = -\frac{1}{2}u^{-2}$ and evaluating the integrals we obtain the general composite expression for the leading-order asymptotic forms of I, namely,

$$I(\tfrac{1}{2}\lambda, a, b) \sim \begin{cases} \left(a - \frac{1}{2}\lambda\right)^{-1} a^{\frac{1}{2}\lambda} e^{-a} & (\tfrac{1}{2}\lambda < a < b) \\ \sqrt{2\pi}\, \left(\frac{1}{2}\lambda\right)^{\frac{1}{2}(\lambda-1)} e^{-\frac{1}{2}\lambda} & (a < \tfrac{1}{2}\lambda < b), \\ \left(\frac{1}{2}\lambda - b\right)^{-1} b^{\frac{1}{2}\lambda} e^{-b} & (a < b < \tfrac{1}{2}\lambda). \end{cases} \tag{B.3}$$

C

Advective-diffusive Stefan conditions at interfacial porosity transitions

This appendix derives a general Stefan condition applicable for asymptotic regimes where the porosity step is treated as interfacial that allows for diffusive as well as advective transport through the interface, as arises in sections 3.3.1 and 3.4.2.

The total rate of transport of reactant mass in the frame of the front is given, in terms of dimensional variables, by the mass flux

$$F_N(t) = (u - \dot{x}_N)\phi c - D\phi\frac{\partial c}{\partial x} \qquad \text{at } x = x_N(t), \tag{C.1}$$

encompassing both advective and diffusive transport. The resultant consumption of solid volume (per unit area) is $(\phi_* - \phi_0)\dot{x}_N$ equal to $F_N(t)/c_R$. It follows that

$$\dot{x}_N = \frac{1}{(\phi_* - \phi_0)c_R}\left((u - \dot{x}_N)\phi c - D\phi\frac{\partial c}{\partial x}\right) \qquad \text{at } x = x_N(t). \tag{C.2}$$

Upon making $\dot{x}_N$ the subject of the above, we obtain

$$\dot{x}_N = \frac{\phi\left(uc - D\dfrac{\partial c}{\partial x}\right)}{(\phi_* - \phi_0)c_R + \phi c} \qquad \text{at } x = x_N(t). \tag{C.3}$$

The above forms a generalised Stefan condition that accommodates both diffusion and advection of reactant towards a moving interfacial porosity transition.

Section 3.3.1 identified an intermediate time-dependent reactive-diffusive regime in which the frontal porosity step is effectively interfacial relative to the diffusive lengthscale. For this regime, we neglect the advective contribution to (C.3) and apply the continuity condition $c(x_N, t) = 0$, for which (C.3) reduces to

$$\dot{x}_N = \frac{-D}{c_R(\phi_* - \phi_0)} \frac{\partial c}{\partial x} \qquad \text{at } x = x_N(t), \tag{C.4}$$

forming the classical diffusive Stefan condition, represented by (3.31) and (3.55).

The result of (C.3) can also be used to recover the rate of advancement of the travelling wave state U represented non-dimensionally by (3.41). Upon setting $u = Q/\phi_*$ and $c = c_0$, corresponding to the prescribed upstream flux conditions, we obtain the reactant flux towards the transition as $F = (U - V)\phi_* c_0$. Equation (C.3) then yields

$$\dot{x}_N = V = \frac{S_*}{(1 + S_*)} U, \tag{C.5}$$

which gives the dimensional version of (3.41).